Technische Universität München
TUM School of Natural Sciences

Chemical proteomic studies into the human side-effects of fluoroquinolone antibiotics and elucidation of the dual mode of action of novel indolin-2-one nitroimidazole antibiotics

Dissertation zur Erlangung des akademischen Grades eines Doktors der Naturwissenschaften von

Till Nicolas Reinhardt

München 2023

Technische Universität München

TUM School of Natural Sciences

Chemical proteomic studies into the human side-effects of fluoroquinolone antibiotics and elucidation of the dual mode of action of novel indolin-2-one nitroimidazole antibiotics

Till Nicolas Reinhardt

Vollständiger Abdruck der von der TUM School of Natural Sciences der Technischen Universität München zur Erlangung des akademischen Grades eines

Doktors der Naturwissenschaften (Dr. rer. nat.)

genehmigten Dissertation.

Vorsitz:	Prof. Dr. Cathleen Zeymer
Prüfer*innen der Dissertation:	1. Prof. Dr. Stephan A. Sieber
	2. Prof. Dr. Michael Groll

Die Dissertation wurde am **14.08.2023** bei der Technischen Universität München eingereicht und durch die TUM School of Natural Sciences am **22.09.2023** angenommen.

Für meine Eltern, Familie und Freunde

"Science knows no country because knowledge belongs to humanity and is the torch which illuminates the world."

– Louis Pasteur

Danksagung

Viele großartige Menschen haben mich auf dieser abenteuerlichen Reise unterstützt, ohne die all das nicht möglich gewesen wäre und die sie zu einem unvergesslichen Erlebnis gemacht haben. An dieser Stelle möchte ich mich sehr herzlich bei ihnen bedanken:

Zuallererst möchte ich mich bei meinem Doktorvater *Prof. Stephan Sieber* für seine Unterstützung bei den Projekten und auch abseits davon herzlich bedanken. Vielen Dank für die Möglichkeit an den interessanten und abwechslungsreichen Projekten zu arbeiten, für dein großes Interesse und deinen Glauben an die Projekte, die vielen Anregungen und das entgegengebrachte Vertrauen. Außerdem vielen Dank für die wissenschaftlichen Freiheiten eigene Ideen einzubringen und die Möglichkeiten die Forschung auf internationalen Konferenzen zu präsentieren.

Außerdem geht mein herzlicher Dank an die Prüfungskommission, *Prof. Cathleen Zeymer* und *Prof. Michael Groll* für die Begutachtung und Prüfung dieser Dissertation. Für die kritische Korrektur dieser Arbeit und die guten Anmerkungen danke ich *Konstantin Eckel*, *Dietrich Mostert*, *Michael Zollo*, *Max Bottlinger* und *Michaela Fiedler*.

Für die gemeinsame Arbeit an dem Nitroimidazol-Hybrid Projekt danke ich insbesondere *Kyu M. Lee*, der das Projekt initiiert, gestartet und maßgeblich vorangetrieben hat, bevor ich es übernommen habe und wir es zusammen erfolgreich publiziert haben. Ein ganz großer Dank auch an alle anderen großartigen Kollaborationspartner auf diversen Projekten, mit deren Kompetenz, Einsatz und Mithilfe die diverse und aufregende Forschung überhaupt möglich wurde. *Lukas Niederegger* und *Prof. Corinna Hess* danke ich für die Hilfe bei den CV-Messungen. Bei *Nina Bach* möchte ich mich ganz herzlich bedanken für ihre Hilfe und Motivation am gemeinsamen Fluoroquinolone-Projekt. In diesem Kontext geht mein Dank insbesondere auch an *Adrian Jauch* und *Prof. Stefan Zahler* für die mitochondrialen Isolierungen und Messungen und an *Franziska Traube* für die FACS- and epigenetischen Marker-Messungen. Die herausragende Zusammenarbeit hat mir sehr viel Spaß gemacht. *Sigrid Mueller-Deubert* und *Prof. Denitsa Docheva* danke ich besonders für die Hilfe bei Experimenten zu MMPs und die Bereitstellung der Ligament-Zelllinien. Vielen Dank auch an *Timo Risch* für seine Hilfe bei SCARB1. Bei *Alex Rothemann* und *Prof. Jan Riemer* bedanke ich mich für ihren fortwährenden Einsatz bei der Validierung von AIFM1. An *Prof. Michael Groll* ein großer Dank für die Hilfe und seinen persönlichen Einsatz bei der Klonierung, Expression und Aufreinigung von IDH2, die sicherlich auch noch glücken wird.

Insbesondere gilt mein Dank auch meinen PraktikantInnen und StudentInnen, die in ihren Forschungspraktika und Abschlussarbeiten großartige Hilfe und Motivation an den Projekten gezeigt haben und deren Betreuung mir besonders viel Spaß gemacht hat. Vielen Dank, *Lei*, *Brigit*, *Constantin*, *Emilia*, *Luna*, *Philipp*, *Felicia*, *Luis*, *Michaela*, *Yassmine* und *Martin*.

Für die arbeitskritische Organisation, Administration und Hilfe im Labor danke ich *Mona Wolff*, *Katja Bäuml*, *Nina Bach*, *Barbara Seibold* und *Christina Brumer*. Vielen Dank für eure Magie, ohne die wir im Chaos versinken würden.

Bei *Annina Steinbach* und *Dominik Schum* bedanke ich mich für die gute Zusammenarbeit und vielen Stunden beim Troubleshooting am TimsTOF Blauwal und der HPLC. Vielen Dank *Josef Braun* für das gemeinsame, oft haarige Putzen des Chewies und *Jan-Niklas Dienemann* für die Zusammenarbeit in der Zellkultur.

Ein großer Dank auch an alle anderen KollegInnen, die bisher unerwähnt geblieben sind. Eure Hilfsbereitschaft schätze ich sehr und die gemeinsamen Aktionen abseits der Forschung haben mir sehr viel Spaß gemacht. Ohne euch wäre die Atmosphäre in der Arbeitsgruppe nicht so unvergleichlich freundschaftlich und großartig. Vielen Dank *Davide Boldini*, *Max Bottlinger*, *Tao Wang*, *Angela Weigert Muñoz*, *Laura Eck*, *Wei Ding*, *Konstantin Eckel*, *Katrin Eisenmenger*, *Yassmine El Harraoui*, *Martin Köllen*, *Franziska Elsen*, *Maximilian Schuh*, *Alexandra Geißler*, *Markus Schwarz*. Ich wünsche euch viel Erfolg für eure Promotion und viel Freude auf eurem weiteren Weg.

Auch bei allen Alumni des AK Siebers und AK Hackers möchte ich mich herzlich bedanken, von denen ich so viel gelernt habe, die immer mit Rat und Tat zu Seite standen, und mit denen ich eine so gute Zeit hatte. Vielen Dank *Stephan Hacker*, *Thomas Gronauer*, *Markus Lakemeyer*, *Philipp Le*, *Pavel Kielkowski*, *Barbara Eyermann*, *Anja Fux*, *Katja Gliesche*, *Volker Kirsch*, *Jonas Drechsel*, *Ines Hübner*, *Mathias Hackl*, *Christian Fetzer*, *Carolin Gleißner*, *Dóra Balogh*, *Theresa Rauh*, *Patrick Allihn*, *Patrick Zanon*, *Franziska Mandl*, *Isabel Wilkinson*, *Lisa Lewald*, *Stuart Ruddell*, *Martin Pfanzelt* und *Robert Macsics*.

Für die unvergessliche Zeit in Lab D mit bester Laune und Musik bis an die Schmerzgrenze danke ich *Anja Fux*, *Volker Kirsch*, *Ines Hübner*, *Katja Bäuml*, *Robert Macsics*, und den Nachfolgern *Alexandra Geißler* und *Konstantin Eckel*. In der neuen CPA-Sitzecke danke ich *Max Bottlinger*, *Michael Zollo*, *Angela Weigert Muñoz*, *Yassmine El Harraoui* und *Franziska Elsen* für die gute Stimmung, die Lab D-Playlist bleibt euch ja auch erspart.

Auch abseits der Forschung und Uni danke ich *Konstantin Eckel* für das ein oder andere „*Herrlisch*“ und „*Ärgerlisch*“, *Josef Braun* für Erinnerungen auf der Alm und *Markus Schwarz* und *Dietrich Mostert* für den besonderen Humor (it´s a YES from me!), der einfach nur gute Laune macht.

Fürs Schwitzen beim Radeln, Bouldern, Fußball, Squash, Spike-Ball und Co ein erschöpfter, aber inniger Dank an: *Martin Pfanzelt*, *Volker Kirsch*, *Thomas Gronauer* (was für ein gezielter Schuss!), *Patrick Allihn*, *Patrick Zanon*, *Theresa Rauh*, *Davide Boldini*, *Markus Schwarz*, *Dietrich Mostert* und *Max Bottlinger*.

Jonas Drechsel, *Ines Hübner*, *Robert Macsics*, *Patrick Allihn*, *Angela Weigert Muñoz*, *Patrick Zanon* und *Dietrich Mostert* danke ich für die ausgiebigen Abenteuer mit Kletteraktionen und dem ein oder anderen Bier (Wein für Angela).

Abschließend möchte ich mich bei all meinen Freunden und meiner Familie bedanken, die mich in allen möglichen Situationen über die Jahre so sehr unterstützt haben. Insbesondere *Alexia Christoforou* für ihre liebevolle Unterstützung, ihre Motivation und ihr Verständnis, das ein oder andere Mal für ihre Geduld und einfach ganz generell für die wunderschöne gemeinsame Zeit. Mein größter Dank gilt meinen Eltern *Christine* und *Frieder Reinhardt*, die diese lange und aufregende Reise überhaupt erst möglich gemacht haben. Vielen Dank für all die bedingungslose Unterstützung, den Antrieb und Rückhalt und das Verständnis in allen Lebensbereichen. Mein Vater, der uns letztes Jahr leider unerwartet und viel zu früh verlassen musste, wird diese Zeilen nicht mehr lesen können – ich bin mir aber sicher er war sich meines Dankes bewusst und ich bin dankbar für jeden gemeinsamen Tag und die wunderschönen Erinnerungen.

Denn alles verändert sich (auf dieser Reise) mit dem,

der neben einem ist – oder neben einem fehlt.

Till Reinhardt

München, 2023

Abstract

Fluoroquinolones are broad-spectrum antibiotics targeting the essential topoisomerase IV and gyrase enzymes in both Gram-negative and Gram-positive bacteria. Although commonly used fluoroquinolones, such as Ciprofloxacin and Levofloxacin, are generally well-tolerated by humans, recent years have unveiled the potential for severe, disabling, and long-lasting side-effects in certain patients. These encompass adverse effects, such as neuropathy, CNS disturbances, aortopathy, tendinopathy and dysregulations in glucose levels. Recognized as the "Fluoroquinolone-associated disability" by the FDA in 2015, this has led to "black box warnings" and more cautious usage recommendations. Despite ongoing efforts, a full understanding of the reasons behind individual sensitivities to fluoroquinolones remains elusive. While general mechanisms such as ion chelation, oxidative stress, and mitochondrial dysfunction have been implicated, there are likely multiple factors contributing to these intricate adverse effects. In this study, unbiased and comprehensive chemo-proteomic methods were employed to identify protein off-targets of fluoroquinolones in human cells. Whole proteome analyses revealed fluoroquinolone-induced dysregulation of the electron-transport chain, especially of the complexes I and IV. Furthermore, affinity-based protein profiling and thermal proteome profiling were performed revealing various potential protein off-targets. Validation studies confirmed the fluoroquinolone-mediated inhibition of the mitochondrial isocitrate dehydrogenase IDH2, a key enzyme in metabolic rewiring, redox homeostasis, and the regulation of matrix metalloprotease activity. Furthermore, the hydrolase NUDT1, responsible for clearing oxidized and methylated nucleoside triphosphates, was identified as another off-target. Further experiments looking into the downstream effects, the mode of IDH2 inhibition and into mitochondrial AIFM1, that was also addressed by fluoroquinolones-derived probes and could potentially be the causal link to the complex I and IV dysregulation, are currently ongoing. Given the urgency of the antimicrobial resistance crisis, innovation within this class of antibiotics is crucial and this project aims to understand and alleviate current limitations posed by adverse effects and guide the development of safer fluoroquinolone generations.

&

Nitroimidazoles such as Metronidazole are used as anti-infective drugs against anaerobic bacteria. Upon *in vivo* reduction of the nitro group, reactive radicals damage DNA and proteins in the absence of oxygen. Unexpectedly, a recent study of nitroimidazoles linked to an indolin-2-one substituent revealed potent activities against aerobic bacteria. This suggested a different, yet undiscovered mode of action (MoA). To decipher this MoA, whole proteome analysis of compound-treated cells was performed, revealing an upregulation of bacteriophage-associated proteins, indicative of DNA damage. Since direct DNA binding of the compound was not observed, activity-based protein profiling (ABPP) for target discovery was applied. Labeling studies revealed the topoisomerase IV, an essential enzyme for DNA replication, as the most enriched hit in pathogenic *Staphylococcus aureus* cells. Subsequent topoisomerase assays confirmed the inhibition of DNA decatenation in the presence of the indolin-2-one nitroimidazole with an activity comparable to Ciprofloxacin, a known inhibitor of this enzyme. Furthermore, significantly increased redox potentials of indolin-2-one nitroimidazoles compared to classic 5-nitroimidazoles such as Metronidazole were determined, which facilitate *in vivo* reduction. Overall, this study unraveled that indolin-2-one functionalized nitroimidazoles feature an unexpected dual MoA: Firstly, the direct inhibition of the topoisomerase IV and secondly the classic nitroimidazole MoA of reductive bioactivation leading to damaging reactive species. Importantly, this dual MoA impairs resistance development. Given the clinical application of this compound class, the new mechanism could be a starting point to mitigate resistance.

Zusammenfassung

Fluorchinolone sind Breitspektrum-Antibiotika, welche die essenziellen Enzyme Topoisomerase IV und Gyrase in Bakterien hemmen. Obwohl die häufig verwendeten Fluorchinolone Ciprofloxacin und Levofloxacin im Allgemeinen vom Menschen gut vertragen werden, hat sich in den letzten Jahren gezeigt, dass sie bei bestimmten Patienten schwere und langanhaltende Nebenwirkungen hervorrufen können. Diese umfassen zum Beispiel Neuropathien, Störungen des zentralen Nervensystems, Aortopathien, Tendinopathien und Störungen des Glukosespiegels. Dies wurde 2015 von der FDA als "Fluorchinolon-assoziierte Behinderung" anerkannt und hat zu "Black-Box-Warnungen" und restriktiveren Anwendungsempfehlungen geführt. Trotz laufender Bemühungen ist ein vollständiges Verständnis der Gründe für die individuelle Empfindlichkeit gegenüber Fluorchinolonen noch nicht gegeben. Obwohl allgemeine Mechanismen wie Ionen-Komplexierung, oxidativer Stress und mitochondriale Dysfunktion gezeigt wurden, gibt es wahrscheinlich mehrere Faktoren, die zu diesen komplizierten, unerwünschten Nebenwirkungen beitragen. In dieser Studie wurden unvoreingenommene und umfassende chemo-proteomische Methoden eingesetzt, um Protein-Off-Targets von Fluorchinolonen in menschlichen Zellen zu identifizieren. Proteom Analysen ergaben, dass Fluorchinolone eine Dysregulation der Elektronentransportkette, insbesondere der Komplexe I und IV, bewirken. Darüber hinaus wurden affinitätsbasiertes Protein-Profiling und thermisches Proteom Profiling angewendet, wodurch verschiedene potenzielle Protein-Off-Targets identifiziert wurden. Validierungsstudien bestätigten die Hemmung der mitochondrialen Isocitrat-Dehydrogenase IDH2 durch Fluorchinolone, ein Schlüsselenzym im Metabolismus, der Redox-Homöostase und der Regulierung der Matrixmetalloprotease-Aktivität. Darüber hinaus wurde die Hydrolase NUDT1, die für die Verwertung oxidierter und methylierter Nukleosid-Triphosphate zuständig ist, als weiteres Off-Target von Fluorchinolonen in menschlichen Zellen identifiziert. Weitere Experimente, die sich mit den nachgeschalteten Effekten und der Wirkungsweise der IDH2-Hemmung sowie mit dem mitochondrialen AIFM1 Protein befassen, das ebenfalls mit Fluorchinolon-abgeleiteten Sonden angereichert wurde und möglicherweise das kausale Bindeglied für die Dysregulation der Komplexe I und IV darstellt, werden derzeit durchgeführt. Angesichts der Dringlichkeit der antimikrobiellen Resistenzkrise sind Innovationen innerhalb dieser Antibiotikaklasse von entscheidender Bedeutung, und dieses Projekt zielt darauf ab, die derzeitigen Beschränkungen durch unerwünschte Nebenwirkungen zu verstehen und zu lindern, indem es die Entwicklung von sichereren Fluorchinolon-Generationen unterstützt.

&

Nitroimidazole wie z.B. Metronidazol werden als Antiinfektiva gegen anaerobe Bakterien eingesetzt. Bei der *in vivo* Reduktion der Nitrogruppe entstehende reaktive Radikale schädigen in Abwesenheit von Sauerstoff die DNA und Proteine. Unerwarteterweise zeigte eine aktuelle Publikation über Nitroimidazole, die mit einem Indolin-2-on-Substituenten verbunden wurden, starke Aktivitäten gegen aerobe Bakterien. Dies deutete auf einen anderen, noch unentdeckten Wirkmechanismus hin. Um diese Wirkungsweise zu entschlüsseln, wurde eine vollständige Proteomanalyse von mit der Substanzklasse behandelten Zellen durchgeführt, die eine Hochregulation von Bakteriophagen-assoziierten Proteinen ergab, was auf DNA-Schäden hindeutete. Da keine direkte DNA-Bindung des Wirkstoffs beobachtet werden konnte, wurde ein aktivitätsbasiertes Protein-Profiling (ABPP) zur direkten Identifizierung von Targets durchgeführt. Markierungsstudien ergaben, dass die Topoisomerase IV, ein für die DNA-Replikation essenzielles Enzym, in pathogenen *Staphylococcus aureus* Zellen am stärksten angereichert war. Anschließende Topoisomerase Aktivitätstests bestätigten die Hemmung des Enzymes in Gegenwart der neuen Substanzklasse mit einer Aktivität, die mit der von Ciprofloxacin, einem bekannten Inhibitor dieses Enzyms, vergleichbar war. Darüber

hinaus wurden deutlich erhöhte Redoxpotentiale im Vergleich zu klassischen 5-Nitroimidazolen festgestellt, was die *in vivo* Reduktion erleichtert. Insgesamt enthüllte diese Studie, dass Indolin-2-on-funktionalisierte Nitroimidazole eine unerwartete duale Wirkungsweise aufweisen: Erstens die direkte Hemmung der Topoisomerase IV und zweitens den klassischen Nitroimidazol-Wirkmechanismus der reduktiven Bioaktivierung, die zu schädlichen reaktiven Spezies führt. Des Weiteren, verlangsamt dieser duale Mechanismus die Resistenzentwicklung. In Anbetracht der klinischen Anwendung dieser Wirkstoffklasse könnte der neue Mechanismus ein Ansatzpunkt zur Verhinderung der Resistenzentwicklung sein.

Introductory remarks

Results of this dissertation have been published as follows:

T. Reinhardt*, K. M. Lee*, L. Niederegger, C. R. Hess, S. A. Sieber, Indolin-2-one Nitroimidazole Antibiotics Exhibit an Unexpected Dual Mode of Action. *ACS Chem. Biol.* **17**, 3077–3085 (2022).

* Authors contributed equally

T. Reinhardt, N. Bach, A. Jauch, F. Traube, A. Rothemann, S. Mueller-Deubert, Y. El-Harraoui, M. Köllen, T. Risch, D. Docheva, J. Riemer, S. Zahler, S. A. Sieber. Chemical proteomic studies into the human side-effects of fluoroquinolone antibiotics. *Manuscript in preparation.*

Publications not mentioned in this dissertation:

M. Meßner, M. M. Mandl, M. W. Hackl, **T. Reinhardt**, M. A. Ardelt, K. Szczepanowska, J. E. Frädrich, J. Waschke, I. Jeremias, A. Fux, M. Stahl, A. M. Vollmar, S. A. Sieber, J. Pachmayr, Small molecule inhibitors of the mitochondrial ClpXP protease possess cytostatic potential and re-sensitize chemo-resistant cancers. *Sci. Rep.* **11**, 11185 (2021).

S. L. Kidd, E. Fowler, **T. Reinhardt**, T. Compton, N. Mateu, H. Newman, D. Bellini, R. Talon, J. McLoughlin, T. Krojer, A. Aimon, A. Bradley, M. Fairhead, P. Brear, L. Díaz-Sáez, K. McAuley, H. F. Sore, A. Madin, D. H. O'Donovan, K. V. M. Huber, M. Hyvönen, F. Von Delft, C. G. Dowson, D. R. Spring, Demonstration of the utility of DOS-derived fragment libraries for rapid hit derivatisation in a multidirectional fashion. *Chem. Sci.* **11**, 10792–10801 (2020).

Conference presentations:

Chemical proteomic studies into the human off-targets of fluoroquinolone antibiotics.
Talk, Hengstberger Symposium "Update on antimicrobial research: Joint struggle against the silent pandemic", 17th – 19th March 2023, Heidelberg, Germany.

Indolin-2-one Nitroimidazole Antibiotics Exhibit an Unexpected Dual Mode of Action.
Poster presentation, Gordon Research Seminar and Conference on Bioorganic Chemistry, 11th – 17th June 2022, Proctor Academy, Andover, New Hampshire, United States.

Table of contents

I – Background and motivation

1. Antibiotics

1.1 Antibiotics – A brief history & overview

Nowadays, antibiotics are omnipresent. They are used to treat bacterial infections in human patients, their preventive application enables complicated surgeries and is paramount in domestic livestock farming.[1,2] Precisely because they are so frequently used and present in our daily lives, it is easy to forget that antibiotics made their way into clinical application only just over 100 years ago. Their systematic discovery and utilization was one of the greatest medical advances of the 20th century.[3] Although antibiotic extracts and poultices, e.g. from medical soils and moldy bread, have been used in traditional and ancient medicine for a long time, the deliberate isolation and synthesis of the active molecules as anti-infective drugs started only in the 1910-1930s with pioneering studies by *Paul Ehrlich*, *Gerhard Domagk* and *Alexander Fleming* (**Figure 1**).[3] *Paul Ehrlich* developed the first synthetic antibiotic Salvarsan (salvation arsenic) that was clinically used to treat syphilis and effectively laid the foundation for the overall principle of chemotherapy.[4,5] *Gerhard Domagk* and colleagues at Bayer discovered the sulfonamide Prontosil, the first broad-spectrum antibiotic in clinical use.[6] Also the identification of penicillin by *Alexander Fleming* in 1928, that was approved for clinical use in 1942, was a breakthrough in antimicrobial research.[7]

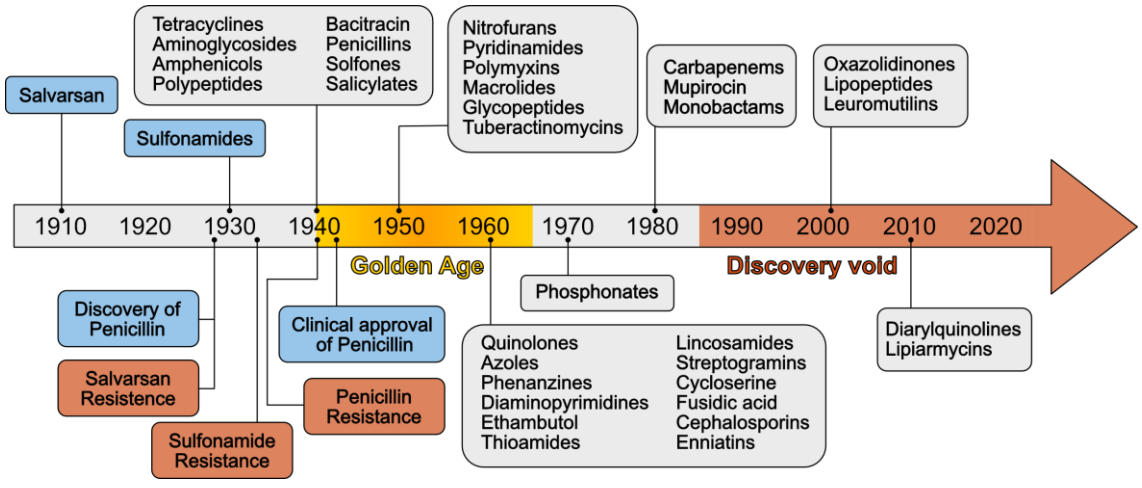

Figure 1: Timeline of antibiotic discovery. If not noted otherwise, the decade in which the antibiotic class was approved for clinical use is depicted. The golden age of antibiotic discovery was in the 1940s to 1960s. After this surge, the discovery pipeline slowed down significantly, often described as the discovery void. Figure based on *Hutchings et al.*[3]

Motivated by the observations that many antibiotic compounds are produced by microorganisms, *Selman Waksman* initiated systematic screenings of microbes to identify novel (antibiotic) natural products (NPs), leading to the "golden age" of antibiotic

development from the 1940s to 1960s, with the discovery of numerous antibiotic molecules and classes.[3,8] However, from the 1970 onwards, the discovery of new antibiotics declined significantly. The reason for this downward trend is multifactorial: After the surge of NP discovery, it became more and more challenging to identify novel compounds and especially novel classes, leading to the notion that the "low-hanging fruits" have been picked.[3] This came along with a common belief that the infection problem has been solved and the need for further antibiotic compounds was low. Additionally, from an economical perspective, the development of novel antibiotics was unfavorable and deprioritized by most pharmaceutical companies.[9]

Despite the seemingly large number of known individual antibacterial compounds, many derivatives cluster in a relatively small number of molecular classes and more importantly, the currently addressed molecular targets and modes of action (MoAs) of those classes are very finite (**Figure 2A, left**). Common antibiotic MoAs include the interference with nucleic acid (DNA or RNA) synthesis, the inhibition of cell wall synthesis, protein biosynthesis or folate synthesis and the impairment of bacterial membrane integrity.[3,10]

A

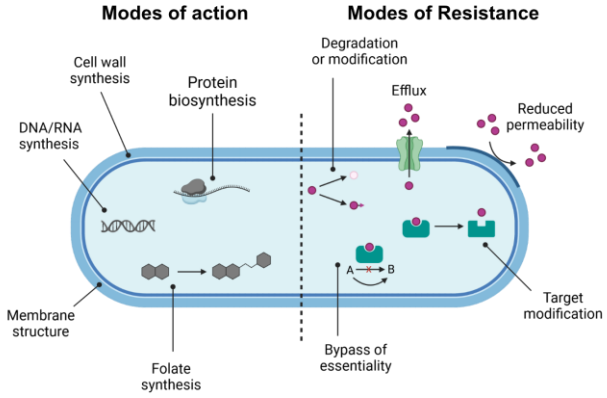

Molecular Target	Antibiotic classes	Example
Nucleic acid synthesis (DNA / RNA)	Nitrofurans	Nitrofurantoin
	(Fluoro)quinolones	Ciprofloxacin
	Phenazines	Clofazimine
	Azoles	Metronidazole
	Lipiarmycins	Fidaxomicin
	Ansamycins	Rifamycin SV

Molecular Target	Antibiotic classes	Example
Folate synthesis	Sulfonamides	Mafenide
	Salicylates	4-Aminosalicylic acid
	Sulfones	Dapsone
	Diaminopyrimidines	Trimethroprim

B

Molecular Target	Antibiotic classes	Example
Protein synthesis	Aminoglycosides	Kanamycin A
	Tetracyclines	Tetracycline
	Amphenicols	Chloramphenicol
	Macrolides	Erythromycin
	Tuberactinomycins	Viomycin
	Lincosamides	Clindamycin
	Streptogramins	Pristinamycin
	Fusidic acid	Fusidic acid
	Pleuromutilins	Retapamulin
	Oxazolidinones	Linezolid
Cell wall & Cell wall synthesis	Glycopeptides	Vancomycin
	Cycloserins	Seromycin
	Phosphonates	Fosfomycin
	Carbapenems	Meropenem
	Lipopeptides	Daptomycin
	Polypeptides	Gramicidin A
	Bacitracin	Bacitracin A
	Polymyxins	Colistin
	Monobactams	Aztreonam
	Penicillins	Amoxicillin
	Enniatins	Fusafungine
	Cephalosporins	Cefacetrile
	Pyridinamides	Isoniazid
	Ethambutol	Ethambutol
	Thioamides	Ethionamide

Figure 2: Outline of antibiotic classes and their modes of action and resistance formations. (**A**) Schematic overview of the limited modes of action (MoAs) of current antibiotics (**left**) and possible ways of resistance development (**right**) towards antibiotics by bacteria. Figure based on *Lakemeyer et al.*[10] (**B**) Table of clinically used antibiotic classes grouped by their MoAs and one exemplary compound per class. Table based on *Hutchings et al.*[3]

1.2 Antimicrobial resistance development

Many of the antibiotics discovered in the golden age are still in use today, however numerous bacterial resistances evolved against those drugs. In fact, the development of antimicrobial resistance (AMR) has been observed from the beginning of the antibiotics. Resistances against Salvarsan were found already in the 1930s, resistances against penicillin were identified even before its approval for the clinical market (**Figure 1**).[3,11,12] Since then, AMR rose to be a significant global threat to human health. A recent study estimated that in 2019 globally 4.95 million (95% uncertainty intervals: 3.62-6.57 million) deaths were associated with AMR of bacteria, of those 1.27 million (95% UI: 0.911-1.71 million) were directly attributable to bacterial AMR.[13] The study identified the pathogens *Escherichia coli*, *Staphylococcus aureus*, *Klebsiella pneumoniae*, *Streptococcus pneumoniae*, *Acinetobacter baumannii* and *Pseudomonas aeruginosa* as main threats in AMR associated deaths.[13] Additionally, pathogen-drug combinations, such as methicillin-resistant *S. aureus*, multidrug-resistant *Mycobacterium tuberculosis*, carbapenem-resistant *A. baumannii* and fluoroquinolone-resistant *E. coli* have been found to be responsible for the most deaths attributed to AMR by the authors.[13] Those findings are in strong agreement with other studies, in 2017 the WHO declared the so-called ESKAPE pathogens to be especially concerning and requiring prioritization in anti-AMR efforts (ESKAPE = *Enterococcus faecium*, *Staphylococcus aureus*, *Klebsiella pneumoniae*, *Acinetobacter baumannii*, *Pseudomonas aeruginosa* and *Enterobacter species*).[14,15]

As bacterial cell proliferation and division are fast, the evolutionary process of bacteria to respond to the selective pressure posed by treatment with antibiotics is also swift. Spontaneously and randomly forming mutations during replication can enable a bacterial cell to be less susceptible to the antibiotic.[10] As a consequence, the mutated bacterial cell can survive, whereas still remaining sensitive bacterial cells are killed. This leads to a rapid selection for insensitive, less susceptible bacteria and resistances arise.[10,16,17] Strategies to gain resistances include metabolic changes to bypass the target´s essentiality or to degrade or modify the antibiotic. Further mechanisms comprise the modification of binding sites of the antibiotic target, increased efflux of the active antibiotic or the reduction of the penetration of the drug through the cell envelope (**Figure 2A, right**).[10,16,17] As those resistances are often encoded on plasmids that are easily transferrable between different bacteria by horizontal gene transfer, e.g. bacterial conjugation, the conferred selective advantage of antibiotic resistances is rapidly shared between different bacterial populations

and even between different bacterial species.[18,19] Consequently, the AMR problematic is going to intensify and exacerbate in the future.[13]

Apart from the discussed "classical" mechanism of resistance acquisition, three additional factors can mitigate antibiotic susceptibility. Firstly, planktonic bacteria can attach to surfaces and encapsulate themselves into an extracellular polymeric structure (EPS). In these so-called biofilms bacteria are well-protected and especially hard to treat with antibiotics increasing the risk for chronic infections.[20] Secondly, individual bacteria entering metabolic resting-states are exaggerating the problem, as they enter metabolically dormant states and are hardly susceptible to antibiotic therapies, as most antibiotic classes require an active bacterial metabolism for their MoAs. Those so-called persister cells can therefore withstand even prolonged antibiotic treatment regimens and can afterwards reactivate and lead to relapses of infections.[21,22] The development of antibiotic persistence is often connected to biofilm formation.[20] Lastly, there is increasing evidence, that certain bacteria can be internalized into the human host cells and thereby be, to some extent, protected from antibiotic treatment. For example, multidrug-resistant *S. aureus* has been shown to feature a 100-fold higher minimal inhibitory concentration (MIC) by vancomycin when located intracellularly.[23]

1.3 Tackling the AMR crisis & motivation of this dissertation

Predictions show that AMR could be responsible for 10 million deaths per year in 2050.[24] Although exact numbers are discussed controversially, the exaggerating threat and urgent need for solutions is well-accepted across the scientific community, as well as governmental and non-governmental organization such as the U.S. Centers for Disease Control and Prevention (CDC) and the World Health Organization (WHO).[25–28] The posing threat of a post-antibiotic era leads to a resurgence of antibiotic research and development (R&D) efforts, mainly in academia, but increasingly also again in industrial settings.[29] Various avenues can be pursued to counter the AMR crisis. Important measures start with the restriction of the ubiquitous use of antibiotics, as the overuse increases the development of resistances. Antibiotic stewardship programs aim to educate and change prescription and use preferences to promote a responsible (and limit an unnecessary) use of antibiotics.[30] The discovery of novel antibiotics is of paramount importance, ideally compound classes with new MoAs and novel molecular targets to limit cross-resistances. Predictions show approx. 300 essential genes in bacteria, highlighting the potential to address unprecedented targets.[31]

Natural products (NPs) have always been the fundamental source of bioactive, including antibiotic, compounds.[32,33] Focusing on under-explored environments and ecological niches and research into naturally silent biosynthetic gene clusters (BGCs) are promising routes to venture into non-discovered chemical- and correspondingly activity-space.[3,10] Also synthetic chemistry approaches, such as Diversity-Oriented Synthesis (DOS) are excellent strategies to explore novel chemical space for drug discovery including antibiotics.[34–36] Apart from novel compounds, also the reduction of limitations and the increase of feasibility of current antibiotics are effective efforts to tackle the AMR crisis, e.g. *via* detailed structure-activity relationship (SAR) or molecular target studies to direct improved drug generations.[29,37,38] Moreover, drug repurposing programs can be viable starting points. Here, already existing therapeutics are reevaluated for different molecular targets and settings and subsequently tailored for the new target. This strategy has the advantage that the starting molecule already has good drug-like properties, such as solubility, permeability and stability.[39,40]

In general, more specialized and pathogen-focused narrow-spectrum antibiotics are better to mitigate AMR, as they do not target the healthy human microbiome as unselectively as broad-spectrum antibiotics do. This leads to less side-effects and resistances in the microbiome. On the offsite, a narrow-spectrum treatment is only possible with fast diagnostics of the infection in question.[41,42] Molecules that simultaneously address multiple targets or feature more than one MoA in the bacterium are especially advantageous, as it is significantly less likely for the bacterium to acquire all resistances.[43–45]

Traditional antibiotics inevitably lead to resistance formation, as they enforce a selective pressure on the bacteria. Alternative approaches are being studied, in which the pathogenicity and virulence of bacteria is being targeted rather than killing the bacteria, exhibiting less selective pressure.[10,46,47] Also, combinatory treatment strategies with antibiotics and antivirulence drugs are conceivable.[48] Apart from small molecules and NPs, also bacteriophages are capable of eradicating bacteria and avenues into their clinical application are being investigated.[49–51]

In addition to R&D efforts, changes on a political level can and must be made. New financial cues and models are needed to facilitate antibiotic research on academic and industrial level. Funding gaps between basic research in academia and the translation of the innovation into the commercial sector are problematic. Although progress has been made with the foundation of various public-private partnerships and health organizations, such as the *Global Antibiotic Research and Development Partnership* (GARDP), the *Combating*

Antibiotic-Resistant Bacteria Biopharmaceutical Accelerator (CARB-X) and the *Replenishing and Enabling the Pipeline for Anti-Infective Resistance* (REPAIR) *Impact Fund*, improvements are needed to drive antibiotic innovation.[29,52,53] Pull incentives, such as a subscription model, where fixed financial compensations are given to antibiotic development companies and delinkage models, additionally rewarding the development of drugs with high development costs and low sales prices, are being discussed.[29,54] In fact, the United Kingdom has recently started a subscription model funding two antibiotic drugs.[55]

To conclude, there are numerous and diverse ways to fight the so-called "silent pandemic" of rising bacterial resistances, not limited to the ones briefly described above.[10,29,30,34,54,56] Each of the approaches have their merit, as the solution to the posing problem most likely lies in multidisciplinary and multidirectional efforts. In this dissertation two avenues were pursued: Firstly, the identification of human off-targets of marketed fluoroquinolone antibiotics, to understand the current limitations and restrictions of this antibiotic class on a molecular and mechanistic level and thereby supporting the development of new, less problematic fluoroquinolone derivatives. In the second project, the mode of action of a novel, yet underexplored compound class of indolin-2-one nitroimidazoles featuring potent antibiotic activities was elucidated providing important understandings for a potential future evolution of this compound class.

2. Chemical proteomics for (off-)target elucidation

Although in principle not absolutely necessary, the identification of the target(s) of a bioactive molecule is highly advantageous for the further investigation and development of a compound to a potential lead molecule, both in fundamental research and drug discovery. Understanding the mode of action (MoA) of the compound of interest and mapping the binding site to the target aids lead development significantly.[37,38] A wide variety of methodologies has been developed to elucidate the molecular targets of small molecules. In the context of antibiotics, target identification is often performed with genomic approaches, such as the generation of resistance mutants and their subsequent sequencing to identify the resistance gene locus. Innovative technologies, such as high-throughput screenings of barcoded mutant libraries are being developed and facilitate genomic target identification strategies.[57–59] However, the generation of the prerequisite resistance mutants, can be difficult in some circumstances and, as discussed earlier, resistances can also arise from higher efflux, reduced permeability and bypass of target essentiality and not only from target modification or mutation. In those cases, genomic approaches to elucidate the direct molecular target face limitations. Additionally, small molecules often have multiple targets and (off)-targets making target identification more complex and challenging.[60–62] For antibiotics, off-target discovery is especially important to explore and rationalize potential unspecific side-effects in human cells, where the generation of resistant mutants is not an option.[29,63]

Alternative target identification methods study alterations or interactions on proteome level to infer protein targets. Here, approaches utilizing a chemical probe based on the compound of interest and strategies directly applying the unmodified parent compound can be differentiated. Chemical probe-centered strategies include activity-based protein profiling (ABPP) and affinity-based protein profiling (AfBPP).[64–68] Non-probe methodologies include computational models, biophysical technologies, such as thermal shift assays (TSA), protein pathway analyses and multi-omics approaches.[69] Usually target identification methodologies are applied initially to provide potential molecular hits, that are further validated in-depth by orthogonal approaches, such as activity- or binding assays.

2.1 Activity-based protein profiling (ABPP)

Activity-based protein profiling is a chemo-proteomic approach applying activity-based probes (ABPs) for target identification. The method is suitable for small molecules featuring intrinsic covalent reactivity with protein targets, e.g. electrophilic moieties such as epoxides, lactones and *Michael acceptors*, reacting with nucleophilic amino acids of proteins, such as cysteines and serines. Pioneered in the laboratories of *Cravatt* and *Bogyo*, ABPP was initially used with electrophilic libraries to study whole enzyme classes such as serine hydrolases, cysteine proteases, kinases and oxidoreductases.[64–66,68] It is however also feasible to use ABPP to study protein targets of specific, covalently reacting NPs and small molecules.

An ABP usually is comprised of three chemical modalities (**Figure 3A**): Firstly, the structural scaffold of the compound of interest including its chemical warhead, responsible for the target binding. Secondly, a reporter group, such as a fluorophore for visualization or biotin for enrichment. Thirdly, a linker connecting both functionalities.[70]

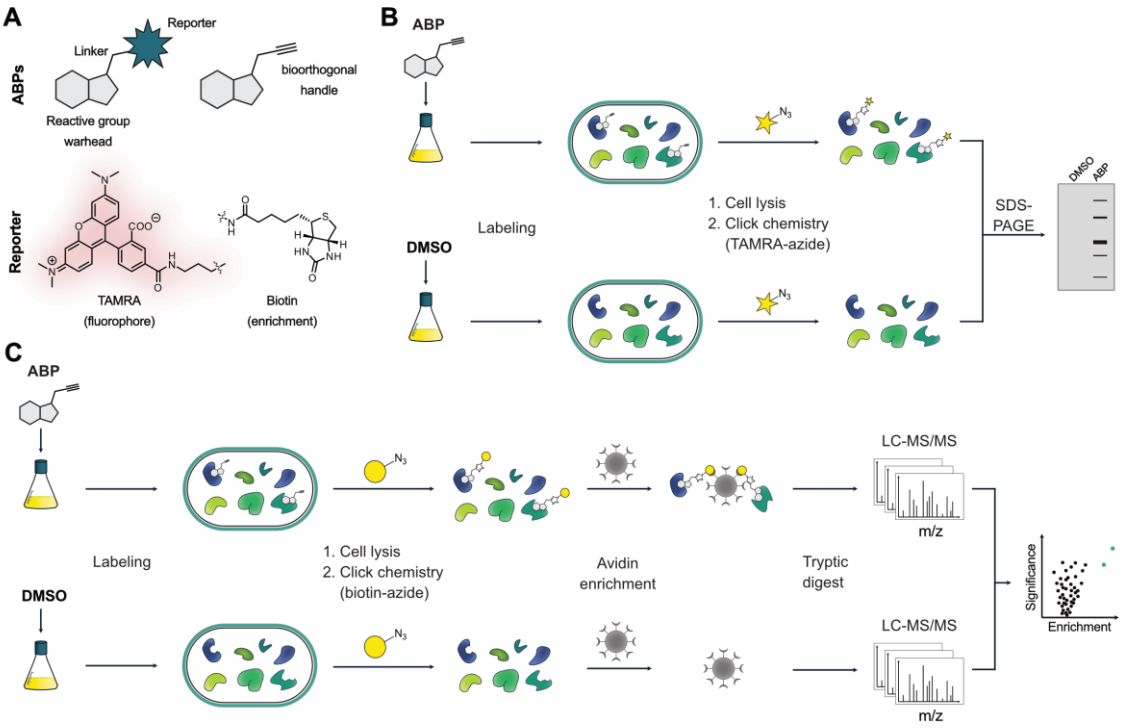

Figure 3: Schematic workflow of activity-based protein profiling (ABPP). (**A**) Analytical gel-based ABPP. Cells are treated either with activity-based probe (ABP) or vehicle control, after the labeling step cells are lysed and a fluorophore appended to the alkyne handle by CuAAC chemistry. Subsequent SDS-PAGE with fluorescence read-out reveals the distinct labeling pattern of the ABP. (**B**) Preparative MS-based ABPP. Cells are treated with ABP or vehicle control. Following lysis, biotin is conjugated to the alkyne handle in order to enrich labeled proteins on avidin beads. After on-bead tryptic digest the samples are measured *via* LC-MS/MS to identify and quantify labeled proteins. The data is usually visualized with volcano plots depicting enrichment values of ABP-treated samples over control samples and the statistical significance. Figure adopted and modified from *Reinhardt et al.*[71]

A more elegant approach is to install a biorthogonal handle (e.g. an alkyne or azide) at the ABP to append the reporter group after incubation of the cells or lysate with the probe *via*

copper(I)-catalyzed azide-alkyne cycloaddition (CuAAC) click chemistry.[72] As the CuAAC handle is significantly smaller than a direct modification with a linker conjugated with a fluorophore or biotin, target engagement of the probe is significantly less impaired.[70]

In analytical gel-based ABPP, cells or cell lysate is incubated with the ABP or vehicle control, respectively. After cell lysis a fluorophore is appended and labeled protein targets of the ABP visualized with fluorescence-scanning SDS-PAGE (**Figure 3B**). The distinct labeling pattern reveals the selectivity or promiscuity of the used ABP and is usually performed initially to optimize labeling conditions, such as ABP concentration and incubation time. Subsequently, in preparative MS-based ABPP, a biotin tag – instead of a fluorophore – is appended to the probe after cell incubation enabling enrichment of targeted proteins on avidin beads (**Figure 3C**). On-bead digest of enriched proteins results in the corresponding peptides that are measured on LC-MS/MS instrumentation and the raw data is analyzed to infer and quantify putative protein targets of the ABP. The data is usually represented in volcano plots comparing probe-treated samples versus vehicle control samples depicting $\log_2$-fold enrichment values versus the negative logarithmic *P*-values of the statistical test.

To minimize false-negative and false-positive identifications and help prioritization of subsequent target validation studies often a set of ABPs with the handle located at different positions of the scaffold are tested simultaneously and additionally competitive ABPP is performed.[69] In competition experiments, the cells are pre-treated with the unmodified parent compound (often in excess) before addition of the ABP. Consequently, the binding site of targets of the parent compound are already occupied when the probe is added and those valid targets are shown as fully or partially outcompeted on the gel or in the volcano plot, depending on the read-out.

2.2 Affinity-based protein profiling (AfBPP)

If the compound of interest does not feature intrinsic covalent reactivity, potential non-covalent interactions with protein targets are in most cases not deducible with a classical ABP, as the affinity is not strong enough to withstand harsh enrichment and MS-sample preparation procedures. In those cases, Affinity-based Protein Profiling (AfBPP), also called photoaffinity labeling-ABPP (PAL-ABPP) can be used.[69,73] Here, a molecular probe is additionally modified with a photosensitive moiety that upon UV irradiation enforces an

irreversible covalent interaction with bound target proteins enabling the read-out of transient, non-covalent and reversible interactors. Commonly used photoaffinity groups are benzophenones, aryl azides and diazirines (**Figure 4A**).

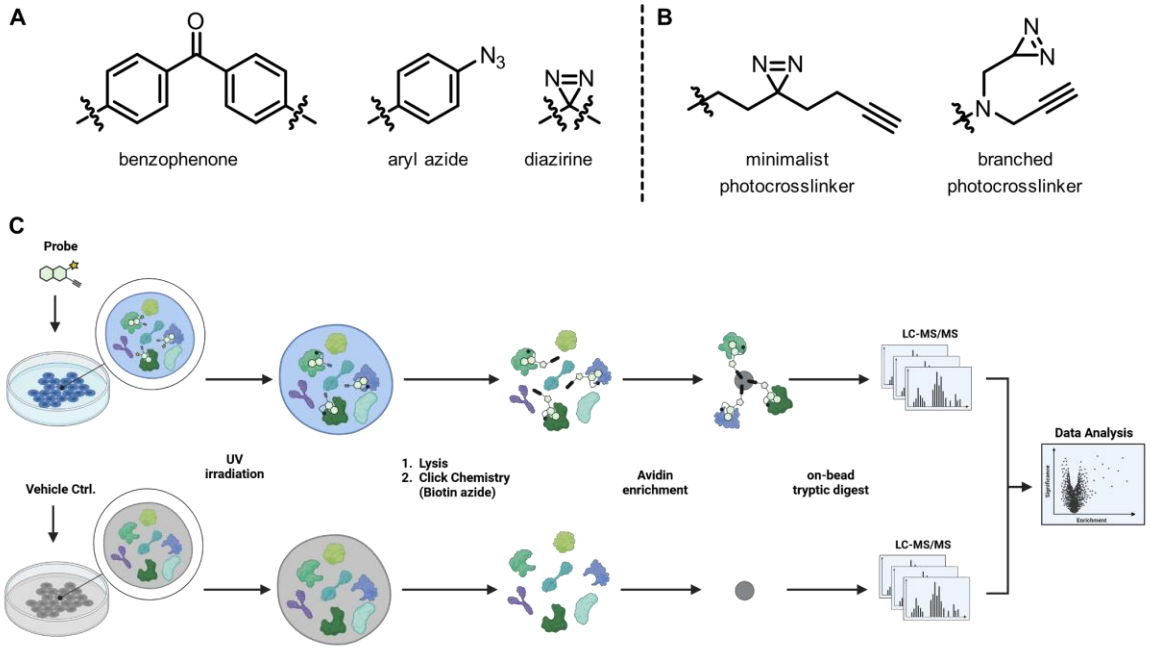

Figure 4: Affinity-based protein profiling (AfBPP). (**A**) Structures of commonly used photo-crosslinker moieties. (**B**) Examples of photo-crosslinkers including a terminal alkyne as biorthogonal handle. The minimalist photo-crosslinker developed by *Li et al.* and the branched system published by *Conway et al.*[74,75] (**C**) Schematic workflow of AfBPP. After incubation of cells (or lysate) with the probe or vehicle control, the samples are irradiated with UV light to enforce the covalent bond between the probe and interacting proteins. Analogous to ABPP, lysis is followed by conjugation of the reporter (e.g. biotin) for enrichment and LC-MS/MS measurement for target identification and quantification. Alternatively, a fluorophore can be attached for visualization *via* SDS-PAGE.

Diazirines are especially advantageous due to their small molecular footprint and react *via* diazo- or carbene-intermediates with proteins.[76] The photoaffinity group and the alkyne handle can be located at different positions of the probe or can be included at the same position. Various systems have been developed, such as the minimalist photo-crosslinker by *Li et al.* and the branched photo-crosslinker with a terminal diazirine developed by *Conway et al.* (**Figure 4B**).[74,75] Analogous to ABPP, AfBPP can be performed with a gel-based or MS-based read-out. The workflows are fundamentally equal, except for the UV irradiation step to trigger the covalent reactivity after incubation of cells or lysate with the probe (**Figure 4C**).

2.3 Thermal proteome profiling (TPP)

Thermal proteome profiling (TPP) is a derivatization-free chemo-proteomic technique for target identification. Contrary to ABPP and AfBPP, no probe is needed, and the unmodified

parent compound can be applied directly. TPP is based on the principle, that proteins can be heat-denatured leading to the irreversible denaturation of their folding state and aggregation. The temperature at which 50% of the protein is denatured is defined as its melting temperature T_m. As the protein stability, including its thermostability, can be affected by ligand binding their corresponding T_m can consequently also change upon ligand binding. Protein stabilization leads to a shift to higher melting temperatures, whereas destabilization decreases T_m (**Figure 5A**).[77] This principle has been applied in scientific research for a long time *in vitro* using isolated and purified protein in thermal shift assays (TSA).[78] *Molina et al*. evolved this concept to the cellular thermal shift assay (CETSA), were protein-ligand binding studies by protein stabilization and/or destabilization can be performed in live cells.[79,80] In CETSA, live cells or lysate are incubated with the molecule of interest and aliquots subjected to a temperature gradient. After lysis aggregated proteins, that were denatured due to the temperature gradient, are removed and the soluble fractions investigated for the proteins of interest by western blot experiments, giving intensity read-outs for a selected protein for each temperature point. By comparison to a vehicle control sample a T_m shift can be detected. This live cell approach lifts various limitations of the classical thermal shift assays: As the abundance of proteins in cells is highly diverse, a live cell CETSA approach also takes the selectivity of the compound in the cellular context into account. Additionally, proteins are often integrated in complex structures with various subunits, adapter proteins and transient interaction partners. A potential ligand binding is consequently also dependent on the functional state of those complexes and can often only be detected in live settings. Lastly, some molecules act as prodrugs, that need to be metabolically activated before they can engage their target, thus this interaction can also only be monitored with intact cells. Although being a significant innovation, classical CETSA experiments are limited in throughput as each protein of interest has to be analyzed using specific antibodies for western blot analysis. Thermal proteome profiling (TPP), also called MS-CETSA and first reported by *Savitski et al*. in 2014, utilizes a MS-based read-out of the soluble protein fraction instead of western blotting.[81] This has the profound advantage, that protein stabilization and destabilization can be monitored globally in the proteome simultaneously and is not restricted to single protein monitoring. Consequently, an unbiased target identification experiment is possible, without prior knowledge of which potential protein targets to study. TPP has originally been applied in non-adherent human cells, but has since then been evolved to applications in adherent human cells and also bacteria.[82] If the experiment is performed *in situ* with intact cells rather than in cell lysate, in addition to direct

de-/stabilization effects by ligand-binding to the proteins also down-stream and secondary effects can be observed, e.g. the destabilization of an entire complex or pathway if one subunit or protein is targeted by the compound of interest. TPP performed in cell lysate leads to less complex data usually revealing only direct target effects by ligand-binding.[83]

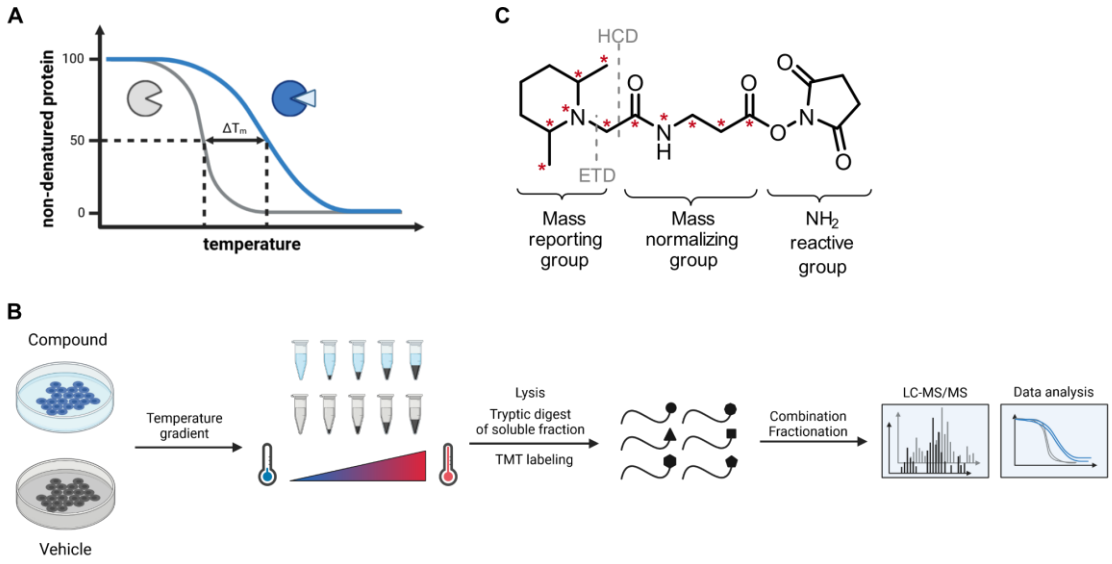

Figure 5: Thermal proteome profiling (TPP). (**A**) Underlying concept of thermal shift assays. Stabilization (as exemplary shown in the figure) or destabilization of a protein is a consequence of ligand binding leading to a shift of the melting temperature T_m of the protein. (**B**) Schematic workflow of thermal proteome profiling (TPP). Cells (or lysate) are treated with the compound of interest or vehicle control, respectively, and aliquots subjected to a temperature gradient. After lysis, denatured and aggregated proteins are removed, and the remaining soluble protein fraction digested. The resulting peptides are labeled with isobaric TMT-labels (one channel per temperature point) and after combination and offline fractionation subjected to LC-MS/MS measurement followed by data analysis to globally infer melting curves and T_m shifts of proteins. (**C**) General structure of the tandem mass tag (TMT) 10-plex system bearing an amine-reactive NHS-ester to label the peptides, a mass reporting group to produce a specific reporter mass for each of the 10 different TMT channel tags upon fragmentation in the mass spectrometer with higher-energy collisional dissociation (HCD) or electron transfer dissociation (ETD) and a mass normalizing linker to ensure the overall isobaric nature of each of the TMT-10plex members. Positions of potential isotopic permutations to create 10 different reporter channels and balance the overall isobaric mass of the tags are indicated with the asterisk.

The workflow is outlined in **Figure 5B**: Intact cells or lysate are treated in duplicates with the compound of interest and the vehicle control, respectively. Aliquots of treated cells or lysate are subjected to a temperature gradient with usually 10 temperature points. As the general protein stability range varies between organisms, e.g. depending on their natural habitat, the range of this gradient can be optimized for the organism in question.[84] For human settings usually a temperature range of 37 – 67 °C is chosen. After lysis (if intact cells are used) heat-denatured and aggregated proteins are separated by ultracentrifugation or filtering and the remaining fraction of soluble proteins subjected to standard proteomic sample preparation procedures including reduction, alkylation, and tryptic digest of the proteins. The resulting peptides of each individual time-point are isotopically labeled with isobaric tandem mass tag (TMT)-labels, that feature the same mass in the full MS (MS^1) scan, however can be differentiated due to the fragmentation reporter groups in the LC-MS/MS

(MS^2) and optional LC-MS/MS/MS (MS^3) scans of the MS-instrument (**Figure 5C**).[85,86] This enables multiplexing, meaning the combination of each time-point per sample into one sample to save on instrument time and additionally enables more precise TMT-based quantification in a MS^3-based fashion limiting ratio-compression.[85] Accordingly, when 10 temperature points were employed, the TMT-10plex system is used to enable labeling of each temperature point with one channel. The pooled TMT-labeled samples are offline fractionated to reduce the complexity of the samples and achieve deeper proteome coverage by the MS instrument. Examples for orthogonal offline fractionation methods are HILIC and high pH C18 chromatography.[87,88] Following the measurement using online-coupled C18 low pH chromatography by mass spectrometry, the raw data can be analyzed by search engines such as *MaxQuant* to identify and quantify the proteins.[89,90] Using a R-Script provided by *Franken et al.* the search engine output can be further analyzed and melting curves of individual proteins over the 10 temperature points can be inferred.[87]

In the described thermal response TPP experiments (TPP-TR) multiple potential direct and indirect protein targets of a ligand can be deciphered.[83] By locking the temperature treatment to one constant value and testing a ligand concentration gradient instead, the affinity of the ligand towards those targets can be studied due to concentration-dependent stabilization. This type of experiment is called concentration range TPP (TPP-CCR).[83] Both techniques can be combined in a comprehensive 2D-TPP approach to infer both putative targets and their respective affinities.[91]

2.4 Limitations of ABPP/AfBPP and TPP

Probe-based target identification strategies, such as ABPP and AfBPP, require labor-intensive synthetic derivatization of the parent compound to obtain a suitable probe. Depending on the complexity and incorporated functional groups, this can be synthetically very challenging. Especially when late-stage modifications directly on the parent compound are not possible to introduce the necessary derivatization on a suitable position, total- or semi-syntheses are necessary. The positioning of the modification can potentially hamper target engagement (false-negatives) and in some cases can also lead to false-positives. False-negatives can potentially be deciphered by testing a library of different probes, while false-positives can be identified by competition experiments with the parent compound, but this can be laborious. Especially in the context of AfBPP, transient interactions e.g. during uptake, transport and efflux can additionally be stably enriched beside direct target

engagements due to the action of the photo-crosslinker. This photome background is depending on the used photoaffinity group and has been catalogued by *Kleiner et al.* for various affinity groups to help the prioritization of putative target proteins.[92] For example, alkyl diazirines used in the minimalist photo-crosslinker have been reported to enrich especially membrane and acidic proteins with highly negative surfaces.[76] Notably, modified enrichment procedures enable the binding-site identification *via* the probe pinpointing the covalently modified amino acid in the target protein and giving an additional important information for the MoA and potential later compound evolution.[93–95]

The advantage of modification-free approaches, such as TPP, is that the parent compound can be applied directly. Nonetheless, TPP has its own limitations. In the beginning, TPP was restricted to non-membrane associated proteins, but has since been expanded to include membrane proteins by using a mild detergent during cell lysis.[96] Moreover, TPP experiments are very resource-intensive and expensive both in preparation and in MS-instrument measurement time. An alternative approach called Proteome Integral Solubility Alteration (PISA) has been developed by *Gaetani et al*. in 2019. Here, the samples of each temperature point are pooled and the integral of soluble protein S_m of each detected protein is compared between treated and untreated conditions.[97] As each temperature point does not need to be chemically labeled individually, a TMT-10plex system can be used to multiplex 5 biological replicates (5× treated and 5× untreated) within one sample (that additionally can be offline fractionated to reduce complexity). This results in less MS sample amount, higher statistical power due to more replicates and the possibility to include more than 10 temperature points or conditions. 2D-PISA experiments to include a dose-dependent range are also an option.[97] Most importantly however, not every ligand-protein-pair enforces a strong melting temperature alteration and change in protein structure/folding and can therefore be studied by TPP or PISA.[77] Moreover, direct binding-site identification is not possible with those technologies.

Overall, every (chemo-)proteomic methodology for target elucidation has its advantages and disadvantages. In many cases it is beneficial to apply multiple orthogonal approaches to obtain a more comprehensive picture of targeted proteins. In either case, subsequent target validation studies, e.g. *via* activity or binding assays or target knock-out/down studies, are needed to reliably confirm the target of the compound of interest.

II – Chemical proteomic studies into the human side-effects of fluoroquinolone antibiotics

---

The manuscript for the journal publication of the research presented in this chapter is currently in preparation:

T. Reinhardt, N. Bach, A. Jauch, F. Traube, A. Rothemann, S. Mueller-Deubert, Y. El Harraoui, M. Köllen, T. Risch, D. Docheva, J. Riemer, S. Zahler, S. A. Sieber. Chemical proteomic studies into the human side-effects of fluoroquinolone antibiotics. *Manuscript in preparation.*

Contributions:

TR planned the project and performed chemical synthesis, proteomics experiments, protein expression and purification, bioactivity assays, data analysis, data visualization and representation. N. Bach performed proteomics experiments and planned the project. A. Jauch performed lysosomal cell imaging and analyzed mitochondrial NADPH levels. F. Traube performed pathway analyses, conducted FACS and hmdC level measurements. A. Rothemann conducted AIFM1 target validation studies. S. Mueller-Deubert performed MMP qPCR experiments. Y. El Harraoui and M. Köllen conducted chemical synthesis. T. Risch performed SCARB1 MST measurements. D. Docheva provided PDL cells and planned qPCR experiments. J. Riemer planned AIFM1 target validation. S. Zahler planned cell imaging and NADPH level analyses. S.A. Sieber conceived, planned and supervised the project.

1. Fluoroquinolone antibiotics

Fluoroquinolones (FQs) are a class of broad-spectrum antibiotics with excellent potencies against both Gram-negative and Gram-positive bacteria.[98] Discovered as an impurity in the synthesis of the antimalarial drug chloroquine, 7-chloroquinolone set the foundation for the first class of fully synthetic antibiotics, the quinolones, which are not rationally designed or derived from natural products with antibacterial activities.[99] The lead compound was further evolved to nalidixic acid by *Lesher et al.* in 1962, featuring a 1,8-naphtyridine core, that has been used extensively for urinary tract infections (**Figure 6**).[99,100] The consecutive introduction of a fluorine atom at the 6-position of the quinolone scaffold significantly increased the tissue penetration and the spectrum of activity of the compounds resulting in the first FQ Flumequine in 1973.[99,101] Extensive structure-activity relationship (SAR) studies have been performed that gave rise to multiple generations of FQs comprising a large variety of derivatives.[98,102] Today, the most prominent marketed members of this class for use in human settings are Ciprofloxacin, Levofloxacin and Moxifloxacin, but the scaffold is still subject to ongoing research and recently approved FQs are Finafloxacin (2014) and Delafloxacin (2017).[103,104]

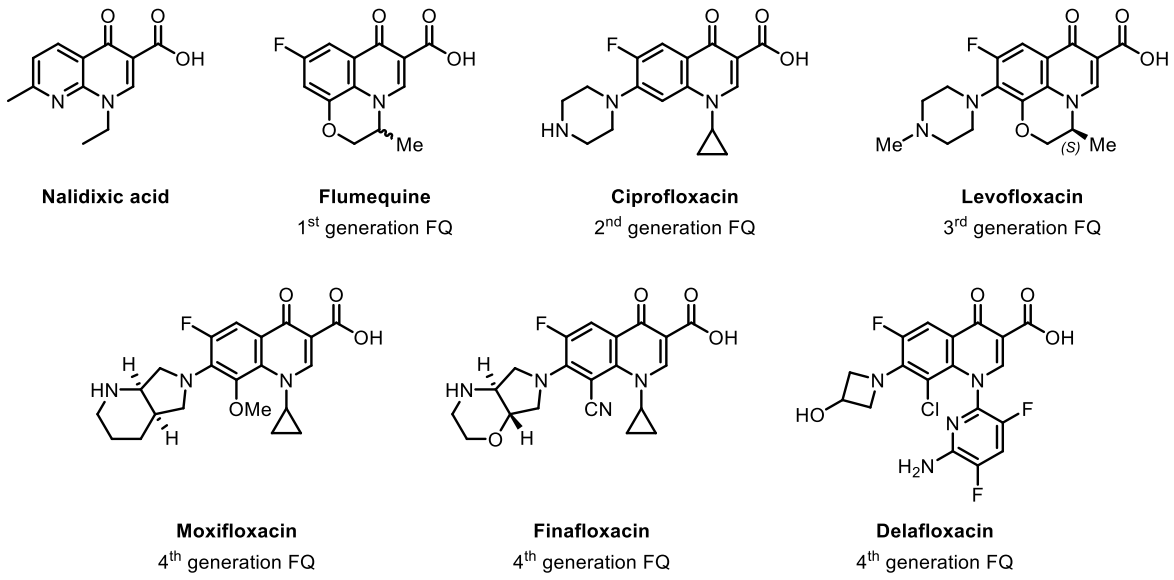

Figure 6: Selection of fluoroquinolone (FQ) antibiotics. Based on the naphthyridine scaffold of nalidixic acid the first FQ Flumequine was developed. Since then, multiple generations of FQs were generated and the core is still subject to research. Exemplary FQs of each generation are given, as discussed in the main text.

The mode of action (MoA) of FQs is the inhibition of the bacterial topoisomerase IV and gyrase, both essential type-II topoisomerases for prokaryotic DNA replication.[98,105] By binding to the topoisomerases that act on DNA, FQs form stable ternary complexes with the enzymes and the DNA. Thus the re-ligation of the DNA double-strand breaks induced by

the topoisomerases to control DNA supercoiling and decatenation states is inhibited.[106] The resulting critical DNA damage leads to the engagement of the bacterial DNA damage SOS-response, cellular stress and bacterial cell death.[98,105] While SAR studies showed synthetic flexibility at the C7-position and to some extend at the C1- and C8-position of the quinolone, the β-keto acid moiety is crucial for the antibiotic effect.[98] This is due to the binding mode of FQs, chelating Mg^{2+} ions in the active center of the topoisomerases thereby tightly binding to conserved serine and acidic residues in the enzymes (especially in the ParC subunit in topoisomerase IV and the GyrA subunit in the gyrase) *via* water-metal ion bridges (**Figure 7A**).[107]

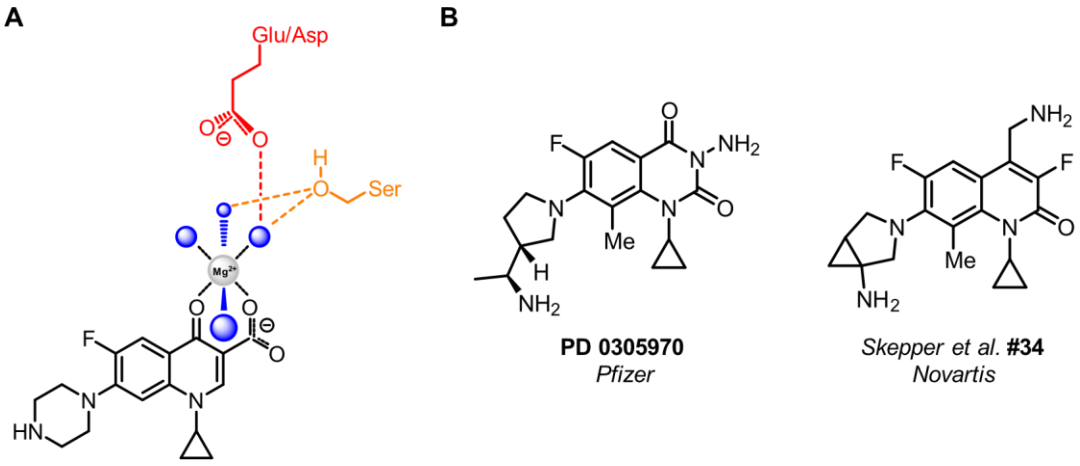

Figure 7: FQ binding mode and resistances. (**A**) Binding mode of FQs to topoisomerases *via* chelation of active-site Mg^{2+} ions resulting in metal-water bridges to conserved serine and glutamate/aspartate moieties in the topoisomerase IV and gyrase. Mutation of those residues leads to strong resistance formation. (**B**) Structures of alternative quinazolinediones and 4-(aminomethyl)-quinoline-2(1*H*)-ones binding to the type-II topoisomerases independently of water-ion bridges and therefore featuring only minimal cross-resistances with FQs.

As a result, these amino acid residues mediating FQ-topoisomerase binding are frequently mutated in bacteria with FQ resistances and are therefore called the quinolone resistance-determining region (QRDR, e.g. Ser83 and Asp87 in *E. coli* GyrA).[108,109] While other resistance mechanisms also exist, such as restricted uptake and elevated efflux, no FQ-degrading enzymes exist.[110] Large-scale drug development programs e.g. by *Pfizer* and *Novartis*, have led to the discovery of quinazolinediones and 4-(aminomethyl)quinoline-2(1*H*)-ones inhibiting the topoisomerases independently of the water-metal bridges essential for classical FQ binding (**Figure 7B**).[109,111–113] As a consequence, they feature only minimal cross-resistances with FQs. However, none of those alternatives have reached the market yet and the classical FQs are still more potent and one of the major antibiotic classes to treat bacterial infections.

For adults, FQs were the most often prescribed class of antibiotics in the U.S. in 2002.[114] More recently, in 2011-2017 FQs were the number four of outpatient antibiotic prescribing

according to the CDC.[115–121] Since 2018 FQs are, however, not in the top 5 of antibiotic classes in the U.S. anymore.[122–125] The decline of FQ usage is mainly due to FQ-derived adverse effects becoming more and more apparent leading to several warnings by the regulatory authorities. Noteworthy, various FQs, such as Temafloxacin and Grepafloxacin have been withdrawn from the market before due to drug safety issues already in 1992 and 1999, respectively.[126,127] The most used marketed members of this class today, Ciprofloxacin, Levofloxacin and Moxifloxacin are generally well-tolerated, however in the past decade it became increasingly apparent that they can lead to severe and potentially long-lasting or permanent adverse effects in some patients.[128–131] Reported adverse effects include neuropathy[132–134] and various CNS effects[135,136], aortopathy[137–139], tendinopathy and tendon rupture[140–143], hypoglycaemia and hyperglycaemia.[131]

This diverse range of adverse effects was defined as the "Fluoroquinolone-associated disability" (FQAD) by the FDA in 2015 and as a response, the U.S. authority issued "black box warnings" for FQs and recommended their restricted use to treatment situations without effective alternatives.[144] Warnings included the increased risk of tendinitis and tendon rupture (July 2008), potential irreversible peripheral neuropathy, i.e. serious nerve damage, (August 2013), the recommendation for restricted use for infections without effective alternatives (May 2016) and increased risk of aortopathy and effects on blood sugar levels (October and December 2018).[144,145] The European counterpart, the EMA, acted accordingly in 2018.[146]

Onset of the side-effects can be swift, according to the study of *Huruba et al.* adverse effects start most frequently within 7 days of treatment, in the majority within the first month and adverse effects were exhibited for more than 30 days in most of the reports.[132] Also, other studies showed that the effects are potentially long-lasting or permanent.[135,147]

Incidents rates are generally rare, but significant, hard to describe and controversially discussed in the literature.[135] A basic problem is the low rate of adverse effect reporting and the direct attribution of side effects to FQs when multiple medications and therapies are used simultaneously.[131] In the U.S. only approx. 10% of cases are estimated to be reported to the FDA.[131,148] For tendinopathy most often the Achilles tendon is affected.[135,149] FQs increase the risk of acute tendinopathy approx. 2-4 fold.[135,150] With an absolute incidence of up to 2% in FQ-using patients (65 years and older) and approx. 0.9% in the general population.[135,150,151] For aortic aneurysms an approx. 2-3 fold increased risk is reported.[135,152] Absolute incidence rates are, however, also reported to be low at less than 0.1%.[135,153] Other

studies did not find a significant connection between FQ treatment and aortic aneuryms.[135,154] For peripheral neuropathy FQs increase the risk about 1.5-fold, with a low absolute risk of approx. 0.02-0.04% per year in treated patients.[135,155,156]

The cause of individual sensitivities to FQs is not well understood at this point. No genomic studies of affected patient cohorts have been published yet, however studies on genetic predispositions are apparently pursued and a patent application is pending according to remarks in publications and conference communications.[136,144,157] A widely accepted theory is drug accumulation in some patients leading to higher systemic concentrations and thereby toxicities.[132,135,158–160] Accordingly, impaired renal function has been identified as a risk factor, potentially leading to increased serum concentrations.[132] Also age is considered to be a risk factor for experiencing FQAD.[160,161] As elderly patients feature significantly different pharmacokinetics, e.g. reduced renal clearance and a greater area under the concentration-time curve (AUC) of Ciprofloxacin, this is also attributed to higher effective drug concentrations and accumulation.[159] Concomitant corticosteroid prescriptions are serious risk factors and studies showed in this case an up to 14-fold increase of ruptures.[135,150,162]

Molecular causes leading to the adverse effects are not well understood yet. Many studies focusing on mechanistic reasons have highlighted the potent iron-chelating properties of FQs. This capability hinders diverse enzymatic reactions by forming complexes with the metal-cofactors. One potential outcome is the inhibition of iron-dependent dioxygenases, which could potentially trigger epigenetic alterations.[163–165] Also, the impact on integrin signaling, crucial for cell adhesion, both intercellularly and with the extracellular matrix, has been shown.[166] Additionally, the function of prolyl 4-hydroxylases, vital for collagen maturation and modification, were reported to be influenced through the coordination of FQs with divalent ions.[143] Furthermore, investigations involving human and animal tenocytes along with human aortic myofibroblasts have unveiled adverse effects like collagen degradation and increased expression and activity of matrix metalloproteases (MMPs) following FQ treatment.[137,167,168] Broader mechanisms such as mitochondrial dysfunction and elevated oxidative stress have also been highlighted.[128,129,143] Additionally, a range of alternative theories explaining the adverse effects of FQs have been suggested. These encompass diverse angles, including the inhibition of $GABA_A$ receptors and $\alpha4\beta2$ nicotinic acetylcholine receptors through compounds like Ciprofloxacin.[134,169–171] Overall, this implies that several interconnected factors might contribute to the toxicity and further research is essentially required.

2. Aim and significance of this project

Despite various studies looking into the mechanistic reasons of FQ-derived adverse effects in human, the understanding is still limited. According to the literature research, no unbiased proteome-wide investigation about exact causes of the FQAD has been performed yet. Especially, because the biochemical and molecular causes of the adverse effects, seem to be multifactorial, a global off-target discovery could be advantageous. For this a three-tiered strategy was envisioned (**Figure 8**): Firstly, the analysis of the effect of FQs on the global proteome of human cells and the determination of significantly dysregulated protein pathways. Secondly, the identification of potential direct off-targets of FQs in human cells by affinity-based protein profiling (AfBPP) using FQ-derived photoaffinity probes. And thirdly, the application of an orthogonal probe-free target discovery approach called thermal proteome profiling (TPP) to generate a comprehensive picture on protein-centered adverse effects of FQs. By performing *in situ* TPP also indirectly affected pathways could be detected. The resulting insights into the molecular causes for the FQAD can facilitate and potentially drive the development of novel, safer FQ generations minimizing adverse effects and lifting the current restrictions of this important antibiotic class. Identified off-targets and pathways could support studies to understand why individual patients are affected by FQAD while many are not. Especially in the light of the AMR crisis, innovation in this antibiotic class is important and could lead to impactful improvements.

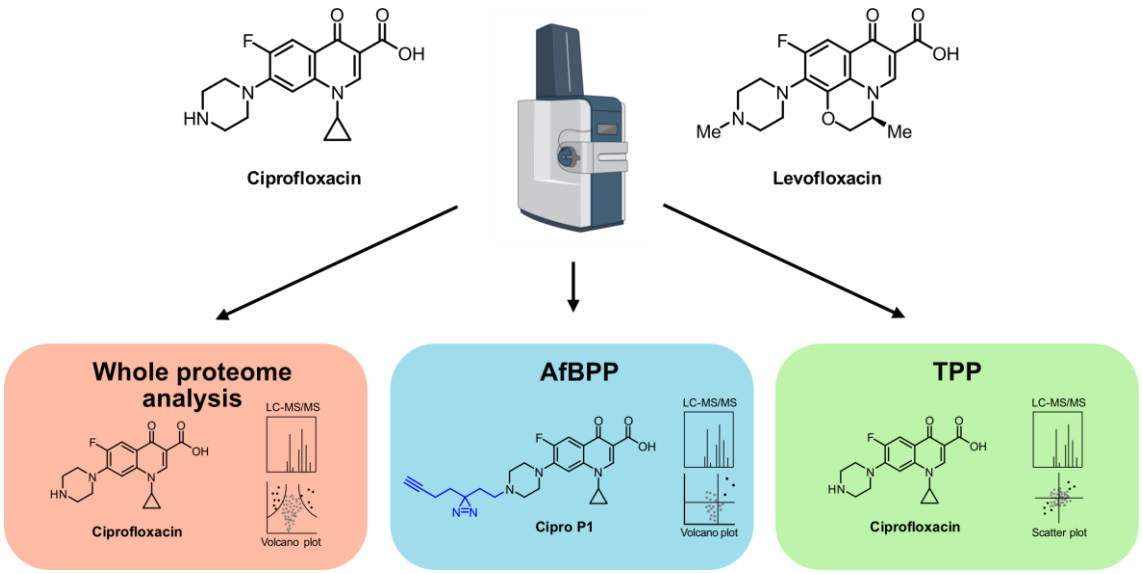

Figure 8: Three-tiered chemo-proteomic strategy to identify human FQ off-targets. Ciprofloxacin and Levofloxacin were selected for structural diversity. Firstly, whole proteome analyses of FQ-treated human cells is envisioned for the assessment of dysregulated proteins and pathways. Secondly, (off-)target identification by FQ-derived photoaffinity probes with affinity-based protein profiling (AfBPP) and thirdly probe-free thermal proteome profiling (TPP) were planned.

3. Results and discussion

3.1 Proteome regulation upon FQ treatment

3.1.1 Whole proteome analysis in HEK-293 cells

To gain first insights into affected protein pathways in human cells upon FQ treatment, whole proteome analyses were performed. In an initial experiment human HEK-293 cells were continuously treated with Ciprofloxacin for 3 hours, 3 days, 7 days and 2 weeks to cover the range of a typical therapeutic regime of FQs.[172] The co-incubation was performed at a low concentration of 7.5 µM, corresponding to reported regular plasma levels after Ciprofloxacin intake and at 75 µM, corresponding to peak levels reported to be reached in certain organelles and tissues.[173–176] The cellular proteome was compared to control-treated cells. After lysis, the proteome was isolated and digested for LC-MS/MS measurement using label-free quantification (LFQ) and subsequent data analysis was performed. The results are depicted in respective volcano plots (**Figure 9**, **Figure 10**).[89]

Already after 3 hours of treatment, significant regulation of proteins involved in iron transport and homeostasis (HBA1, HPX, LTF)[177–179], cellular stress (HMOX1, AATF, GPX3, MST1, PEX10, VNN1)[180–185] and collagen fibril organization (COL18A1, COL1A1, COL1A2, COL1A5, FMOD, FN1, ITGA-1)[186–189] were detected for both high and low concentrations (**Figure 9**). These findings are in line with reported issues of FQs causing cellular oxidative stress, e.g. *via* metal-cofactor complexation, reactive oxygen species (ROS) and tendon-/ ligament defects *via* defective collagen homeostasis.[128,141,163,190]

Analysis of the data of prolonged Ciprofloxacin incubation revealed a strong, concentration- and time-dependent downregulation of subunits of the complex I and complex IV of the electron transport chain (ETC, **Figure 10**). In the case of the higher peak concentration this regulatory shift was already starting to appear after 3 hours and was significantly pronounced after 3 days. For the regular plasma concentration this trend was detectable after 3 days to 7 days and distinctly exhibited after 14 days. Thus, higher concentrations in specific tissues or due to drug accumulation could lead to a faster onset and extent of complex I and IV downregulation, however even regular concentrations result in this effect merely requiring a longer time to develop. Pathway analyses of significantly dysregulated proteins confirmed this pronounced effect on these two ETC complexes indicating strong mitochondrial dysfunction, impaired oxidative phosphorylation, decreased neutrophil extracellular trap signaling, as wells as enhanced granzyme A and sirtuin signaling (**Figure 11**). As

mitochondria are important organelles for cellular processes, including energy production and apoptosis, functional defects are implicated in various serious diseases, such as in neuro-degenerative and cardiovascular pathogenesis states.[191,192] The ETC involved in oxidative phosphorylation, the central metabolic pathway to generate ATP, is located at the inner membrane of the mitochondria, consequently mitochondrial dysfunction is often resulting in impaired oxidative phosphorylation.[192]

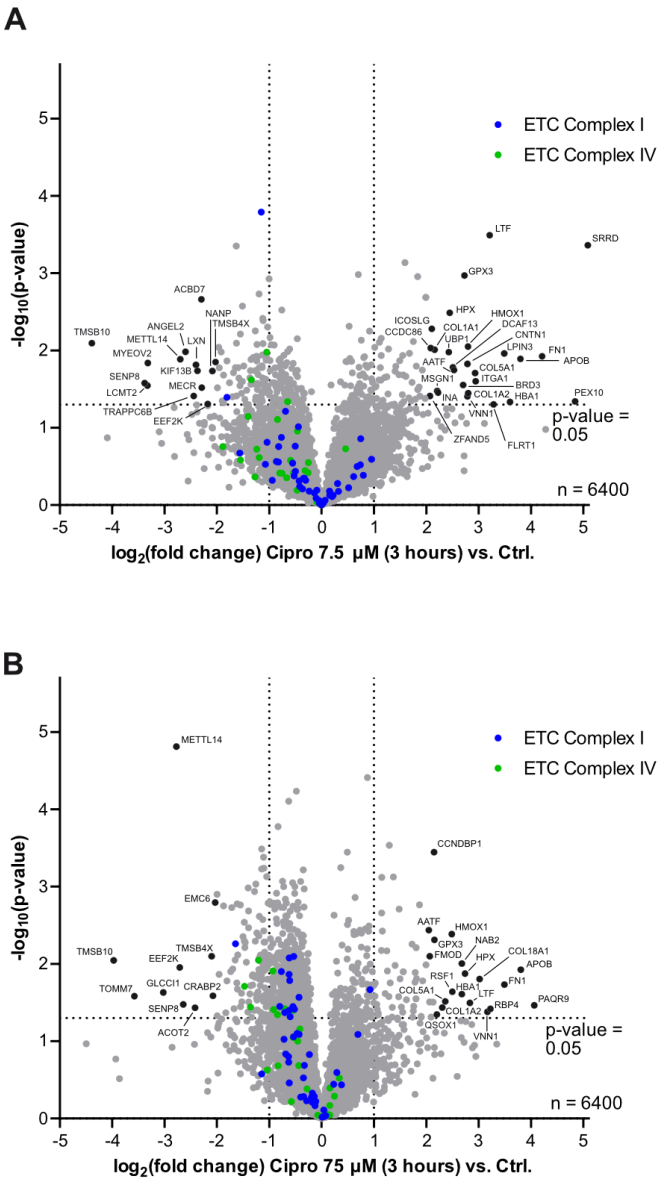

C

Up-regulated proteins (fold-change ≥ $\log_2$ = + 2)

Gene	Protein name
AATF	Protein AATF
APOB	Apolipoprotein B-100
BRD3	Bromodomain-containing protein 3
CCDC86	Coiled-coil domain-containing protein 86
CCNDBP1	Cyclin-D1-binding protein 1
CNTN1	Contactin-1
COL18A1	Collagen alpha-1(XVIII) chain
COL1A1	Collagen alpha-1(I) chain
COL1A2	Collagen alpha-2(I) chain
COL1A5	Collagen alpha-1(V) chain
DCAF13	DDB1- and CUL4-associated factor 13
FLRT1	Leucine-rich repeat transmembr. prot. FLRT1
FMOD	Fibromodulin
FN1	Fibronectin
GPX3	Glutathione peroxidase 3
HBA1	Hemoglobin subunit alpha
HMOX1	Heme oxygenase 1
HPX	Hemopexin
ICOSLG	ICOS ligand
INA	Alpha-internexin
ITGA1	Integrin alpha-1
LPIN3	Phosphatidate phosphatase LPIN3
LTF	Lactotransferrin
MSGN1	Mesogenin-1
MST1	Hepatocyte growth factor-like protein
NAB2	NGFI-A-binding protein 2
PAQR9	Progestin and adipoQ receptor family member 9
PEX10	Peroxisome biogenesis factor 10
QSOX1	Sulfhydryl oxidase 1
RBP4	Retinol-binding protein 4
RSF1	Remodeling and spacing factor 1
SRRD	SRR1-like protein
UBP1	Upstream-binding protein 1
UTP18	U3 small nucleolar RNA-associated protein 18 homolog
VNN1	Pantetheinase
WIPF1	WAS/WASL-interacting protein family member 1
ZFAND5	AN1-type zinc finger protein 5

D

Down-regulated proteins (fold-change ≤ $\log_2$ = −2)

Gene	Protein name
ACBD7	Acyl-CoA-binding domain-containing protein 7
ACOT2	Acyl-coenzyme A thioesterase 2, mitochondrial
ANGEL2	Protein angel homolog 2
CRABP2	Cellular retinoic acid-binding protein 2
EEF2K	Eukaryotic elongation factor 2 kinase
EMC6	ER membrane protein complex subunit 6
GLCCI1	Glucocorticoid-induced transcript 1 protein
KIF13B	Kinesin-like protein KIF13B
LCMT2	tRNA wybutosine-synthesizing protein 4
LXN	Latexin
MECR	Trans-2-enoyl-CoA reductase, mitochondrial
METTL14	N6-adenosine-methyltransferase subunit METTL14
MYEOV2	Myeloma-overexpressed gene 2 protein
NANP	N-acylneuraminate-9-phosphatase
SENP8	Sentrin-specifiфc protease 8
TMSB10	Thymosin beta-10
TMSB4X	Thymosin beta-4
TOMM7	Mitochondrial import receptor subunit TOM7 homolog
TRAPPC6B	Trafficking protein particle complex subunit 6B

Figure 9: Whole proteome analysis of Ciprofloxacin-treated HEK-293 cells after 3 h of incubation. (**A**) Respective volcano plot of cells treated with 7.5 µM Ciprofloxacin reflecting the published plasma concentration versus the vehicle control. (**B**) Volcano plot of cells treated with the peak concentration (75 µM) versus the vehicle control. Vertical threshold lines represent a $\log_2$ regulation of ±1 and $-\log_{10}$ (*P*-value) ≥ 1.3 (two-sided two-sample *t*-test, *n* = 3 replicates per group). Subunits of the electron transport chain (ETC) complexes I (blue) and IV (green) are highlighted. (**C**) Alphabetically sorted table of top up-regulated proteins (threshold: fold-change ≥ $\log_2$ 2 and $-\log_{10}$ (*P*-value) ≥ 1.3). (**D**) Alphabetically sorted table of top down-regulated proteins (threshold: fold-change ≤ $\log_2$ –2 and $-\log_{10}$ (*P*-value) ≥ 1.3). Key proteins involved in iron homeostasis, collagen organization and cellular stress response are being regulated upon Ciprofloxacin treatment.

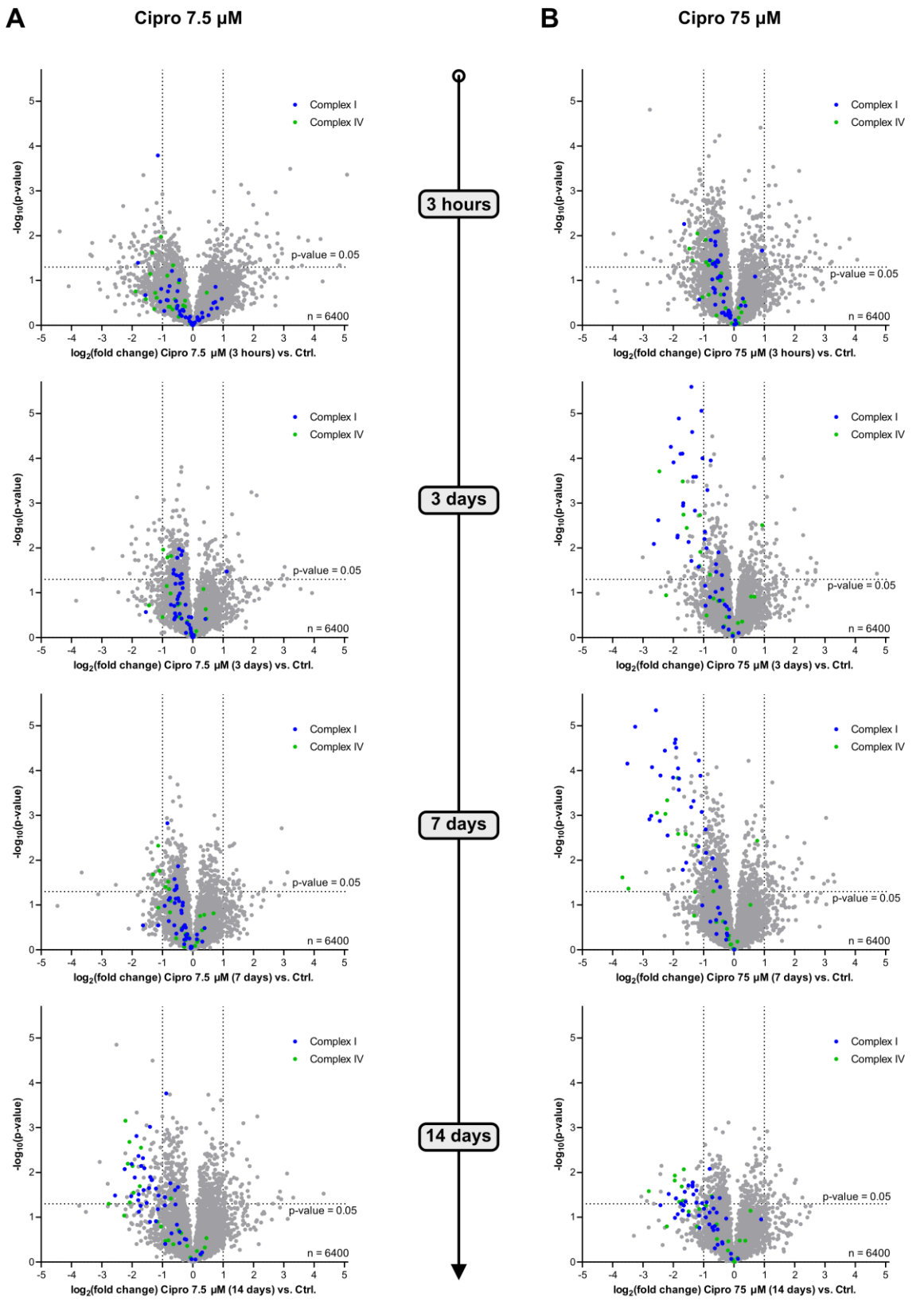

Figure 10: Time-dependent whole proteome analysis of Ciprofloxacin-treated cells over 3 h to 14 days. Human HEK-293 cells were incubated with regular plasma concentration levels (7.5 µM, **A**) and higher peak concentrations (75 µM, **B**) for 3 h, 3 days, 7 days, and 14 days. Subunits of the ETC complex I (blue) and complex IV (green) are highlighted. Significant down-regulation of both complexes was observed along the timeline, at the high concentration already after 3 days, at the low concentration shifted to prolonged treatment times. Vertical threshold lines in the volcano plots represent a $\log_2$ regulation of ±1 and statistical $-\log_{10}$ (*P*-value) ≥ 1.3 (two-sided two-sample *t*-test, *n* = 3 replicates per group).

Dysfunction in neutrophil extracellular trap (NET) signaling, has been shown to be connected with innate immune system defects, as NETs (extracellular filaments mainly composed of DNA) are utilized to trap pathogens.[193,194] Granzyme A signaling is involved in inflammation and caspase-independent cell death.[195,196] Sirtuins are NAD^+-dependent histone deacetylases that are involved in various key metabolic processes including inflammation, apoptosis and redox homeostasis.[197–199] Importantly, the top regulated pathways after 3 days of peak concentration and 14 days of regular concentration are the same and similarly developed in their intensity of dysregulation, underlining the observed concentration- and time-dependent effect.

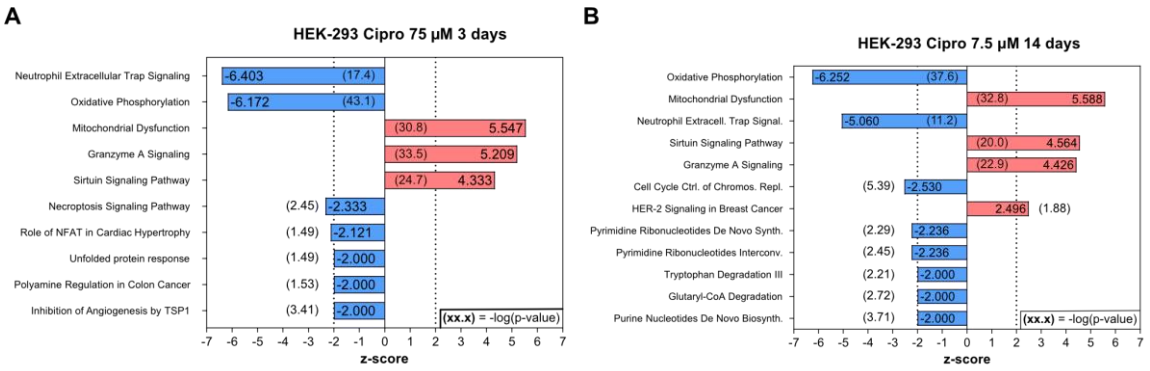

Figure 11: Pathway analyses of proteome regulation in HEK-293 cells upon Ciprofloxacin treatment. (**A**) Pathway analyses after 3 days of incubation with the high concentration. (**B**) Pathway analyses after 14 days of treatment with the low concentration. The extent of the regulation is depicted in the respective z-score (threshold ±2) and the statistical significance given in brackets in form of the negative logarithmic *P*-values. The top regulated pathways in both conditions are comparable in identity and intensity, highlighting that even the regular plasma concentration of Ciprofloxacin is leading to strong dysregulation after prolonged treatment. Pathway analyses were performed with the *Qiagen Ingenuity Pathway Analysis* tool by *Franziska Traube*.

3.1.2 Whole proteome analysis in PDL cells

As discussed, tendon and ligament ruptures are one of the more distinct and abrupt potential side-effects of FQs.[141,143,200,201] Therefore, whole proteome analyses were additionally performed in periodontal ligament (PDL) cells as model cell line for ligaments and tendons. With the results of the previous analyses in mind, an in-depth experiment focusing on 3 days of Ciprofloxacin incubation with both low and high concentrations was designed. To generate a better proteome coverage, the proteomic samples were additionally offline fractionated *via* cation-exchange chromatography, before being subjected to LC-MS/MS measurement. Resulting volcano plots revealed a strikingly similar proteomic dysregulation regarding the concentration-dependent downregulation of ETC complexes I and IV (**Figure 12**).

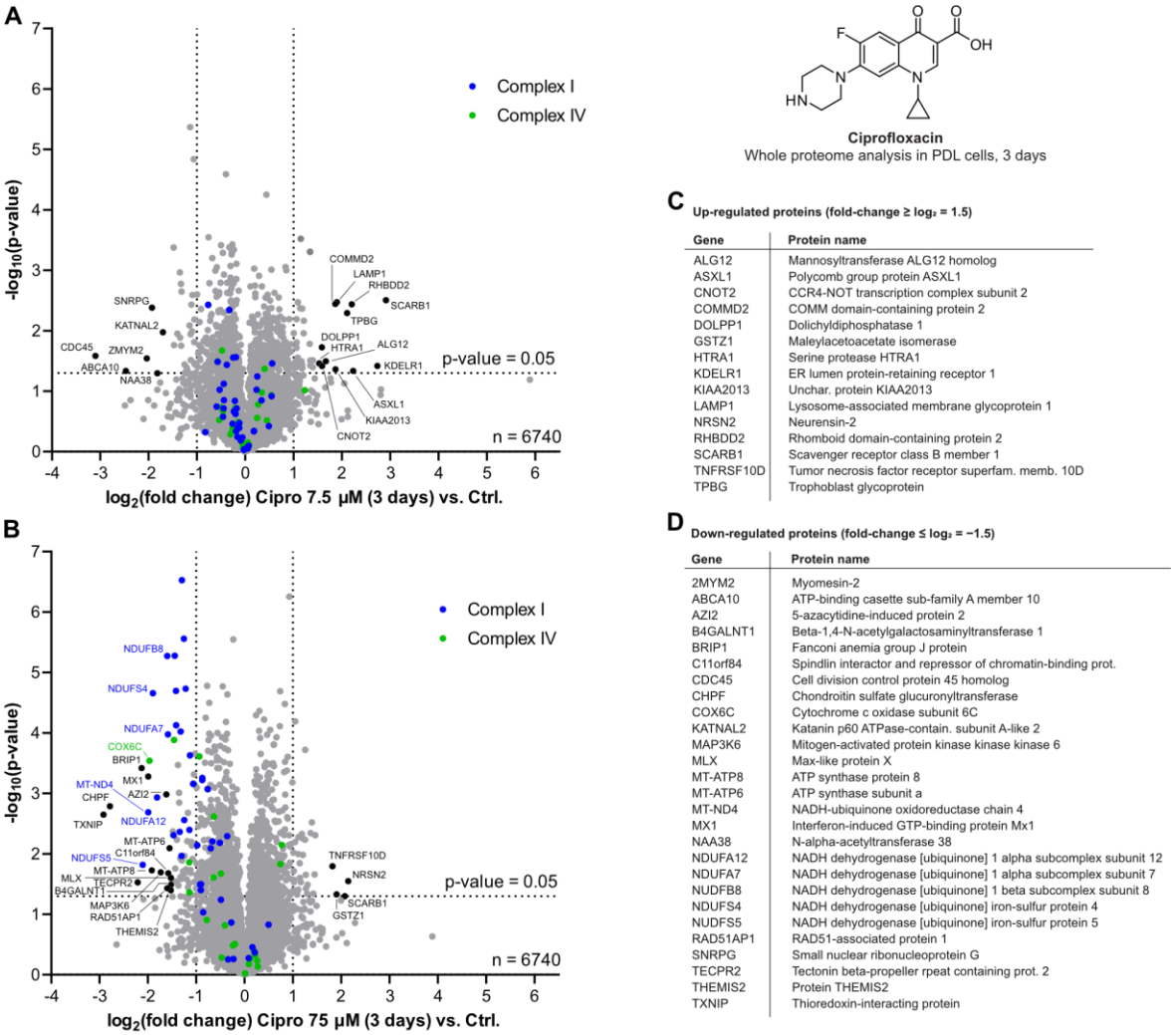

C **Up-regulated proteins (fold-change ≥ $\log_2$ = 1.5)**

Gene	Protein name
ALG12	Mannosyltransferase ALG12 homolog
ASXL1	Polycomb group protein ASXL1
CNOT2	CCR4-NOT transcription complex subunit 2
COMMD2	COMM domain-containing protein 2
DOLPP1	Dolichyldiphosphatase 1
GSTZ1	Maleylacetoacetate isomerase
HTRA1	Serine protease HTRA1
KDELR1	ER lumen protein-retaining receptor 1
KIAA2013	Unchar. protein KIAA2013
LAMP1	Lysosome-associated membrane glycoprotein 1
NRSN2	Neurensin-2
RHBDD2	Rhomboid domain-containing protein 2
SCARB1	Scavenger receptor class B member 1
TNFRSF10D	Tumor necrosis factor receptor superfam. memb. 10D
TPBG	Trophoblast glycoprotein

D **Down-regulated proteins (fold-change ≤ $\log_2$ = −1.5)**

Gene	Protein name
2MYM2	Myomesin-2
ABCA10	ATP-binding casette sub-family A member 10
AZI2	5-azacytidine-induced protein 2
B4GALNT1	Beta-1,4-N-acetylgalactosaminyltransferase 1
BRIP1	Fanconi anemia group J protein
C11orf84	Spindlin interactor and repressor of chromatin-binding prot.
CDC45	Cell division control protein 45 homolog
CHPF	Chondroitin sulfate glucuronyltransferase
COX6C	Cytochrome c oxidase subunit 6C
KATNAL2	Katanin p60 ATPase-contain. subunit A-like 2
MAP3K6	Mitogen-activated protein kinase kinase kinase 6
MLX	Max-like protein X
MT-ATP8	ATP synthase protein 8
MT-ATP6	ATP synthase subunit a
MT-ND4	NADH-ubiquinone oxidoreductase chain 4
MX1	Interferon-induced GTP-binding protein Mx1
NAA38	N-alpha-acetyltransferase 38
NDUFA12	NADH dehydrogenase [ubiquinone] 1 alpha subcomplex subunit 12
NDUFA7	NADH dehydrogenase [ubiquinone] 1 alpha subcomplex subunit 7
NUDFB8	NADH dehydrogenase [ubiquinone] 1 beta subcomplex subunit 8
NDUFS4	NADH dehydrogenase [ubiquinone] iron-sulfur protein 4
NUDFS5	NADH dehydrogenase [ubiquinone] iron-sulfur protein 5
RAD51AP1	RAD51-associated protein 1
SNRPG	Small nuclear ribonucleoprotein G
TECPR2	Tectonin beta-propeller rpeat containing prot. 2
THEMIS2	Protein THEMIS2
TXNIP	Thioredoxin-interacting protein

Figure 12: Whole proteome analysis of Ciprofloxacin in PDL cells after 3 days of treatment. (**A**) Respective volcano plot of the proteome regulation of plasma concentration treated PDL cells (7.5 µM Ciprofloxacin) versus the control. (**B**) Volcano plot of the proteome regulation of peak concentration treated PDL cells (75 µM Ciprofloxacin) versus the control. Vertical threshold lines represent a $\log_2$ regulation of ±1 and $-\log_{10}$ (*P*-value) ≥ 1.3 (two-sided two-sample *t*-test, $n = 4$ replicates per group). Subunits of the ETC complex I and IV are marked in blue and green, respectively. (**C**) Alphabetically sorted table of top up-regulated proteins (threshold: fold-change ≥ $\log_2$ 1.5 and $-\log_{10}$ (*P*-value) ≥ 1.3). (**D**) Alphabetically sorted table of top down-regulated proteins (threshold: fold-change ≤ $\log_2$ –1.5 and $-\log_{10}$ (*P*-value) ≥ 1.3).

In order to investigate if the resulting proteome dysregulation is limited to Ciprofloxacin or a more characteristic feature of the FQ class, the structurally different tricyclic FQ Levofloxacin was similarly studied (**Figure 13**). Indeed, similar results were obtained for Levofloxacin, which was also tested at identical concentrations, although the downregulations of complexes I and IV of the ETC were less pronounced than for Ciprofloxacin. Of note, this might not necessarily translate to an improved side-effect profile for Levofloxacin in therapeutic settings, as the reported plasma concentration of Levofloxacin is also higher with approx. 17 µM.[174]

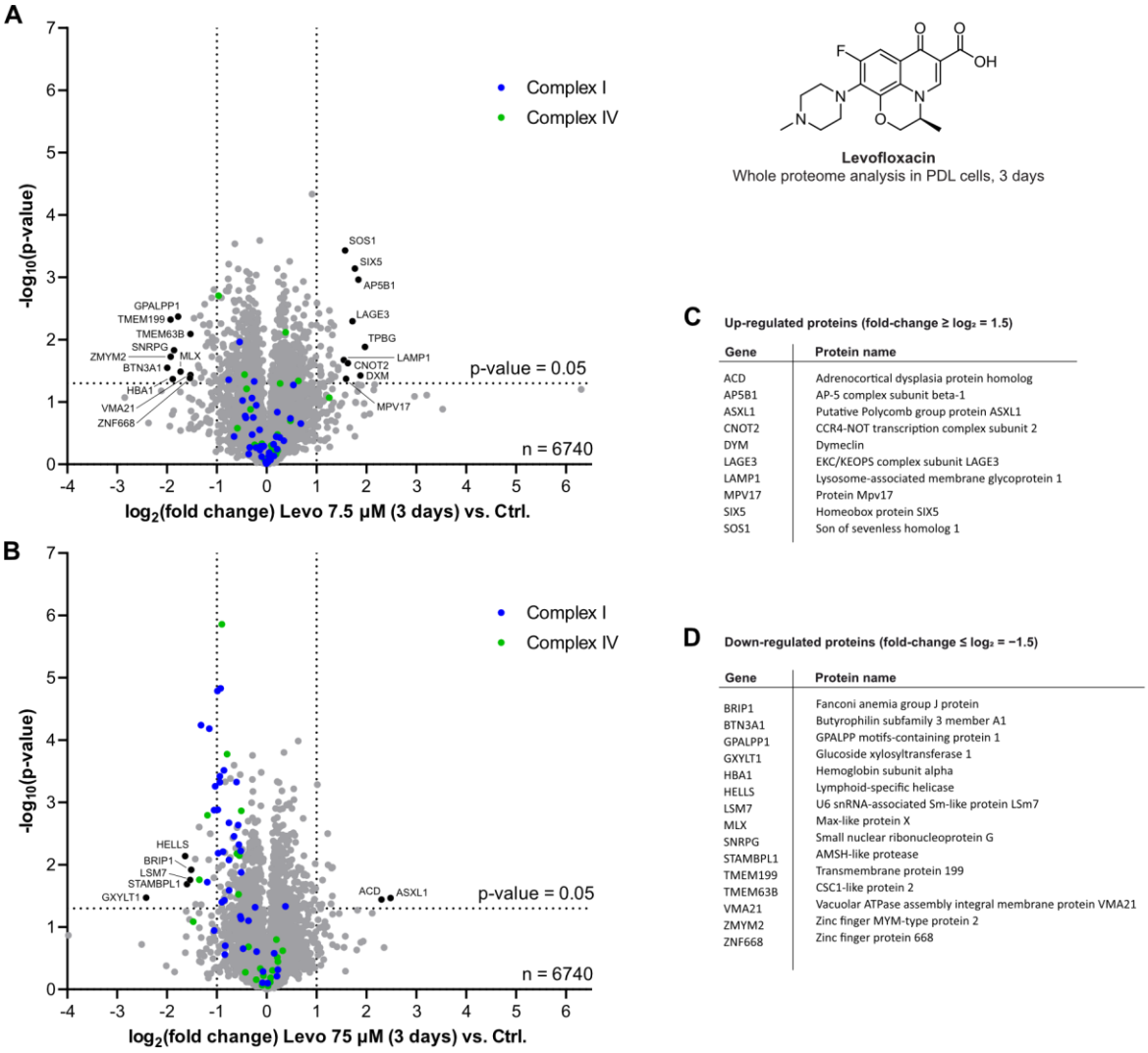

Figure 13: Whole proteome analysis of Levofloxacin in PDL cells after 3 days of treatment. (**A**) Respective volcano plot of the proteome regulation of PDL cells incubated with 7.5 µM Levofloxacin versus the control. (**B**) Volcano plot of the proteome regulation of PDL cells treated with 75 µM Levofloxacin versus the control. Vertical threshold lines represent a $\log_2$ regulation of ±1 and $-\log_{10}$ (*P*-value) ≥ 1.3 (two-sided two-sample *t*-test, $n = 4$ replicates per group). Subunits of the ETC complex I and IV are marked in blue and green, respectively. (**C**) Alphabetically sorted table of top up-regulated proteins (threshold: fold-change ≥ $\log_2$ 1.5). (**D**) Alphabetically sorted table of top down-regulated proteins (threshold: fold-change ≤ $\log_2$ –1.5).

Moreover, the top regulated pathways in the proteome in presence of Ciprofloxacin and Levofloxacin are in accordance with the previous observations in HEK-293 cells. Even at the tested plasma concentration of Ciprofloxacin, a weak but significant onset of the discussed dysregulations in mitochondrial function, oxidative phosphorylation and sirtuin and granzyme A signaling was determined (**Figure 14A**). Consistent with the prior findings in HEK-293 cells, higher systemic drug concentrations led to attenuated effects and to a large variety of additionally affected pathways in PDL cells, including GP6 signaling (the major signaling receptor for collagen)[202,203], purine nucleotide degradation and *de novo* biosynthesis and cholesterol biosynthesis (**Figure 14B**). In line with the less pronounced downregulations of the ETC complexes I and IV upon Levofloxacin treatment, respective

down-stream protein pathways were only shown strongly affected at the high concentration (**Figure 14C-D**).

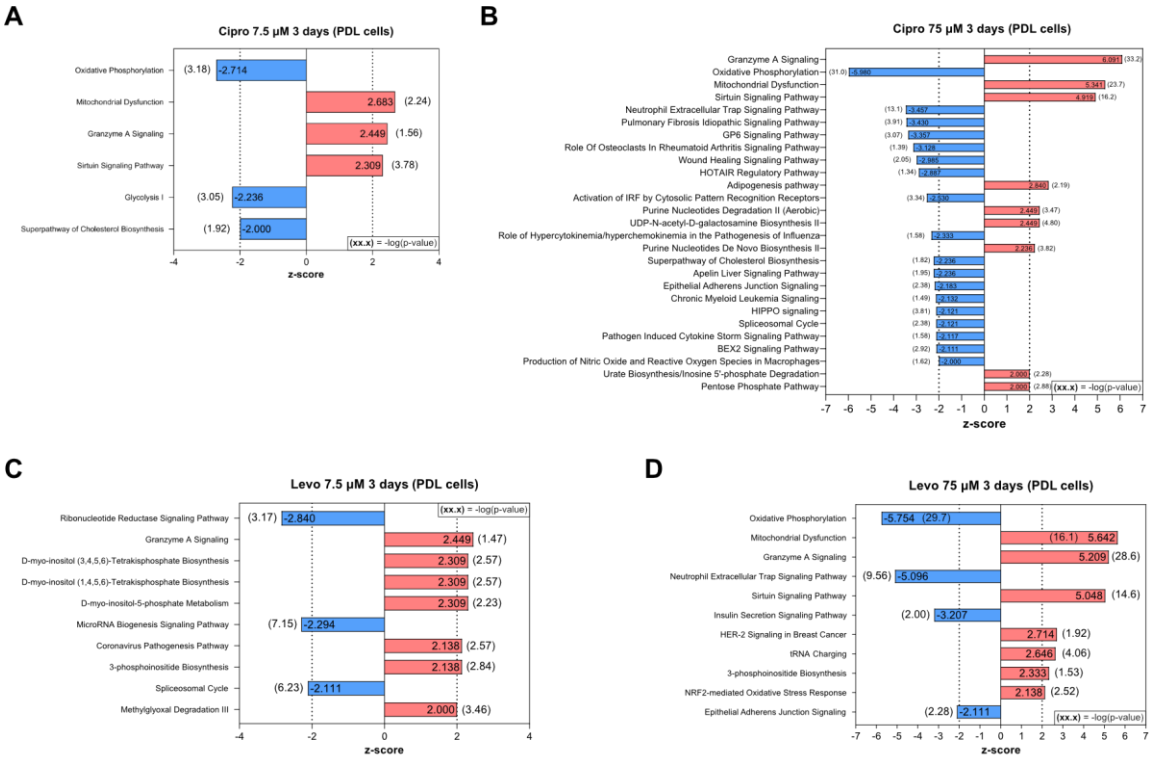

Figure 14: Pathway analyses of proteome regulation in PDL cells upon FQ treatment for 3 days. (**A**) Pathway analyses after 3 days of incubation with the plasma concentration of Ciprofloxacin, revealing an early onset of similar dysregulation of mitochondria, oxidative phosphorylation, granzyme A and sirtuin signaling as observed before in HEK-293 cells. (**B**) Analysis after treatment with the high concentration of Ciprofloxacin, indicating a significant concentration-dependent aggravation of the dysregulation. Respective protein pathway analyses with low (**C**) and high (**D**) concentrations of Levofloxacin. In line with the volcano plots, the impairment of mitochondria-derived pathways is only detectable at the higher concentration, but less pronounced than for Ciprofloxacin. The bar plots depict the extent of the regulation by the z-score (threshold ±2) and the statistical significance in brackets in form of the negative logarithmic *P*-values. Pathway analyses were performed with the *Qiagen Ingenuity Pathway Analysis* tool by *Franziska Traube*.

Consequently, ETC downregulation (especially of complexes I and IV) seemed to be a general characteristic of FQ treatment. Importantly, those dysregulated pathways matched known issues and side-effects of FQs, such as elevated reactive oxygen species (ROS), apoptosis and mitochondrial dysfunction.[128,204,205] Clearly the intensity of cellular impairment was concentration-dependent and side-effects can therefore likely be differentially pronounced due to varying tissues and organelle concentrations in an organism, but also varying between patients due to different pharmacokinetics and drug metabolism. As discussed before, respective risk-factors, such as age and renal impairment, have been reported for the FQAD.[132,141,159–161]

3.2 Impact of FQs on metabolic activity and apoptosis

Due to the pronounced dysregulation in the whole proteome experiments the potential impact on the metabolic activity of HEK-293 and PDL cells was investigated (**Figure 15**). Using a yellow tetrazolium dye (MTT reagent) that can be reduced to insoluble, violet formazan by NAD(P)H-dependent oxidoreductases of metabolically active cells, the relative metabolic activity of compound-treated cells compared to control cells was determined as an indication for the cytotoxicity of the tested substances.[206] As no complete inhibition of the metabolic activity was detected in the solubility range of Ciprofloxacin and Levofloxacin, respective apparent IC_{50} values could only be approximated and can only be a guidance. Although having an impact, approximate apparent IC_{50} values in HEK-293 (Ciprofloxacin > 150 µM, Levofloxacin > 400 µM) are significantly higher than published plasma concentrations of those FQs and in general, the metabolic activity in PDL cells seems to be even slightly less affected by the FQs as in HEK-293 cells (Ciprofloxacin > 175 µM, Levofloxacin > 800 µM). This result is to be expected, as FQs are marketed and well-tolerated by the majority of patients.

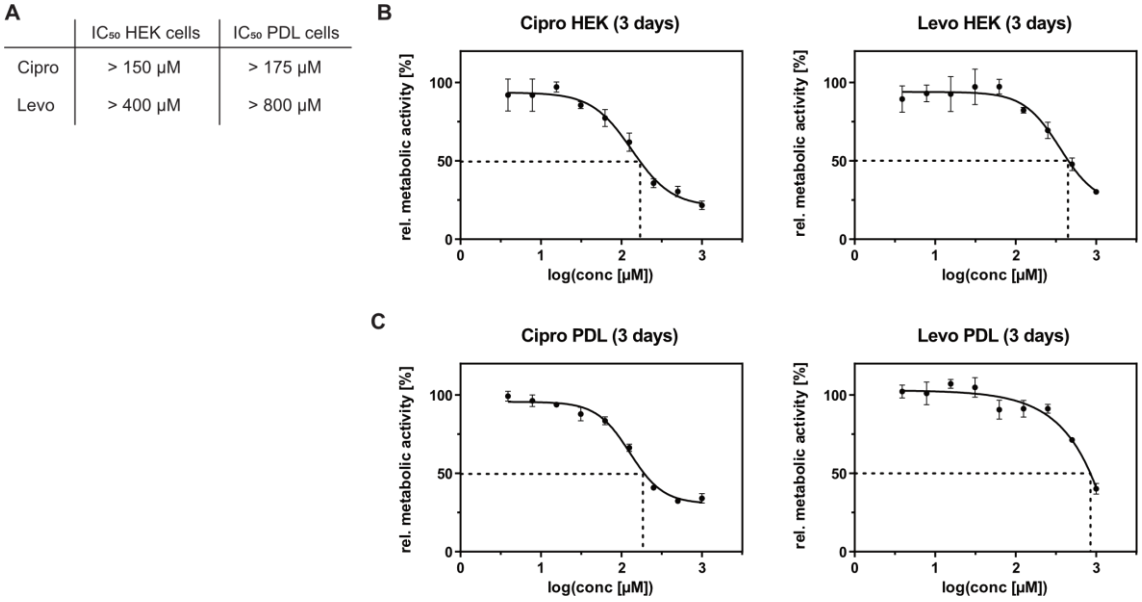

Figure 15: MTT assay of Ciprofloxacin and Levofloxacin after incubation for 3 days. (**A**) Approximate apparent IC_{50} values of Ciprofloxacin (Cipro) and Levofloxacin (Levo) in HEK-293 and PDL cells. Graphs depicting the relative metabolic activity in HEK-293 (**B**) and PDL cells (**C**) relative to control cells. In neither case the tested concentrations in the solubility range led to a complete inhibition of metabolic activity, therefore the apparent IC_{50} values were approximated (dashed lines).

In line with the mitochondrial dysfunction and upregulated sirtuin signaling pathway in the whole proteome analyses, FQs have been reported to induce apoptosis, but tested concentrations in the literature were again significantly higher (350 µg/mL = approx. 1 mM) than published plasma concentrations.[207] The ratio of apoptotic to viable cells can be

determined by fluorescence-activated cell sorting (FACS)-mediated cell live/death assays. Incubating cell populations with a fluorescent Annexin V conjugate, binding to the phosphatidylserine moieties on the outer membrane of apoptotic cells, and the *Sytox* dye, that only permeates cells with compromised plasma membranes, and subsequent fluorescent-based sorting *via* FACS enables the differentiation of the live/death state of individual cells. Accordingly, Annexin V- and *Sytox*-negative cells are viable, Annexin V-positive and *Sytox*-negative cells are defined as early apoptotic, Annexin V- and *Sytox*-positive cells are defined as late apoptotic and Annexin V-negative but *Sytox*-positive cells are necrotic (**Figure 16**).

Using the defined plasma and peak tissue concentrations in PDL cells, the induction of apoptosis was evaluated after 3 days of treatment. While the positive control (H_2O_2 treatment for 30 min, 37 °C) resulted in a strong 23.8% increase of total apoptotic cells (early and late stage) compared to the control cells, Ciprofloxacin (1.5% at 7.5 µM and 4.4% at 75 µM) and Levofloxacin (0.0% at 7.5 µM and 5.2% at 75 µM) resulted only in a weak, but concentration-dependent increase of the apoptotic cell populations (**Figure 16**).

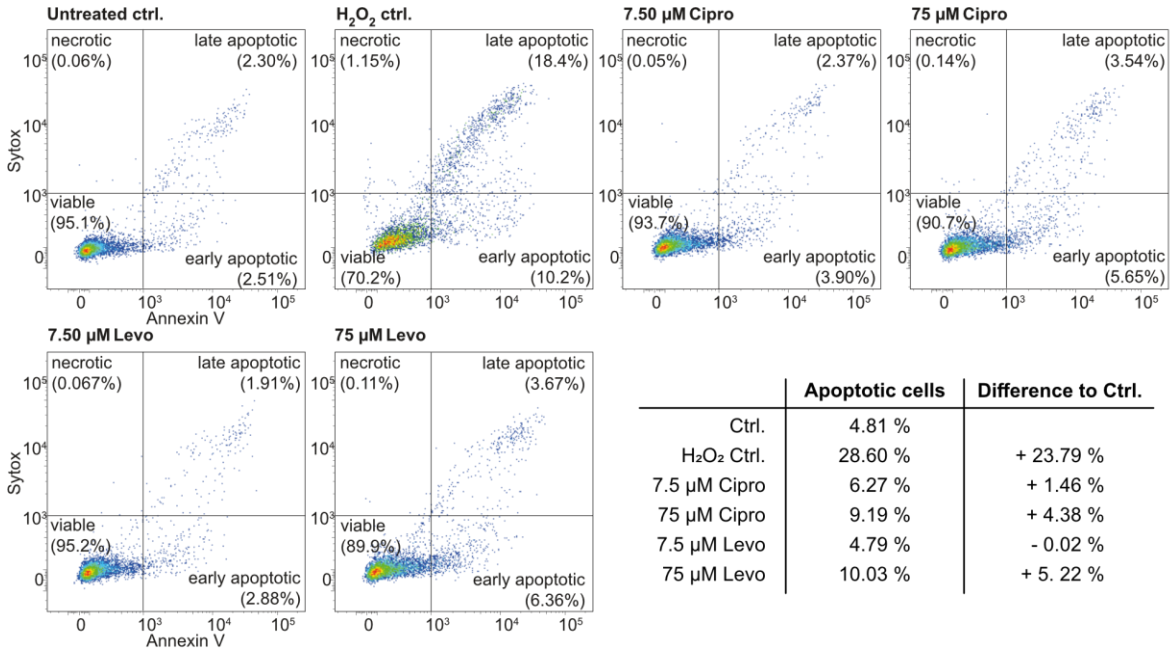

	Apoptotic cells	Difference to Ctrl.
Ctrl.	4.81 %	
H_2O_2 Ctrl.	28.60 %	+ 23.79 %
7.5 µM Cipro	6.27 %	+ 1.46 %
75 µM Cipro	9.19 %	+ 4.38 %
7.5 µM Levo	4.79 %	- 0.02 %
75 µM Levo	10.03 %	+ 5. 22 %

Figure 16: FACS cell death assay of FQs in PDL cells. After incubation for 3 days with Ciprofloxacin (7.5 µM and 75 µM), Levofloxacin (7.5 µM and 75 µM), vehicle control or H_2O_2 (30 min, 37 °C) the cells were detached and incubated with fluorescent Annexin V and *Sytox* dye prior to FACS-mediated fluorescent read-out enabling the quantification (200.000 events per condition) of viable, early apoptotic, late apoptotic and necrotic cell populations. Only weak, but concentration-dependent increases of apoptotic cells (combined population of early and late apoptosis) were detectable with the two FQs.

Considering those metabolic activity (MTT assays) and FACS live/death assay results, pronounced general cytotoxicity and strongly enhanced apoptotic processes are likely only

involved at even higher drug accumulation and/or further down-stream of more prominent side-effects. In any case, the precise molecular mode of action of FQs to cause these side-effects is not well understood and their elucidation was the motivation of the subsequent chemical proteomic experiments.

3.3 FQ off-target discovery *via* chemical proteomics

To decipher potential direct protein off-targets of FQs a two-tiered chemo-proteomic strategy was envisaged employing both probe-based affinity-based protein profiling (AfBPP, compare page 11) and derivatization-free thermal proteome profiling (TPP, compare page 12) for comprehensive off-target discovery. Firstly, the AfBPP approach was pursued.

3.3.1 Synthesis of FQ-derived affinity probes

Chemical affinity probes were designed derived from Ciprofloxacin and Levofloxacin to facilitate the FQ off-target discovery with structural diversity. As discussed on page 10, a photo-crosslinker and bio-orthogonal handle had to be installed to enable covalent off-target trapping and enrichment. Due to their relatively small molecular footprint, it was decided to use the minimalist photo-crosslinker **MPC** developed by *Li et al*.[75] and the branched photo-affinity moiety **BPC** published by *Conway et al*. [208] combining the diazirine photo-affinity group and the alkyne handle in one modification (**Figure 17**). Based on extensive published structure-activity relationship (SAR) studies of antibiotic potencies of FQ-derivatives and good synthetic feasibility, the piperazine ring of both selected FQs was envisaged to be derivatized (**Figure 17A**).[110,209]

As potential human off-targets could use different interfaces of the FQs and not necessarily follow bacterial SAR data, the free carboxylic acid of the two FQs was alternatively modified (**Figure 17B**). While this moiety is essential for their bacterial MoA, it also facilitates the well-established metal complexation of FQs.[163–165] Masking of the free acid could potentially expose metal-binding-independent off-target interactions. Due to known hydrolytic instabilities of esters in cellular systems, an amide modification was aimed for.

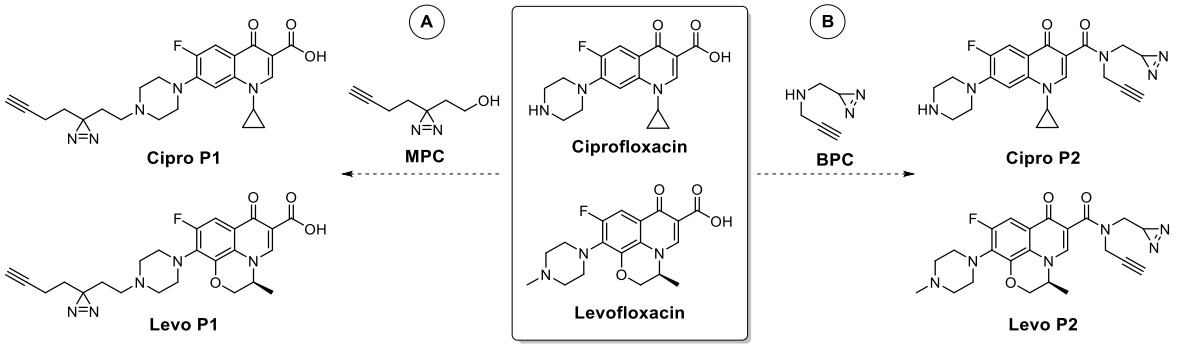

Figure 17: Envisaged affinity-based probes derived from Ciprofloxacin and Levofloxacin.

Nucleophilic substitution conditions at 70 °C overnight with Ciprofloxacin and the literature-known iodo-derivative of the minimalist photo-crosslinker **MPC-I** utilizing $CsCO_3$ as base in aqueous acetonitrile afforded **Cipro P1** in moderate 33% yield after preparative HPLC purification (**Scheme 1**).[75]

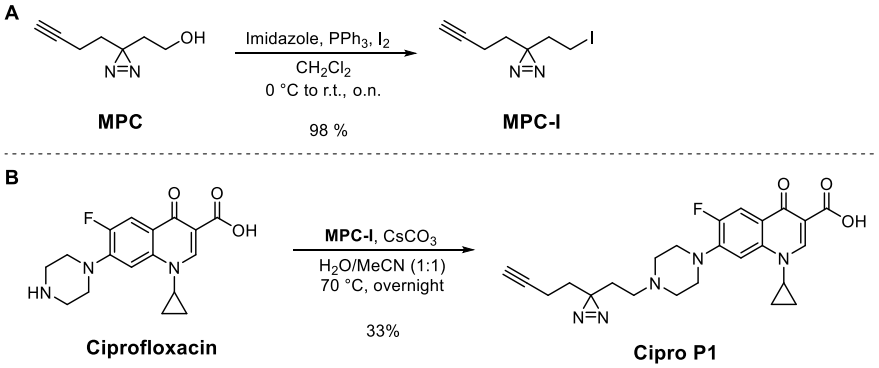

Scheme 1: Synthesis of iodo photo-crosslinker **MPC-I** and **Cipro P1**.

To enable a similar synthetic route towards a respective probe derived from Levofloxacin (featuring itself already a methylated piperazine), an unsubstituted piperazine moiety was appended to **Levofloxacin Q-acid** *via* heat-mediated nucleophilic aromatic substitution in presence of triethylamine as base to afford **1** (**Scheme 2**). The secondary amine **1** was subjected to similar nucleophilic substitution conditions used for the Ciprofloxacin probe to obtain **Levo P1** in 35% yield over two steps.

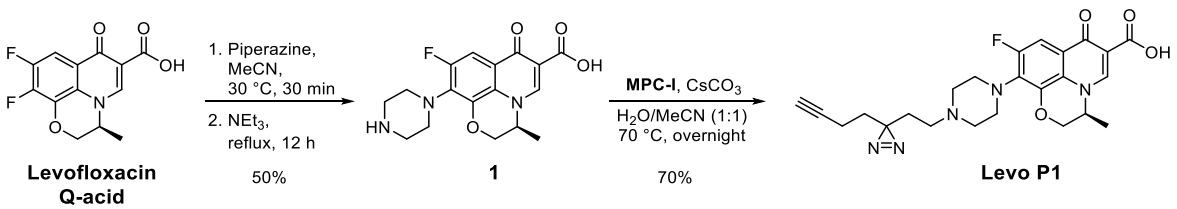

Scheme 2: Synthesis of **Levo P1** probe *via* two steps.

For the synthesis of the second set of probes, first the branched photo-crosslinker **BPC** had to be obtained. The published synthesis commences with commercially available *N*-β-Boc-D-2,3-diaminopropionic acid **5**, however due to delivery problems at that time, this educt had to be first afforded synthetically (**Scheme 3**).[208] Starting from commercially available *N*-benzyloxycarbonyl-L-asparagine **2**, a PIDA-mediated *Hofmann*-rearrangement was performed to obtain amino acid derivative **3** in 93% as reported by *Zhang et al*.[210] Boc-protection of the primary amine gave orthogonally di-protected amino acid **4**, enabling the selective Cbz-deprotection *via* standard hydrogenation conditions to afford the desired *N*-β-Boc-D-2,3-diaminopropionic acid **5** starting material in excellent 83% yield over 3 steps. Subsequent reaction steps were performed as reported by *Conway et al*.[208] Firstly the amino acid **5** was directly transformed into the terminal diazirine **6** again *via* a PIDA-mediated methodology developed by *Glachet et al.* in 2019.[211] By nucleophilic substitution with propargyl bromide the alkyne handle was appended giving **7** in only very moderate 26% yield. Lastly, Boc-deprotection with TFA in dichloromethane afforded the branched photo-crosslinker **BPC** as the corresponding TFA-salt.

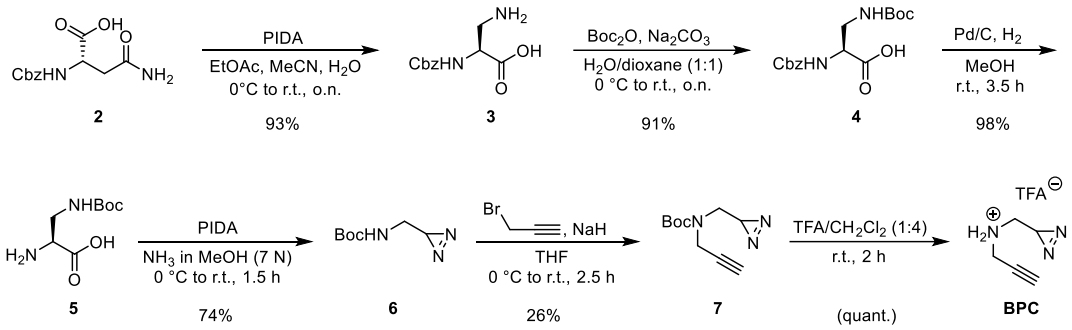

Scheme 3: Synthesis of the branched photo-crosslinker **BPC** *via* 6 steps.

With the branched photo-crosslinker in hand, the piperazine moiety of Ciprofloxacin was Boc-protected in H_2O/dioxane (1:1) yielding **8** in 90% and enabling amide coupling of the affinity linker **BPC** with HBTU and catalytic amounts of DMAP affording amide **9** (**Scheme 4A**). Immediate TFA-mediated deprotection of crude **9** afforded **Cipro P2** in 49% yield over two steps after HPLC purification. Applying the same amide coupling conditions directly to Levofloxacin, the respective probe **Levo P2** was synthesized in 35% isolated yield after HPLC purification (**Scheme 4B**).

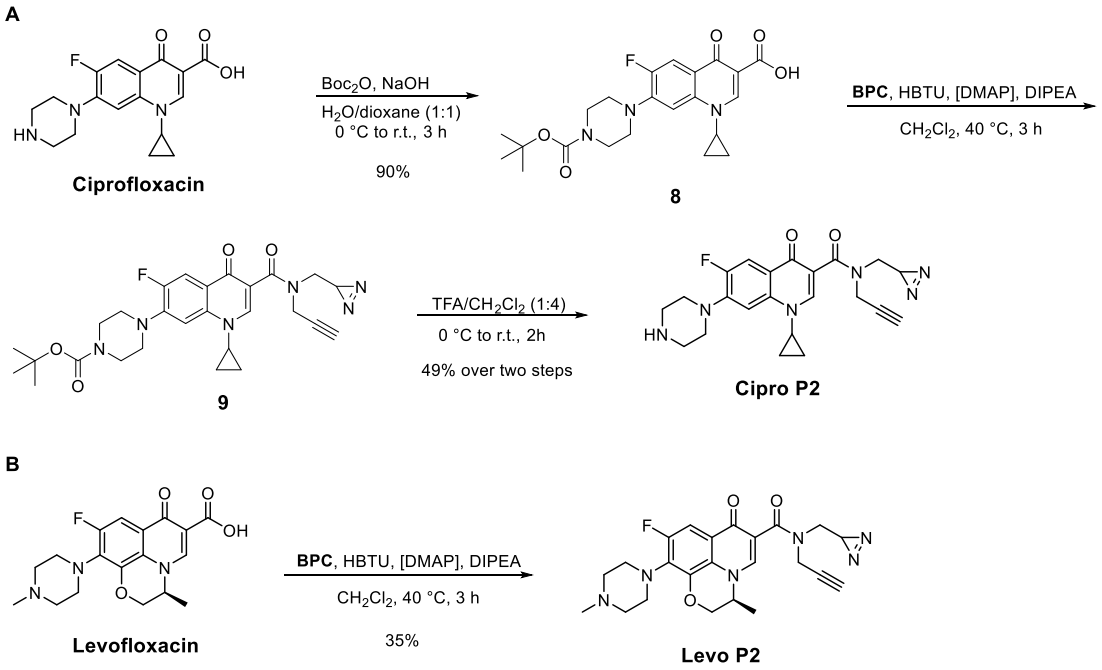

Scheme 4: Synthetic route towards **P2**-probes. (**A**) Synthesis of **Cipro P2**: Boc-deprotection, amide coupling of the branched photo-crosslinker and subsequent deprotection afforded **Cipro P2**. (**B**) Synthesis of probe **Levo P2** *via* amide coupling.

3.3.2 Bioactivity of FQ-derived probes

After the successful synthesis of the small set of FQ-probes, they were tested for their antibiotic activity in comparison to their parent compounds. Both pathogenic Gram-positive *S. aureus* NCTC8325 and Gram-negative *E. coli* MM28 strains were selected for minimal inhibitory concentration (MIC) measurements (**Figure 18A**). While the activities of the **P1** probes against *S. aureus* were only moderately impaired by the synthetic modification (**Cipro P1** 12.5-fold, **Levo P1** 25-fold), the potencies of the **P2** probes dropped significantly with >1600-fold for **Cipro P2** and 3225-fold for **Levo P2**. Considering the mentioned SAR studies this result was to be expected. Interestingly, the antibiotic potencies of active **P1** probes also decreased 100-fold in Gram-negative *E. coli*, which is most likely due to restricted uptake or cell penetration, as their activities in LPS-deficient *E. coli* RFM795 were only 4-times lower compared to their parent compounds. Lipopolysaccharides (LPS) are major components of the outer Gram-negative membrane, deficiencies in their biosynthesis are therefore promoting Gram-negative cell penetration of compounds. In line with the SAR data, the activities of **Cipro P2** and **Levo P2** also decreased significantly in both *E. coli* strains, however interestingly, **Levo P2** still featured a moderate MIC in *E. coli* MM28 and RFM795.

A

Organism	Ciprofloxacin	Levofloxacin	Cipro P1	Levo P1	Cipro P2	Levo P2
S. aureus NCTC8325	62 nM	31 nM	780 nM (12.5×)	780 nM (25×)	> 100 **µM** (> 1600×)	100 **µM** (3225×)
E. coli MM28	15 - 31 n**M**	62 nM	3.1 **µM** (100×)	6.25 **µM** (100×)	50 **µM** (1600×)	25 **µM** (400×)
E. coli RFM795	8 n**M**	15 - 31 nM	31 n**M** (4×)	125 n**M** (4×)	12.5 **µM** (1560×)	3 **µM** (100×)

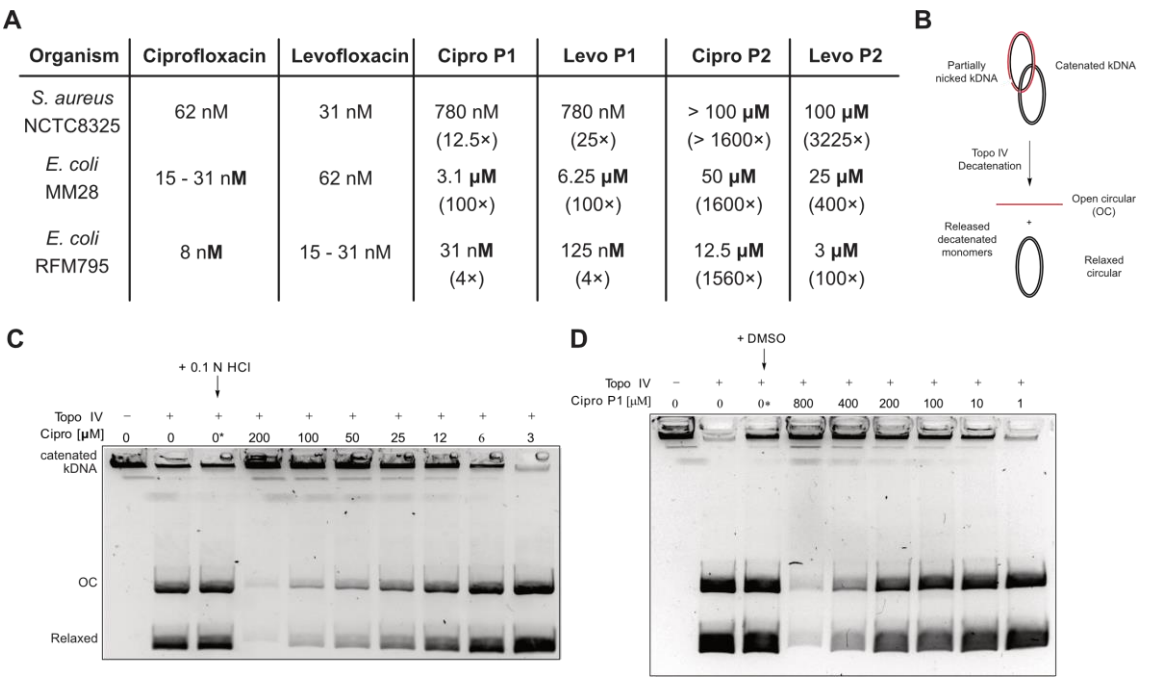

Figure 18: Bacterial bioactivity of FQ-derived affinity probes. (**A**) Minimal inhibitory concentrations (MICs) of the parent FQs and their corresponding probes. For comparison the x-fold decreases in activity are indicated in brackets. **P2** probes, with the essential carboxylic acid being modified, featured generally significantly lower or no potencies at all. (**B**) Principle of the topoisomerase IV activity assay. The enzyme decatenates kDNA into monomers, that can be separated with agarose-gel electrophoresis. When an intercalator is present in the agarose gel, the monomers are resolved in their relaxed circular and their open circular (OC) forms. The latter is derived from partially nicked kDNA. (**C**) Topoisomerase IV activity assay in presence of Ciprofloxacin. The approximate apparent IC_{50} value of Ciprofloxacin was 25 µM. (**D**) Decatenation assay in presence of **Cipro P1** still showed enzyme inhibition, however approx. 16-fold lower inhibitory potency.

In order to further confirm intact target engagement of the **P1** probes, the inhibition of one of the known FQ targets in bacteria was exemplarily tested by **Cipro P1**. Literature-known *S. aureus* topoisomerase IV decatenation assays were performed in which catenated kDNA is being unlinked and resolved into their open-circular and relaxed-circular forms using agarose-gel electrophoresis (**Figure 18B**).[212] In presence of the parent compound Ciprofloxacin, the resulting approximate apparent IC_{50} value was 25 µM, which is in line with literature values (7-20 µM) for this *in vitro* assay (**Figure 18C**).[213,214] In accordance with the MIC results, **Cipro P1** inhibited the topoisomerase IV despite its derivatization with an apparent IC_{50} decrease (approx. 16-fold) in a similar range to the previous increase of the MIC (**Figure 18D**).

Furthermore, the feasibility of the probes in human cells was investigated. As done previously with the parent compounds, MTT assays were performed after 3 days of incubation to determine the relative metabolic activity of HEK-293 and PDL cells as indicator for the cytotoxicity of the probes (**Figure 19**). Both **Cipro P1** and **Levo P1** affected the metabolic activity only at very high concentrations, > 750 µM and > 950 µM in HEK-293 cells, respectively. Those approximate apparent IC_{50} concentrations were even higher than previously determined for the parent compounds (Ciprofloxacin > 150 µM,

Levofloxacin > 400 µM, **Figure 15**). In PDL cells the corresponding values were generally lower, however still not indicating significant toxicity with > 550 µM for Ciprofloxacin and > 380 µM for Levofloxacin.

A

	Cipro P1	Cipro P2	Levo P1	Levo P2
HEK	> 750 µM	> 400 µM	> 950 µM	> 350 µM
PDL	> 550 µM	> 120 µM	> 380 µM	> 150 µM

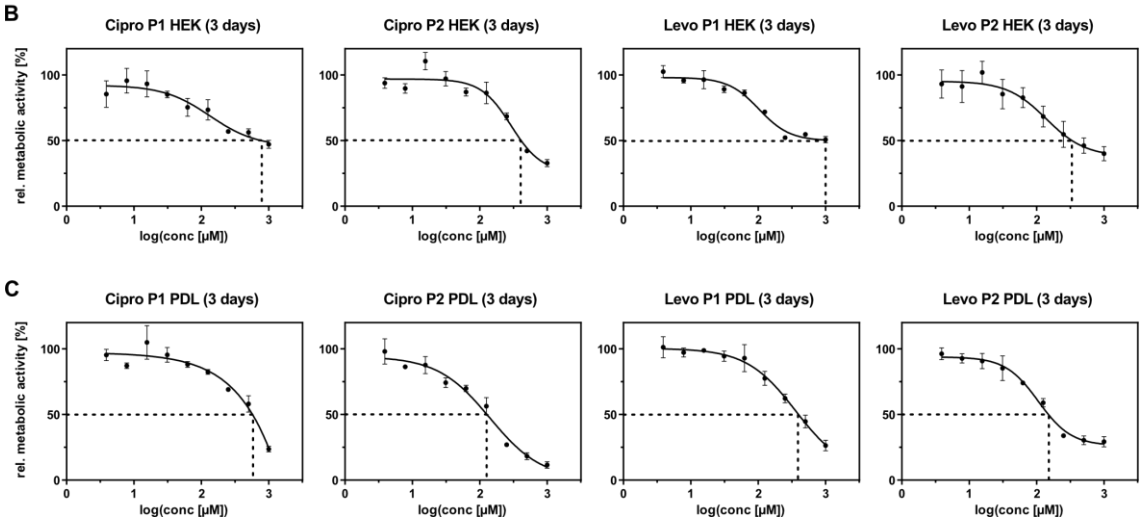

Figure 19: MTT assays of FQ-derived probes in HEK-293 and PDL cells. (**A**) Table summarizing the approximate apparent IC_{50} values of the four probes after 3 days of treatment. Corresponding MTT assay plots in HEK-293 (**B**) and PDL (**C**) cells. As in neither case the tested concentrations in the solubility range up to 1 mM led to a complete inhibition of metabolic activity, the apparent IC_{50} values were approximated (dashed lines).

Approximate apparent IC_{50} values of the **P2** probes showed in both cell lines a slightly more pronounced effect compared to the **P1** probes, but no acute toxicity and effects in the range of the values of the parent compounds (**Figure 19**, **Figure 15**).

Consequently, these initial tests of the probes confirmed that **Cipro P1** and **Levo P1** retained their antibiotic activity and featured no acute toxicity, thus being good tools for off-target discovery. As the aim of this project is the identification of human off-targets, the antibiotically non-active, but also non-toxic probes **Cipro P2** and **Levo P2** were nonetheless projected to the next experiments. As discussed, different SAR principles could be valid for human protein (off-)targets.

3.3.3 Analytical gel-based AfBPP with FQ-derived probe Cipro P1

With the four FQ-derived affinity probes in hand, analytical proof-of-concept experiments were conducted with **Cipro P1** to verify successful protein labeling and determine optimal probe concentrations for subsequent preparative, MS-based AfBPP studies. HEK-292 cells were *in situ*-treated with **Cipro P1** (2, 5, 7.5 and 75 µM) for 1 h at 37 °C in FCS-free medium

and following UV irradiation to activate the photo-crosslinker for 15 min at 360 nm, the cells were lysed and TAMRA-azide fluorophore appended *via* CuAAC chemistry.[215] Read-out with fluorescent scanning SDS-PAGE visualized a distinct, concentration-dependent labeling pattern of **Cipro P1** (**Figure 20A**). Importantly, a good signal-to-noise labeling was already detected at 2 µM and therefore concentrations well above the approximate IC_{50} values of the probes as determined before.

Moreover, both the vehicle control and the non-UV-treated control showed no labeling and the Coomassie-stain of the gel verified equal loading amounts per lane. The *in situ* labeling step is commonly conducted in FCS-free medium, to minimize serum-protein binding. Comparison of analytical labeling in FCS-containing and FCS-free medium confirmed that the labeling intensity was increased in FCS-free medium, the distinct labeling pattern was however not manipulated (**Figure 20B**).

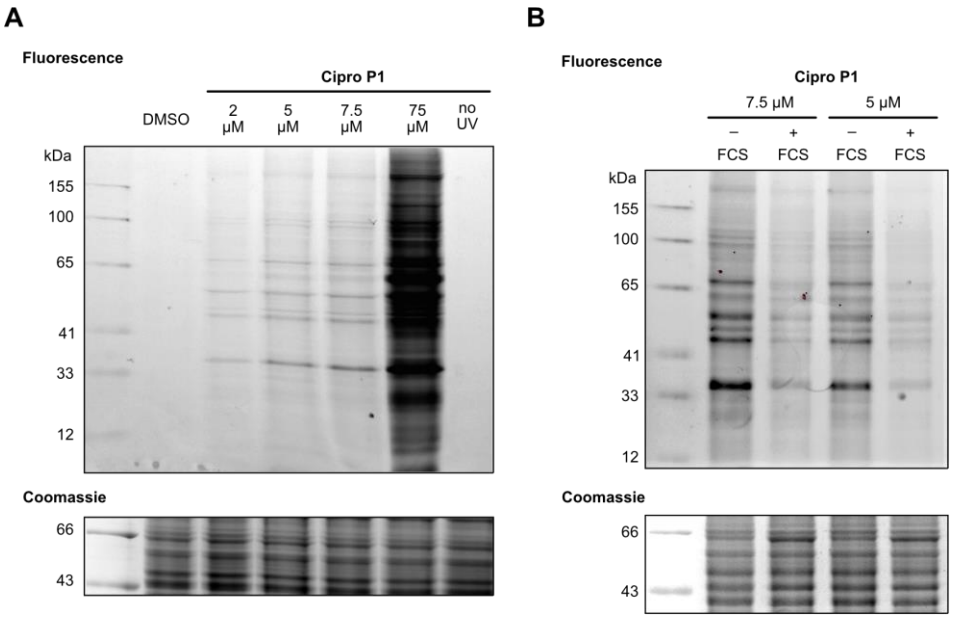

Figure 20: Analytical gel-based AfBPP with **Cipro P1** in HEK-293 cells. (**A**) Cells were *in situ*-treated for 1 h at 37 °C with varying concentrations of **Cipro P1**. After UV irradiation for 15 min at 360 nm, cells were lysed, TAMRA-fluorophore attached to the alkyne *via* CuAAC chemistry and proteins separated by SDS-PAGE. Fluorescent scanning of the gel revealed concentration-dependent and distinct labeling of the proteome by **Cipro P1**. Vehicle- and non-irradiated controls showed no labeling and the corresponding Coomassie stain verified equal protein loading per lane. (**B**) Analytical AfBPP experiment with the same conditions comparing labeling in FCS-free and FCS-containing medium. Serum-free labeling increased the intensity but did not change the labeling pattern.

3.3.4 Preparative MS-based AfBPP with Cipro P1

Considering the analytical results, the AfBPP proof-of-concept study with **Cipro P1** was expanded to the MS-based workflow to identify potential (off-)targets of Ciprofloxacin for the first time. By appending biotin azide instead of the fluorophore to the alkyne after cell lysis, putative interacting proteins can be enriched on avidin beads and, after tryptic digest, quantified and identified *via* LC-MS/MS (see **Figure 4**). Comparing probe-treated versus control-treated samples utilizing two-sided two-sampled *t*-tests, the data is usually represented in volcano plots depicting $\log_2$-fold enrichment of proteins in relation to the statistical significance (–log(*P*-value)). In AfBPP experiments, common thresholds for proteins to be considered potential protein targets are a $\log_2$(enrichment) of ≥ 2, equaling $\geq$ 4-fold enrichment in probe versus control samples, and a –log(*P*-value) of 1.3, representing a false-discovery rate (FDR) of 5%.

The first MS-based AfBPP experiment was also performed in HEK-293 cells in dose-dependent manner applying (0.5, 1.0 and 2.5 µM Cipro P1) for 1 h at 37 °C in four biological replicates each. In contrast to the analytical labeling the UV irradiation time was decreased to 10 min to minimize unspecific labeling. The resulting volcano plots are depicted in **Figure 21A**. Photo-crosslinkers have been shown to feature common unspecific protein labeling, these so-called photome hits, have been categorized before and are highlighted in red in the volcano plots to be disregarded for further investigations.[92] Excluding 4 photome hits, 12 potential proteins of interest remained, both subsets are listed in **Figure 21B-C**. Importantly, all remaining potential (off-)targets showed concentration-dependent enrichment by increasing probe concentration (**Figure 21D**).

To evaluate if this rather large set of putatively engaged targets is only specific to HEK-293 cells, the same experiment was repeated in diverse A549 lung cancer cells (**Figure 22**). Interestingly, a wide range of these potential protein (off-)targets appeared to be conserved with 12 proteins overlapping between both cell lines (**Figure 22D**). Additional three proteins (ClpP, ABCC4 and TRIM21) were generally enriched, however just below the threshold of $\log_2$(enrichment) ≥ 2 in either of the two cell lines.

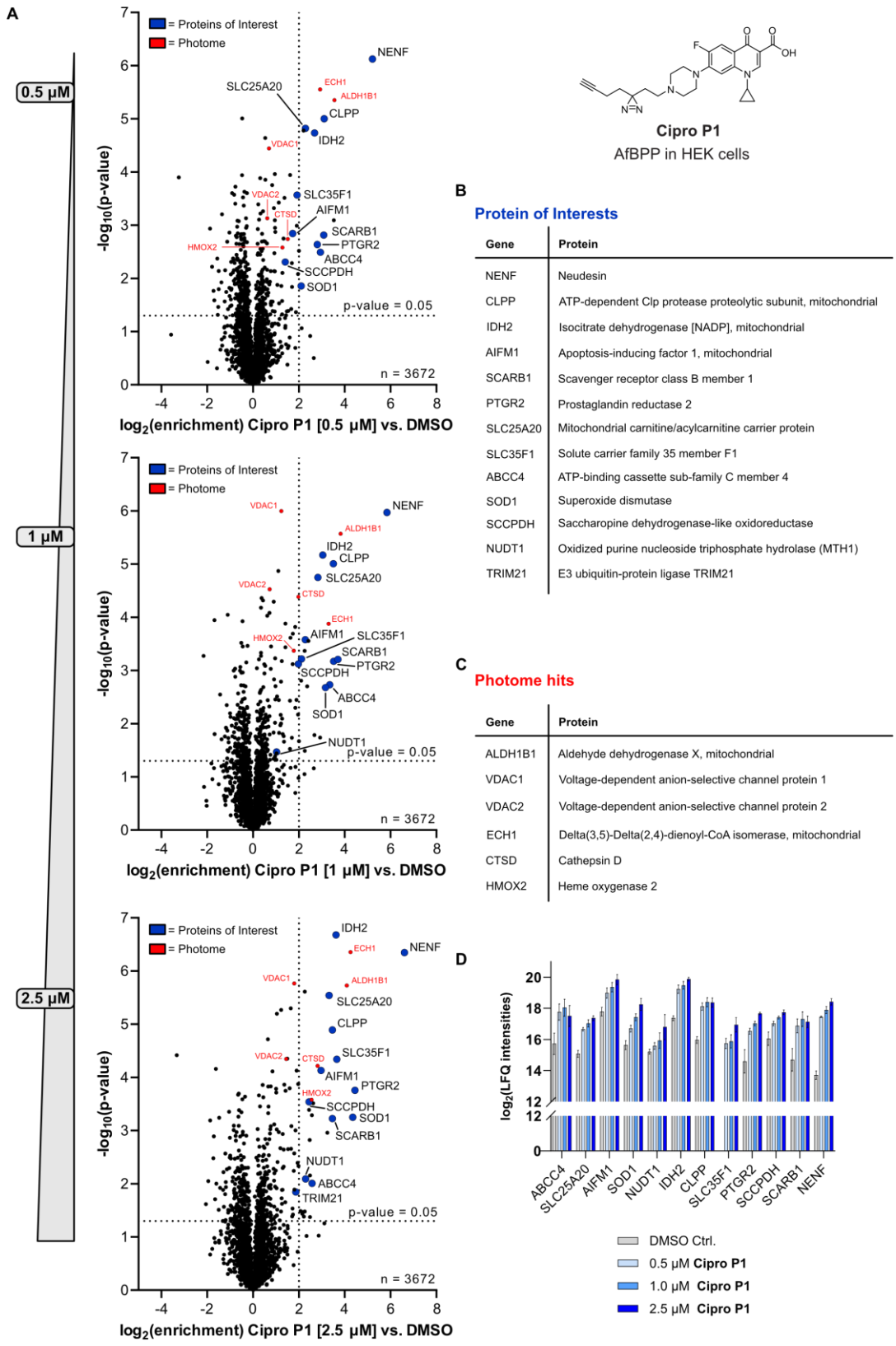

Gene	Protein
NENF	Neudesin
CLPP	ATP-dependent Clp protease proteolytic subunit, mitochondrial
IDH2	Isocitrate dehydrogenase [NADP], mitochondrial
AIFM1	Apoptosis-inducing factor 1, mitochondrial
SCARB1	Scavenger receptor class B member 1
PTGR2	Prostaglandin reductase 2
SLC25A20	Mitochondrial carnitine/acylcarnitine carrier protein
SLC35F1	Solute carrier family 35 member F1
ABCC4	ATP-binding cassette sub-family C member 4
SOD1	Superoxide dismutase
SCCPDH	Saccharopine dehydrogenase-like oxidoreductase
NUDT1	Oxidized purine nucleoside triphosphate hydrolase (MTH1)
TRIM21	E3 ubiquitin-protein ligase TRIM21

Gene	Protein
ALDH1B1	Aldehyde dehydrogenase X, mitochondrial
VDAC1	Voltage-dependent anion-selective channel protein 1
VDAC2	Voltage-dependent anion-selective channel protein 2
ECH1	Delta(3,5)-Delta(2,4)-dienoyl-CoA isomerase, mitochondrial
CTSD	Cathepsin D
HMOX2	Heme oxygenase 2

Figure 21: MS-based AfBPP with **Cipro P1** in HEK-293 cells. (**A**) Dose-dependent AfBPP of **Cipro P1** (0.5, 1.0 and 2.5 µM for 1 h at 37 °C). Volcano plots depict probe- versus control-treated cells and dashed threshold lines indicate a $\log_2$ enrichment ≥ 2 and the statistical significance $-\log_{10}(P \text{ value}) \geq 1.3$ (two-sided two-sample *t*-test, $n = 4$ replicates per group). Reported unspecific photome hits of diazirine photo-crosslinkers are marked in red, putative proteins of interest labeled in blue. (**B**) Table of corresponding proteins of interest based on the volcano plots. (**C**) Table of common photome hits indicated in red in the volcano plots. (**D**) Profile plot depicting the $\log_2$(LFQ intensities) and respective SD of the 12 proteins of interest adhering to the thresholds indicating concentration-dependent engagement of the probe.

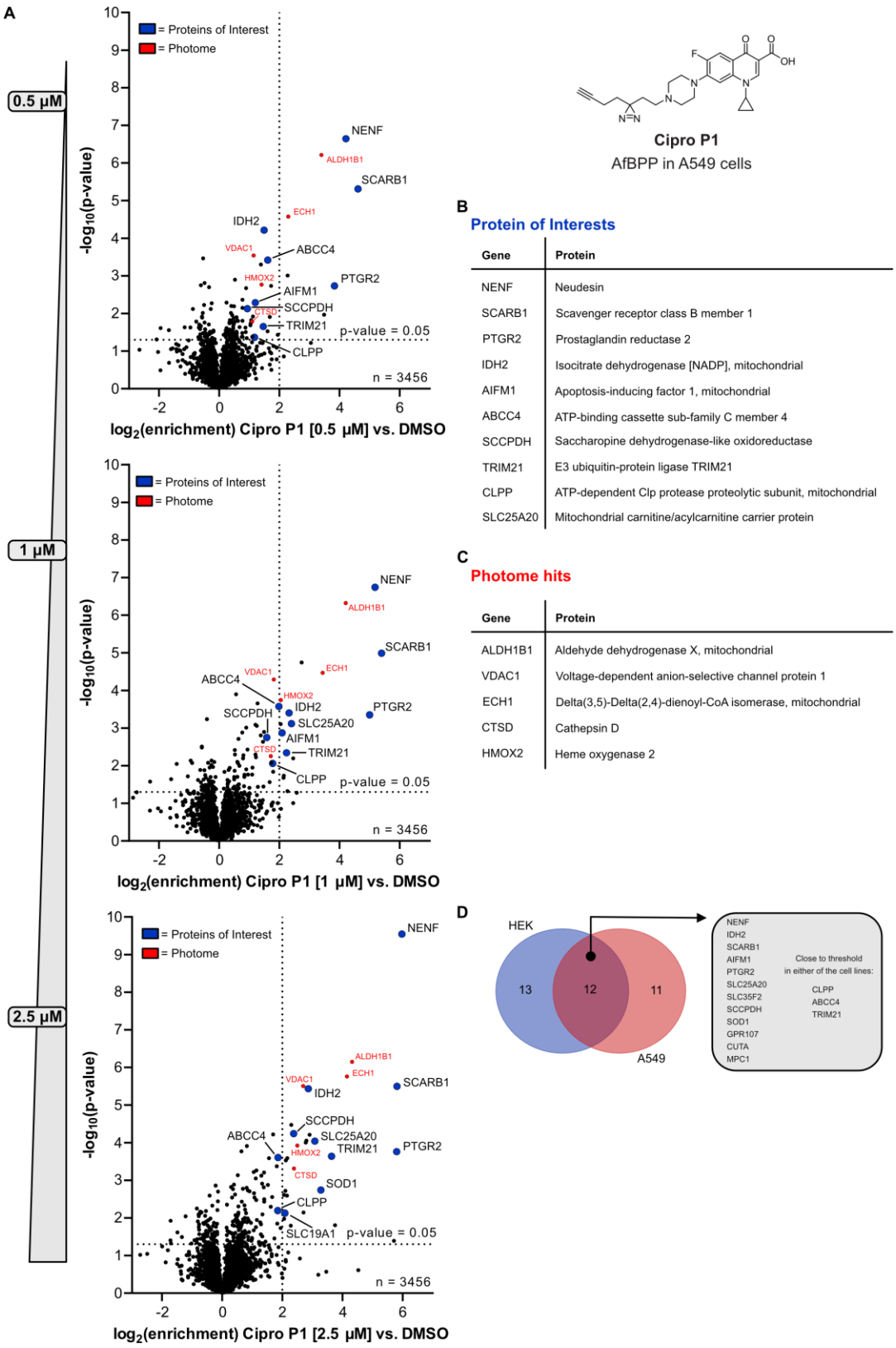

Figure 22: MS-based AfBPP with **Cipro P1** in A549 cells. (**A**) Dose-dependent AfBPP of **Cipro P1** (0.5, 1.0 and 2.5 µM for 1 h at 37 °C). Volcano plots depict probe- versus control-treated cells and dashed threshold lines indicate a $\log_2$ enrichment ≥ 2 and the statistical significance $-\log_{10}(P \text{ value}) \geq 1.3$ (two-sided two-sample *t*-test, $n = 4$ replicates per group). Reported unspecific photome hits of diazirine photo-crosslinkers are marked in red, putative proteins of interest labeled in blue. (**B**) Table of corresponding proteins of interest based on the volcano plots. (**C**) Table of common photome hits indicated in red in the volcano plots. (**D**) Venn-diagram illustrating the overlapping proteins of interest between **Cipro P1** in HEK-293 and A549 cells adhering to the standard thresholds. Additionally, three further proteins are given that are enriched, but just below the threshold of $\log_2 \geq 2$ in either of the two cell lines.

Encouraged by the conserved results of the proof-of-concept studies with **Cipro P1** in the two cells lines, the full set of FQ-derived probes (**Cipro P1**, **Cipro P2**, **Levo P1** and **Levo P2**) was applied in the PDL cells, as model for tendon- and ligament-derived cells. As the publication describing the development of the branched photo-crosslinker used in the **P2** probes reported the need for higher probe concentrations for good signal-to-noise ratios in the labeling, again gel-based AfBPP studies were performed beforehand (**Figure 23**). As the terminal diazirine also features a different optimal activation wavelength, 300 nm instead of 360 nm was used during UV irradiation for the **P2** probes. Both the *in situ* incubation (1 h, 37 °C) with **Cipro P2** and **Levo P2** resulted in concentration-dependent labeling in the tested range from 6.25 to 100 µM. As expected, a higher concentration was needed for a well-pronounced signal.

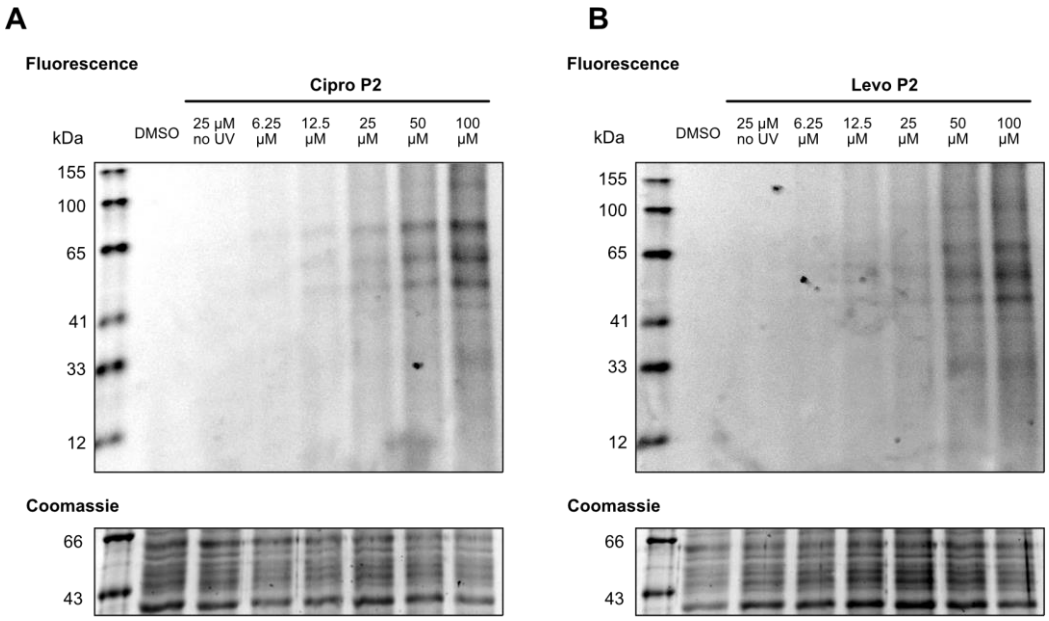

Figure 23: Analytical gel-based AfBPP with **Cipro P2** and **Levo P2** in PDL cells. (**A**) Gel-based labeling of **Cipro P2**. (**B**) Gel-based labeling of **Levo P2**. As reported, the branched photo-crosslinker used in the **P2** probes needed higher concentrations compared to **P1** probes for sufficient labelling.[208] Cells were *in situ*-treated for 1 h at 37 °C with varying concentrations of the probes. After UV irradiation for 10 min at 300 nm, cells were lysed, TAMRA-fluorophore attached to the alkyne *via* CuAAC chemistry and proteins separated by SDS-PAGE. Fluorescent scanning of the gel revealed concentration-dependent and distinct labeling of the proteome. Vehicle and non-irradiated controls showed no labeling and the corresponding Coomassie stain verified equal protein loading per lane.

Accordingly, the MS-based AfBPP investigations of the **P2** probes were performed with 25 µM, the **P1** probes were tested at 5 µM (**Figure 25** and **Figure 26**). Comparing the results of **Cipro P1** in the PDL cells with the data of the proof-of-concept studies in HEK-293 and A549 cells, the 6 proteins NENF, IDH2, AIFM1, SCARB1, SCCPDH and SLC25A20 were shared (**Figure 24A**). The protein ClpP was shared between HEK-293 and PDL cells, TRIM21 and SLC19A shared between A549 and PDL cells. The HEK-293 and A549 cells

featured an additional strong overlap of 6 proteins. These results further substantiated the notion of a conserved set of (off-)targets across diverse cell lines.

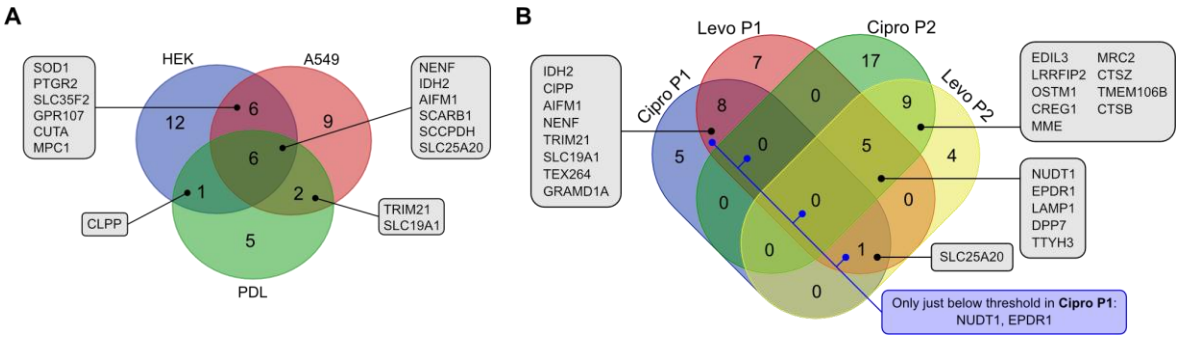

Figure 24: Venn-diagrams illustrating the conserved (off-)target hits. (**A**) Relation of proteins adhering to the standard thresholds with **Cipro P1** in the three cell lines HEK-293, A549 and PDL. (**B**) Relation of proteins adhering to the standard threshold with the full probe set in PDL cells.

Interestingly, **Cipro P1** and **Levo P1**, derived from structurally diverse FQs, enriched a common set of 8 proteins (**Figure 24B**). However, compared to the **P1** probes, both **P2** probes revealed a widely different set of proteins, with no mutual hits across all 4 probes. Among each other, **Cipro P2** and **Levo P2** shared 9 proteins. Notably, there was an overlap between **Levo P1** and both **P2** probes with 5 proteins, including NUDT1, EPDR1 and LAMP1. Of these proteins, NUDT1 and EPDR1 were actually only just below the standard threshold of $\log_2(\text{enrichment}) \geq 2$ with **Cipro P1** (**Figure 25A**).

The fact that the two **P1** probes and the two **P2** probes engaged with significantly different proteins, but shared many hits within each probe group, suggested that the modification of the free carboxylic acid or the general localization of the photo-crosslinker has a strong influence on the labeling specificity. Closer inspection of the engaged proteins by the **P2** probes revealed a pronounced cluster of lysosomal proteins as indicated in **Figure 26C-D** with an asterisk. Likely the masking of the free acid changes the isoelectric point the FQs, facilitating their protonation and thereby trapping in the acidic lysosomes. On the other hand lysosomal accumulation has also been reported for unmodified Ciprofloxacin and therefore this phenomenon was subject of further investigations later in the project.[207]

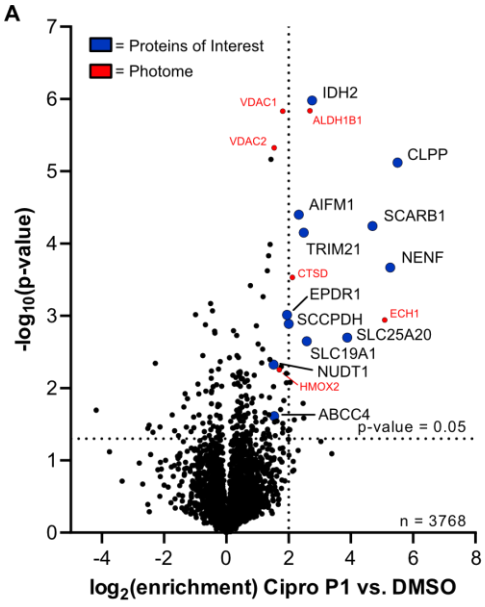

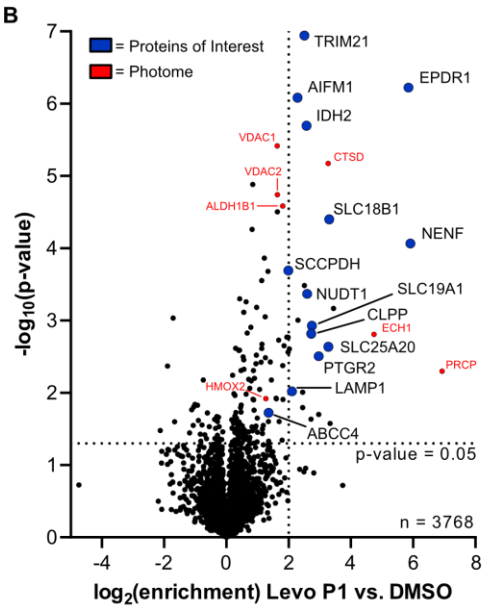

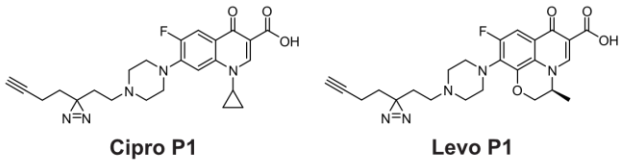

AfBPP at 5 µM in PDL cells

C **Protein of Interests**

Gene	Protein
IDH2	Isocitrate dehydrogenase [NADP], mitochondrial
CLPP	ATP-dependent Clp protease proteolytic subunit, mitochondrial
AIFM1	Apoptosis-inducing factor 1, mitochondrial
SCARB1	Scavenger receptor class B member 1
TRIM21	E3 ubiquitin-protein ligase TRIM21
NENF	Neudesin
SLC19A1	Reduced folate transporter
SLC25A20	Mitochondrial carnitine/acylcarnitine carrier protein
NUDT1	Oxidized purine nucleoside triphosphate hydrolase (MTH1)
EPDR1	Mammalian ependymin-related protein 1
SLC18B1	MFS-type transporter SLC18B1
PTGR2	Prostaglandin reductase 2
LAMP1	Lysosome-associated membrane glycoprotein 1
SCCPDH	Saccharopine dehydrogenase-like oxidoreductase
ABCC4	ATP-binding cassette sub-family C member 4

D **Photome hits**

Gene	Protein
VDAC1	Voltage-dependent anion-selective channel protein 1
VDAC2	Voltage-dependent anion-selective channel protein 2
ALDH1B1	Aldehyde dehydrogenase X, mitochondrial
CTSD	Cathepsin D
ECH1	Delta(3,5)-Delta(2,4)-dienoyl-CoA isomerase, mitochondrial
HMOX2	Heme oxygenase 2
PRCP	Lysosomal Pro-X carboxypeptidase

Figure 25: MS-based AfBPP with **P1** probes in PDL cells. After incubation with the respective probe (1 h, 37 °C), the cells were UV-irradiated at 360 nm for 10 min. (**A**) Volcano plot of **Cipro P1** versus control. (**B**) Volcano plot of **Levo P1** versus control. Dashed threshold lines indicate a $\log_2$ enrichment ≥ 2 and the statistical significance $-\log_{10}(P \text{ value}) \geq 1.3$ (two-sided two-sample *t*-test, $n = 4$ replicates per group). Putative proteins of interest are labeled in blue and listed in (**C**). Reported unspecific photome hits of diazirine photo-crosslinkers are marked in red and listed in (**D**).

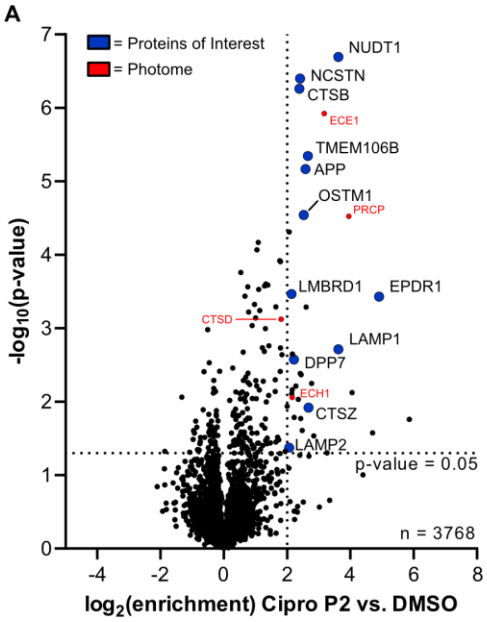

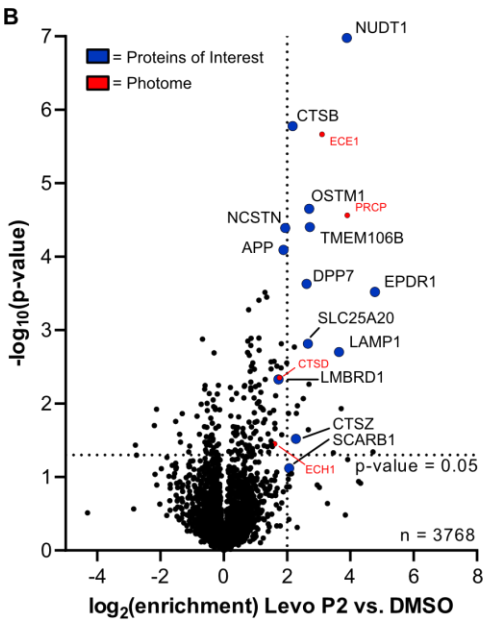

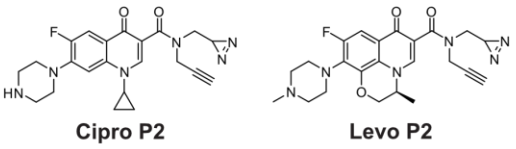

AfBPP at 25 µM in PDL cells

C

Protein of Interests

	Gene	Protein
	NUDT1	Oxidized purine nucleoside triphosphate hydrolase (MTH1)
*	NCSTN	Lysosomal Pro-X carboxypeptidase
*	CTSB	Mammalian ependymin-related protein 1
*	TMEM106B	Transmembrane protein 106B
	APP	Amyloid-beta precursor protein
*	OSTM1	Osteopetrosis-associated transmembrane protein 1
*	LMBRD1	Lysosomal cobalamin transport escort protein LMBD1
*	EPDR1	Mammalian ependymin-related protein 1
*	LAMP1	Lysosome-associated membrane glycoprotein 1
*	LAMP2	Lysosome-associated membrane glycoprotein 2
*	DPP7	Dipeptidyl peptidase 2
*	CTSZ	Cathepsin Z

D

Photome hits

	Gene	Protein
*	CTSD	Cathepsin D
	ECH1	Delta(3,5)-Delta(2,4)-dienoyl-CoA isomerase, mitochondrial
*	PRCP	Lysosomal Pro-X carboxypeptidase
	ECE1	Endothelin-converting enzyme 1

* = Protein localized in the lysosome

Figure 26: MS-based AfBPP with **P2** probes in PDL cells. After incubation with the respective probe (1 h, 37 °C), the cells were UV-irradiated at 300 nm for 10 min. (**A**) Volcano plot of **Cipro P2** versus control. (**B**) Volcano plot of **Levo P2** versus control. Dashed threshold lines indicate a $\log_2$ enrichment ≥ 2 and the statistical significance $-\log_{10}(P \text{ value}) \geq 1.3$ (two-sided two-sample *t*-test, $n = 4$ replicates per group). Putative proteins of interest are labeled in blue and listed in (**C**). Reported unspecific photome hits of diazirine photo-crosslinkers are marked in red and listed in (**D**). A large fraction of enriched proteins is located in the lysosome as indicated by the asterisk.

3.3.5 Thermal proteome profiling (TPP) with Ciprofloxacin

Before prioritization of proteins for FQ (off-)target validation, an orthogonal, derivatization-free approach for (off-)target discovery was pursued in order to develop a more comprehensive picture in human cells. For this, thermal proteome profiling (TPP, page 12) monitoring the proteome-wide ligand-induced stabilization and/or destabilization of proteins upon incubation with the compound of interest was selected.

Interestingly, TPP with Ciprofloxacin has already been performed in *E. coli* as one of the exemplary drugs tested in the proof-of-concept publication of this technique in bacteria.[82] *Mateus et al.* found GyrB, the subunit B of the known gyrase-target of FQs in bacteria, significantly stabilized, as well as multiple down-stream effects involved in the SOS DNA damage response, such as stabilization of RecA and YebG and destabilization/degradation of LexA.[82]

Encouraged by those detectable proteome stabilization effects for Ciprofloxacin in bacteria, the technique was conducted with Ciprofloxacin in intact human HEK-293 cells using the high concentration of 75 µM and 1 h of incubation at 37 °C. After sample preparation, LC-MS/MS measurement and data analysis with published TPP R-scripts by *Franken et al.*, several potential direct or indirect (off-)targets of Ciprofloxacin were revealed (**Figure 27**, **Figure 28**).[87]

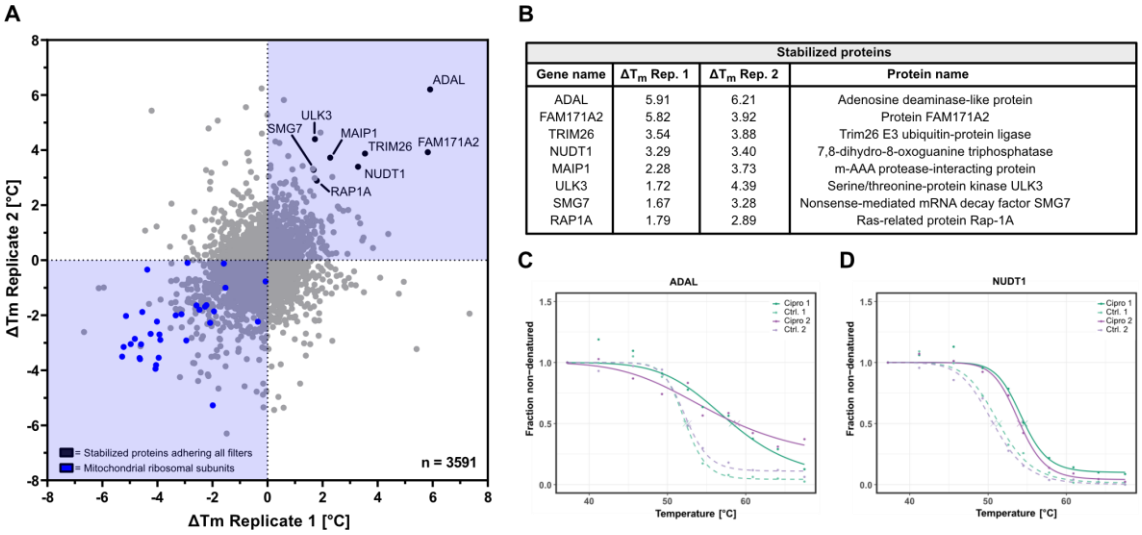

Stabilized proteins			
Gene name	ΔT_m Rep. 1	ΔT_m Rep. 2	Protein name
ADAL	5.91	6.21	Adenosine deaminase-like protein
FAM171A2	5.82	3.92	Protein FAM171A2
TRIM26	3.54	3.88	Trim26 E3 ubiquitin-protein ligase
NUDT1	3.29	3.40	7,8-dihydro-8-oxoguanine triphosphatase
MAIP1	2.28	3.73	m-AAA protease-interacting protein
ULK3	1.72	4.39	Serine/threonine-protein kinase ULK3
SMG7	1.67	3.28	Nonsense-mediated mRNA decay factor SMG7
RAP1A	1.79	2.89	Ras-related protein Rap-1A

Figure 27: Observed stabilization of proteins in TPP with Ciprofloxacin in HEK-293 cells. (**A**) Scatter plot depicting the melting point differences of both Ciprofloxacin-treated replicates (75 µM, 1 h, 37 °C) versus their vehicle-treated controls. Stabilized proteins adhering to all filters are labeled in black. Identified mito-ribosomal subunits are depicted in blue and appeared to be significantly destabilized. (**B**) Table of stabilized proteins adhering to all filters. (**C**) Respective melting curve of the top stabilized protein adenosine deaminase-like protein ADAL1. (**D**) Respective melting curve of the protein 7,8-dihydro-8-oxoguanine triphosphatase NUDT1, representing the single overlapping protein between AfBPP and TPP (off-)target identification strategies.

Application of the suggested standard filters (*P*-values <0.05 in one replicate and <0.01 in the other replicate, melting point shifts (ΔT_m) in the same direction in each replicate versus control, ΔT_m in each compound vs. control replicate greater than the ΔT_m between both control replicates and a minimum slope of the inferred melting curve < -0.06 in each compound versus control experiment), revealed 8 stabilized proteins due to direct compound-binding or indirect proteotypic effects (**Figure 27A-B**). The most significantly stabilized protein was the adenosine deaminase-like protein ADAL1 with ΔT_m shifts of 5.91 °C and 6.21 °C in the two replicates compared to the controls. The inferred melting curves of ADAL1 are depicted in **Figure 27C**. Especially noteworthy was also the apparent stabilization of the 7,8-dihydro-8-oxoguanine triphosphatase NUDT1, as this represented the single overlapping protein between AfBPP and TPP (off-)target identification experiments. The respective melting curves of NUDT1 are depicted in **Figure 27D**.

Vice versa, 15 proteins were detected to be directly destabilized or their expression indirectly affected by the incubation of intact HEK-293 cells with Ciprofloxacin (**Figure 28A-B**). Of these, 10 were proteins of the small (28S) mitochondrial ribosomal subunit, indicating yet again mitochondrial dysfunction, here explicitly impaired mitochondrial translation.

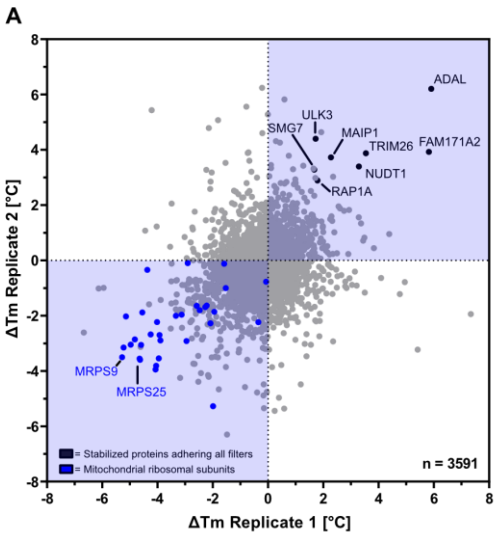

B

Destabilized proteins

Gene name	ΔT_m Rep. 1	ΔT_m Rep. 2	Protein name
ZNF574	– 3.18	– 4.25	Zinc finger protein 574
MRPS22	– 4.97	– 3.05	28S ribosomal protein S22, mitochondrial
RAD51C	– 2.53	– 3.45	DNA repair protein RAD51 homolog 3
MRPS12	– 4.07	– 3.95	28S ribosomal protein S12, mitochondrial
F8A1	– 6.67	– 2.61	40-kDa huntingtin-associated protein
DAP3	– 4.25	– 2.68	28S ribosomal protein S29, mitochondrial
MRPS25	– 4.63	– 3.59	28S ribosomal protein S25, mitochondrial
MRPS5	– 5.23	– 3.15	28S ribosomal protein S5, mitochondrial
MRPS15	– 4.05	– 3.81	28S ribosomal protein S15, mitochondrial
MRPS9	– 5.28	– 3.51	28S ribosomal protein S9, mitochondrial
MRPS39	– 4.60	– 3.06	28S ribosomal protein S39, mitochondrial
MRPS26	– 4.65	– 3.55	28S ribosomal protein S26, mitochondrial
MED11	– 4.62	– 3.13	Mediator of RNA polymerase II transcription subunit 11
SIK3	– 2.61	– 1.84	Serine/threonine-protein kinase SIK3
MRPS17	– 3.96	– 3.55	28S ribosomal protein S17, mitochondrial

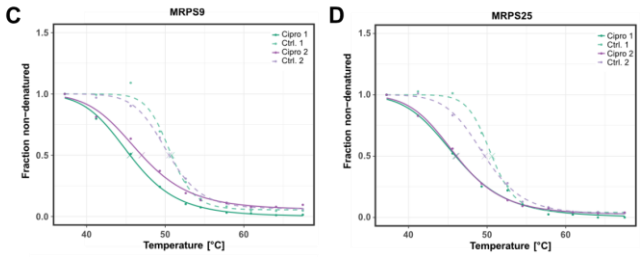

Figure 28: Observed destabilization of proteins in TPP with Ciprofloxacin in HEK-293 cells. (**A**) Scatter plot depicting the melting point differences of both Ciprofloxacin-treated replicates (75 µM, 1 h, 37 °C) versus their vehicle-treated controls. Stabilized proteins adhering to all filters are labeled in black. Identified mito-ribosomal subunits are depicted in blue and appeared to be significantly destabilized. This is likely a secondary down-stream effect revealed by *in situ* TPP in intact cells. (**B**) Table of destabilized proteins adhering to all filters. Exemplary melting curves of mito-ribosomal subunits MRPS9 (**C**) and MRPS25 (**D**).

Two exemplary sets of melting curves for affected mito-ribosomal proteins MRPS9 and MRPS25 are given in **Figure 28C-D**.

3.3.6 Prioritization of putative off-targets for validation studies

Having performed two orthogonal chemo-proteomic approaches to elucidate the human protein off-targets of FQs, the resulting putative hits were scrutinized and prioritized for subsequent validation studies. Firstly, ADAL1 as strongest TPP hit and NUDT1 as only shared hit between TPP and AfBPP (where it was also part of the small set of proteins enriched with both **P1** and **P2** probes) were selected for validation experiments. In general, the limited overlap between TPP and AfBPP highlighted the merit of performing both approaches and could be due to multiple reasons. On the one hand, the modification of the FQs with the affinity groups for AfBPP could lead to additional false-positive identifications or reversely to impaired target engagement by the derivatization leading to false-negatives. Also, a non-optimal positioning of the photo-crosslinker could lead to no enrichment of target proteins, despite successful engagement by the probe. On the other hand, detection of ligandability by TPP requires a significant shift in ΔT_m upon compound binding, which is not always the case. Especially for intrinsically stabilized proteins, e.g. membrane proteins or protein oligomers and complexes, this can be challenging.

In addition to ADAL1 and NUDT1, the AfBPP hit proteins ClpP, AIFM1, IDH2, SCARB1 and PTGR2 were selected for further validation. Those proteins were not only strong candidates according to the proteomic data, but also their activities and functions relate to observed adverse effects and dysregulations of FQs: Inflammation and lipid metabolism (PTGR2)[216–218], cholesterol homeostasis (SCARB1)[219,220], mitochondrial maintenance (ClpP)[221–223], ROS homeostasis and involvement with matrix metalloproteinase (MMP) activity (IDH2)[224,225] and ETC complex I and IV biogenesis (AIFM1)[226–228]. Furthermore, a potential lysosomal trapping mechanism was selected to be considered, due to the pronounced enrichment of lysosomal proteins with the **P2** probes and reported lysosomal accumulation of Ciprofloxacin itself.[207]

As discussed, known photome hits classified by *Kleiner et al*. were excluded.[92] Furthermore, proteins known to interact with xenobiotics during import and export, as well as proteins frequently labeled with the minimalist photo-crosslinker in the literature with diverse probe structures, such as SCCPDH, SLC25A20, SLC19A1 and ABCC4 were disregarded.[229–237] Moreover, the secreted protein neudesin (NENF) was excluded because of its reported overexpression in immortalized human cell lines and cancer cells.[238] Despite their exclusion for direct target validation studies, the enrichment of those proteins could potentially still be

interesting, as their transient labeling could indicate uptake and efflux routes of the probes and FQs.

3.4 Synthesis of metabolites of Ciprofloxacin

In order to include a set of metabolic products of FQs into target validation studies, the four known metabolites of Ciprofloxacin were synthesized.[175] Although Ciprofloxacin is excreted mainly non-metabolized *via* renal and transintestinal pathways, studies showed 11.3% of an oral dose excreted as metabolites *via* the urine and 7.5% excreted as metabolites *via* faeces.[175] The percentage of metabolites in the urine was comprised of the three known metabolites **Desethylene-Cipro** (1.4%), **Sulfo-Cipro** (3.7%) and **Oxo-Cipro** (6.2%). The fourth metabolite **Formyl-Cipro** has been isolated only in trace amounts.[175]

All four metabolites were synthesized by *Martin Köllen* during his master´s thesis according to literature procedures. **Sulfo-Cipro** was synthesized by sulfonation of Ciprofloxacin with chlorosulfonic acid, resulting in 45% crude yield that decreased during purification *via* preparative HPLC to 7% isolated yield (**Scheme 5A**).[239] **Formyl-Cipro** was afforded in 50% yield by heat-mediated formylation of Ciprofloxacin with dimethylformamide (DMF) as *in situ* source of carbon monoxide and subsequent recrystallization in hot methanol (**Scheme 5B**).[240]

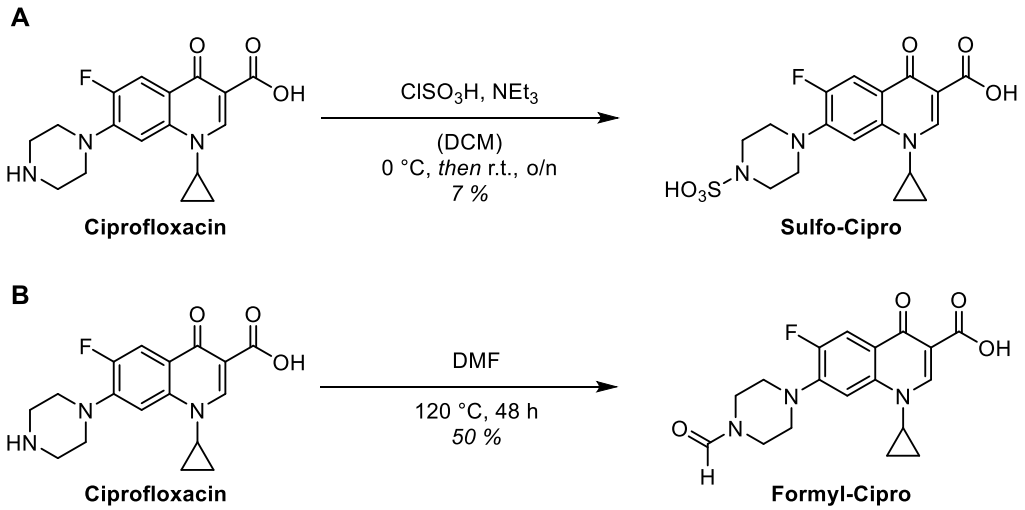

Scheme 5: Synthesis of Ciprofloxacin metabolites **Sulfo-Cipro** and **Formyl-Cipro**. (**A**) Sulfonation of Ciprofloxacin with chlorosulfonic acid afforded **Sulfo-Cipro**. (**B**) Formylation of Ciprofloxacin with dimethylformamide (DMF) yielded **Formyl-Cipro**. The syntheses were performed by *Martin Köllen* as part of his master´s thesis according to literature-known procedures.[239,240]

Nucleophilic aromatic substitution (S_NAr) of di-fluoroquinolone **10** with previously prepared Boc-protected di-amino ethylene **12** in DMSO at 130 °C in presence of

1,4-diazabicyclo[2.2.2]octane (DABCO) as base afforded **Desethylene-Cipro** after TFA-mediated Boc-deprotection and recrystallization in hot methanol in 65% over 2 steps (**Scheme 6A**).[241] Similar S_NAr conditions with piperazinone **13** gave **Oxo-Cipro** in 20% yield, after selective precipitation of the product at pH 5 (**Scheme 6B**).

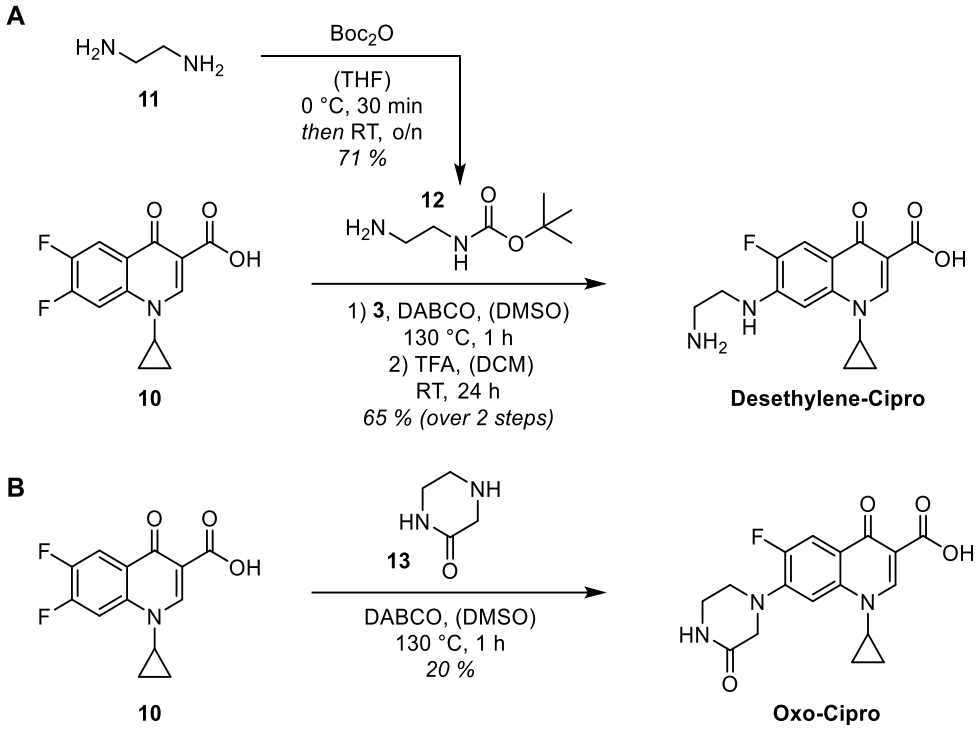

Scheme 6: Synthesis of Ciprofloxacin metabolites **Desethylene-Cipro** and **Oxo-Cipro**. (**A**) **Desethylene-Cipro** was synthesized by nucleophilic aromatic substitution of di-fluoroquinolone **10** with Boc-protected diaminoethane **12** and subsequent deprotection. (**B**) Similar nucleophilic aromatic substitution of di-fluoroquinolone **10** with piperazinone **13** gave **Oxo-Cipro**. The syntheses were performed by *Martin Köllen* as part of his master´s thesis according to literature-known procedures.[241,242]

3.5 Target validation studies of mitochondrial off-targets

Mitochondrial dysfunction in consequence of FQ treatment is well-reported in the literature.[128,129,143] Previously performed and discussed whole proteome analyses of FQ-treated cells (compare page 26) highlighted a respective proteotype with significant dose-dependent downregulation of the ETC, especially of the complexes I and IV. Furthermore, the *in situ* TPP experiment with Ciprofloxacin revealed a pronounced destabilization of the 28S mito-ribosomal subunit proteins (compare page 49). Therefore, especially potential mitochondrial (off-)targets identified *via* AfPPP or TPP were of interest for validation experiments.

3.5.1 Target validation studies for mitochondrial ClpP

Activity of ClpP and implications into mitochondrial dysfunction

The proteolytic subunit of the mitochondrial caseinolytic protease P (ClpP) was consistently enriched with **Cipro P1** in HEK-293 and PDL cells and to a smaller degree also by **Levo P1** (**Figure 24**). Human ClpP is important for the maturation, quality control and maintenance of many mitochondrial proteins, including proteins of the ETC and the mitoribosome.[243] The homo-tetradecameric ClpP subunit comprised of two heptameric rings stacked back-to-back together can form a complex with up to two ClpX hexameric rings constituting a symmetrical protease complex. The AAA+ chaperone ClpX is unfolding proteins and transferring them into the proteolytic barrel of ClpP.[243] Overactivation of ClpP, that is in some cases bypassing the need for the ClpX chaperone, is known to lead to enhanced proteolysis of mitoproteins impairing respiratory function.[243] Also the inhibition of ClpP resulting in the accumulation of misfolded or damaged mitochondrial proteins, including respiratory chain subunits, has been shown to impair oxidative phosphorylation and lead to mitochondrial dysfunction.[222] Especially the balanced turnover of the N-module of the complex I by the mitochondrial ClpXP protease, essential for the correct function of the ETC, has been shown to be vital.[244] Furthermore, Ishizawa *et al.* identified numerous ClpP substrates *via* Bio-ID that overlap with regulated proteins in the whole proteome analysis of FQ-treated cells, e.g. complex I and IV subunits.[243]

ClpP target validation experiments

To investigate if a potential dysregulation of ClpP by FQs could be responsible for the observed effects on the ETC complexes I and IV in the whole proteome analyses of FQ-treated cells, similar studies were performed with the imipridone ONC201, a commercially available overactivator of human ClpP.[245] Indeed, the resulting proteotype and the dysregulated pathways upon ONC201 treatment (1 µM, 24 h, 37 °C in HEK-293 cells) were strikingly similar to the prior results with FQ-treated cells (**Figure 29A-B**, compare **Figure 10** and **Figure 11**). However, with ONC201 the mitochondrial dysfunction was not focused on the complexes I and IV but was observed to be more severe and extended to further ETC complexes and the mitoribosome.

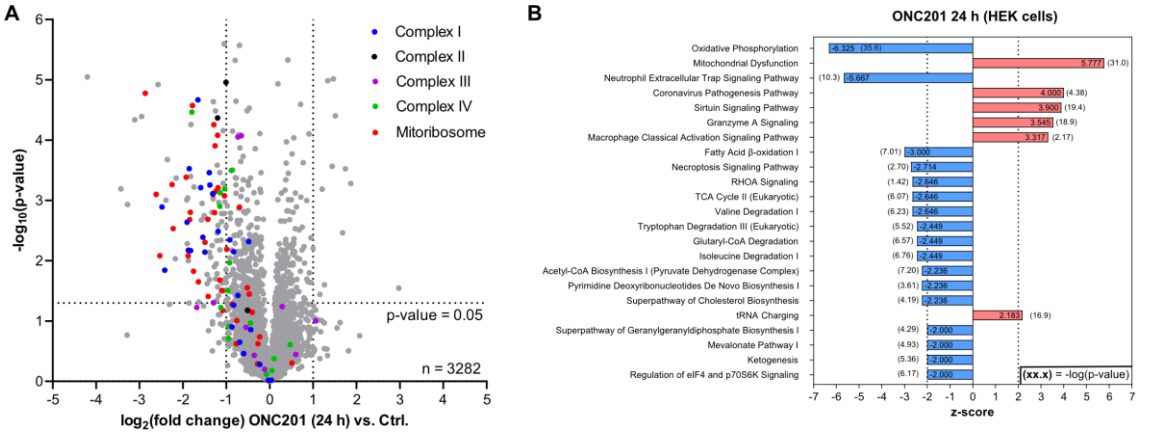

Figure 29: Whole proteome analysis in presence of ClpP overactivator Onc201. (**A**) Volcano plot of ONC201 (1 µM, 24 h, 37 °C) treated HEK-293 cells versus control cells. Vertical threshold lines represent a $\log_2$ regulation of ±1 and $-\log_{10}$(*P*-value) ≥ 1.3 (two-sided two-sample *t*-test, $n = 4$ replicates per group). Subunits of the ETC complexes I to IV and the mitoribosome are highlighted in different colors. (**B**) Respective pathway analysis of the resulting proteotype. The bar plot depicts the extent of the regulation by the z-score (threshold ±2) and the statistical significance in brackets in form of the negative logarithmic *P*-values. Both the volcano plot and the pathway analyses revealed a similar dysregulation as FQ-treated cells, however the effect was not limited to the complexes I and IV, but more pronounced. Pathway analyses were performed with the *Qiagen Ingenuity Pathway Analysis* tool by *Franziska Traube*.

Nonetheless those results were encouraging, as the stronger observed effect by ONC201 treatment could be based on the higher potency against ClpP compared to FQs. ONC201 is known to engage human ClpP with an EC_{50} of 12.5 µM with regards to its *in vitro* peptidase activity, whereas for FQs, likely less affine off-targets are the focus of this project.[245] Therefore, human ClpP was expressed and purified as described previously and the proteolytic activity tested in presence of Ciprofloxacin in established peptidase assays.[246] While published controls for ClpP activation (ONC201) and inhibition (TG42) resulted in strong effects, Ciprofloxacin and its four metabolites did not affect ClpP peptidase activity in a significant and concentration-dependent manner (**Figure 30A**).[245,247]

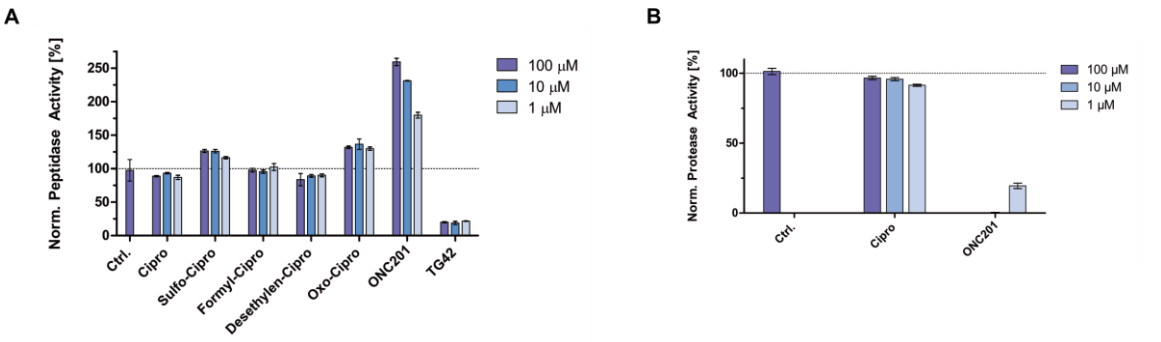

Figure 30: Activity assays of ClpP in presence of FQs. (**A**) *In vitro* ClpP peptidase activity assay in presence of Ciprofloxacin and its four metabolites. While incubation with overactivation control (ONC201) and inhibition control (TG42) evoked strong effects, the FQs did not result in significant and concentration-dependent activity changes. (**B**) *In vitro* ClpXP protease activity assay showing no significant and concentration-dependent effect of Ciprofloxacin. The respective Onc201 control resulted in strong inhibition due to the impairment of active ClpXP complex formation.

To investigate if FQs could instead affect the combined ClpXP protease complex, respective ClpXP protease assays were performed. For ClpXP protease activity assays, human ClpP and *E. coli* ClpX (kindly provided by *Thomas Gronauer*) was used and the experiments conducted as described before with minor modifications.[246,248] As recombinant human ClpX is instable and *E. coli* ClpX recognizes peptides C-terminally tagged with a short amino acid sequence (so-called ssrA-tag) and forms a functional complex with *H. sapiens* ClpP, it is suitable as a human ClpX substitute for *in vitro* protease activity assays.[248] Also in the protease assays no significant effect of Ciprofloxacin was observed, whereas ONC201 very potently inhibited the protease activity by preventing the formation of the ClpXP complex (**Figure 30B**).

Consequently, *in vitro* activity assays of both active individual ClpP and combined ClpXP did not substantiate ClpP being a human off-target of FQs, despite in theory being a coherent and logical possibility. To conclusively de-validate the involvement of ClpP in the FQ-derived proteome dysregulation, a whole proteome analysis of HEK293T *ΔclpP* knockout cells (kindly provided by *Prof. Aleksandra Trifunovic*, *CECAD Cologne*) versus wild-type cells was performed.[223] Analyzing the proteome regulation in the ClpP knockout (KO) cells in presence of Ciprofloxacin (75 µM, 3 days, 37 °C) compared to untreated KO cells, the typically observed strong downregulation of ETC complexes I and IV was still detected (**Figure 31A**). Consequently, the observed dysregulation of complexes I and IV resulting from FQ treatment is independent of ClpP. The proteotypes of FQ-treated wild-type and ClpP KO cells were widely comparable, as depicted in the scatter plot of treated versus untreated $\log_2$(fold-changes) in wild-type and ClpP KO cells (**Figure 31B**). While the data did not conclusively exclude a potential direct interaction of FQs with mitochondrial ClpP, the *in vitro* assays and the whole proteome analyses indicated that ClpP is not responsible for FQ-derived proteome dysregulation and toxicity.

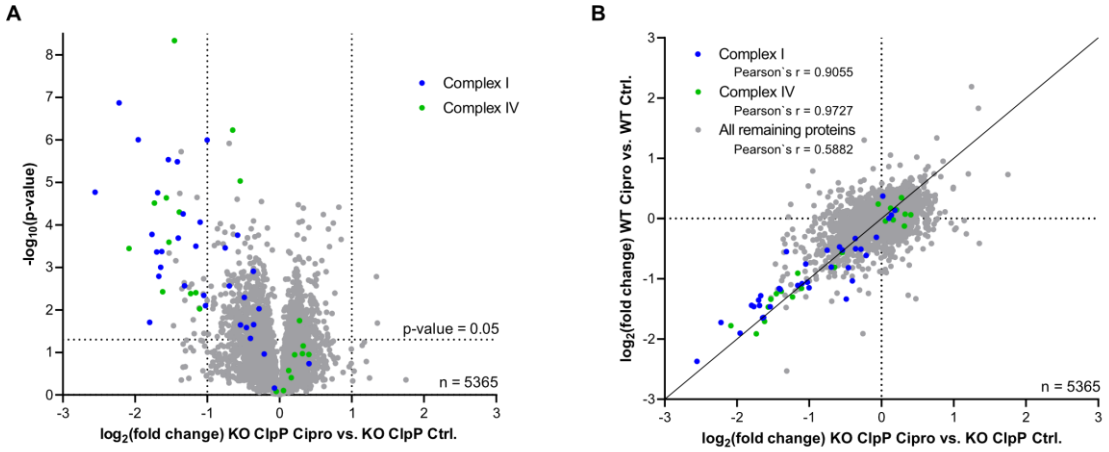

Figure 31: Whole proteome analysis of ClpP knockout cells. (**A**) Volcano plot of Ciprofloxacin-treated (75 µM, 3 days, 37 °C) HEK293T ClpP KO cells versus untreated KO cells. Vertical threshold lines represent a $\log_2$ regulation of ±1 and $-\log_{10}$ (*P*-value) ≥ 1.3 (two-sided two-sample *t*-test, *n* = 4 replicates per group). (**B**) Scatter plot comparing the differences in $\log_2$(fold-changes treated vs. untreated) in wild-type and ClpP KO cells. In both plots, subunits of the ETC complexes I (blue) and IV (green) are highlighted. Despite the ClpP knockout (KO), the typical down-regulation of complexes I and IV in presence of FQs was observed, excluding ClpP as a functional human off-target of FQs regarding the proteome dysregulation. In the scatter plot the Pearson's r correlations are indicated, in each case the *P*-value of the correlation was < 0.0001 as determined in *GraphPad Prism* (version 9).

3.5.2 Target validation studies for mitochondrial IDH2

Function of IDH2 and involvement in metabolic rewiring

An additional important mitochondrial enzyme consistently enriched with both **P1** probes in human cells is the isocitrate dehydrogenase 2 (IDH2). Three catalytic isozymes of the IDH are present in human, IDH1 located in the cytosol and peroxisomes, IDH2 and IDH3 located in the mitochondrion. While IDH1 and IDH2 are $NADP^+$-dependent, IDH3 is NAD^+-dependent.[249] IDH enzymes oxidatively decarboxylate isocitrate (IC) to α-ketoglutarate (αKG, **Figure 32** (**1**)). Active IDH2 is a homodimer comprised of two $NADP^+$, isocitrate and metal binding sites each. The enzymatic activity of the oxidative function of IDH2 is regulated by the mitochondrial deacetylase SIRT3.[250] Acetylation of lysine side-chains masks the positive charge and thereby influences the protein conformation. It has been shown that deletion of SIRT3 led to an impairment of IDH2 dimerization and accordingly an acetylation-mimicking IDH2 K413Q mutant inhibited dimerization.[250,251] As SIRT3 is NAD^+-dependent, the regulation is likely redox-sensing, i.e. dependent on the mitochondrial NADH/NAD^+ ratio.[250]

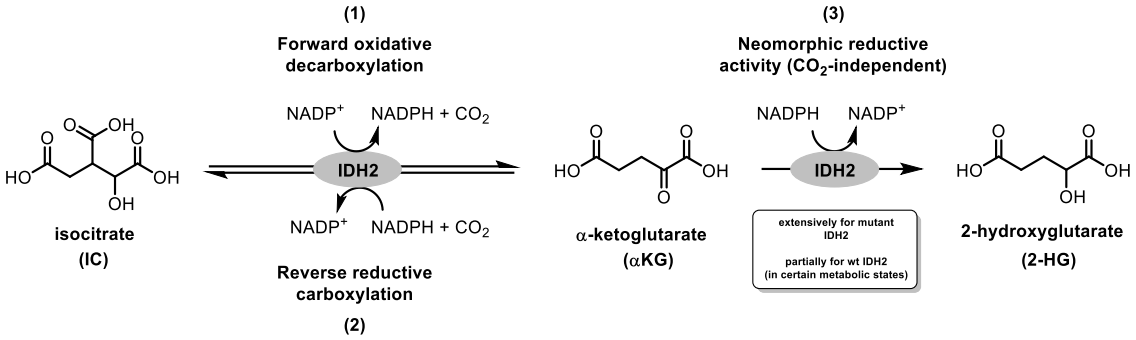

Figure 32: Enzymatic reactions of the isocitrate dehydrogenase 2 (IDH2). Three reactions are known for this enzyme: (**1**) The classical forward-directed and $NADP^+$-dependent oxidative carboxylation converts isocitrate (IC) to α-ketoglutarate (αKG). (**2**) The reverse reductive CO_2- and NADPH-dependent carboxylation converts αKG to IC. (**3**) NADPH-dependent, but CO_2-independent reduction converts αKG to 2-hydroxyglutarate (2-HG). This reaction is pronounced in IDH2 point mutants but has also been observed for the wild-type enzyme, however in significantly smaller extent.[250]

Importantly, in certain metabolic states, the reverse reaction of the CO_2- and NADPH-dependent reductive carboxylation of αKG to IC can also occur or is even the major direction (**Figure 32** (**2**)).[250,252] This reverse reaction has been shown to be especially important in brown adipocytes.[253] Interestingly, a pronounced reversed enzymatic direction was also detected in cells proliferating under hypoxia conditions or when the hypoxia-inducible factor 1 (HIF1) is constitutively activated.[254,255] Importantly, especially in the context of FQ-treated cells, the same phenomenon has been observed in a study of *Mullen et al.* in cells with mitochondrial dysfunction.[256] Cancer cells bearing mutations in the electron transport chain (ETC), or the presence of complex I (e.g. rotenone) or complex III inhibitors (e.g. antimycin) exhibited a change from a normal metabolism involving the forward oxidative carboxylation to a metabolism using reverse reductive carboxylation within 1 h of treatment.[256]

The cause of this metabolic rewiring has been traced back to the citric acid cycle and glutaminolysis *via* monitoring of isotopically labeled carbon-precursors, so-called ^{13}C-metabolic flux profiling.[256] The mechanisms are depicted in **Figure 33A**. In normal physiological settings and especially in cultured cells in high glucose medium and standard growing conditions (21% O_2, 5% CO_2) citrate is produced mainly from glucose-derived acetyl-CoA and oxidative glutaminolysis utilizing the critic acid cycle (**Figure 33A** – green pathway). However, in hypoxic conditions or in mitochondrial dysfunction, e.g. impairment of the ETC, glutamine is becoming the main carbon source *via* reductive glutaminolysis utilizing the reverse reductive carboxylation of IDH2 to produce isocitrate, that is isomerized to citrate, which is in turn the precursor for acetyl-CoA for lipogenesis and further metabolites (**Figure 33A** – red pathway).[253–256]

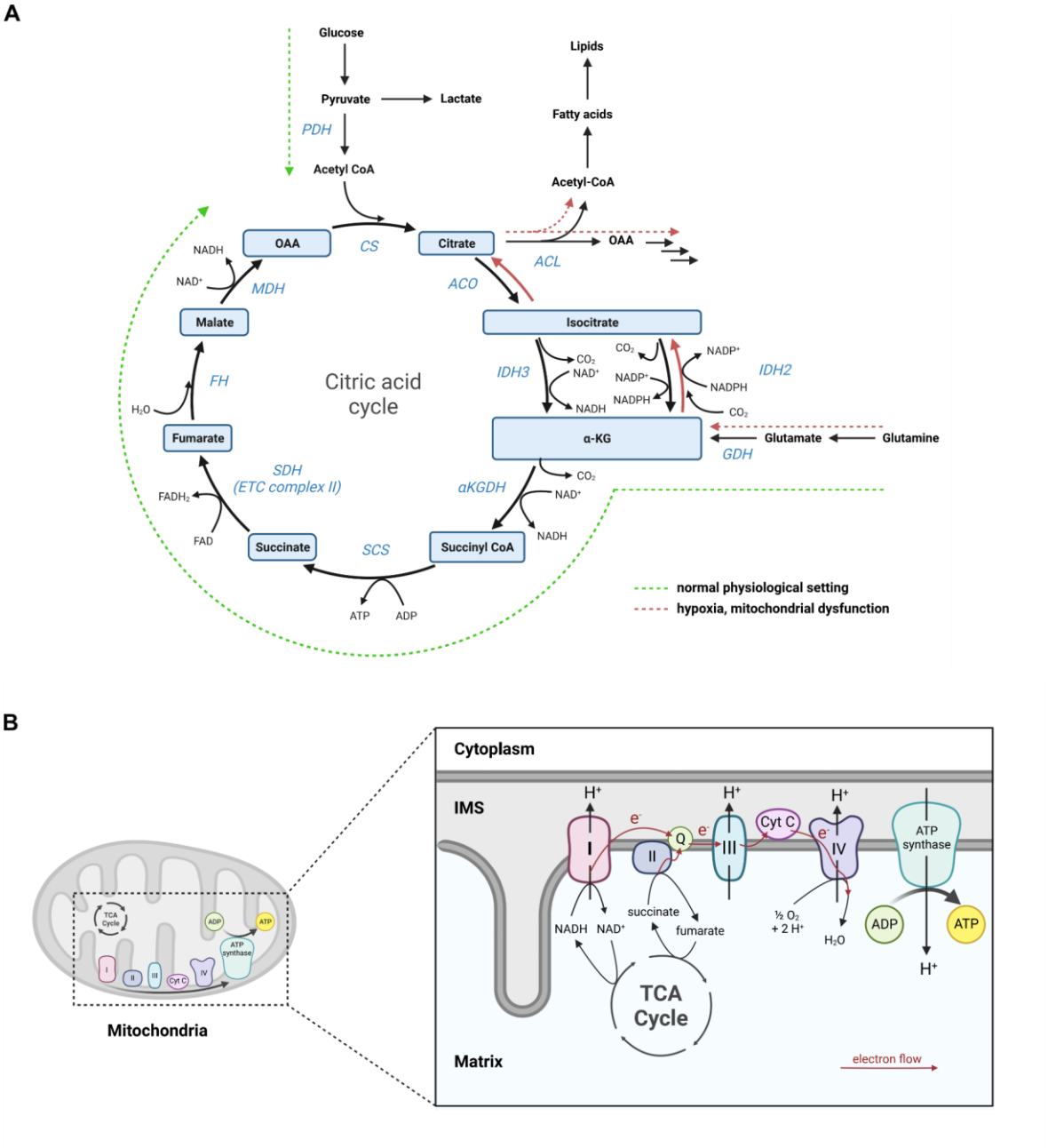

Figure 33: IDH2 in the context of key mitochondrial metabolic pathways. (**A**) Both IDH3 and IDH2 are localized in the mitochondrion. While IDH3 is catalyzing the monodirectional oxidative decarboxylation of isocitrate to α-ketoglutarate (αKG) within the citric acid cycle and is NAD^+-dependent, IDH2 catalyzes bidirectionally between isocitrate and αKG in an $NADP^+$/NADPH-dependent manner. Therefore, IDH2 is a key enzyme for metabolic rewiring. In normal physiological conditions glucose-derived acetyl-CoA is the main source of citrate in addition with citrate derived from oxidative glutaminolysis (green pathways). However, in conditions such as hypoxia or mitochondrial dysfunction, glutamine processed *via* the reductive glutaminolysis pathway is the main source of carbon to form citrate *via* IDH2-mediated reductive carboxylation and subsequent isomerization by aconitase (red pathway). The switch between those pathways is likely redox-dependent on the NAD^+/NADH ratio. (**B**) The electron transport chain located at the inner mitochondrial membrane utilizing the electron donor NADH produced in the citric acid cycle (TCA cycle) to create a proton gradient across the membrane and transferring the electrons to oxygen (in aerobic respiration). The proton gradient is used by the ATP synthase to produce ATP from ADP and inorganic phosphate. The complete process is called oxidative phosphorylation. In mitochondrial dysfunction, e.g. complex I impairment, the NAD^+/NADH ratio is increasing. This is leading to metabolic rewiring as discussed in panel **A**, partially because the TCA cycle is in 3 steps NAD^+-dependent. Figures created with *biorender.com*. PDH = pyruvate dehydrogenase, CS = citrate synthase, ACL = ATP citrate lyase, ACO = aconitase, IDH = isocitrate dehydrogenase, GDH = glutamate dehydrogenase, αKGDH = α-ketoglutarate dehydrogenase, SCS = succinyl-CoA synthetase, SDH = succinic dehydrogenase, FH = fumarase, MDH = malate dehydrogenase, OAA = oxaloacetate.

The switch from oxidative to reductive glutamine metabolism and accordingly the switch from forward oxidative decarboxylation by IDH2 to the reverse reductive carboxylation reaction are both in hypoxia and in mitochondrial dysfunction likely due to the decreasing mitochondrial and cellular NAD^+/NADH ratio. Typically, a NAD^+/ NADH ratio of 10:1 is present in mitochondria. The inhibition of the complex I, the major converter of NADH to NAD^+ in normal conditions, leads to a decreasing NAD^+/ NADH ratio (**Figure 33B**).[250,257] Consequently the citric acid cycle requiring NAD^+ in 3 steps is impaired and additionally, increases of NADH could lead to higher NADPH levels by action of NAD(P)-transhydrogenases and thereby favoring the NADPH-dependent reductive carboxylation by IDH2 (and potentially cytosolic IDH1).[250,253,254,256] Initial studies by *Smolková et al*. with cells expressing the acetylation-mimicking IDH2 K413Q protein indicated that the acetylation, which in turn is also indirectly regulated by the NAD^+/NADH ratio, because of the NAD^+-dependency of SIRT3, could also have a regulatory effect by increasing the reverse reductive reaction of IDH2.[250] Moreover, the hypoxia-inducible factor HIF1 has been shown to promote pyruvate to lactate conversion indirectly inhibiting the pyruvate dehydrogenase that converts pyruvate to acetyl CoA. This effectively limits the supply of the carbon precursors entering the citric acid cycle in hypoxic conditions.[254,255]

IDH2 in cancer and epigenetic dysregulation

Apart from its role in metabolic rewiring, IDH1 and IHD2 have been especially well studied in the field of cancer research due to their tumor-suppressing roles.[225] IHD2 has been found to be downregulated in various cancer types, such as in glioma, melanoma and bladder cancer.[258–260] In osteosarcoma cells IDH2 downregulation pronounced proliferation, malignant progression and metastasis.[225] Additionally, IDH2 and also its cytosolic homolog IDH1 are frequently mutated in cancer cells, such as in glioma and AML.[249,261] Point mutations (R172 or R140 in IDH2 and R132 in IDH1) result in neomorphic activities of the dehydrogenases in which αKG is reduced to the important oncogene 2-hydroxyglutarate (2-HG, **Figure 32** (**3**)).[249] This reaction represents a reverse NADPH-dependent, but CO_2-independent direction. As a result, this reaction competes with αKG-dependent enzymes effectively depleting αKG levels. Additionally, 2-HG has been shown to competitively inhibit αKG-dependent enzymes as a weak antagonist of αKG.[253,262] Impairment of αKG-dependent dioxygenases, such as histone demethylases and methyl-cytosine dioxygenases (TET enzymes) results in epigenetic dysregulation.[261,262] Also wild-type IDH2 has been shown to produce 2-HG, e.g. in breast cancer cells, however in much smaller extent than the point mutants.[250] Importantly, an increased reverse carboxylation of αKG to isocitrate by

IDH2 (**Figure 32** (**2**)) also resulted in higher 2-HG levels in the cells, due to being basically a truncated version of the reverse reductive reaction without carboxylation.[254]

IDH2 and matrix metalloproteases (MMPs)

In addition to epigenetic dysregulations upon IDH2 mutation or metabolic rewiring, a third literature-reported down-stream effect is especially interesting in the context of IDH2 being a potential (off-)target of FQs in human. Again, studied in respect of cancers, IDH2 downregulation has been shown to increase matrix metalloprotease (MMP) activity, often connected to increased nuclear factor 'kappa-light-chain-enhancer' of activated B-cells (NF-κB) transcription factor signaling. In Saos-2 and MG63 cells, both human osteosarcoma cell lines, IDH2 downregulation resulted in elevated NF-κB transcriptional activity and increased phosphorylation of the inhibitor of NF-κB (IκB), marking it for degradation.[225] Similarly, the IDH2 downregulation increased the relative MMP9 activity in those cell lines.[225] In gastric cancer IDH2 levels were also found to be significantly lower, inversely correlating with high levels of MMP-7 in an NF-κB-dependent fashion.[224] Addition of an NF-κB signaling inhibitor (MG132) to IDH2-knockdown gastric cancer cells did not alter IDH2 levels, but abolished the activation of MMP-7.[224] Other studies in glioma cancer also detected increased secretion levels of MMP-2 and MMP-9 due to low αKG levels (as a results of the IDH2 R172 mutations) pronouncing the stabilization of HIF-1α.[249]

MMPs are important in the degradation of extracellular matrix (ECM) proteins, tissue remodeling and maintenance. In cancer upregulated MMPs are involved in elevated metastasis and cancer invasion but they are also important for ligament, tendon and muscle maintenance.[225] As collagen IV is the main component of the ECM, it is especially relevant in cancer research. In the light of tendons and ligaments especially collagen I and III are important.[167] Tendons are comprised of approximately 90% collagen I and 10% type III.[167] Also the aorta is comprised of 80-90% collagen of the types I and III, connecting MMPs to cardiovascular diseases and aortic aneurysms.[263]

Importantly, also FQs have been reported to increase MMP activity.[143,166–168,264] In corneal wound-healing models in rats, FQs have been shown to increase the expression of the gelatinases MMP-2 and MMP-9. Most significantly was Ciprofloxacin with fold-changes of 4.02 for MMP-9 and 3.17 for MMP-2 expression.[265] Conversely, *Tsai et al.* found MMP-2 activity elevated in Ciprofloxacin-treated rat tendon cells resulting in collagen I degradation, however detected no changes for MMP-9.[167] Other studies have shown Ciprofloxacin to potentiate interleukin (IL)-stimulated expression of MMP-3 in tendon derived cells.[168,264]

Despite varying results for individual MMPs depending on the model system used, the overall picture of upregulated activity of collagenolytic MMPs upon FQ treatment is valid and is a strong correlation with IDH2-derived pathologies.

Connection of IDH2 to NF-κB and HIF1 signaling

In general, there are two signaling pathways being connected in the literature with IDH1/2 dysregulation or mutation. Firstly, increased nuclear factor 'kappa-light-chain-enhancer' of activated B-cells (NF-κB) signaling and secondly, increased hypoxia-inducible factor HIF1 signaling. Effects on both pathways are discussed to be αKG-dependent. Levels of αKG are dependent on metabolic states, but also on IDH actions. IDH1 knockdown by more than 75% reduced cellular αKG levels approx. to 50% and expression of the IDH1 R132 mutant led to a dose-dependent decrease of αKG.[266] Similar changes have been reported for IDH2.[250]

NF-κB is an important transcription factor implicated in the regulation of key processes, such as stress and inflammation responses and the inhibition of apoptosis.[225,267] As those responses provide favorable conditions for tumor cell progression, NF-κB is often constitutively activated in cancer cells.[224] For increased NF-κB signaling, this was shown to be due to the increased phosphorylation of the inhibitor IκBα in IDH2 downregulated cells.[225] Phosphorylation of IκBα leads to its ubiquitinoylation and subsequent degradation. The exact mechanism are still not completely understood, however, at high αKG levels the αKG-dependent activity of prolylhydroxylases (PHD) is enhanced, suppressing the kinase IKKβ to phosphorylate the inhibitor IκBα and thereby suppressing NF-κB signaling (**Figure 34**).[268] At low αKG levels (e.g. IDH2 downregulation, inhibition or mutation) the PHD activity is impaired, leading downstream to more IκBα degradation and increased NF-κB signaling. In accordance with this notion, artificial αKG supplementation in piglet and intestinal porcine epithelial cells rescued the strong lipopolysaccharide (LPS)-induced activation of NF-κB inflammation pathways.[269]

On the other hand, *Wang et al.* showed in brain tumor cells that under low glucose conditions, glutamate dehydrogenase 1 (GDH1)-produced αKG directly (independently of PHD) activated IKKβ leading to the phosphorylation and subsequent degradation of the NF-κB inhibitor IκBα and, as a consequence, NF-κB transcriptional activity led to the expression of target genes.[270] Additionally, 2-HG, produced by mutant IDH1/IDH2 and to some extent also by their wild-type forms, was reported to induce activation of NF-κB signaling independent of the action of the kinase IKKβ.[271] Consequently, various cellular stimuli can apparently trigger opposite regulations, the form of metabolism and cell type

seems to be important and further research is needed. Inconsequent of the exact mechanism, in either case αKG (or its antagonist 2-HG) influenced NF-κB signaling as a secondary messenger and IDH1 and IDH2 are central hubs for this outcome.

For hypoxia-inducible factor (HIF1) signaling, αKG -dependent prolylhydroxylases (PHD), hydroxylating and thereby promoting the degradation of the HIF1α subunit are also discussed (**Figure 34**). Studies showed, that decreased IDH1 and/or IDH2 activity and resulting lower αKG levels stabilized HIF1α levels, i.e. decreased HIF1α degradation.[249,266] As HIF1α is an important subunit of the HIF-1 transcription factor, thereby HIF1 target genes were shown to be expressed. Mutant IDH and addition of IDH inhibitors led to the same outcome.[249,266]

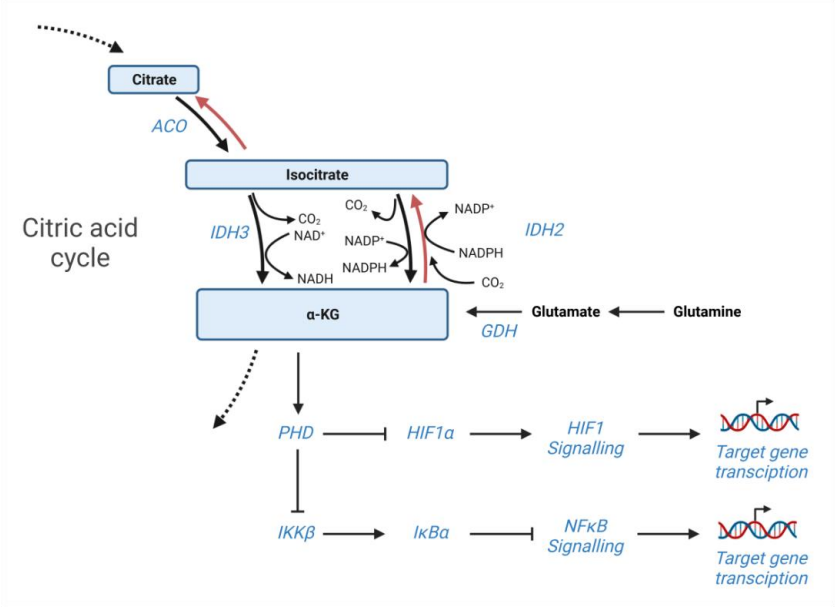

Figure 34: IDH2 and α-ketoglutarate (αKG) in context of HIF1 and NF-κB signaling pathways. αKG-dependent prolylhydroxylases (PHD) promote the degradation of HIF1α, thereby inhibiting the HIF1 signaling pathway. Additionally, PHD suppresses the kinase activity of IKKβ to phosphorylate IκBα, the inhibitor of NF-κB signaling. At low αKG levels, PHD activity is impaired resulting in less HIF1α degradation (i.e. stabilization) and HIF1 target gene transcription. Accordingly, IKKβ is able to phosphorylate IκBα, marking the inhibitor for degradation and inducing NF-κB target gene transcription. The exact mechanisms are still subject to research and alternatives are discussed in the main text.

In summary, the mitochondrial isocitrate dehydrogenase 2 (IDH2) is a very complex and sophisticatedly regulated enzyme capable of three different reactions, depending on regulation state, cellular metabolic/redox state and potential point mutations. Down-stream effects of IDH2 dysregulation include epigenetic changes, changes in redox homeostasis and in HIF1 and NF-κB signaling. Taking the extensive IDH2 research into consideration the enrichment of IDH2 by AfBPP with FQ-derived probes could potentially explain multiple adverse effects observed by FQ treatment. Inhibition of IDH2 by FQs could potentially be the causal link for the literature-known overactivation of MMPs upon FQ treatment that has

been connected with tendon and ligament problems, as well as the cause of epigenetic long-term effects and oxidative stress and inflammation responses.[128,129,137,142,167,168]

IDH2 *in vitro* activity assays in presence of FQs

Therefore, activity assays with commercially available wild-type IDH2 expressed in baculovirus as full-length protein with a C-terminal FLAG-tag in presence of FQs were performed. The forward oxidative decarboxylation of isocitrate to αKG was monitored with a coupled enzymatic reaction of NADPH-dependent diaphorase (**Figure 35A**). Resazurin is converted to resorufin by action of the diaphorase, resulting in an fluorescent read-out at 585 nm (λ_{Ex} = 550 nm).[272] Utilization of this coupled read-out has the advantage that the excitation and emission wavelength can be red-shifted compared to monitoring the fluorescence of NADPH (λ_{Ex} = 340 nm, λ_{Em} = 460 nm) itself in a range where tested compounds frequently show fluorescence as well. Ciprofloxacin for example features an emission maximum at approx. 440 nm. Of note, for active wild-type IDH2 homodimers the *in vitro* monitoring of the reverse direction is not feasible, as arising $NADP^+$ inhibits the reaction.[250,253]

Indeed, Ciprofloxacin inhibited the IDH2 activity partially in a concentration-dependent fashion at micromolar concentrations (**Figure 35C**). Although only showing approx. 25-30% inhibition at 100 µM, and approx. 20% at 10 µM, these concentrations are in a relevant range as discussed before and reasonable in the context of off-targets, featuring lower affinities as selective primary targets. Even this partial inhibition of a key metabolic enzyme could potentially lead to adverse down-stream effects, especially over a longer treatment time. As control, Enasidenib (AG-221), a first-in-class inhibitor for mutant IDH2 for the treatment of acute myeloid leukemia was tested. Although inhibiting the IDH2 mutants more potently, it also inhibits wild-type IDH2.[261] The originally published IC_{50} value of Enasidenib for wild-type IDH2 after 1 h of preincubation is approx. 40 ± 10 µM, in the in-house assay 50% inhibition was reached at approx. 100 µM, but the results were consistent and reproducible (**Figure 35D**).[261] Levofloxacin also inhibited the IDH2 forward reaction weakly, but significantly (**Figure 35E**). However, the inhibition was slightly less than for Ciprofloxacin with approx. 20% inhibition at 100 µM.

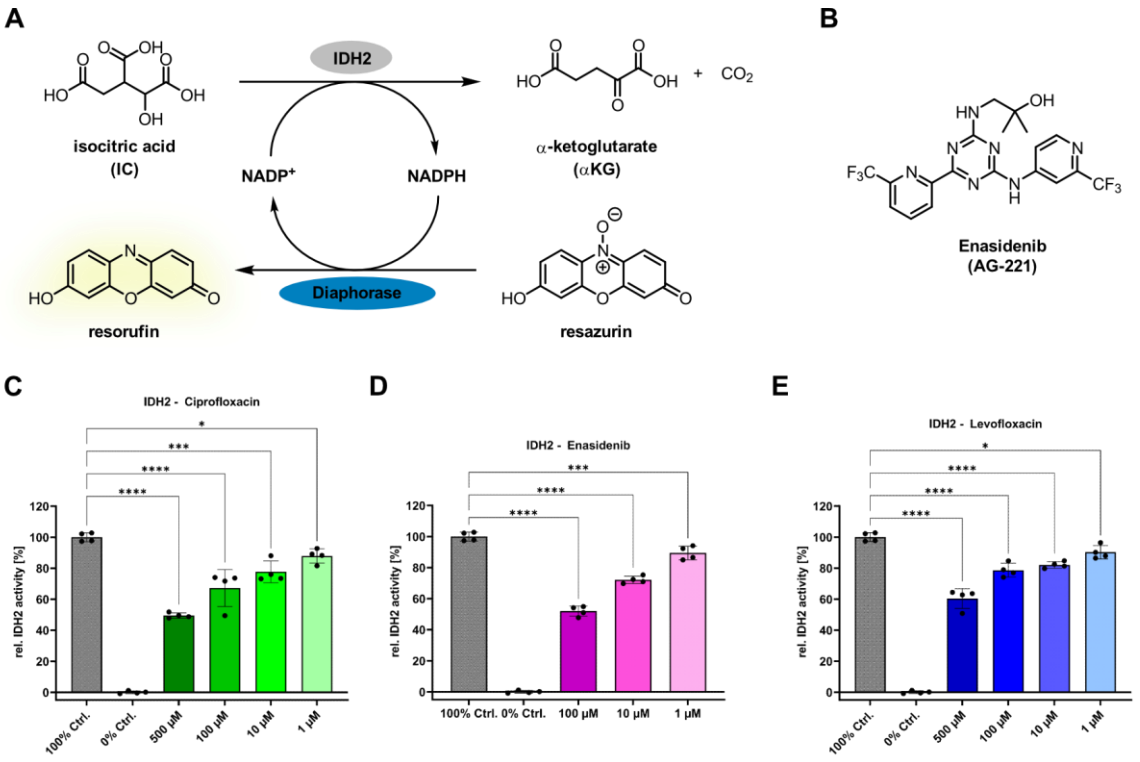

Figure 35: Activity assay of IDH2 in presence of FQs. (**A**) Diaphorase-coupled dehydrogenase activity assay. Isocitrate is oxidatively decarboxylated by $NADP^+$-dependent IDH2. Generated NADPH is used by the diaphorase to convert resazurin to fluorescent resorufin. (**B**) Chemical structure of IDH2 inhibitor Enasidenib (AG-221). (**C**) Activity assay in presence of Ciprofloxacin featuring partial, but concentration-dependent inhibition within a physiological relevant concentration range. (**D**) Activity assay using literature known IDH2 inhibitor. Enasidenib is more potent against mutant IDH2, however also weakly inhibits wild-type IDH2 at micromolar concentrations. (**E**) Levofloxacin also partially inhibited IDH2, however weaker than Ciprofloxacin. In the bar plots the statistical relevance based on one-way ANOVA with Dunnett´s multiple comparison test is depicted (ns meaning P-value > 0.05, * P-value ≤ 0.05, ** P-value ≤ 0.01, *** P-value ≤ 0.001, **** P-value ≤ 0.0001).

NF-κB target genes are regulated upon FQ treatment

With this validation of weak *in vitro* activity modulation in mind, upregulated proteins in the whole proteome analysis of HEK-293 cells after 3 h of incubation with Ciprofloxacin (7.5 µM and 75 µM) was re-evaluated in respect to HIF1 and NF-κB signaling (**Figure 9**). As discussed IDH2 inhibition can lead to elevation of those signaling pathways, and indeed various validated gene targets of those signaling pathways were upregulated within the thresholds (fold-change ≥ 1, –log(*P*-value) ≥ 1.3), including COL1A1, FN1, LTF, GNAI2, COL1A2, HMOX1, CD44, COL5A1, MDK and GPRIN1. For various others, such as ICOSLG, BRCA1, APOB, THBS4, COL18A1, GUCY1B3 and RSF1 involvement in NF-κB signaling was also found. Of, note the annotation was done manually by checking publications and provided online lists concerning the NF-κB transcription of the *Gilmore* laboratory.[273,274] Although the selection is very likely not comprehensive due to the manual approach and incomplete annotation in the resources, this represented a further strong

indication for the involvement of IDH2 and also suggested, that the observed *in vitro* activity modulation is translated into physiological changes.

Outlook of studies into mechanistic and downstream-effects of the IDH2 (off-)target

To facilitate further mechanistic studies of the IDH2 engagement by FQs, efforts to recombinantly express the human protein in *E. coli* were undertaken. As discussed, posttranslational modification (PTM) by lysine-acetylation in human deactivates the activity by impairment of the homodimer formation.[250] Therefore, the PTM-free expression in *E. coli* should pose no activity problem, although initial recombinant expressions of a IDH2-R140Q mutant were performed in baculovirus expression systems in *Spodoperta frugiperda* (Sf9) cells for crystallization.[275] In fact, both mutant and wild-type IDH1 and IDH2 have been expressed in *E. coli* before, for example by *Leonardi et al.*, but recombinant wild-type IDH2 yields were reported to be extremely poor as opposed to recombinant wild-type IDH1.[253] Therefore, a codon-optimized gene synthesis of wild-type IDH2(40-452) without the first 39 residues representing the mitochondrial targeting sequence (MTS) was ordered and the protein expressed in pET28a(+) with a C-terminal His_6-affinity tag in *E. coli* BL21 for 19 h at 18 °C after induction with ITPG. As the overexpression in general was weak (**Figure 36A**) and led to extensive aggregation and inclusion-body formation during preparative expression and/or purification, the strategy was revised in collaboration with *Prof. Michael Groll* and a His_6-SUMO-IDH2(40-452) construct cloned and expressed to facilitate recombinant protein solubility and stability.[276] Although being expressed (19 h, 18 °C) and eluted from the nickel-affinity column in trace amounts (as determined by intact-protein MS), a purification of reasonable amounts of the recombinant protein was not possible, however this time no excess amount of inclusion bodies was observed. Optimization efforts are ongoing, potentially the overexpression of the protein is metabolically problematic for *E. coli*, as it catalyzes a redundant reaction to the citric acid cycle.

Once optimized and purification has been successful, various biophysical methodologies, such as isothermal calorimetry (ITC), will be possible to determine binding affinities. Additionally, analytical size-exclusion chromatography could be used to analyze FQ-mediated effects on the dimerization state of active IDH2. Generating a co-crystal structure of Ciprofloxacin and IDH2 would be the ultimate goal for the mechanistic studies on protein level. Binding-site identification of the photo-crosslinker probe **Cipro P1** to the commercially available IDH2 for initial information on the location of FQ binding by UV-crosslinking and subsequent tryptic digest and LC-MS/MS analysis were unsuccessful so

far, as no matching modified peptide was observed. After successful expression and purification of recombinant IDH2, more detailed experiments, e.g. testing various digestion enzymes will be possible was well. Literature-described regulatory mechanism and inferred melting curves from the TPP experiment potentially suggest FQ binding impairing the dimerization state rather than changing the conformation of the monomer, as IDH2 thermo-stabilization was not affected in the TPP experiment (**Figure 36B**).

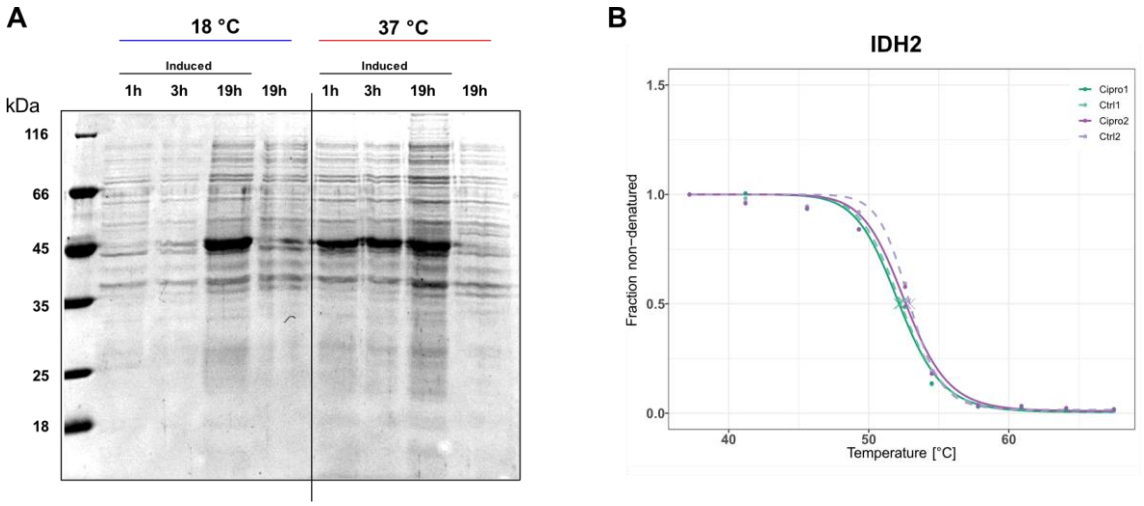

Figure 36: Outlook for mechanistic IDH2 inhibition studies. (**A**) Test expression of IDH2 as pET28a(+) construct in *E. coli* BL21 at 18 °C and 37 °C. Samples were taken after indicated times after induction and a non-induced sample was taken at the last time point as control. The samples were directly denatured in 2× SDS-loading buffer and analyzed *via* SDS-PAGE. In general, the over-expression band of recombinant IDH2 (47,811 kDa) was rather small indicating only weak overexpression. (**B**) Inferred melting curve of IDH2 in the *in situ* TPP experiment with Ciprofloxacin (1 h, 75 µM, 37 °C). The MS-quantification data enabled a good fit of the melting curve and showed excellent reproducibility across the two replicates. However, the melting temperature (ΔT_m) of IDH2 of approx. 52 °C was not altered by Ciprofloxacin incubation, suggesting that the conformation of the protein monomer itself is not changed, but potentially the dimerization could be affected.

In addition to mechanistic studies of the IDH2 inhibition by FQs, the resulting physiological down-stream effects were started to be investigated. As experiments are ongoing, only preliminary results are discussed and a brief outlook is given. In the reverse decarboxylative reaction IDH2 generates NADPH from $NADP^+$. As NADPH is an important co-factor, e.g. in fatty acid and cholesterol biosynthesis, the activity of IDH2 has implications on various pathways.[224,225] Moreover, NADPH is essential for the regeneration of the glutathione reactive-oxygen species (ROS) scavenging system. Consequently, IDH2-mediated NADPH production is important for the cells ability to defend against ROS, however the extend seems to be tissue and cell specific.[225,277]

To investigate physiological implications of the IDH2 activity modulation by FQs, the mitochondrial NADPH levels were determined in native mitochondria isolated from PDL cells. In accordance with a partial inhibition of the IDH2 forward reaction, the NADPH levels after 6 h of incubation with 7.5 µM Ciprofloxacin decreased by approx. 25% (**Figure**

37A). Interestingly, preliminary results showed that the mitochondrial NADPH levels significantly increased after 3 days of incubation with 75 µM Ciprofloxacin approx. 3-fold (**Figure 37B**). The preliminary studies suggest that low concentrations and short incubation times with Ciprofloxacin are leading to a reduction of NADPH levels by inhibition of the IDH2 forward reaction. Longer incubation times at higher concentrations are leading to ETC complex I impairment (compare whole proteome results) resulting in metabolic rewiring and high NADH levels that are reversibly interconnected with high NADPH levels by NAD(P)-transhydrogenases (compare **Figure 33** and IDH2 introduction). It is likely that the reverse reductive carboxylation reaction of IDH2, that is pronounced in those conditions, is also inhibited by Ciprofloxacin and therefore additionally contributes to the elevated NADPH levels. To confirm this theory further research is necessary and experiments are ongoing at this time.

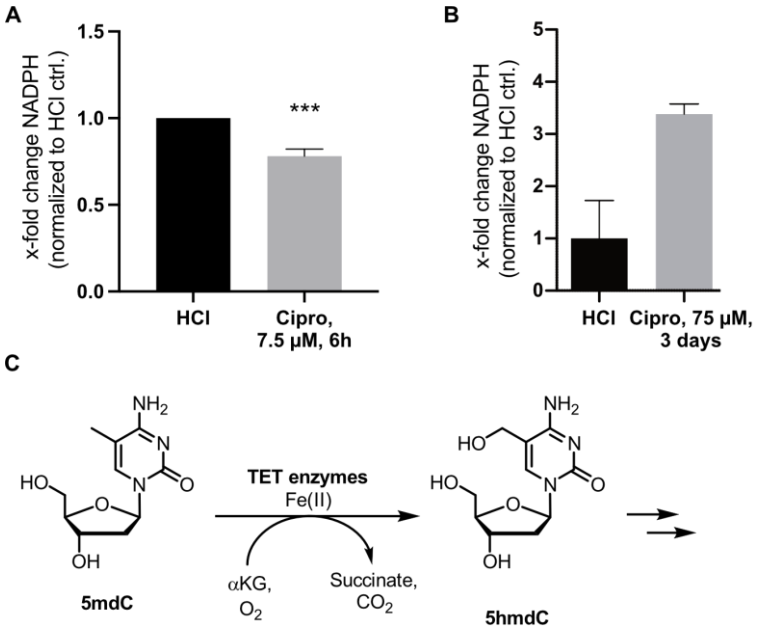

Figure 37: Outlook and preliminary studies into the physiological effects of IDH2 modulation by FQs. (**A**) Mitochondrial NADPH levels after incubation of PDL cells with Ciprofloxacin (7.5 µM, 6 h) are decreased by approx. 25% (P-value ≤ 0.001). (**B**) Preliminary results of mitochondrial NADPH levels being approx. 3-fold increased after incubation with Ciprofloxacin (75 µM) for 3 days. This phenomenon could potentially be due to the shown ETC complex I impairment at this incubation time and concentration resulting in metabolic rewiring as discussed in the main text. (**C**) Schematic of the oxidative action of TET enzymes removing the epigenetic 5-methyldeoxycytosine markers in an αKG-dependent fashion.[278]

As discussed, the activity of IDH2 also has effects on MMP activities that are relevant in FQ-derived side-effects on collagen, such as in tendonitis, tendon ruptures and aortic aneurysms. The activities of MMPs in FQ-treated PDL cells are currently evaluated. In addition to MMP activity assays, the expression of various MMPs and IDH2 in presence or absence of FQs in PDL cells is currently analyzed by qPCR by *Prof. Denitsa Docheva* at the *University of Würzburg*.

Additionally, experiments to determine a potential epigenetic effect of FQs due to IDH2 inhibition and potentially changing αKG levels are ongoing. Epigenetic markers are reversible and of dynamic nature. Various epigenetic mechanisms increase the genomic complexity, e.g. *via* chromatin modifications and direct modifications of the DNA.[279] DNA methyltransferase (DNMT) enzymes generate 5-methyldeoxycytidine (5mdC) methylation patterns *de novo* and maintain them leading to silencing of genes.[280] Human ten-eleven translocation (TET) enzymes were found to be responsible for the conversion of 5mdC to 5-hydroxymethyldeoxycytidine (5hmdC) and to further derivatives such as 5-formyldeoxycytidine (5fdC) and 5-carboxyldeoxycytidine (5cadC) (**Figure 37C**).[278] As 5hmdC is significantly more abundant than 5fdC and 5cadC, it is believed to be both an intermediate in the removal of the epigenetic methyl mark and a distinct epigenetic mark itself.[281,282] As dioxygenases involved in epigenetics, such as histone demethylases and the methyl-cytosine dioxygenases (TET enzymes) are αKG-dependent the modulation of IDH2 activity could result in epigenetic dysregulation.[261,262] Therefore, the 5mdC and 5hmdC levels of PDL cells incubated with normal and peak concentrations of Ciprofloxacin, Levofloxacin or vehicle control for 3 days are analyzed by LC-MS/MS in collaboration with *Franziska Traube*. Initial results are promising, and effects were detected, experimental replicates for statistical significance are however ongoing. The direct determination of cellular αKG levels with and without FQ treatment either by targeted metabolomics or utilization of specialized assay kits could also be possible.

3.5.3 Target validation studies for mitochondrial AIFM1

Functions of AIFM1 and involvement in the mitochondrial import machinery

Literature-research for the apoptosis-inducing factor 1 (AIFM1) enriched consistently with both **P1** probes in AfBPP resulted in focused validation studies for this protein of interest. AIFM1 is translated in the cytosol and translocated into the mitochondrion, where it is located in the mitochondrial intramembrane space (IMS) and anchored to the inner mitochondrial membrane.[283] The protein is named apoptosis inducing factor due to historical reasons, as it was identified as the first pro-apoptotic protein triggering caspase-independent cell death.[283] The controlled release of pro-apoptotic factors, such as a 57-kDa AIFM1 fragment, from the IMS into the cytosol and their subsequent transfer into the nucleus, where they bind to DNA, can induce DNA fragmentation, chromatin condensation and ultimately

cell death.[283] The exact mechanism of the release of those AIFM1 fragments triggering apoptosis is still subject of ongoing research.[283]

In addition to this pro-apoptotic function of AIFM1, more recent studies showed a second activity, namely its important involvement in the import of mitochondrial proteins, including ETC subunits crucial for oxidative phosphorylation.[226–228] It has been shown that AIFM1 is featuring NADH dehydrogenase activity and dimerizes in the presence of NADH.[284] This dimerization is driving the binding of MIA40 (also called CHCHD4) to the AIFM1 homo-dimer *via* the N-terminal part of MIA40 comprised of 40 amino acids and facilitates MIA40 translocation into the IMS (**Figure 38**).[284] If the N-terminal region of MIA40 is deleted this AIFM1-AIFM1-MIA40 trimeric complex cannot be formed and the amount of MIA40 in the IMS is significantly reduced. Similar effects have been observed for AIFM1 knock-down systems.[283] MIA40 is part of an evolutionary conserved and redox-regulated import system into the IMS. The so-called mitochondrial disulfide relay system facilitates the import and subsequent oxidative folding of important mitochondrial proteins that are encoded in the nucleus and not in mtDNA.[227]

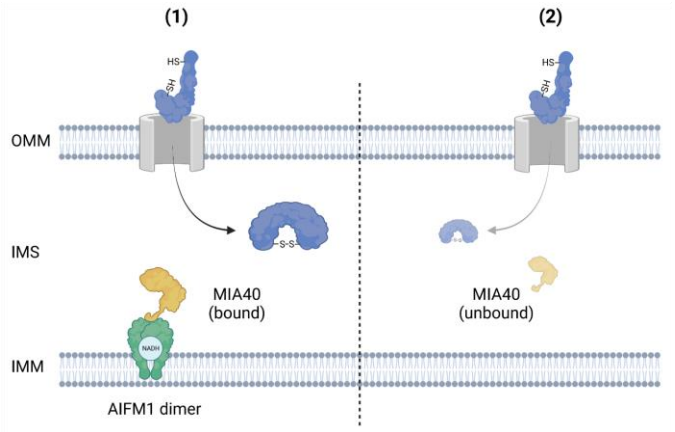

Figure 38: Mechanism of AIFM1 and MIA40 interaction. (**1**) In presence of NADH inner mitochondrial membrane (IMM)-bound AIFM1 dimerizes and the N-terminal region of MIA40 binds to the homodimer facilitating the import of MIA40 into the intermembrane space (IMS) and resulting in a stable AIFM1-AIFM1-MIA40 trimer. MIA40 is part of the mitochondrial disulfide relay system mediating the import and oxidative folding of certain nuclear-encoded mitochondrial proteins. (**2**) In case of AIFM1 knock-down or impairment of the AIFM1-AIFM1-MIA40 interaction, the amount of MIA40 in the IMS and consequently also of its substrate proteins is significantly reduced. The figure is based on *Salscheider et al.*[226]

Consequently, AIFM1 is indirectly, however crucially, involved in the import of ETC subunits into the IMS and has implications on ETC biogenesis and maintenance. Mutant Harlequin (Hq) mice, carrying a heterozygous deletion mutant of AIFM1 feature an approx. 80% reduction of AIFM1 expression and therefore exhibit severe mitochondrial dysfunction.[285] A recent whole proteome analysis of AIFM1 knockout (KO) HEK-293 cells by *Salscheider et al.* revealed a strikingly similar downregulation of ETC complex I and IV

as observed for FQ-treated cells and further studies reported pronounced AIFM1-connected effects especially on complex I and IV.[226] Rescue experiments artificially circumventing a AIFM1-mediated MIA40 import, e.g. by MIA40 overexpression or introducing a mitochondrial targeting sequence (MTS) to MIA40, confirmed that in those cases AIFM1 impairment has no effect on complex I biogenesis.[284]

AIFM1 target validation experiments and outlook

Because of the identification of AIFM1 as a putative FQ (off-)target by AfBPP and the mentioned strong similarities in proteotypes between FQ-treated and AIFM1 KO cells, AIFM1 and its involvement in the MIA40 disulfide relay system was considered to be in a potential causal relationship for FQ-derived mitochondrial dysfunction and validation studies were initiated. Interestingly, no molecular entity is known to this date, that targets and modulates the AIFM1-MIA40 import machinery.[228]

Initially, a potential effect of FQs on either the AIFM1-dimer formation or the AIFM1-AIFM1-MIA40 trimer formation was investigated in a collaboration with *Prof. Jan Riemer* at the *University of Cologne*. As discussed, impairment of the formation of either of those two complexes would lead to impaired ETC assembly and maintenance and mitochondrial dysfunction. Subsequent target validation experiments were performed by *Alex Rothemann*. AIFM1 and MIA40 were recombinantly expressed and purified and their potential aggregation in presence and absence of Ciprofloxacin investigated by SDS-PAGE of the supernatant and pellet fractions after ultracentrifugation (**Figure 39**). No pronounced aggregation of AIFM1 in presence of Ciprofloxacin (500 µM) compared to conditions without the FQ was observed. Similar results were obtained when AIFM1 dimerization was induced by addition of NADH and for MIA40 in presence of NADH. Also, the AIFM1-AIFM1-MIA40 trimer did not aggregate to a stronger extent in presence of Ciprofloxacin.

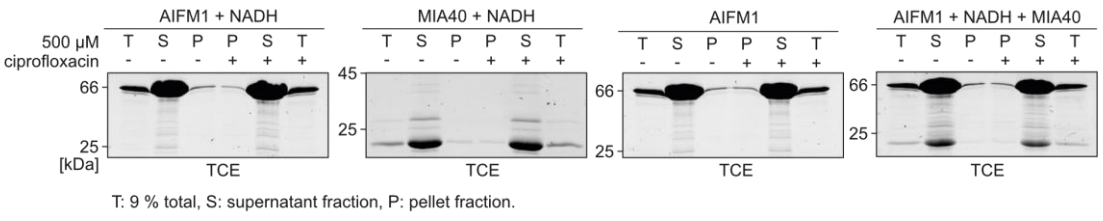

Figure 39: Ultracentrifugation experiment of AIFM1 and MIA40 in presence of Ciprofloxacin. Recombinantly expressed and purified proteins were incubated with or without Ciprofloxacin (500 µM) and their potential aggregation studied by visualization of the soluble and aggregated fraction *via* SDS-PAGE after their separation with ultracentrifugation. AIFM1 was tested as monomer and as dimer by addition of NADH. Additionally, MIA40 was tested in the presence of NADH, as well as the formed AIFM1-AIFM1-MIA40 trimer in presence of NADH. In no condition a significant difference in aggregation was observed by the addition of Ciprofloxacin. The experiments were performed by *Alex Rothemann* at the *University of Cologne*.

Next, the impact of Ciprofloxacin on both the AIFM1-dimer and the AIFM1-AIFM1-MIA40 trimer was studied *via* analytical size-exclusion chromatography (SEC, **Figure 40**). The addition of NADH to AIFM1 monomers induced the formation of the AIFM1 homodimer and shifted the retention volume on the size-exclusion column from approx. 82 mL to 69 mL (**Figure 40A**). Initial results showed a slightly lower normalized amount of the formed dimer and *vice versa* a slightly higher amount of remaining AIFM1 monomer, when additionally incubating with Ciprofloxacin (200 µM, both orders of additions of NADH and Ciprofloxacin were tested). As this effect was not very strong, future experimental replicates are needed to decide if this impact is reproducible and significant or is due to cross-run deviations.

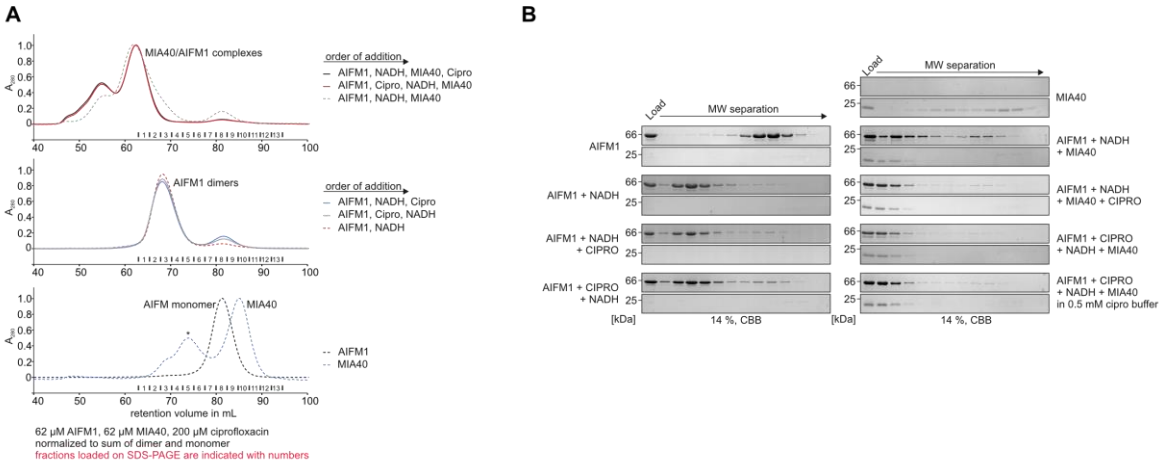

Figure 40: Analytical SEC of AIFM1 and MIA40 in presence of Ciprofloxacin. (**A**) Normalized UV detector traces over the course of analytical size exclusion chromatography (SEC) runs. AIFM1 monomer eluted after approx. 82 mL, MIA40 at approx. 96 mL. Upon addition of NADH to AIFM1, the corresponding homodimer was formed shifting the elution volume to approx. 69 mL. Incubation of AIFM1, MIA40 and NADH led to the trimer formation with an elution volume of approx. 62 mL. (**B**) Collected fractions as indicated in the UV traces were additionally analyzed *via* SDS-PAGE and visualized with Coomassie stain. As discussed in the main text, only minor differences upon addition of Ciprofloxacin were detected, their reproducibility and significance remain to be seen in future experimental replicates. The experiments were performed by *Alex Rothemann* at the *University of Cologne*.

Similarly, no strong effects on the AIFM1-AIFM1-MIA40 trimer formation were detected by SEC in the presence of Ciprofloxacin. Conversely to the homodimer experiment, here the normalized amount of remaining AIFM1 monomer appeared to be slightly higher in the non-FQ-treated sample. Moreover, the addition of Ciprofloxacin resulted in a sharper elution peak of the trimer complex, potentially indicating a difference in the hydrodynamic radius of the complex in presence of FQs.

The collected fractions of the analytical size-exclusion chromatography were additionally visualized *via* SDS-PAGE showing similar minor differences in remaining AIFM1 monomer or when inducing dimer/ trimer formation in the presence of Ciprofloxacin (**Figure 40B**).

At the time of this dissertation, it remains to be validated, if an interaction between AIFM1 and FQs is involved in the human side-effect profile of FQs. Therefore, the analytical size-exclusion experiments will be repeated to conclusively answer the question if an AIFM1-mediated mode of action is responsible for the observed FQ-derived complex I and IV dysregulation. The repeated experiments will also include a condition, where only Ciprofloxacin, but not NADH is present to infer if Ciprofloxacin on its own is potentially sufficient to trigger AIFM1 dimerization or AIFM1-MIA40 trimerization. Additionally, future experiments will explore the binding of Ciprofloxacin to the proteins *via* ITC and functional IMS import assays will be performed to analyze if the activity of the MIA40 import machinery is impaired by FQs.

3.6 Target validation studies of non-mitochondrial off-targets

3.6.1 Target validation studies for PTGR2 and SCARB1

Apart from mitochondrial proteins, several non-mitochondrial proteins were detected *via* AfBPP and TPP. Although mitochondrial dysfunction appeared to be the prominent adverse effect as indicated by published studies and the whole proteome data, these proteins potentially contributing to the human side-effects of FQs were also studied.

The activity of prostaglandin reductase 2 (PTGR2) involved in adipogenesis and lipid metabolism was tested in presence of Ciprofloxacin, but no significant modulation of enzyme activity was detected (tested up to 250 µM Ciprofloxacin, data not shown, experiment performed by *Wiebke Hutwelker*, *Leibniz University Hannover*).[217,218,286]

The scavenger receptor class B member 1 (SCARB1, also called SR-B1) involved in reverse cholesterol transport was identified as a protein of interest by the **P1** probes in AfBPP.[219,287] Interestingly, it was also found to be up-regulated in Ciprofloxacin-treated PDL cells (75 µM, 3 days, **Figure 12**) and the super-pathway of cholesterol biosynthesis was determined to be weakly impaired after Ciprofloxacin incubation both at normal and peak concentrations (**Figure 14A-B**). FQs have also been reported to effect plasma total cholesterol, HDL-cholesterol and LDL-cholesterol in rats and cholesterol imbalance has been connected to tendon pain and damage.[288,289]

As functional assays for the membrane located SCARB1 monitoring the reverse transport of cholesterol are very complex and require specialized equipment and cell lines, initially the potential binding of Ciprofloxacin to recombinant SCARB1 was investigated in

collaboration with the *HIPS*. For this the biophysical microscale thermophoresis (MST) technology was used. In MST, the directed movement of fluorescent molecules in response to a temperature gradient induced by an infra-red laser (thermophoretic movement) is monitored in thin capillaries. Secondly, the temperature related intensity change (TRIC) of fluorescently labeled protein is subject to changes if a ligand is bound. The resulting fluorescent read-out can therefore be used to determine binding affinities.[290]

While for **Cipro P1,** that enriched SCARB1 in AfBPP, a weak interaction (K_d = 394 µM) with recombinant SCARB1 was detected, no binding for Ciprofloxacin itself could be detected and concentrations higher than 500 µM Ciprofloxacin led to protein aggregation in the assay (**Figure 41**).

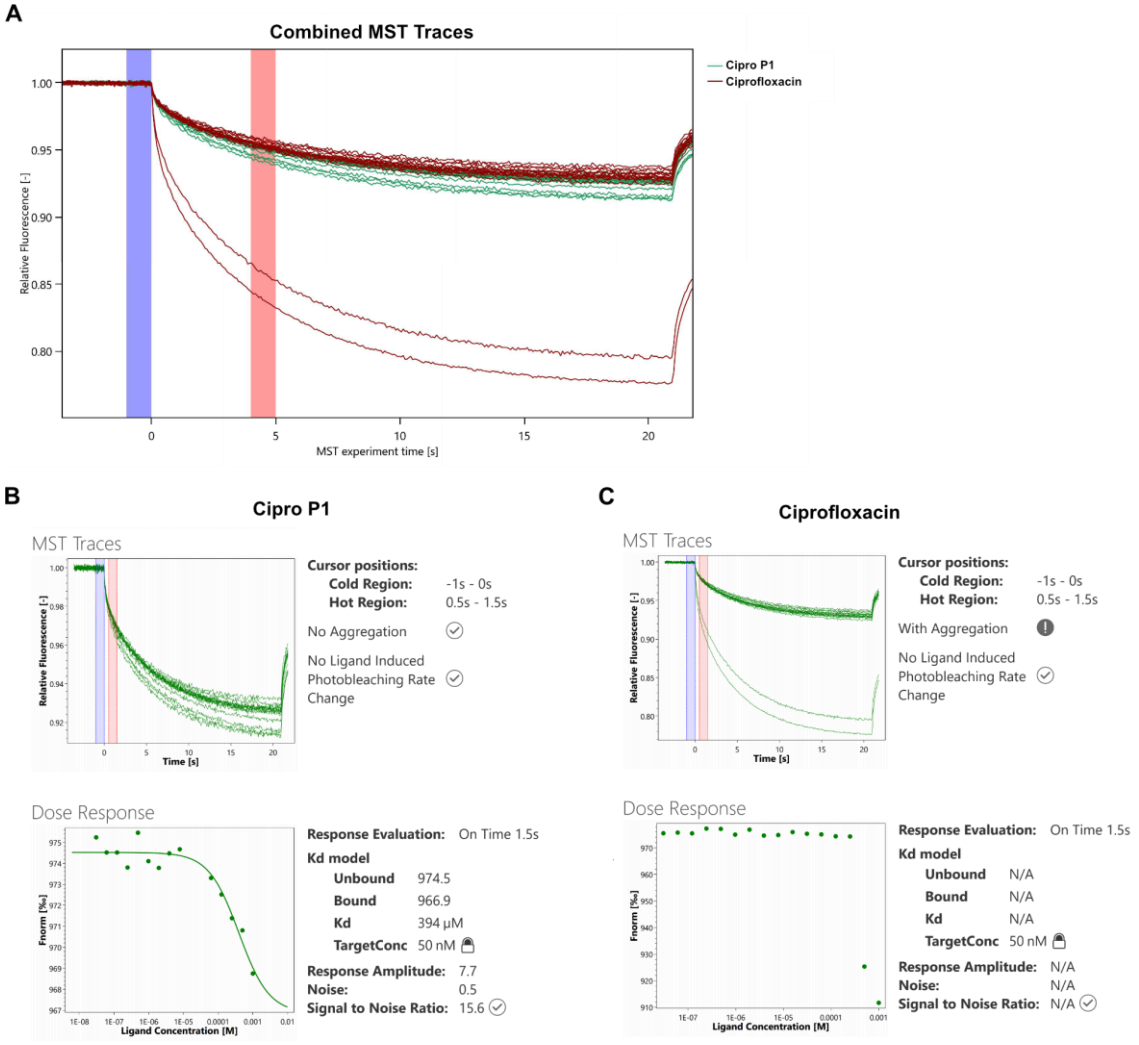

Figure 41: Microscale thermophoresis (MST) binding assay of SCARB1. (**A**) Combined MST traces of **Cipro P1** and Ciprofloxacin capillaries for direct comparison. The two strong shifts of Ciprofloxacin correspond to 500 µM and 1 mM concentrations and are due to protein aggregation as detected by the instrument. (**B**) MST traces and the corresponding dose response of **Cipro P1**. The cold and hot regions are depicted in blue and red, respectively. A binding affinity (K_d) of 394 µM was inferred. (**C**) MST traces and the corresponding dose response of Ciprofloxacin. As no proper dose-response was detected and the two highest concentrations resulted in protein aggregation, no binding affinity for SCARB1 could be inferred. The experiment was performed and analyzed with MO Affinity Analysis software (*NanoTemper*) by *Timo Risch*, at the *HIPS*.

Additionally, surface-plasmon resonance (SPR) studies with Ciprofloxacin and SCARB1 at the *HIPS* did not detect an interaction (data not shown). Consequently, SCARB1 was likely a false-positive hit in AfBPP due to the modification of the **P1** probes and the protein was excluded from further validation studies. Substitution of the piperazine moiety by the photo-crosslinker as in **Cipro P1** results in a significant increase of lipophilicity (cLogP (Ciprofloxacin) = 1.32; cLogP (**Cipro P1**) = 4.09, values calculated with *ChemDraw* version 20.0, **Figure 45**) potentially responsible for the elevated interaction with SCARB1.

3.6.2 Target validation studies for NUDT1

Enzymatic functions of NUDT1

The hydrolase NUDT1 (also called MTH1, meaning MuT homologue 1 and named after the first NUDIX family protein identified in *E. coli*) is converting oxidized purine nucleoside triphosphates, such as 2-oxo-dATP and 8-oxo-dGTP to their corresponding monophosphates and inorganic pyrophosphate p_i (**Figure 42A**).[291] The substrate nucleotides are products of oxidative damage by reactive oxygen species (ROS) and their hydrolysis prevents their incorporation into the DNA during replication, as the oxidized purine nucleoside triphosphates can be utilized by DNA polymerases, whereas their monophosphates cannot. As oxidized nucleotides feature changed base-pairing patterns, their incorporation can lead to point mutations. For 8-oxo-dGTP mainly A:T to C:G mutations and for 2-oxo-dATP G:C to A:T and G:C to T:A mutations have been reported.[292–294] Additionally, also oxidized building blocks of RNA, 2-oxo-ATP and 8-oxo-GTP, have been shown to be substrates of NUDT1, potentially ensuring transcriptional fidelity and subsequent correct translation.[295,296] Interestingly, NUDT1 has also been shown to hydrolyze methylated N^6-methyl-dATP/ATP and thus is in this context potentially acting directly upstream of ADAL1, that was the most significantly stabilized protein in the TPP experiment and is discussed in the next chapter.[297–299]

The NUDIX hydrolase superfamily is conserved across many species and the human genome encodes 24 NUDIX hydrolases responsible for a wide range of substrates. Although enzymatic redundancy for NUDT1 has been discussed, e.g. by NUDT15 and NUDT18, NUDT1 is considered to be the major player in sanitizing the dNTP pool of 2-oxo-dATP and 8-oxo-dGTP.[300] NUDT1 $^{-/-}$ knockout mice are viable and NUDT1 is not essential in normal cells, however this changes under high oxidative stress conditions, such as in certain cancers.[300–302] Indeed, NUDT1 is frequently upregulated in human cancers enabling high

proliferation rates despite high ROS levels and is therefore discussed as an anticancer target.[291,300] Various NUDT1 inhibitors have been developed eradicating cancer cells.[301,303,304] This strategy of treating cancer is referred to as "cancer phenotypic lethality".[301]

Also FQs have been reported to increase ROS in line with mitochondrial dysfunction, suggesting that a modulation of NUDT1 activity by FQs could potentially contribute to their side-effects.[128] Interestingly, various quinolines, quinolinediones and smaller compounds featuring cyclopropyl and piperazine moieties similar to Ciprofloxacin have been reported to inhibit NUDT1 and co-crystal structures have been solved showing the inhibitors occupying the substrate-binding pocket.[305]

NUDT1 target validation experiments

Therefore, NUDT1 was recombinantly expressed and purified in *E. coli* and its activity in presence of Ciprofloxacin and Levofloxacin was assayed using a published malachite green-based assay to quantify inorganic phosphate p_i formation.[300,306] Analogously to the literature, instead of 8-oxo-dGTP, dGTP was used as substrate in the assay.[306,307] Although being more specific for oxidized purine nucleotides, the enzyme can also convert dGTP to dGMP with weaker affinity. Ciprofloxacin inhibited NUDT1 activity concentration-dependently in the micromolar range (**Figure 42B**). Although only partially (approx. 40% inhibition at 100 µM), the inhibition was significant and in a physiologically relevant concentration range as expected for an off-target. For Levofloxacin, the enzymatic *in vitro* inhibition was only statistically significant at the highest concentration tested (500 µM), which is likely not physiologically relevant (**Figure 42C**). Control experiments with the specific NUDT1 inhibitor (*S*)-crizotinib validated the assay and showed potent inhibition at nanomolar concentrations (**Figure 42D**).[304] Additionally, gel-based analytical labeling of the recombinant protein with the **P2** probes, enriching NUDT1 in the human proteome, was performed (**Figure 42D**). The recombinant protein was spiked-in into a human cell lysate to minimize unspecific labeling. Importantly, the heat denatured NUDT1 control abolished labeling by **Cipro P2** and **Levo P2** and labeling was partially outcompeted by the respective parent compound Ciprofloxacin and Levofloxacin. Overall, the experiments validated NUDT1 as an off-target of FQs.

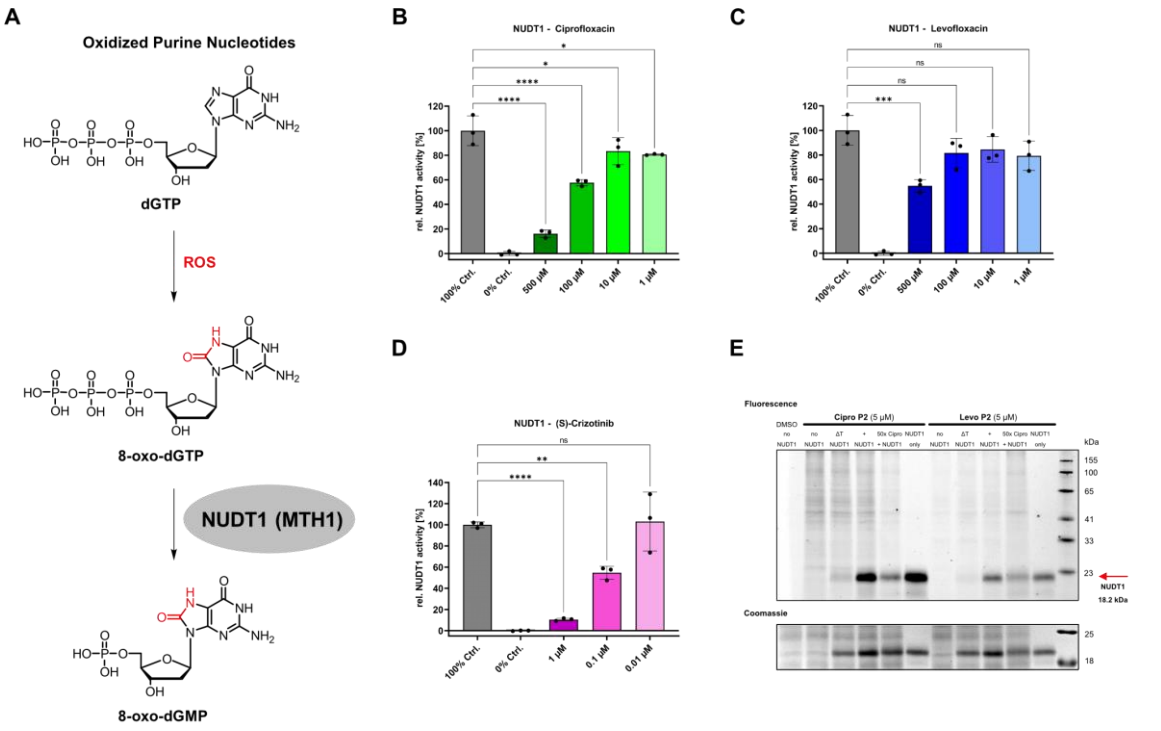

Figure 42: Influence of FQs on NUDT1 hydrolase. (**A**) Schematic of NUDT1 activity exemplary shown for 8-oxo-dGTP. Oxidatively damaged nucleoside triphosphates, e.g. by reactive-oxygen species (ROS), are hydrolyzed to their respective monophosphates by NUDT1 effectively sanitizing the free nucleotide pool. (**B**) NUDT1 activity assay in presence of Ciprofloxacin showing partial and concentration-dependent inhibition in the micromolar range. (**C**) Significant *in vitro* inhibition of NUDT1 with Levofloxacin was only observed at the highest tested concentration of 500 µM. (**D**) NUDT1 activity assay in presence of the known inhibitor (*S*)-crizotinib featuring nanomolar inhibition.[304] (**E**) Gel-based recombinant labeling of NUDT1 in a human cell lysate background. **Cipro P2** and **Levo P2** extensively labeled NUDT1, while in the heat denatured control (ΔT) and in presence of an excess of parent compound the labeling was partially abolished or outcompeted.

Outlook for the NUDT1 off-target of FQs

Efforts to identify the binding-site of the **P2** probes to NUDT1 by tryptic digest after photo-crosslinking to the recombinant enzyme and LC-MS/MS analyses were unsuccessful so far and are ongoing. However, the similarities to specific NUDT1 inhibitors, especially to the quinoline and quinolinediones suggest a similar binding mode in the substrate pocket of NUDT1. Further research is needed to understand the consequences and cellular effects the FQ-mediated inhibition of NUDT1 could entail. Especially in the light of reported elevated ROS levels upon FQ treatment, the inhibition of NUDT1 could have negative effects on the removal of oxidatively damaged purine dNTPs. Increased 8-oxo-dG levels have been reported after FQ treatment of cells.[128] This raises the question if the elevated levels are solely due to increased ROS-mediated damage or also due to an NUDT1 inhibition-mediated accumulation and re-incorporation of 8-oxo-dG into the DNA. The discrimination between those two potential causes is, however, very difficult to decipher.

3.6.3 Target validation studies for ADAL1

Enzymatic function of ADAL1

The adenosine deaminase-like protein ADAL1 was found to be the most strongly stabilized protein in the TPP experiment with Ciprofloxacin (**Figure 27**). The enzyme was discovered in phylogenetic studies as a paralogue closely related to adenosine deaminases (ADAs) in various species.[308] *Schinkmanová et al*. isolated ADAL1 from rat liver in 2006 and identified the activity of selective deamination of N^6-methyl-ATP and N^6-methyl-dATP to inosine monophosphate (IMP) and dIMP. Additionally, ADAL1 has been shown to activate the N^6-substituted purine nucleotide analogue pro-drugs me-PMEDAP, abacavir monophosphate (ABC-MP) and their derivatives featuring antiviral and cytostatic activities (**Figure 43**). As opposed to ADAs, ADAL1 does not catalyze the deamination of AMP or dAMP.[299] The respective human enzyme was studied shortly after.[309]

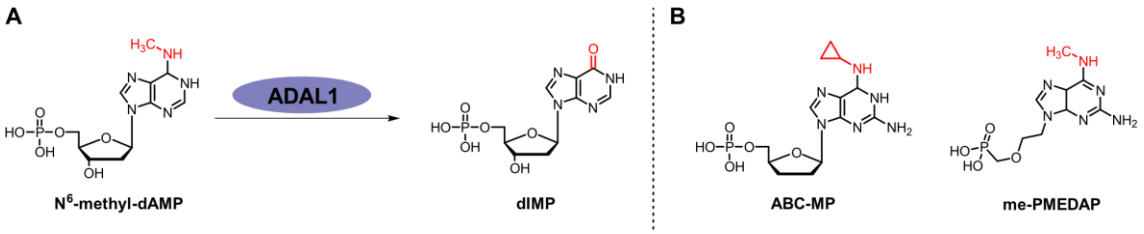

Figure 43: Enzymatic activity of ADAL1. (**A**) The deamination activity of ADAL1 exemplary shown for N^6-methyl-dAMP affording dIMP. (**B**) Structures of antiviral and cytostatic pro-drugs abacavir monophosphate (ABC-MP) and me-PMEDAP that have been shown to be activated *via* deamination by ADAL1.

Investigations by *Murakami et al*. revealed, that ADAL1 can also catalyze the removal of O^6-alkylation on purine nucleoside monophosphate analogues.[298] SAR studies showed that the monophosphate-moiety is essential for substrate-recognition and the enzyme is sensitive to further modification on the sugar scaffold. Consequently, ADAL1 cannot remove methyl-groups from a methylated DNA strand. Further it was shown that ADAL1 is using a catalytic Zn^{2+} ion.[298] The physiological role of ADAL1 resides in the purine nucleotide catabolism and due to its methylated-purine substrates is involved in epigenetics. For example, N^6-methyl adenine is a major posttranslational modification of eukaryotic mRNA and degradation of the modified mRNA generates N^6-methyl-AMP, that is acted upon by ADAL1. The methylation pattern of mRNA is identified by several proteins (e.g. YTHDF1, 2 and 3 and the eukaryotic inhibition factor eIF3) in the cytosol and is therefore influencing mRNA translation and stability.[310] As mentioned, NUDT1 has been reported to hydrolyze methylated N^6-methyl-dATP/ATP to the corresponding AMP-derivatives that are the substrates of ADAL1. Therefore target validation experiments were required to differentiate

between a possible direct engagement of ADAL1 by FQs and a potential detected down-stream effect by the *in situ* TPP experiment.[297–299]

ADAL1 target validation experiments

To enable *in vitro* activity assays, ADAL1 was recombinantly expressed and purified in *E. coli* BL21 (DE3). Prokaryotic expression of the human enzyme has been shown before to retain activity of the human enzyme.[298] To infer the enzymatic activity, the conversion of N^6-methyl-AMP to IMP was monitored using the resulting time-dependent shift in absorbance (**Figure 44B-C**). In presence of Ciprofloxacin, the *in vitro* activity was unaffected until a concentration of > 300 µM (**Figure 44D**). Levofloxacin had no significant influence on ADAL1 activity up to the tested concentration of 500 µM (**Figure 44E**). Although the observed *in vitro* inhibition by Ciprofloxacin is therefore very likely not physiologically relevant, the experiments did explain the observed thermo-stabilization of ADAL in the TPP experiment with Ciprofloxacin.

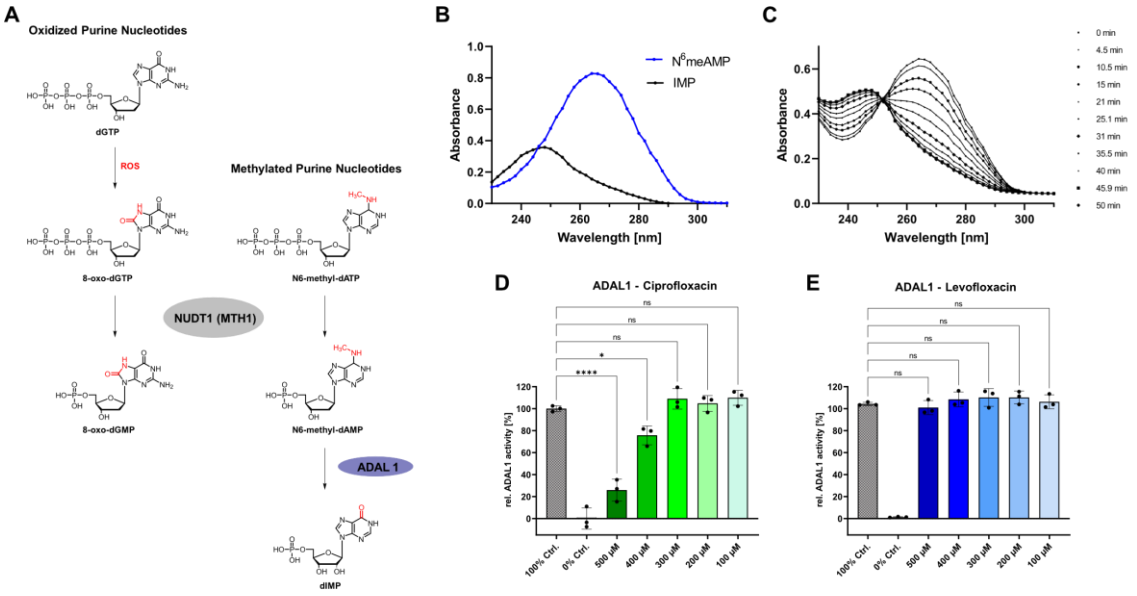

Figure 44: Influence of FQs on ADAL1 *in vitro* activity. (**A**) ADAL1 operates down-stream of NUDT1 on N^6-methyl-dAMP or N^6-methyl-AMP deaminating the molecules to dIMP and IMP, respectively. (**B**) Absorbance spectra of N^6-methyl-AMP and IMP. The strong shift in absorbance maxima was used to monitor the enzymatic conversion. (**C**) Time-dependent monitoring of ADAL1 *in vitro* activity deaminating N^6-methyl-AMP to IMP. (**D**) ADAL1 activity assay in presence of Ciprofloxacin. Significant inhibition is only achieved at concentrations > 300 µM that are very likely not physiologically relevant. (**E**) ADAL1 activity assay in presence of Levofloxacin, showing no activity alteration.

3.6.4 Potential lysosomal accumulation of FQs

Theoretical considerations on lysosomal accumulation

As discussed, AfBPP with probes **Cipro P2** and **Levo P2** resulted in a pronounced enrichment of lysosomal proteins (compare **Figure 26**). Both probes in question were

modified at the carboxylic acid of the respective FQs masking the moiety as an amide functionality. Therefore, an influence of the derivatization on the organelle-specific localization was likely. Lysosomes are compartmentalized by a membrane protecting the cell from the approx. 50 different acid hydrolases in the lysosome degrading and recycling cellular molecules that are imported *via* autophagy.[311] The proton-pumping V-ATPase, as well as chloride channels and other ion transporters ensure an acidic lysosomal pH of 4.5-5 corresponding to the pH optima of the acid hydrolases.[311]

Accordingly, suitable molecules are protonated once being directed to the lysosome and due to the resulting positive charge retained in the lysosome, as they cannot diffuse through the membrane anymore. Considering predicted pK_a values of Ciprofloxacin and the corresponding probes **Cipro P1** and **Cipro P2**, the effect of the derivatization on potential protonation becomes apparent (**Figure 45**). The parent compound Ciprofloxacin and **Cipro P1** are amphoteric, featuring both acidic (free carboxylic acid) and basic (various secondary or tertiary amines) functional groups. As a result, the approximate predicted isoelectric points (pI), defined as the pH at which the molecules are zwitterionic and the net charge is neutral, is approx. 5.5 for Ciprofloxacin and approx. 5.0 for **Cipro P1**. In the context of the lysosomal pH of 4.5-5.0 both molecules are on the verge of carrying a positive net charge in the lysosome. However, **Cipro P2** (predicted pK_a = 8.4) lacks the acidic group due to masking of the acid *via* the amide and is thus definitively protonated and positively charged in the lysosome and can consequently be efficiently trapped in the organelle. Similar effects can be predicted for Levofloxacin and its respective probes.

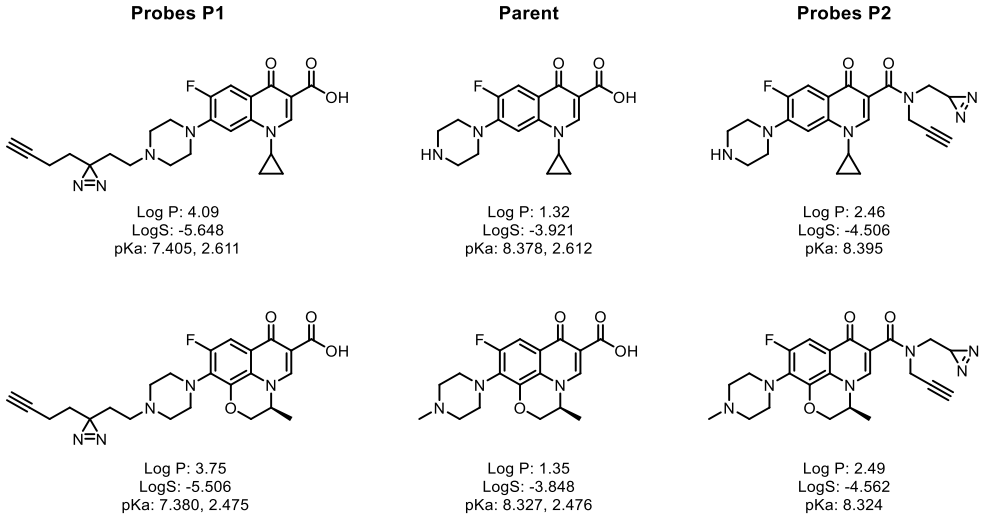

Figure 45: Predicted physicochemical properties of parent FQs and probes. Predicted logP, logS and pK_a values of Ciprofloxacin and Levofloxacin and their corresponding **P1** and **P2** probes. While the parent compounds and **P1** probes are amphoteric and at the edge of the threshold of being net-positive in the lysosome (pH 4.5-5.0), probes **P2** are definitively net-positive at the lysosomal pH and can therefore be efficiently trapped in the organelle. Values were predicted with *ChemDraw* version 20.0.

Although the modification explains the pronounced enrichment of lysosomal proteins by the **P2** probes, also **P1** probes, especially **Levo P1**, enriched lysosomal proteins to some extent, such as EPDR1, LAMP1, CTSD and PRCP (**Figure 25**). This suggested merely an intensifying effect by **P2** probes rather than an absolute switch of cellular localization. In fact, Ciprofloxacin has been shown to be a lysosomotropic agent accumulating in the lysosome and inducing lysosomal membrane permeabilization (LMP).[207]

Using the self-fluorescence of Ciprofloxacin, *Boya et al*. incubated HeLa cells with 10 µg/mL (≈ 30 µM, a concentration well in range of physiologic conditions after FQ treatment) Ciprofloxacin and observed both lysosomal and nucleolar accumulation. Monitoring the diffusion of cathepsin B and D from lysosomes upon treatment of HeLa cells with Ciprofloxacin for 8 h and subsequent immuno-cytochemistry, they concluded that Ciprofloxacin treatment is causing LMP resulting in the diffusion of cathepsins into the cytosol and causing caspase-independent cell death. Unfortunately, it is not unambiguously described at which FQ concentration the cathepsin-diffusion immunocytochemistry experiment was performed, however their FACS-mediated cell live/death assay was performed at an extensively high concentration of 350 µg/mL (= 1.05 mM) of Ciprofloxacin. Therefore, the transferability of those results to physiological conditions after FQ treatment of patients is questionable. Also, the claim of the induction of caspase-independent cell death and FQ-mediated lysosomal membrane permeabilization (LMP) preceding mitochondrial membrane permeabilization (MMP) is not completely conclusive. Bafilomycin A1 (Baf A_1), an inhibitor of the vacuolar H^+ ATPase (V-ATPase) preventing the fusion between lysosomes and autophagosomes, was used to differentiate between LMP- and MMP-mediated cell death.[207] In fact, inhibition of hallmarks of apoptosis, such as the loss of mitochondrial membrane potential and loss of cellular viability, by the inhibitor of autophagy Baf A_1 only started to appear at Ciprofloxacin concentrations equal or even higher than 350 µg/mL (= 1.05 mM). At 300 µg/mL (= 905 µM) Ciprofloxacin, a concentration that is still more than one order of magnitude higher than published peak concentrations in certain tissues (approx. 75 µM)[173–176] no significant effect of Baf A_1 and in general on the mitochondrial membrane potential and viability (even without Baf A_1) was observed.[207]

Lysosomal cell imaging using Cipro-derived probes

Despite the discussed concerns, a potential involvement of FQ accumulation into the human side-effect profile was investigated. As the instrumentation to monitor the self-fluorescence of Ciprofloxacin (λ_{Ex} = 275 nm, λ_{Em}= 440 nm) was not available, **Cipro P2** was used in immunocytochemistry experiments to study the intracellular localization, explicitly the lysosomal localization, in collaboration with *Prof. Zahler* at the *LMU Munich*.

For the co-localization experiment antibodies for the lysosome-associated membrane glycoprotein 1 (LAMP1), that also was consistently enriched with the **P2** probes and **Levo P1**, was selected. Utilization of the probes enabled the appendage of an orthogonal fluorophore to analyze the co-localization of the molecules with LAMP1, i.e. lysosomes. Both LAMP1 and **Cipro P2** channels revealed clear cytoplasmic punctuate signals, anticipated for lysosomal labeling (**Figure 46**). Overlay of all channels showed a strong co-localization of LAMP1 and **Cipro P2** clearly indicating lysosomal accumulation of **Cipro P2**. Performing the experiment in three independent replicates, a strong Pearson's r correlation of 0.6033 for LAMP1 and **Cipro P2** was validated (**Figure 47**).

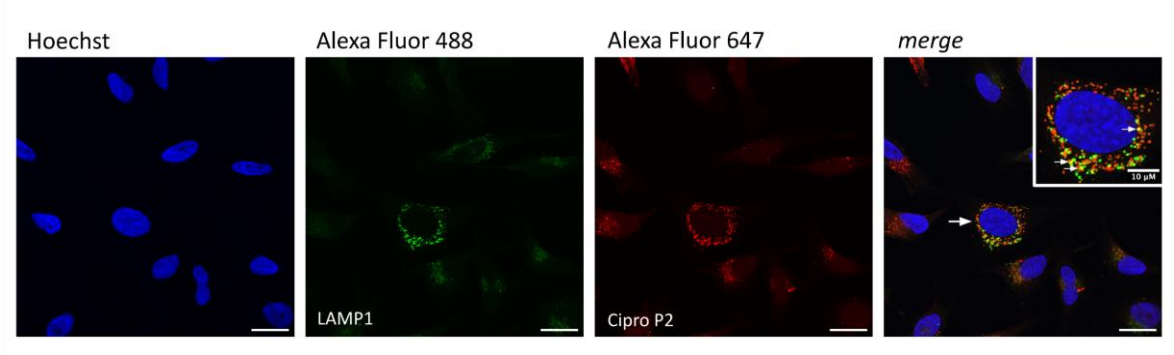

Figure 46: Lysosomal co-staining with **Cipro P2**. Representative immunocytochemistry pictures of **Cipro P2** and the lysosome-associated membrane glycoprotein 1 (LAMP1) in HeLa cells. Cell nuclei were stained with *Hoechst* dye, LAMP1 visualized by a respective primary antibody followed by an Alexa Fluor 488-conjugated secondary antibody and **Cipro P2** (20 µM) localization detected by appending Alexa Fluor 647 to the alkyne handle of the probe *via* CuAAC chemistry. Merging of all channels revealed a pronounced co-localization. The scale indicates 20 µm. The experiment was performed by *Adrian Jauch, LMU Munich.*

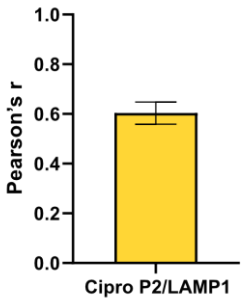

Figure 47: Significance of **Cipro P2** and LAMP1 co-localization. The bar plot depicts the strong correlation (Pearson`s r of 0.6033) of **Cipro P2** and LAMP1 in localization (mean of n = 3 independent experiments with 50 cells analyzed each with SD is plotted). The experiment was performed by *Adrian Jauch, LMU Munich*.

Unfortunately, for **Cipro P1** no localized signal at all could be detected in similar immunocytochemistry studies, suggesting either a general unfeasibility of the probe for these types of experiments or no clear and distinct localization. An alternative approach to use propargylated Ciprofloxacin (similar to **Cipro P1** with a propargylic alkyne at the piperazine, but without the diazirine) were as well unsuccessful.

Considering the results, the strong **Cipro P2**-mediated enrichment of lysosomal proteins and its lysosomal accumulation (at a tested concentration of 20 µM) is very likely due to masking of the carboxylic acid-moiety. Although, a prominent accumulation of the parent compound Ciprofloxacin and **Cipro P1** in the lysosome at high dosing concentrations cannot be comprehensively excluded, the enrichment data and the whole proteome regulation of FQ-treated cells at relevant concentrations, indicated more selective mode of actions evoking adverse effects with cytoplasmic and mitochondrial proteins.

4. Summary and outlook

The fluoroquinolone-associated disability (FQAD) comprises a set of severe and potentially long-lasting adverse events connected to FQ treatment.[144] Although infrequent, the symptoms are well-documented and regulatory agencies have issued various warnings and recommended their restricted use.[144,145] Accordingly, the prescriptions rates of FQs have significantly declined.[114,122–125] As the molecular causalities for the side-effects are not well understood, in this project a global and un-biased off-target discovery of FQs in the human proteome was performed.[144] Whole proteome analyses of FQ-treated cells revealed concentration- and time-dependent dysregulation of the ETC, especially of the complexes I and IV. Employing affinity-based protein profiling with tailored FQ-derived affinity probes and probe-free thermal proteome profiling as chemo-proteomic approaches, various potential protein off-targets have been identified. While for some, such as ClpP, SCARB1, PTGR2 and ADAL1 significant activity modulations by FQs could not be validated, functional interactions with others were established. The mitochondrial isocitrate dehydrogenase IDH2 was shown to be concentration-dependently inhibited by FQs. Due to its central role in metabolic rewiring and involvement in redox homeostasis, MMP regulation and epigenetics the validated inhibition of IDH2 by FQs could be a cornerstone of FQ-derived adverse effects. While preliminary results in each of these down-stream implications have been encouraging, the studies are ongoing at this time and discussed in detail in the respective chapter. Furthermore, a potential cause of the selective complex I and IV

downregulation has been identified by the enrichment of mitochondrial AIFM1 that is involved in the mitochondrial import of ETC subunits. The validation experiments for AIFM1 are also ongoing at this point, preliminary results were discussed. Moreover, the non-mitochondrial nucleoside triphosphate hydrolase NUDT1, which plays an important role in maintaining the integrity of the nucleotide pool by removing oxidatively damaged precursors, has been confirmed as an off-target of FQs. Furthermore, reported chelation of bivalent ions by FQs and other literature-reported mode of actions could be involved in the adverse effects.[134,163–165,169–171] Clearly, a variety of factors contribute to the intricate negative side-effects, and the severity of these effects likely correlates with the overall systemic concentrations of the FQs within the individual patients. Detailed mechanistic and functional studies for the validated IDH2 and potential AIFM1 engagement are ongoing to facilitate future development of safer FQ derivatives.

III – Indolin-2-one nitroimidazole antibiotics exhibit an unexpected dual mode of action

---

The chapter is based on the journal publication:

T. Reinhardt*, K. M. Lee*, L. Niederegger, C. R. Hess, S. A. Sieber, Indolin-2-one Nitroimidazole Antibiotics Exhibit an Unexpected Dual Mode of Action. *ACS Chem. Biol.* **17**, 3077–3085 (2022).

* Authors contributed equally

Contributions:

T. Reinhardt and K. M. Lee contributed equally to this work. K. M. Lee, T. Reinhardt. and S. A. Sieber conceived and designed the project. K. M. Lee and T. Reinhardt synthesized compounds. K. M. Lee performed MS experiments. K. M. Lee and T. Reinhardt analysed MS data. K. M. Lee and T. Reinhardt performed assays. L. Niederegger and C. R. Hess performed and planed circular voltammetry measurements. T. Reinhardt and S. A. Sieber wrote the manuscript of the journal publication.

1. Nitroimidazole antibiotics

A variety of nitroaromatic compounds feature antibiotic activities, e.g. molecules derived from imidazoles, furans and thiazoles. The first nitroimidazole discovered in the golden age of antibiotic development was the natural product Azomycin in *Steptomyces spp.* cultures in the 1950s.[312] Initial synthetic attempts to obtain derivatives of Azomycin, a 2-nitroimidazole, were unsuccessful. Research therefore focused on 5-nitroimidazoles, which led to the discovery of Metronidazole also in the 1950s (**Figure 48A**).[313]

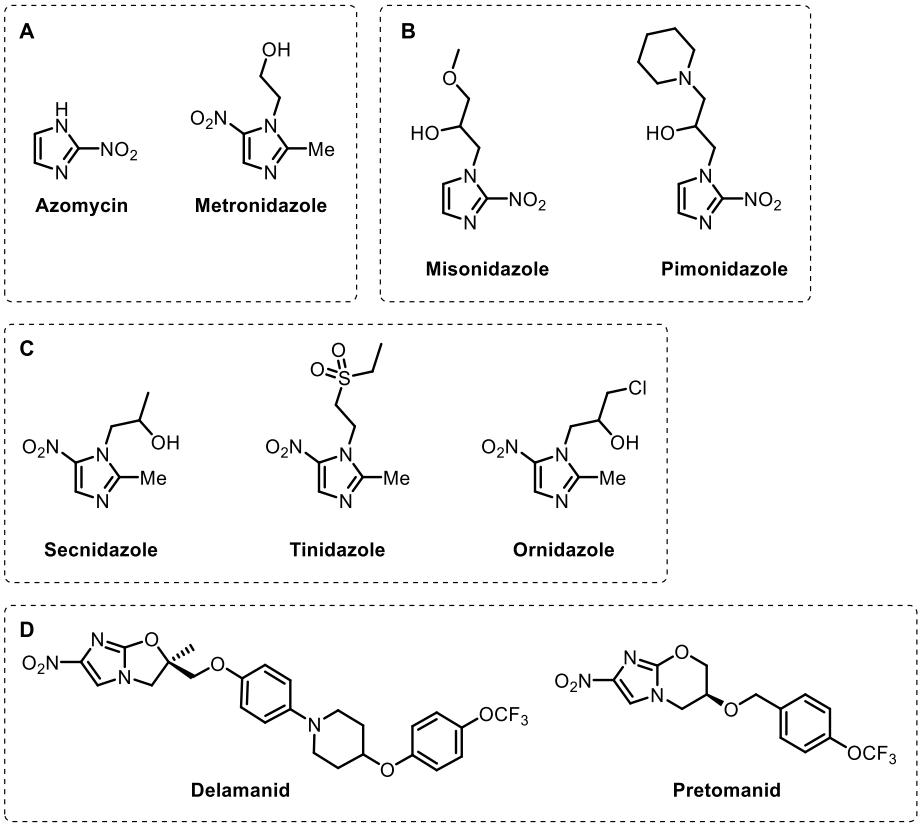

Figure 48: Structures of various nitroimidazole compounds. (**A**) The discovery of the natural product Azomycin lead to the development of the 5-nitroimidazole Metronidazole in the 1950s. (**B**) Synthesis of 2-nitromidazole derivatives was successful in 1965. Misonidazole and Pimonidazole are however only used in tumor hypoxia imaging due to mammalian cytotoxicity. (**C**) A second generation of 5-nitromimidazoles including compounds such as Secnidazole, Tinidazole and Ornidazole were developed in the 1960s to 70s. (**D**) In the 2000s bicyclic 5-nitroimidazoles including Delamanid and Pretomanid were developed.

Structure activity relationship (SAR) studies clearly indicated that the nitro-group is essential for the prokaryotic cytotoxicity and it was discovered that nitroimidazoles exert antimicrobial activity *via* a prodrug mechanism involving reductive bio-activation within the bacteria.[314,315] Since only microaerophilic an anaerobically growing bacteria have sufficiently low cellular redox potentials to allow for a pronounced activation, Metronidazole is only active in these bacteria. Synthesis of 2-nitroimidazoles was eventually successful in 1965, however because of their intrinsically higher reduction potentials, they

are readily activated by mammalian cells leading to cytotoxicity and other side-effects.[313,316,317] Consequently, 2-nitroimidazoles, such as Misonidazole and Pimonidazole, are mainly used in cancer therapy and tumor hypoxia imaging (**Figure 48B**).[318,319] In the 1960s and 1970s a second generation of 5-nitroimidazole derivatives, such as Secnidazole, Tinidazole and Ornidazole were developed (**Figure 48C**).[313] Furthermore, bicyclic compounds including Delamonid and Pretomanid were developed in the 2000s (**Figure 48D**).[320,321]

The best studied and most commonly prescribed nitroimidazole antibiotic is Metronidazole, that is used as first-line therapeutic against microaerophiles, such as *Helicobacter pylori*, protozoa, such as *Entamoeba histolytica*, and anaerobic bacteria, such as *Clostridioides Difficile*.[322] Also facultative anaerobic bacteria, e.g. *E. coli*, can be susceptible in oxygen-free conditions and activity against anaerobic *Mycobacterium tuberculosis* was also shown.[316,323] Although on the market for more than 45 years, the mode of action (MoA) of Metronidazole – and nitroimidazoles in general – is still not completely understood.[322] Uptake of metronidazole into the bacteria is considered to be passive, potentially dependent on the proton gradient of the electron transport chain.[324–326] In line with the prodrug mechanism, Metronidazole and other nitroimidazoles are bio-activated by reduction of the nitro-group (**Figure 49**).

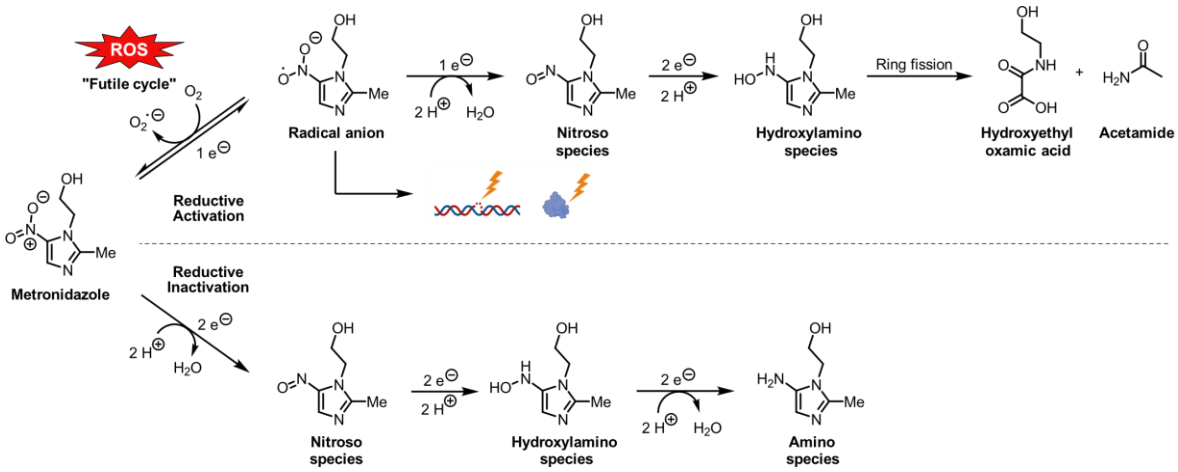

Figure 49: Reductive activation and inactivation of Metronidazole. Reductive activation of Metronidazole proceeds in various one- and two-electron transfer steps. The initially formed radical anion can directly damage DNA and proteins or indirectly lead to reactive-oxygen species (ROS) in the presence of oxygen or other oxidation agents resulting in the regeneration of the parent compound in a process called "futile cycling". Cytotoxic ring fission products of the imidazole ring of the hydroxylamino species have also been investigated. Reductive inactivation of Metronidazole to form the non-toxic amino species has been shown to proceed *via* oxygen-insensitive (type I) nitroreductases. The figure is based on *Dingsdag et al.*[325]

Reactive intermediates, such as radicals, can directly and indirectly lead to DNA and protein damage.[313,325] In the presence of oxygen, one-electron transfer-activated radical anion species of the nitroimidazoles can rapidly be reoxidized to the parent molecule. However,

this so-called "futile cycle" also leads to reactive oxygen species (ROS), initially in the form of superoxide. Accordingly, *E. coli* deficient in SOS DNA repair enzymes have been shown to be more susceptible to Metronidazole.[327,328] Furthermore, the reductive activation of Metronidazole diverts the normal cellular electron flow impairing the normal bacterial redox state, metabolism and thereby the carbon flow.[325]

Exact activation and toxicity mechanisms vary from species to species and multiple pathways have been proposed. One potential enzymatic system to activate nitroimidazoles is the pyruvate:ferredoxin oxidoreductase (PFOR) that is oxidatively decarboxylating pyruvate to acetyl phosphate during fermentation.[313,325,329] Also thioredoxin reductase (TrxR), flavodoxins and oxygen-sensitive (type II) nitroreductases are being discussed to activate nitroimidazoles.[313,325] *In vivo* investigations on exact metabolites and intermediates leading to the bacterial toxicity is challenging, as they are short-lived and especially the radical species highly reactive.[325] Ring fission of a hydroxylamino-species formed *via* multiple one-electron and two-electron transfers has been proposed to give rise to various cytotoxic metabolites, such as hydroxyethyl oxamic acid and acetamide, as well as other products such as glyoxal and guanidine derivatives.[313,325]

In addition to the reductive activation, Metronidazole has also been shown to be reductively inactivated, e.g. by oxygen-insensitive (type I) nitroreductases leading to the formation of the non-toxic 5-amino species.[325,330] Due to the prodrug mechanism, adverse effects of Metronidazole are in general infrequent and are reported only at high doses with peripheral neuropathy and encephalopathy.[331,332]

Bacterial resistance against Metronidazole has been first reported in 1978.[333] Due to their dependence on the nitro-group activation, alterations in activity or expression of those reducing enzymes is one possible way of resistance development against nitroimidazoles.[334] Mutations impairing the PFOR system in *Clostridium perfringens* and *Trichomonas spp.* have been shown to cause approximately 100-fold decreased susceptibility to Metronidazole.[325,335,336] The fact that these bacteria are still partially susceptible to the drug again indicates that further pathways can activate these prodrugs that remain to be discovered. Due to the reductive inactivation mechanism, also upregulation of specific nitroreductases to increase deactivation is a possible resistance strategy.[337] As discussed on page 5, reduced uptake and increased efflux can also infer Metronidazole resistances. An additional resistance mechanism is the up-regulation of DNA repair enzymes.[325]

2. Aim and significance of the project

As discussed, the mode of action of nitroimidazoles is complex, potentially different in various species and not comprehensively understood yet. Despite its discovery already in the 1950s, Metronidazole is still the antibiotic of choice for the treatment of several anaerobic and microaerophilic infections. Due to rising resistances against virtually all antibiotic classes and after years of neglecting the discovery of new antibiotics, efforts in the antibiotic research are being ramped up again in academia and in industry. In a recent publication, *Zhou et al.* reported nitroimidazole conjugates with an indolin-2-one scaffold exhibiting potent, nanomolar potencies against aerobic bacteria (**Figure 50**).[338] This represents a fundamental switch of the activity of nitroimidazole antibiotics, classically being restricted to anaerobic or microaerophilic bacterial infections. The aim of this project was to unravel the molecular and mechanistic cause of this activity in aerobic bacteria. Detailed understanding of the mode of action of these hybrid compounds could facilitate further studies to lift limitations of current nitroimidazole antibiotics, support the discovery of novel lead compounds and ultimately contribute to the interdisciplinary efforts against the antibiotic resistance crisis.

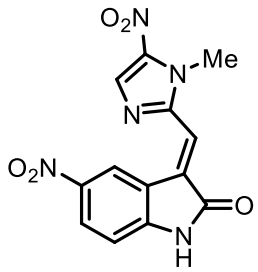

Hybrid 1
(Compound 5c in original publication by *Zhou et al.*)

Figure 50: Structure of the most potent nitroimidazole indolin-2-one conjugate. The compound is hereinafter referred to as: **Hybrid 1** and was originally reported by *Zhou et al.* featuring nanomolar activities against both Gram-positive and Gram-negative bacteria in aerobic conditions.[338] The aim of this project is to decipher the mode of action of this scaffold and understand the cause of antibiotic activity in aerobic bacteria. This research could facilitate the development of novel nitroimidazole-containing antibiotics.

3. Results and discussion

Disclaimer: *This project was started and pursued by Kyu M. Lee during his doctoral studies and continued by me after his dissertation (see contributions, page 87). For clarity and context, the project is described comprehensively in this thesis.*

3.1 Antibacterial activity & whole proteome analysis

For initial studies, the indolin-2-one nitroimidazole **Hybrid 1** was synthesized according to literature procedures (**Figure 51A**).[338] To validate and reference the published antibacterial activity of the compound to in-house conditions, its minimal inhibitory concentrations (MICs) for various Gram-negative and Gram-positive pathogens was tested (**Figure 51B**). In line with the literature, the compound featured potent activities against both Gram-positive (*S. aureus* NCTC 8325, MIC = 130 nM) and Gram-negative (*P. aeruginosa* PAO1, MIC = 1.3 µM; *E. coli* MM28, MIC = 1.25 µM).[338] The activity in aerobic bacteria is in contrast to the potencies of classical 5-nitroimidazole antibiotics, such as marketed Metronidazole, that typically feature only antimicrobial activities in anaerobic or microaerophilic conditions. For example, against *S. aureus* NCTC8325, no MIC of Metronidazole could be determined up to the highest tested concentration of 1 mM. After confirmation of these interesting results, indicating a potentially different mode of action (MoA) of the indolin-2-one nitroimidazole conjugates, target identification studies were initiated to explain the aerobic activity.

Firstly, a whole proteome analysis in presence of **Hybrid 1** versus the vehicle control was performed to study regulated proteins and pathways upon compound treatment (**Figure 51C-D**). Because of the strong activity in *S. aureus* NCTC8325, this strain was incubated with 60 nM of **Hybrid 1** for 2 h at room temperature, representing half of the MIC. Strikingly, the majority of upregulated proteins were bacteriophage related. Bacteriophages are viruses that insert into bacterial hosts hijacking their replication machinery for proliferation of their own DNA. On the other hand, also the bacteria benefit from the phages, as they provide advantages in virulence, pathogenesis, diversification and adaptation to environmental cues.[339] Phages can replicate either as prophages in their so-called lysogenic state or in their lytic state by producing virions. While in the lysogenic cycle the prophages insert into the hosts DNA, replicating alongside the bacteria with mutual benefits, in the lytic form the phages produce virions as progeny, killing the bacterial host at the same time. This switch from lysogenic to lytic cycle is usually dependent on stress cues, such as DNA damage and resulting activation of the bacterial SOS-response.[340–342] Due to the pronounced

upregulation of phage-related proteins upon incubation with **Hybrid 1**, a DNA-centered MoA of the compound was considered.

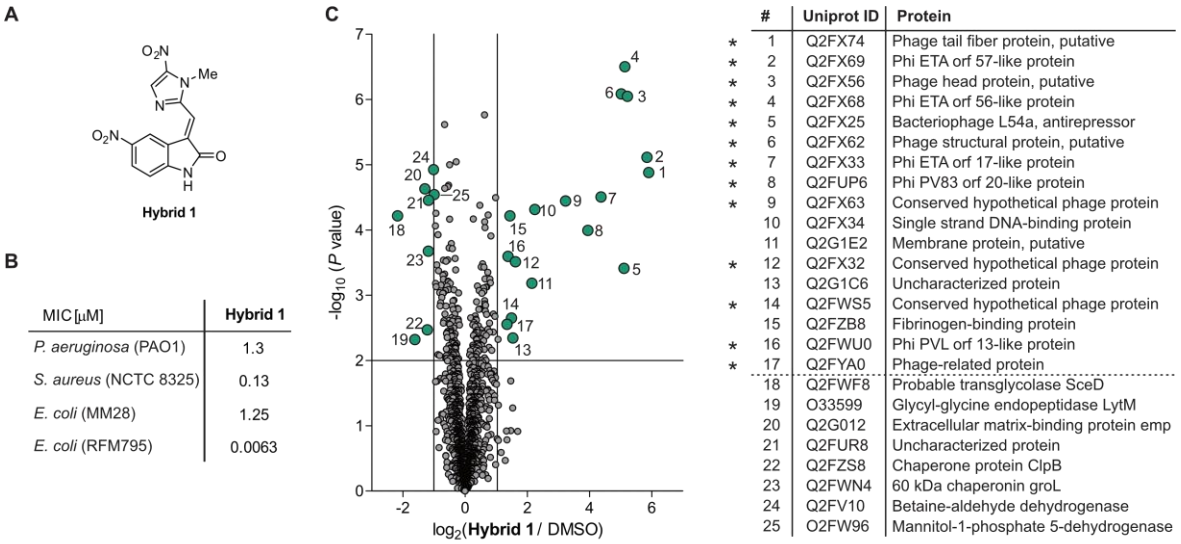

MIC [µM]	Hybrid 1
P. aeruginosa (PAO1)	1.3
S. aureus (NCTC 8325)	0.13
E. coli (MM28)	1.25
E. coli (RFM795)	0.0063

	#	Uniprot ID	Protein
*	1	Q2FX74	Phage tail fiber protein, putative
*	2	Q2FX69	Phi ETA orf 57-like protein
*	3	Q2FX56	Phage head protein, putative
*	4	Q2FX68	Phi ETA orf 56-like protein
*	5	Q2FX25	Bacteriophage L54a, antirepressor
*	6	Q2FX62	Phage structural protein, putative
*	7	Q2FX33	Phi ETA orf 17-like protein
*	8	Q2FUP6	Phi PV83 orf 20-like protein
*	9	Q2FX63	Conserved hypothetical phage protein
	10	Q2FX34	Single strand DNA-binding protein
	11	Q2G1E2	Membrane protein, putative
*	12	Q2FX32	Conserved hypothetical phage protein
	13	Q2G1C6	Uncharacterized protein
*	14	Q2FWS5	Conserved hypothetical phage protein
	15	Q2FZB8	Fibrinogen-binding protein
*	16	Q2FWU0	Phi PVL orf 13-like protein
*	17	Q2FYA0	Phage-related protein
	18	Q2FWF8	Probable transglycolase SceD
	19	O33599	Glycyl-glycine endopeptidase LytM
	20	Q2G012	Extracellular matrix-binding protein emp
	21	Q2FUR8	Uncharacterized protein
	22	Q2FZS8	Chaperone protein ClpB
	23	Q2FWN4	60 kDa chaperonin groL
	24	Q2FV10	Betaine-aldehyde dehydrogenase
	25	O2FW96	Mannitol-1-phosphate 5-dehydrogenase

Figure 51: Antibacterial activity and whole proteome analysis of **Hybrid 1**. (**A**) Structure of the indolin-2-one nitroimidazole conjugate being the compound of interest in these mechanistic investigations. (**B**) Excellent minimal inhibitory concentrations (MICs) of **Hybrid 1** in various Gram-positive and Gram-negative strains. (**C**) Volcano plot of the whole proteome analysis of intact *S. aureus* NCTC8325 cells treated with **Hybrid 1** (60 nM = approx. 0.5× MIC, 2 h, room temperature). Threshold lines represent a $\log_2$ regulation of ±1 and a $-\log_{10}(P \text{ value})$ of 2 (two-sided two-sample *t*-test, $n = 4$ replicates per group). The table lists the top 25 regulated proteins. A significant amount of bacterio-phage related proteins (indicated by the asterisk) was found to be upregulated. Figure modified and based on *Reinhardt et al.*[71]

As the addition of exogeneous DNA to MIC experiments did not alter the potency of the compound in so-called MIC-shift assays, a direct interaction of **Hybrid 1** with DNA could be excluded (**Table 1**). While the DNA-intercalating antibiotic Actinomycin D decreased in activity relative to the amount of supplemented exogenous DNA, the activity of the negative control Gentamicin was also not affected.

Table 1: MIC-shift assays of **Hybrid 1** in presence and absence of exogenous DNA.

c(DNA)	Actinomycin D	**Hybrid 1**	Gentamicin
0 µg/mL	62 nM	130 - 250 nM	1.25 µM
5 µg/mL	195 nM	130 - 250 nM	1.25 µM
50 µg/mL	780 nM	130 - 250 nM	1.25 µM
500 µg/mL	12.4 µM	130 - 250 nM	1.25 µM

3.2 Target identification by ABPP

For indolin-2-one nitroimidazole **Hybrid 1** this implicated either the necessity of an *in situ* bio-activation leading to DNA interaction, as established for classical nitroimidazole antibiotics in anaerobic conditions, or a direct engagement of a target modulating DNA maintenance or topology. In order to elucidate potential protein interactions of the hybrid compound, activity-based protein profiling (ABPP, see page 10), was envisioned. The methodology enabled both the discovery of potential direct, covalent protein targets *via*

intrinsic covalent reactivities, such as the *Michael acceptor* of **Hybrid 1**, but also the identification of protein interactions after a putative *in situ* bio-activation.

Consequently, various activity-based probes (ABPs) bearing an alkyne as enrichment handle were synthesized by *Kyu M. Lee* (**Figure 52A,** refer to the publication for detailed synthesis).[71] Of note, the (*E*)-configuration of the probes and the parent compound **Hybrid 1** was determined and verified by ROESY 2D-NMR spectroscopy (see Appendix). As discussed before, the positioning and manner of derivatization necessary for the incorporation of the alkyne into the scaffold can affect the potential target engagement and thereby the antibiotic activity of the compound. Therefore, **ABP1-4** were tested in MIC assays against the previously selected panel of pathogens (**Figure 52B**).

A

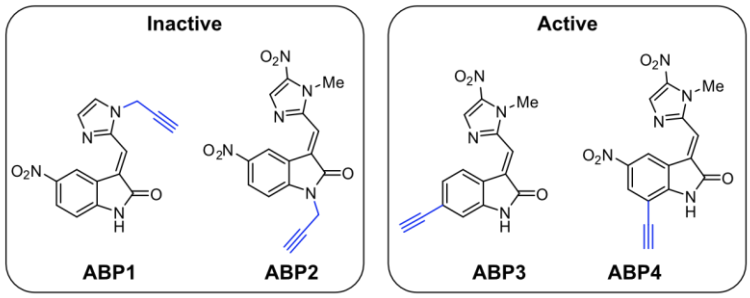

B

MIC [µM]	Hybrid 1	ABP1	ABP2	ABP3	ABP4
P. aeruginosa (PAO1)	1.3	> 50	> 50	> 50	> 50
S. aureus (NCTC8325)	0.13	> 50	> 50	0.63	0.13
E. coli (MM28)	1.25	> 10	> 10	> 10	> 10
E. coli (RFM795)	0.0063	> 1.25	0.078	0.050	0.025

Figure 52: Activity-based probes (ABPs) derived from the indolin-2-one nitroimidazole **Hybrid 1**. The probes were synthesized by *Kyu M. Lee*. (**A**) Structures of **ABP1-ABP4** classifying into antibiotically active and inactive as result of their modification. Their synthesis is discussed in detail in the publication.[71] (**B**) Minimal inhibitory concentrations (MICs) of the probes and the parent compound. Figure modified and based on *Reinhardt et al*.[71]

ABP1 lacking the nitro-group at the imidazole lost activity in in all tested strains, indicating the essentiality of this functional group for the MoA. Also, indolin-2-one *N*-propargylated **ABP2** did not show antibiotic activity, despite featuring the nitro-group, except in the LPS-deficient *E. coli* RFM795 strain, potentially suggesting an impaired uptake in Gram-negative in addition to weaker target engagement. In Gram-positive *S. aureus*, **ABP3**, lacking the indolin-2-one nitro-group, retained activity with an approx. 4.8-fold decrease in activity and **ABP4** retained the activity of the parent compound completely. However, in both Gram-negative *P. aeruginosa* (PAO1) and *E. coli* (MM28) **ABP3** and **ABP4** featured no activity. As potency was restored in the LPS-deficient *E. coli* RFM795 strain, this was indicative of

restricted uptake of the probes due to their modification. Lipopolysaccharides (LPS) are crucial components of the Gram-negative cell walls and when their synthesis is dysfunctional the bacteria can be penetrated more easily. Consequently, **ABP1** and **ABP2** were classified as "inactive" and were envisioned as potential controls, while **ABP3** and **ABP4** were classified as antibiotically "active".

To decipher potential covalent protein targets with the probes, initial analytical gel-based ABPP experiments were performed to assess the labelling reactivities of the probes and optimal concentrations. *In situ* treatment of *S. aureus* NCTC8325 with the probes afforded extensive concentration-dependent labeling patterns with all probes in the low micromolar range (**Figure 53**). Interestingly, **ABP1** lacking the nitro-group at the imidazole featured significantly less pronounced labeling, while **ABP3** lacking the nitro-group at the indolin-2-one scaffold labeled intensively. This result further highlighted the notion that the nitro-imidazole is crucial for target engagement.

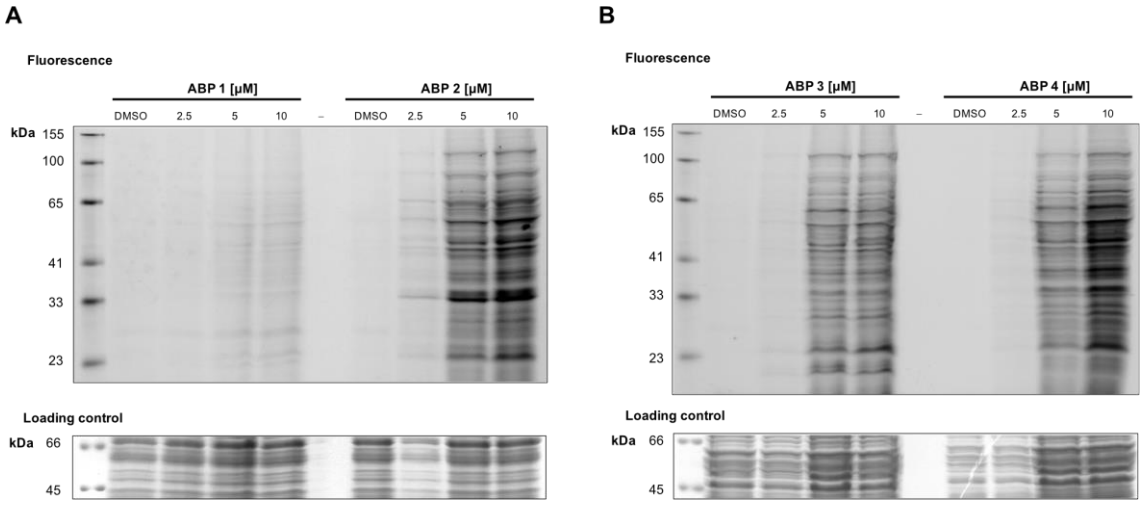

Figure 53: Analytical gel-based ABPP of **ABP1**-**ABP4** in *S. aureus* NCTC8325. The bacteria were treated *in situ* with various concentrations of the probes (2.5 – 10 µM) for 2 h at room temperature and after lysis labeled proteins were visualized by appending TAMRA-azide *via* CuAAC and read-out was performed by SDS-PAGE with fluorescence scanning. (**A**) Analytical ABPP of "inactive" **ABP1** and **ABP2**. (**B**) Analytical ABPP of "active" **ABP3** and **ABP4**. All probes exhibited concentration-dependent covalent reactivity, **ABP1** lacking the nitro-group at the imidazole featured significantly less intense labeling. Coomassie staining was performed as loading control. Figure based on *Reinhardt et al*.[71]

Subsequently, preparative MS-based ABPP in *S. aureus* NCTC8325 was performed to identify targeted proteins. For this experiment 5 µM of the probes was used, as it resulted in intensive labeling in the gel-based studies. In quantitative MS-ABPP, bacteria are treated with probe or vehicle control (DMSO) and after lysis biotin is appended to probe-labeled proteins *via* the CuAAC chemistry. Enrichment on avidin beads, tryptic digest and LC-MS/MS analysis using label-free quantification (LFQ) enables the identification and

quantification of target proteins (see page 10). The data are usually depicted in volcano plots, showing the $\log_2$-fold enrichment and the statistical significance in form of the –log(*P*-value). In line with the gel-based results, **ABP1** did not lead to extensive enrichment within the thresholds ($\log_2$-fold enrichment ≥ 2 and $-\log_{10}(P \text{ value}) \geq 2$, **Figure 54A**). As opposed to **ABP1**, for the second antibiotically inactive **ABP2** 16 protein targets were identified by ABPP, making the probe a valuable control for deciphering the antibiotic target (**Figure 54B**).

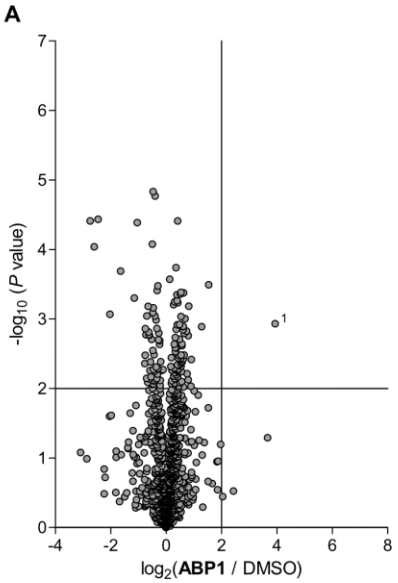

#	Uniprot ID	Gene	Protein name
1	Q2G2E2	SAOUHSC_00651	DUF2179 domain-containing protein

#	Uniprot ID	Gene	Protein name
1	Q2G170	SAOUHSC_00284	5'-nucleotidase, lipoprotein e(P4) family
2	Q2FVD5	SAOUHSC_02778	Uncharacterized oxidoreductase
3	Q2FVX3	fdhD	Sulfur carrier protein FdhD
4	Q2FVK5	sbi	Immunoglobulin-binding protein Sbi
5	Q2G0M2	SAOUHSC_00538	Haloacid dehalogenase-like hydrolase, putative
6	Q2G270	SAOUHSC_02568	bPH_3 domain-containing protein
7	Q2G1X0	hly	Alpha-hemolysin
8	Q2FV27	SAOUHSC_02912	3-dmu-9_3-mt domain-containing protein
9	Q2FV52	isaA	Probable transglycosylase IsaA
10	Q2G0G2	SAOUHSC_00607	Uncharacterized protein
11	Q2G0L4	sdrD	Serine-aspartate repeat-containing protein D
12	Q2FW33	rplQ	50S ribosomal protein L17
13	P02976	spa	Immunoglobulin G-binding protein A
14	Q2FWA8	SAOUHSC_02390	Lytic regulatory protein, putative
15	Q2FXA0	SAOUHSC_01977	UPF0342 protein SAOUHSC_01977
16	Q2FVE7	cntA	Metal-staphylopine-binding protein CntA

Figure 54: MS-based ABPP of **ABP1** (**A**) and **ABP2** (**B**) in *S. aureus* NCTC8325. Bacteria were incubated with the respective probe or vehicle control (DMSO) for 2 h at room temperature, lysed and subjected to CuAAC chemistry with biotin azide. After enrichment of labeled proteins on avidin beads and tryptic digest, the protein targets were identified and quantified *via* LC-MS/MS using LFQ. The volcano plots visualize the $\log_2$-fold enrichment versus the vehicle control and the statistical significance in form of the –log(*P*-value) based on a two-sided two-sample *t*-test with n = 3 replicates in each group. Threshold lines indicate a $\log_2$-fold enrichment of ≥ 2 and –log(*P*-value) ≥ 2. The tables list details of the enriched proteins. Figure based on *Reinhardt et al.*[71]

Active probes **ABP3** and **ABP4** enriched diverse protein targets, noteworthy the extent of enrichment with **ABP3** was lower than for **ABP4** either because of the position of the alkyne or because of the missing indolin-2-one nitro-group (**Figure 55A-B**). Considering the whole proteome analysis results suggesting an involvement of DNA modulation in the MoA of the parent **Hybrid 1**, especially the identification of parE, the subunit B of the DNA topoisomerase IV, with **ABP4** was interesting.

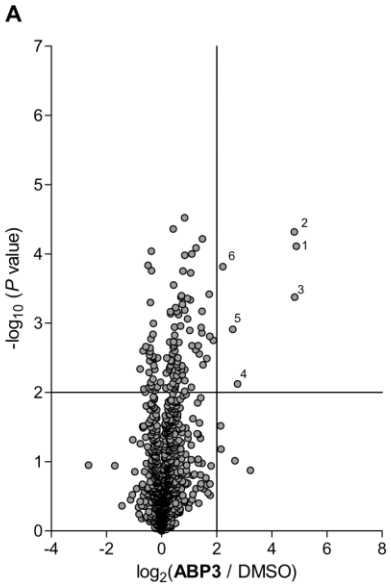

#	Uniprot ID	Gene	Protein name
1	Q2FVX3	fdhD	Sulfur carrier protein FdhD
2	Q2FVD5	SAOUHSC_02778	Uncharacterized oxidoreductase
3	Q2FYL3	SAOUHSC_01427	Probable CtpA-like serine protease
4	Q2FVK5	sbi	Immunoglobulin-binding protein Sbi
5	Q2FW33	rplQ	50S ribosomal protein L17
6	Q2FV27	SAOUHSC_02912	3-dmu-9_3-mt domain-containing protein

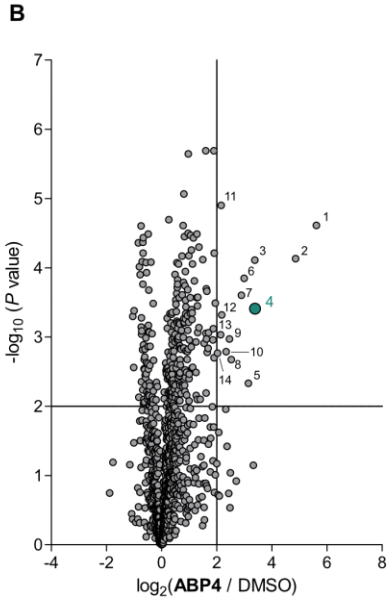

#	Uniprot ID	Gene	Protein name
1	Q2FVD5	SAOUHSC_02778	Uncharacterized oxidoreductase
2	Q2FVX3	fdhD	Sulfur carrier protein FdhD
3	Q2G0M2	SAOUHSC_00538	Haloacid dehalogenase-like hydrolase, putative
4	Q2FYS5	parE	DNA topoisomerase 4 subunit B
5	Q2FVK5	sbi	Immunoglobulin-binding protein Sbi
6	Q2G270	SAOUHSC_02568	bPH_3 domain-containing protein
7	Q2FW33	rplQ	50S ribosomal protein L17
8	Q2G1I7	SAOUHSC_00135	Uncharacterized protein
9	P02976	spa	Immunoglobulin G-binding protein A
10	Q2G2T9	SAOUHSC_00711	Uncharacterized protein
11	Q2G0J8	SAOUHSC_00562	Phosphomethylpyrimidine kinase
12	Q2G280	SAOUHSC_01999	NADH-dependent peroxiredoxin
13	Q2FXA0	SAOUHSC_01977	UPF0342 protein SAOUHSC_01977
14	Q2FZ45	rpsP	30S ribosomal protein S16

Figure 55: MS-based ABPP of **ABP3** (**A**) and **ABP4** (**B**) in *S. aureus* NCTC8325. Bacteria were incubated with the respective probe or vehicle control (DMSO) for 2 h at room temperature, lysed and subjected to CuAAC chemistry with biotin azide. After enrichment of labeled proteins on avidin beads and tryptic digest, the protein targets were identified and quantified *via* LC-MS/MS using LFQ. The volcano plots visualize the $\log_2$-fold enrichment versus the vehicle control and the statistical significance in form of the –log(*P*-value) based on a two-sided two-sample *t*-test with $n = 3$ replicates in each group. Threshold lines indicate a $\log_2$-fold enrichment of ≥ 2 and –log(*P*-value) ≥ 2. The tables list details of the enriched proteins. The subunit B of the DNA topoisomerase IV (parE) is highlighted in color. Figure based on *Reinhardt et al.*[71]

In fact, when comparing the enrichment of the most active probe **ABP4** with the enrichment of the intensively labeling inactive probe **ABP2**, parE stood out as the sole putative target

within the standard thresholds (**Figure 56A**). To further validate parE engagement by the probe and the parent compound, competitive ABPP was performed. Bacteria were incubated with the parent **Hybrid 1** at various concentrations for 2 h at room temperature, before addition of **ABP4** and additional incubation for 2 h at room temperature. The subsequent MS-based ABPP workflow revealed a weak, but statistically significant and concentration-dependent competition of parE labelling by **Hybrid 1**, indicating that the protein is a valid target (**Figure 56B-D**).

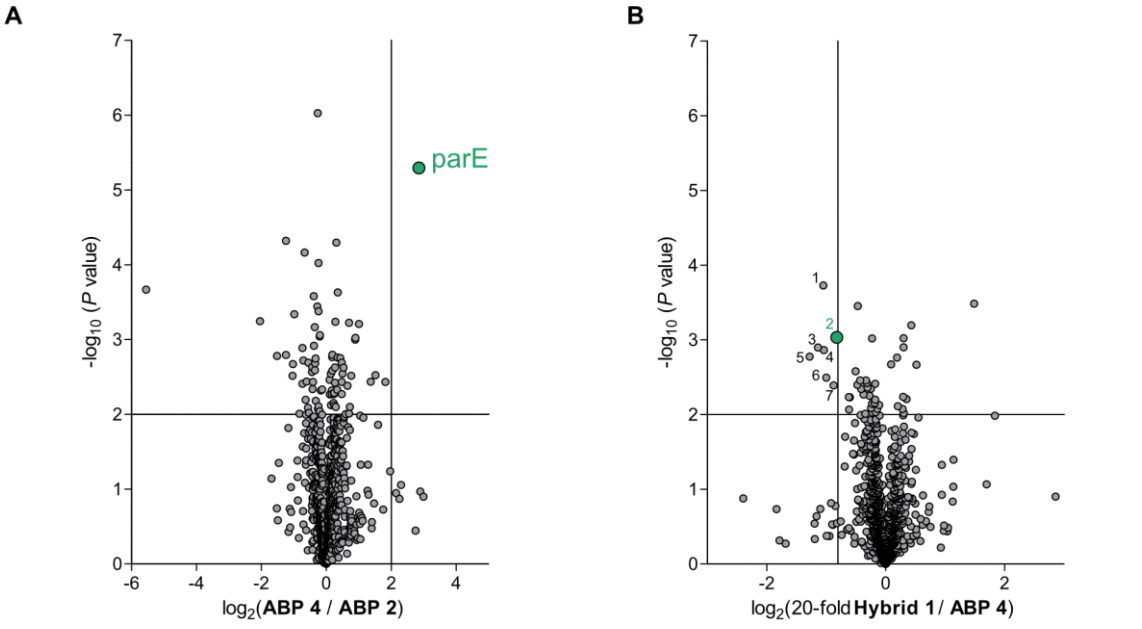

#	Uniprot ID	Gene	Protein name
1	Q2FV27	SAOUHSC_02912	PhnB-like protein
2	Q2FYS5	parE	DNA topoisomerase 4 subunit B
3	Q2G0M2	SAOUHSC_00538	Haloacid dehalogenase-like hydrolase
4	Q2G1J2	isdI	Heme oxygenase 2 isdI
5	Q2G282	perR	Peroxide-responsive repressor PerR
6	Q2G0G1	adh	Alcohol dehydrogenase adh
7	Q2FXM3	SAOUHSC_01812	uncharacterized protein

Figure 56: Competitive ABPP implicated parE as target of nitroimidazole indoline-2-one hybrids. (**A**) Volcano plot of ABPP studies in *S. aureus* NCTC8325 comparing active **ABP4** with inactive **ABP2** (5 µM probes, 2 h, room temperature). The DNA topoisomerase IV subunit B (parE) is the sole target within the thresholds of $\log_2$ enrichment of ≥ 2 and statistical significance –log(*P*-value) of ≥ 2 (two-sided two-sample *t*-test, $n = 3$ replicates per group). (**B**) Competitive ABPP *S. aureus* NCTC8325 with pre-treatment of 20-fold excess of parent **Hybrid 1** (2 h, room temperature) before addition of **ABP4** (5 µM, 2 h, room temperature). ParE is highlighted in color and weakly, but statistically significantly outcompeted. Threshold lines represent a $\log_2$-fold competition of ≥ 0.8 and –log(*P*-value) of ≥ 2 (two-sided two-sample *t*-test, $n = 3$ replicates per group). (**C**) Table listing all outcompeted proteins based on the volcano plot in panel **B**. (**D**) Plot depicting the concentration-dependent competition of **ABP4** by the parent **Hybrid 1** as judged by the LFQ intensities (average and SD of $n = 3$ replicates each). Figure modified and based on *Reinhardt et al.*[71]

3.3 Topoisomerase IV target validation studies

As parE was the only outcompeted essential protein in *S. aureus* (as judged by the *S. aureus Nebraska* transposon mutant library)[343] and is additionally implicated in the maintenance of DNA topology it was prioritized for target validation studies. Published and commercially available *S. aureus* topoisomerase IV decatenation assays in presence of parent **Hybrid 1** were performed, in which catenated kDNA is being unlinked and resolved into their open-circular and relaxed-circular forms using agarose-gel electrophoresis (**Figure 57A**). The *in vitro* activity assays revealed an inhibition of the topoisomerase IV by **Hybrid 1** with an apparent IC_{50} of 28.6 ± 3.4 µM validating the enzyme as a target (**Figure 57B-C**). Importantly, the in vitro IC_{50} is in a similar range to literature and in-house values of the known topoisomerase IV inhibitor Ciprofloxacin (literature 7-20 µM, in-house: approx. 25 µM, **Figure 57B**).[213,214]

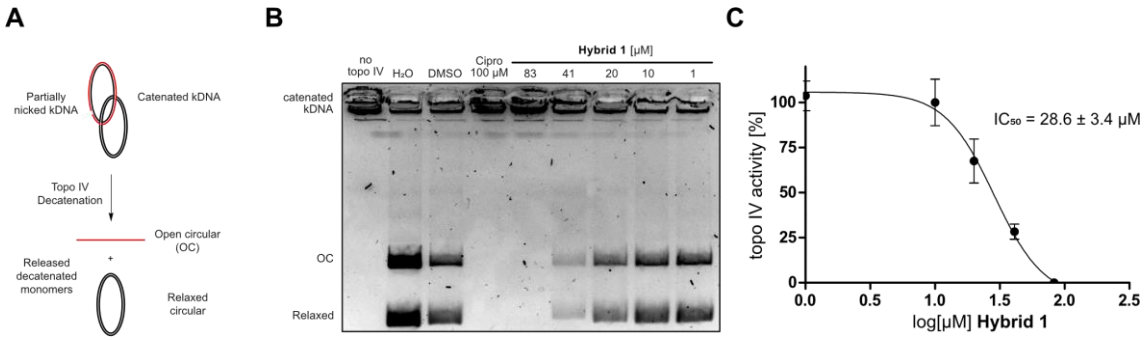

Figure 57: *In vitro* topoisomerase IV assay for target validation. (**A**) Principle of the topoisomerase IV activity assay. The enzyme decatenates kDNA into monomers, that can be separated with agarose-gel electrophoresis. When an intercalator is present in the agarose gel, the decatenated monomers are resolved in their relaxed circular and their open circular (OC) forms. The latter is derived from partially nicked kDNA. (**B**) Decatenation assay in presence of **Hybrid 1** revealing inhibition of the *S. aureus* topoisomerase IV activity in presence of the compound. Known topoisomerase inhibitor Ciprofloxacin was used as positive control. (**C**) Quantification of the bands of the decatenated species revealed an apparent IC_{50} of 28.6 ± 3.4 µM of **Hybrid 1**. The average and SD of $n = 3$ independent experiments are plotted. Figure modified and based on *Reinhardt et al*.[71]

The nature of this *in vitro* assay, lacking the possibility of *in situ* bio-activation of the nitroimidazole, indicated a direct, activation-independent MoA of the compound against the topoisomerase. To explore the importance of the *Michael acceptor* for the SAR, it was synthetically removed by reduction with sodium borohydride affording **Hybrid 2** (**Figure 58A**). As no inhibition of *S. aureus* topoisomerase IV was detected anymore with **Hybrid 2**, the *Michael acceptor* is crucial for the target engagement, either by rigidifying the conformation of the compound scaffold or by conveying intrinsic covalent reactivity (**Figure 58C**). In line with these results, the MIC of **Hybrid 2** was significantly higher with 10 µM compared to 130 nM of **Hybrid 1**. Experiments trying to identify covalent adducts or the

binding-site of **Hybrid 1** within the topoisomerase by MS-based approaches were not successful.

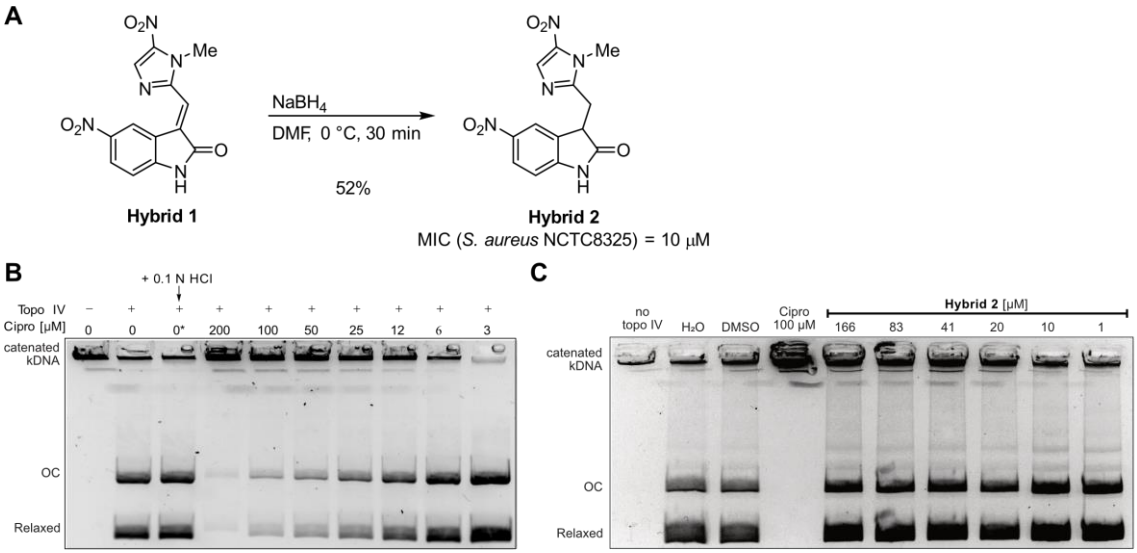

Figure 58: SAR studies of **Hybrid 2** lacking the *Michael acceptor*. (**A**) Chemical reduction of **Hybrid 1** to **Hybrid 2** by sodium borohydride with 52% purified yield. (**B**) *S. aureus* topoisomerase IV decatenation assay of Ciprofloxacin as control, revealing a similar range of apparent approx. IC_{50} of 25 µM in line with literature values.[213,214] (**C**) Decatenation assay in presence of **Hybrid 2** lacking the *Michael acceptor* detecting no inhibition anymore and suggesting essentiality of the moiety for the MoA independent of classical bio-activation of nitroimidazoles. Figure modified and based on *Reinhardt et al*.[71]

Intrigued by the apparent activation-independent inhibition of the topoisomerase, **Hybrid 1** was incubated with recombinant *E. coli* nitroreductase NfsB to determine if an *in situ* enzymatic activation is not possible in general. By monitoring the decrease of the absorbance maximum of **Hybrid 1** (λ_{max} = 355 nm), the fundamental possibility of reductive activation by nitroreductases was however shown (**Figure 59A**). By pre-treating **Hybrid 1** with NfsB for various durations before assessing the topoisomerase IV inhibition in the decatenation assays, it was determined that the inhibition is not only independent of bio-activation, but also not detectable after the enzymatic reduction (**Figure 59B**). In summary, the experiments validated the topoisomerase IV as target in *S. aureus*, likely an additional and competing MoA to the classical enzymatic activation of nitroimidazoles. Direct inhibition of the topoisomerase IV is at least to some extend the cause for the aerobic activity of the hybrid compounds.

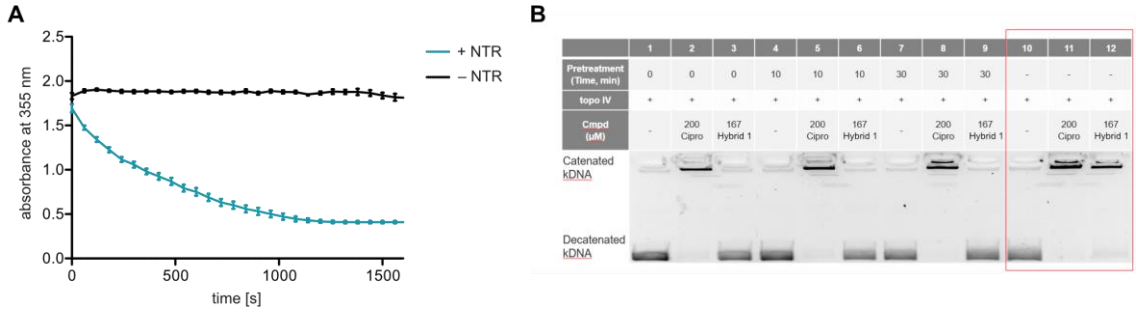

Figure 59: Nitroreductase-mediated conversion of **Hybrid 1**.Photometric monitoring of the conversion of **Hybrid 1** by recombinant *E. coli* nitroreductase NfsB by decreasing absorbance at the absorbance maximum of **Hybrid 1** (355 nm). (**B**) Topoisomerase IV decatenation assay after pre-treatment of **Hybrid 1** with nitroreductase (NTR) abolishing the inhibitory effect. As inhibition is only detectable without NTR (red box), the non-converted form of **Hybrid 1** is responsible for the inhibition. Figure modified and based on *Reinhardt et al.*[71]

3.4 Studies into the bio-activation of nitroimidazole hybrids

In prior experiments it was shown that the general possibility of enzymatic reductive bio-activation of nitroimidazoles could potentially be translated to the nitroimidazole indoline-2-one conjugates. Apart from the *in vitro* treatment with *E. coli* nitroreductase NfsB (**Figure 59A**), also the less pronounced labelling intensity in analytical ABPP with **ABP1** lacking the imidazolic nitro-group suggested the involvement of bio-activation (**Figure 53A**). Therefore, analytical ABPP with **ABP4** in *S. aureus* lysate with and without nitroreductase pre-treatment was conducted, revealing significantly elevated labeling intensities in nitroreductase-positive conditions (**Figure 60**). Consequently, the nitroimidazole indoline-2-one hybrids feature a dual MoA, firstly the direct inhibition of the topoisomerase IV and secondly the classical bio-activation-mediated MoA of nitroimidazoles.

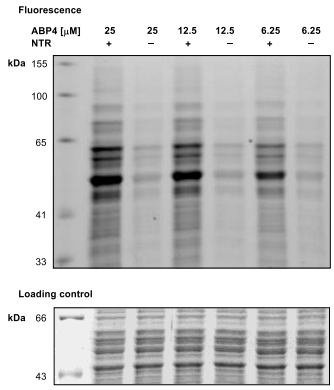

Figure 60: Analytical ABPP of **ABP4** with and without nitroreductase treatment. Gel-based labelling in S. *aureus* lysate with **ABP4** pre-treated (+ NTR) and non-treated (– NTR) with recombinant *E. coli* NfsB nitroreductase and NADH in phosphate buffer for 20 min at 30 °C. After subsequent lysate labelling for 2 h at room temperature, CuAAC-mediated appendage of TAMRA-fluorophore and SDS-PAGE, the labelling pattern was analyzed by fluorescence scanning. Figure modified and based on *Reinhardt et al.*[71] Nitroreductase pre-treated samples featured pronounced labelling intensities. Additionally, Coomassie staining was performed as loading control.

In collaboration with *Prof. Corinna R. Hess* and *Lukas Niederegger* the redox potential of **Hybrid 1** was determined using cyclic voltammetry (CV) measurements in aqueous conditions. In CV, the potential of a working electrode, that is measured in relation to a reference electrode, is increased and subsequently decreased in a set potential range. The resulting current is measured and plotted against the potential of the working electrode leading to cyclic voltammograms with peak currents reached at the reduction potential of the analyte in solution in the forward scan and at the re-oxidation (if possible) of the analyte in the reverse scan. If the redox reaction is reversible, so-called redox couples in the CV trace are visible. For compounds with more complex redox reactions involving various electron-transfers and intermediates, the CV trace can feature various peaks depending on the set scan range of the potential of the working electrode.[344]

The first monitorable reductive event is determinative for the reduction potential needed to activate the nitroimidazole derivatives. For **Hybrid 1** the first reductive event was detected at a cathodic peak potential ($E_{p,c}$) of –340 mV_{NHE} (potential versus the normal hydrogen electrode, NHE, **Figure 61A**). To facilitate relative understanding of the redox potentials of **Hybrid 1** in aqueous solution, a panel of anaerobically active nitroimidazole antibiotics (Metronidazole), aerobically active nitro-bearing antibiotics (Nitrofural) and derivatives and precursors of **Hybrid 1** (nitroindolin-2-one, **ABP1**) were additionally tested (**Figure 61B**, **Figure 62**).

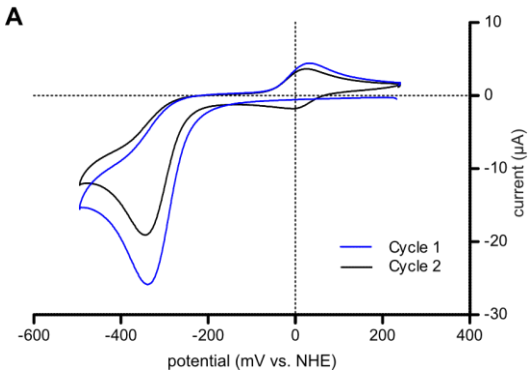

B

Compound	$E_{p,c}$ of first reduction (mV_{NHE})
Hybrid 1	–340
Metronidazole	–645
nitroindolin-2-one	–668
ABP1	–684
Nitrofural	–380

Figure 61: Redox potentials of various nitroaromatic derivatives. (**A**) Cyclic voltammogram showing the first reductive event of **Hybrid 1** at a cathodic peak potential ($E_{p,c}$) of –340 mV_{NHE} (potential versus normal hydrogen electrode, NHE). **Hybrid 1** is reduced in the first scan (blue trace) and the reduced species can be re-oxidized in the reverse, oxidative scan forming a new redox couple in the second cycle (black trace). (**B**) Cathodic peak potential ($E_{p,c}$) of the first reductive events of various nitroaromatic compounds for relative comparison and facilitating the attribution of the higher redox potential of **Hybrid 1** to the imidazolic nitro-group in conjugation with the π-system of the indolin-2-one scaffold (see main text and **Figure 62** for details). Figure modified and based on *Reinhardt et al*.[71]

Strikingly, the $E_{p,c}$ of the first reductive event of **Hybrid 1** is significantly higher than for aerobically inactive Metronidazole (–645 mV_{NHE}), but comparable to the aerobically active nitro-furan antibiotic Nitrofural (–380 mV_{NHE}). Studying the $E_{p,c}$ of the first reductive event

for nitroindoline-2-one and hybrid **ABP1** lacking the imidazolic nitro-group, the cause of the high peak potential of **Hybrid 1** could be associated with the imidazolic nitro-group being in conjugation with the indolin-2-one π-system. A higher reduction potential indicates a more readily proceeding reduction, i.e. a weaker reducing agent is needed and a rapid quenching (re-oxidation) of the reactive reduced species by oxygen in the so-called "futile-cycle" is diminished. In summary, the hybrid compounds feature, in addition to the direct topoisomerase IV inhibition, a second MoA involving the reductive activation as known for nitro-containing antibiotics, such as Metronidazole and Nitrofural. The high redox potentials of the hybrids represent an additional explanation for their activity in aerobic bacteria.

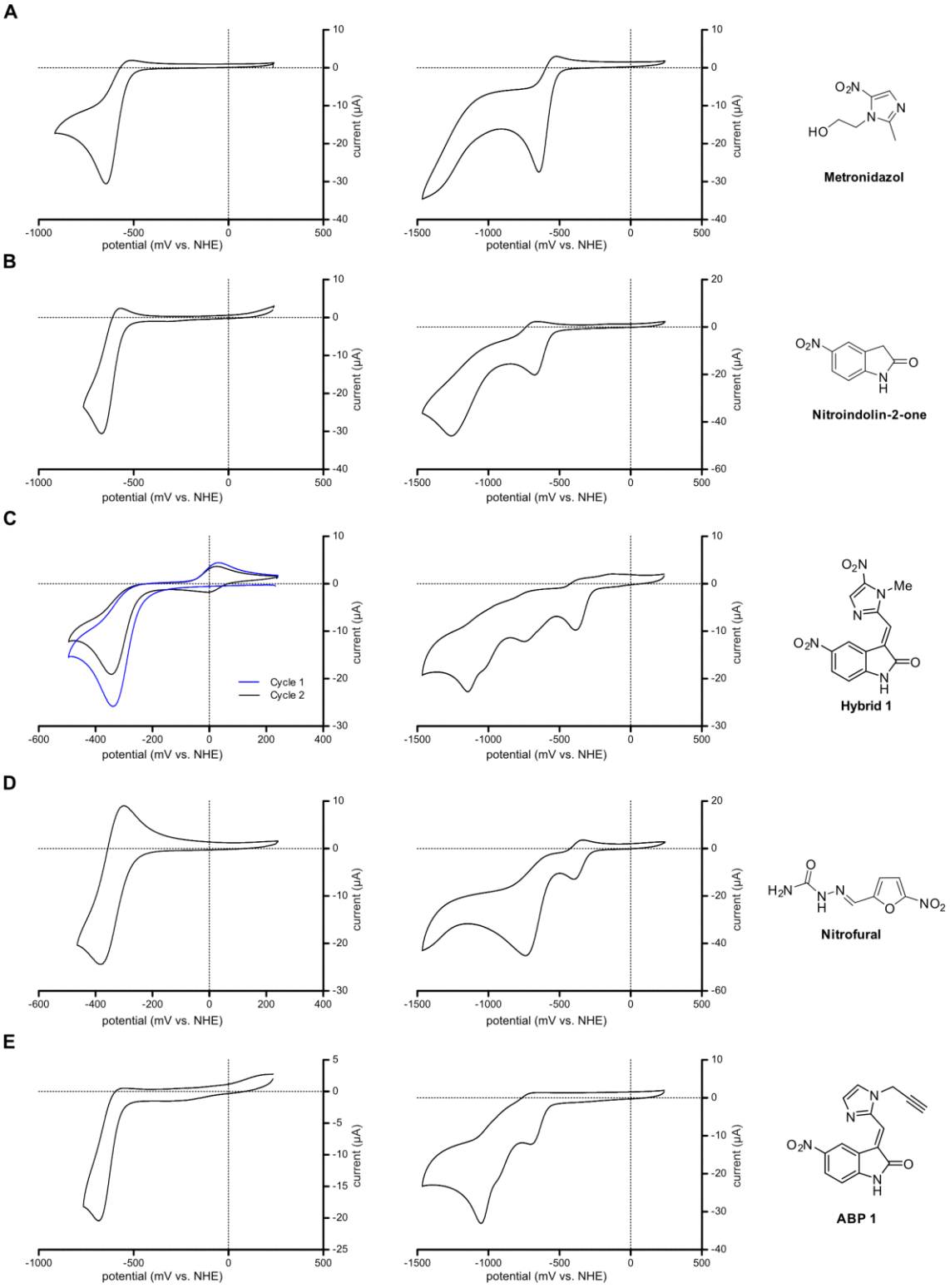

Figure 62: Cyclic voltammograms of various nitroaromatic compounds. On the **left** cyclic voltammetry (CV) scans limiting the potential cycle on the first reductive event of the compounds are shown. Their respective cathodic peak potential ($E_{p,c}$) of the first reductive event is listed in the table in **Figure 61B**. Additionally, the full CV scans from 300 mV_{NHE} to – 1500 mV_{NHE} are depicted on the **right**. In general, only the second scan cycle is depicted in black, except of for compounds were the formation of a novel redox couple after the first scan (blue trace) has been observed. Figure modified and based on *Reinhardt et al.*[71]

3.5 Resistance development and mammalian cytotoxicity

As discussed in the introduction (see page 5) development of bacterial resistances against antibiotics is a common issue and can arise *via* various mechanisms. Dual-targeting drugs have been proposed to be beneficial in this regards with delayed or yet undetected resistances, as more than one mutation or resistance pathway needs to be developed by the bacteria to render themselves insensitive against the antibiotic.[43–45] Therefore, the frequency of resistance formation of the **Hybrid 1** in *S. aureus* NCTC8325 was determined in comparison to the marketed topoisomerase-inhibiting antibiotic Ciprofloxacin. Importantly, the frequency of resistance development of Ciprofloxacin was approx. 50-times higher than for the **Hybrid 1**, indicating the benefit of the two fundamentally different MoAs (**Figure 63A**).

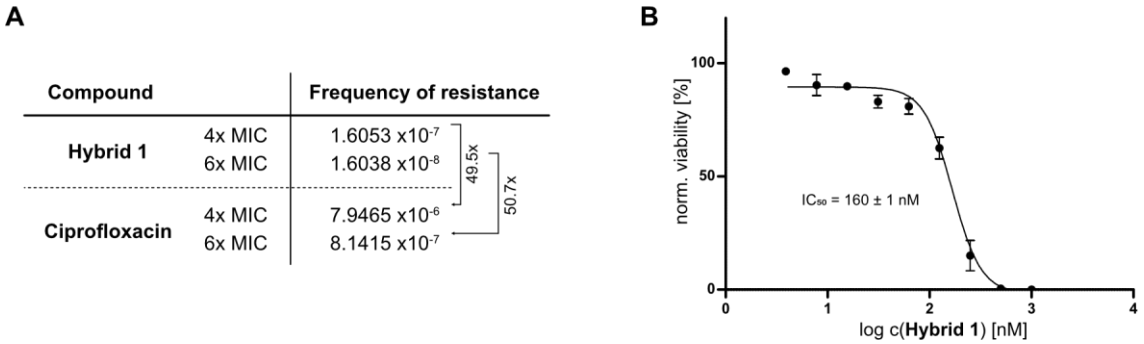

Figure 63: Resistance development and mammalian toxicity of **Hybrid 1**. (**A**) The frequency of resistance of **Hybrid 1** in *S. aureus* NCTC8325 is approx. 50-times lower than for the marketed topoisomerase inhibitor Ciprofloxacin. (**B**) MTT assay of **Hybrid 1** in human HeLa cells indicating strong toxicity (IC_{50} = 160 nM) based on read-out of metabolic activity. Figure modified and based on *Reinhardt et al*.[71]

On the other hand, nitro-group featuring compounds are often red-flags in drug discovery due to toxicities in mammalian cells that requires careful fine-tuning of molecular properties.[345] In the original publication of the indolin-2-one nitroimidazole molecules *Zhou et al*. stated low hemolytic rates of **Hybrid 1** suggesting favorable toxicity parameter. However, by performing MTT assays in human HeLa cells to infer the metabolic activity upon treatment with **Hybrid 1** as an indicator for cytotoxicity, a potent apparent IC_{50} of 160 nM of **Hybrid 1** was determined (**Figure 63B**). This is in accordance with the literature for nitroaromatic compounds with higher redox potentials, e.g. nitrofural and 2-nitroimidazoles, facilitating reduction also by mammalian cells and leading to cytotoxicity.[346]

In an effort to balance the antibiotic versus mammalian activity, a derivative lacking the indolin-2-one nitro-group was synthesized affording **Hybrid 3** (**Figure 64A**). Removal of the strongly electron-withdrawing nitro-group lowered the measured reductive peak

potential to – 410 mV_{NHE} and accordingly the mammalian cytotoxicity was improved to a half-maximal effective concentration EC_{50} of 12.1 µM (inferred IC_{50} approx. 18 µM, **Figure 64B-D**). **Hybrid 3** maintained a good antibiotic activity of 1.5 – 3.1 µM in *S. aureus* NCTC8325. Although not being an ideal therapeutic window yet, this proof-of-concept derivative indicated the potential for further optimization and the discovery of improved hybrid compounds.

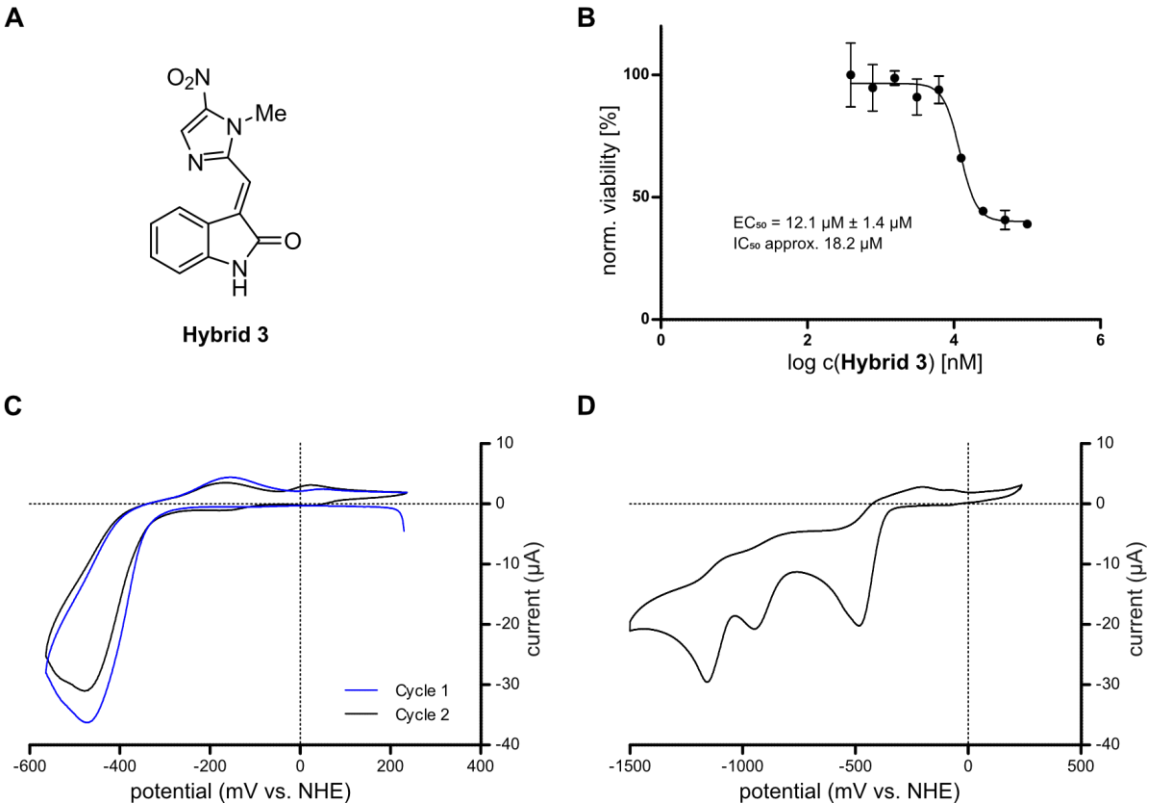

Figure 64: Improved derivative **Hybrid 3**. (**A**) Structure of **Hybrid 3** lacking the indoline-2-one nitro-group. (**B**) MTT assay of **Hybrid 3** in HeLa cells showing an improved toxicity profile with an EC_{50} of 12.1 ± 1.4 µM and an approx. IC_{50} of 18.2 µM. (**C**) Cyclic voltammetry (CV) scans limiting the potential cycle on the first reductive event of **Hybrid 3** with an cathodic peak potential ($E_{p,c}$) of –410 mV_{NHE} (potential versus normal hydrogen electrode, NHE) that is lower than the $E_{p,c}$ of **Hybrid 1**. The first scan (blue trace) and second scan (black trace) are depicted. (**D**) The full CV scans from 300 mV_{NHE} to – 1500 mV_{NHE} of **Hybrid 3**. Figure modified and based on *Reinhardt et al.*[71]

4. Summary and outlook

As discussed throughout this dissertation interdisciplinary and multidirectional efforts are needed to tackle the increasing bacterial resistance crisis. While in the first project the mechanistic understanding of adverse effects of marketed broad-spectrum fluoroquinolone antibiotics was pursued to lift limitations of this class in the future, here novel antibiotic compounds were in the center of the research focus. One promising strategy to discover potent novel small molecules is the application of drug-repurposing and polypharmacology,

combining bioactive moieties into one scaffold to discover new mode of actions, engage potentially novel targets or create molecules affecting multiple targets at once.[39,40,43–45] For example the conjugation of rifamycin and the nitroimidazole scaffold by *Ma et al.* lead to the discovery of a potent compound against anaerobic and microaerophilic bacteria.[347] *Zhou et al.* recently reported aerobically potent hybrids of nitroimidazoles and indolin-2-one moieties. In this project, mechanistic studies into those hybrids deciphered an unprecedented dual mode of action of topoisomerase IV inhibition and reductive bio-activation in pathogenic *S. aureus*. Using a chemo-proteomic target identification methodology employing hybrid-derived probes, the topoisomerase IV was identified as a direct target of the compounds independent of the typical reductive bio-activation of nitroimidazoles. This target was validated both by competition and *in vitro* activity experiments. Secondly, cyclic voltammetry measurements revealed significantly higher redox potentials of the hybrid compounds facilitating their reductive activation also in aerobic conditions. Further, it was demonstrated that this dual mode of action is highly advantageous in respect to low resistance development. On the downside, the higher redox potentials of the hybrid compounds also lead to increased toxicity in mammalian cells, however proof-of-concept studies demonstrated the possibility to develop fine-tuned compounds minimizing the adverse effects. Considering the increasing bacterial resistance crisis, these mechanistic investigations could support the discovery of novel nitroimidazole-containing antibiotics. Regarding this hybrid scaffold, future investigations of the topoisomerase IV binding mode could facilitate SAR studies and enable the rational design of evolved molecules maximizing target engagement with balanced redox properties to mitigate mammalian cytotoxicity.

IV – Materials and methods

1. Materials and methods of the fluoroquinolone project

1.1 General remarks

The fluoroquinolones (FQs) Ciprofloxacin (*Sigma-Aldrich, St. Louis, USA, Cat.# 17850*) and Levofloxacin (*Alfa Aesar, Haverhill, USA, Cat.# J66943*) stocks were prepared in sterile-filtered 0.1 N HCl to a maximum concentration of 50 mM. HCl was used as vehicle control. In the cell culture, the vehicle control did not exceed 0.1% (v/v) in any experiment.

1.2 Biochemistry experiments

1.2.1 Human cell culture

Cell culture experiments were performed in HEK293, A549 or PDL cells cultured in DMEM medium (*Sigma-Aldrich, St. Louis, USA, Cat.# D5671*) supplemented with 10% FCS (*Sigma-Aldrich, St. Louis, USA, Cat.# S0615*) and 2 mM glutamine (*Sigma-Aldrich, St. Louis, USA, Cat.# G7513*) in 5% CO_2 atmosphere at 37 °C in *Heracell 150i* incubators (*Thermo Fisher Scientific, Waltham, USA).* The periodontal ligament (PDL) cells were provided by *Prof. Denitsa Docheva*. During standard cell passaging *Accutase* (*Sigma-Aldrich, St. Louis, USA, Cat.# A6964*) was used for cell detachment. Cell dishes in various sizes (10 cm, 15 cm) and flasks (T75, T175) were used for cultivation (*Sarstedt, Nümbrecht, Germany, Cat.# 83.3902, 83.3903, 83.3911.002, 83.3912.002*). Sterile cell culture 6-well and 96-well plates were from *Thermo Fisher Scientific* (*Waltham, USA, Cat.# 130184, 130188*).

1.2.2 MTT assays

HEK or PDL cells (1,500 per well) were seeded into a 96-well plate and grown for 24 h. Subsequently, the medium was carefully removed by suction and 100 µL standard DMEM medium (10% FCS, 2 mM glutamine) with either vehicle control (1% (v/v), DMSO or sterile-filtered 0.1 N HCl) or a concentration range of the compounds (1% final DMSO or 0.1 N HCl concentration) was added. The cells were grown in presence of the compound and controls for 72 h and 20 µL thiazolyl blue tetrazolium bromide (MTT, 5 mg/mL in PBS, *Sigma-Aldrich, St. Louis, USA, Cat.# M2128*) were added and incubated for 2 h at 37 °C, 5% CO_2 to allow the MTT reagent to be metabolized. The medium was removed by suction and the formed formazan crystals dissolved in 200 µL DMSO. The read-out was performed

with an *Infinite M200 Pro* microplate reader (*Tecan, Männedorf, Switzerland*) at 570 nm and background was subtracted at 630 nm. The absorbance values were normalized to DMSO/ 0.1 N HCl controls and the apparent IC_{50} value inferred and plotted in *GraphPad Prism* (Version 5.03) by regression. As in many cases no complete metabolic inhibition in the concentration range of the compounds was detected, approximate apparent IC_{50} values are indicated (e.g. > 400 µM). The experiment was performed with triplicates per condition in at least two independent experiments for each compound.

1.2.3 FACS live/death cell assay

PDL cells were seeded into 6-well plates and grown for 24 h. The medium was removed and fresh prewarmed medium with compound or vehicle control in the respective concentration was added and the cells incubated for 24 h. Subsequently, the medium was again removed and fresh medium with compound/ vehicle control added for 24 h. This step was repeated after 48h of total compound inhibition and cells washed with PBS after a total compound incubation time of 72 h. As positive control, cells were treated with H_2O_2 (2 mM, 30 min, 37 °C). Cells were detached by *Accutase*, centrifuged (500 ×g, 5 min), the *Accutase*-containing medium removed and cells resuspended in fresh medium and stored on ice until further processing. The cells were washed with cold PBS (2 × 1 mL) and each sample resuspended in 200 µL Annexin V binding buffer (*BD Biosciences, Franklin Lakes, USA, Cat.# 556454*). Annexin V-FITC (1 µL, *BD Biosciences, Franklin Lakes, USA, Cat.# 556419*) and Sytox Red (0.2 µL, *Thermo Fisher Scientific Waltham, USA, Cat.# S34859*) was added and incubated for 15 min at room temperature in the dark. Subsequently, samples were stored on ice in the dark until FACS measurement (within 30 min). Directly before the measurement, the cells were filtered through a 35 µm strainer. Parameters of the FACS instrument (*FACSCanto, BD Biosciences, Franklin Lakes, USA*) were set as follows: FITC 350 V, PE 517 V, PerCP-Cy5-5 704 V, PE-Cy7 873 V, APC 380V. For each condition 200.000 cells were analyzed.

1.2.4 Bacterial Cultivation

Bacteria of safety category S1 were cultivated in *Innova 40* or *Innova 44* incubators (*New Brunswick Scientific, Edison, USA*).

Bacterial strains and media

Table 2: Bacterial strains and their appropriate cultivation media.

Species	Strain	Medium for cultivation
Staphylococcus aureus	NCTC8325	B
Escherichia coli	MM28	LB
	RFM795	LB

Table 3: Composition of the media used for the cultivation of bacteria.

Media	Composition
B	10.0 g peptone ex casein 5.00 g NaCl 5.00 g yeast extract in 1 L ddH2O, pH = 7.5
LB (lysogeny broth)	10.0 g peptone ex casein 5.00 g NaCl 5.00 g yeast extract 1.00 g K2HPO4 in 1 L ddH2O, pH = 7.5

Overnight cultures

Overnight cultures were prepared using 5 mL of the respective medium inoculated with 5 µL of the desired bacterial cryostock (1:1,000) in a culture tube (*VWR, Radnor, USA, Cat.# 60818-725*). The culture was incubated overnight (routinely 16 h) by shaking at 200 rpm at 37 °C. All overnight cultures were prepared freshly to avoid genetic variation. A sterile control was added each time (medium without bacteria).

Cryostocks

5 mL of an overnight culture of the desired bacteria were harvested by centrifugation (6,000 ×g, 10 min, 4 °C) and the supernatant was removed. The bacteria pellet was resuspended in 750 µL of fresh sterile medium. Sterile glycerol was added to reach a final concentration of 50%. The stock was mixed and stored at –80 °C in cryotubes (*Sarstedt, Nümbrecht, Germany, Cat.# 72.377.007*).

1.2.5 Minimal inhibitory concentrations (MIC) assay

MIC were determined with the broth dilution method. The overnight culture was diluted 1:10,000 in fresh medium and 99 µL aliquots were added to 96-well plates containing various concentrations of compounds (1 µL, 100× in DMSO or 0.1 N HCl) and the respective vehicle control (1 µL) as negative control in triplicates. After 20 h incubation at 200 rpm at 37 °C, the turbidity of the wells was analyzed.

1.2.6 Topoisomerase IV decatenation assay

The assay was performed as described before.[71] Briefly, *S. aureus* topoisomerase IV decatenation assay kit was purchased from *Inspiralis (Norwich, UK, Cat.# SAD4001*) and conducted according to manufacturer conditions. Briefly, 1 U *S. aureus* topoisomerase IV was used to decatenate 200 ng kDNA by incubating in presence of controls or compound in provided assay buffer (10 mM Tris pH 7.5, 1 mM $MgCl_2$, 1 mM DTT, 0.3 mM ATP, 70 mM potassium glutamate, 0.01 mg/mL albumin) in 30 µL total volume for 30 min at 37 °C. The reactions were stopped by addition of 2.25 µL EDTA (250 mM) and mixed with appropriate amounts of agarose loading buffer. 10 µL aliquots were separated on a 0.8% agarose gel at 80 V for 1 h. Since an intercalator (*Gel-Red, Biotium, Fremont, USA, Cat.# B-41003*) was present for visualization, decatenated products resolved in open circular and relaxed forms.

1.3 Proteomics experiments

For MS sample preparation solvents of LC-MS or HPLC-MS grade from various suppliers were used. Including *VWR* (*Radnor, USA*), *Merck* (*Darmstadt, Germany*) and *Thermo Fisher Scientific* (*Waltham, USA*).

1.3.1 Whole proteome analyses

Cell treatment and lysis

The respective cells were seeded into 10 cm dishes and incubated for 24 h at standard cell culture conditions (5% CO_2 atmosphere, 37 °C). The cells were treated with compound for the desired time in replicates per condition depending on the experiment as indicated in **Table 4**. For the whole proteome analysis of Ciprofloxacin-treated HEK293 cells over 14 days, the cells were passaged every 3 days using fresh medium and compound. For

experiments monitoring the FQ treatment in-depth after 3 days, fresh medium with compound was applied every 24 h to simulate daily drug application.

Table 4: Treatment conditions of human cell lines for the different whole proteome analyses.

Experiment	Compound	Concentration	Incubation times	Replicates per condition
FQ Proteome Analysis in HEK293	Ciprofloxacin	7.5 µM	3 h 3 days 7 days 14 days	3
		75 µM	3 h 3 days 7 days 14 days	
	0.1 N HCl vehicle control	Same volume	14 days	
FQ Proteome Analysis in PDL	Ciprofloxacin	7.5 µM	3 days	4
		75 µM		
	Levofloxacin	7.5 µM		
		75 µM		
	0.1 N HCl vehicle control	Same volume		
Onc201 Proteome Analysis in HEK293	Onc201	1 µM	24 h	4
	DMSO vehicle control	Same volume		
FQ Proteome Analysis in ClpP KO HEK293	Ciprofloxacin in wild-type HEK293	75 µM	3 days	4
	Ciprofloxacin in ClpP KO HEK293	75 µM		
	0.1 N HCl vehicle control in wild-type HEK293	Same volume		
	0.1 N HCl vehicle control in ClpP KO HEK293	Same volume		

Cells were lysed at the respective time-points by removing the medium from the plates, washing the cells with cold PBS once and addition of 300 µL pre-cooled lysis buffer (50 mM Tris pH 7.5, 150 mM NaCl, 1% (v/v) NP40, 0.1% (w/v) sodium deoxycholate, 1 mM EDTA) supplemented with 1 tablet of protease inhibitor (*cOmplete Mini EDTA-free, Roche, Basel, Switzerland, Cat.# 04693159001*) per 10 mL lysis buffer directly into the dishes. After incubation on ice for 15 min, the lysate was collected, snap-frozen and stored at –80 °C until further processing. The lysate was cleared by centrifugation (12,000 ×g, 15 min, 4 °C), the total protein concentration measured using *RotiQuant universal* bicinchoninic acid assay (BCA) assay (*Carl Roth, Karlsruhe, Germany, Cat.# 0120.*1) with BSA (*Sigma-Aldrich, St. Louis, USA, Cat.# P5619*) calibration curve according to manufacturer instructions. Equal protein amounts per sample (typically 100-300 µg) were precipitated using 4× excess volume of cold acetone (–20 °C) overnight at –80 °C. The precipitated proteins were pelletized (12,000 ×g, 10 min, 4 °C), and the supernatant was disposed. The proteins were washed three times with 1 mL cold methanol (–80 °C). Resuspension was achieved by

sonication (10 s, 10% intensity, pulse 5) using a *Bandelin SONOPULS* equipped with *Bandelin UW2070* and *MS73* lance (*Bandelin electronic, Berlin Germany*) and the proteins were pelletized *via* centrifugation (12,000 ×g, 20 min, 4 °C). The protein pellet was resuspended in UA buffer (100 µL, 8 M urea in 100 mM Tris pH 8.5) and subjected to the filter aided sample preparation (FASP protocol).[348] Briefly, 30 kDa cut-off *Micron* centrifugal filters (*Merck, Darmstadt, Germany, Cat.# Millipore MRCFC0R030*) were washed once with NaOH (0.05 N, 500 µL) by centrifugation (12,000 ×g, 15 min, r.t.) and subsequently equilibrated with 500 µL UA buffer. The dissolved protein pellets were reduced with 1 mM DTT (1 µL of 100 mM DTT in H_2O to 100 µL sample) for 1 h at 37 °C, 500 rpm in thermoshaker and applied to the filters. After centrifugation (12,000 ×g, 15 min, r.t.), the samples on the filters were washed with 200 µL UA buffer, centrifuged (12,000 ×g, 15 min, r.t.) and the flow-through discarded. Alkylation was performed by addition of 100 µL IAA solution (0.05 M iodoacetamide in UA buffer) per filter and incubation for 20 min at r.t. without mixing. The filter units were centrifuged (12,000 ×g, 15 min, r.t.), washed twice with 100 µL UA buffer (12,000 ×g, 15 min, r.t., each) and subsequently twice with 100 µL ABC buffer (0.05 M NH_4HCO_3 in H_2O). Trypsin (enzyme to protein amount ratio 1:100) in 40 µL ABC buffer was added to the filters and protein digest performed in a wet chamber at 37 °C, 200 rpm over for 16 h. The filter units were transferred into new 1.5 mL low-bind Eppendorf tubes and centrifuged (12,000 ×g, 10 min, r.t.). The samples were acidified with formic acid to pH < 6 and desalted by stage-tipping. Stage-tips were prepared with two *Empore Supelco* C18 discs (*Merck, Darmstadt, Germany, Cat.# 66883-U*) and washed once with 50 µL of MeOH, once with 200 µL of 80% (v/v) acetonitrile and 0.5% (v/v) FA in H_2O and once with 200 µL of 0.5% (v/v) FA in H_2O by centrifugation (1-2 min, 500 ×g) without running the stage-tips dry. The samples were loaded on the tips and washed twice with 200 µL of 0.5% (v/v) FA in H_2O by centrifugation (1-2 min, 500 ×g) without running the stage-tips dry. Desalted peptides were eluted consecutively by 60 µL and 30 µL of 80% (v/v) acetonitrile and 0.5% (v/v) FA in H_2O. The eluates were lyophilized and for MS measurement the samples were dissolved in 1% (v/v) FA in H_2O by pipetting up and down, vortexing and sonication for 2× 5 min (brief centrifugation after each step). *Millipore* centrifugal filter units (*Durapore PVDT 0.22 µm, Merck, Darmstadt, Germany, Cat.# UFC30GVNB*) were equilibrated with 300 µL 1% FA (13,000 ×g, 2 min, room temperature) and samples were filtered through the equilibrated filters (centrifugation: 13,000 ×g, 1 min, room temperature). The samples were subjected to LC-MS/MS measurement (**1.3.4**).

1.3.2 Affinity-based protein profiling (AfBPP)

Analytical gel-based AfBPP

Analytical gel-based AfBPP was performed as described before with modifications for human cell lines.[71] Respective cells were seeded into 6-well plates and grown until 80-90% confluency. The cells were washed with pre-warmed sterile PBS (1 mL), 1 µL probe (1:100 stock in DMSO) or DMSO as vehicle control in 1 mL DMEM medium (without FCS, except in +/- FCS comparison experiment) added and the cells incubated in standard conditions (5% CO_2 atmosphere, 37 °C) for 1 h. None-UV-irradiation controls were lysed at this point by medium removal, washing of the cells with pre-cooled PBS (1 mL) and addition of 100 µL pre-cooled lysis buffer (50 mM Tris pH 7.5, 150 mM NaCl, 1% (v/v) NP40, 0.1% (w/v) sodium deoxycholate, 1 mM EDTA) supplemented with 1 tablet of protease inhibitor (*cOmplete Mini EDTA-free, Roche, Basel, Switzerland, Cat.# 04693159001*) per 10 mL lysis buffer directly into the dishes and incubation on ice for 15 min. Subsequently, all other samples were irradiated on cool packs at 365 nm for **P1** probes (*TL-D BLB 18 W, Philips, Amsterdam, The Netherlands*) or 300 nm for **P2** probes (*LZC-UVB 8 W, Luzchem, Ottawa, Canada*) for 10 min. Lysis was performed as before for non-irradiated controls. The lysate was cleared by centrifugation (12,000 ×g, 15 min, 4 °C), the total protein concentration measured using *RotiQuant universal* bicinchoninic acid assay (BCA) assay (*Carl Roth, Karlsruhe, Germany, Cat.# 0120.*1) with BSA (*Sigma-Aldrich, St. Louis, USA, Cat.# P5619*) calibration curve according to manufacturer instructions. Equal protein amounts per sample (typically 100-300 µg) were adjusted to 90 µL and 8 µL CuAAC master mix (1 µL TAMRA-azide (10 mM in DMSO, *Baseclick, Neuried, Germany, Cat.# BCFA-008-10*), 5 µL BTTAA (10 mM in H_2O, *Jena Bioscience, Jena, Germany, CLK-067*), 2 µL $CuSO_4$ (50 mM in H_2O)) added. The click reaction was started by addition of 2 µL sodium ascorbate (100 mM in H_2O) and the reaction incubated in the dark for 1 h. Subsequently, the reaction was stopped by precipitation of the proteins by 500 µL cold acetone (–20 °C, MS grade) for 2 h to overnight at –20 °C. The precipitated proteins were pelletized (12,000 ×g, 10 min, 4 °C), and the supernatant was disposed. The proteins were resuspended in 100 µL PBS and 100 µL 2× SDS loading buffer and the samples heated to 95 °C for 10 min. After SDS-PAGE (7.5% gel) applying 40 µL of each sample, utilizing *BenchMark* fluorescent protein standard marker (*Invitrogen, Thermo Fisher Scientific, Waltham, USA, Cat.# LC5928*) and *Roti-Mark* standard protein marker (*Carl Roth, Karlsruhe, Germany, Cat.# T851.1*) or *PeqGold* protein marker I (*VWR, Radnor, USA, Cat.# 27-1010 I*), fluorescent bands were visualized by a *Las-3000* fluorescence darkbox (*Fujifilm, Minato,*

Japan) with a *Fujinon* VRF 43LMD Lens, 605DF40 filter and 520 nm EPI excitation wavelength. Subsequently, total protein bands were visualized by Coomassie staining as loading controls.

Preparative MS-based AfBPP

Preparative MS-based AfBPP was performed as described before with modifications for human cell lines.[71] Respective cells were seeded into 15 cm dishes and grown until 80-90% confluency. The cells were washed with pre-warmed sterile PBS (10 mL), 10 µL probe (1:100 stock in DMSO) or DMSO as vehicle control in 10 mL pre-warmed DMEM medium (without FCS) added and the cells incubated in standard conditions (5% CO_2 atmosphere, 37 °C) for 1 h. Dishes were irradiated on cool packs at 365 nm for **P1** probes (*TL-D BLB 18 W, Philips, Amsterdam, The Netherlands*) or 300 nm for **P2** probes (*LZC-UVB 8 W, Luzchem, Ottawa, Canada*) for 10 min and the medium removed subsequently. The cells were washed with 10 mL pre-cooled PBS and lysis was performed by addition of 1 mL pre-cooled lysis buffer (50 mM Tris pH 7.5, 150 mM NaCl, 1% (v/v) NP40, 0.1% (w/v) sodium deoxycholate, 1 mM EDTA) supplemented with 1 tablet of protease inhibitor (*cOmplete Mini EDTA-free, Roche, Basel, Switzerland, Cat.# 04693159001*) per 10 mL lysis buffer directly into the dishes and incubation on ice for 15 min. The lysate was transferred into 1.5 mL Eppendorf tubes and optionally snap-frozen and stored at –80 °C until further processing. The lysate was cleared by centrifugation (12,000 ×g, 15 min, 4 °C), the total protein concentration measured using *RotiQuant universal* bicinchoninic acid assay (BCA) assay (*Carl Roth, Karlsruhe, Germany, Cat.# 0120.*1) with BSA (*Sigma-Aldrich, St. Louis, USA, Cat.# P5619*) calibration curve according to manufacturer instructions and samples adjusted to 430 µL (0.5 mg/mL protein concentration). Subsequently, 10 µL 10% (w/w) SDS in PBS (c_{final} = 0.4%) and 40 µL CuAAC master mix (5 µL Biotin-PEG3-N3 (10 mM in DMSO, *Sigma-Aldrich, St. Louis, USA, Cat.# 76024*), 25 µL BTTAA (10 mM in H_2O, *Jena Bioscience, Jena, Germany, CLK-067*), 10 µL $CuSO_4$ (50 mM in H_2O)) was added, the click reaction started by addition of 10 µL sodium ascorbate (100 mM in H_2O) and incubated in the dark for 1 h. Proteins were precipitated by addition of 4× excess volume (2 mL) cold acetone (–20 °C) and incubation overnight at –20 °C. The precipitated proteins were pelletized (16,900 ×g, 15 min, 4 °C), and the supernatant was disposed. The Protein pellet was washed two times with 1 mL cold methanol (–80 °C). Resuspension was achieved by sonication (10 s, 10% intensity, pulse 5) using a *Bandelin SONOPULS* equipped with

Bandelin UW2070 and *MS73* lance (*Bandelin electronic, Berlin Germany*) and proteins were pelletized *via* centrifugation (10,000 ×g, 10 min, 4 °C). After the washing steps the supernatant was disposed and the pellet resuspended in 500 µL 0.4% (w/v) SDS in PBS at room temperature by sonication (10 s, 10% intensity). 50 µL avidin-agarose beads (*Sigma-Aldrich, St. Louis, USA, Cat.# A9207*) per sample were prepared by washing three times with 1 mL 0.4% (w/v) SDS in PBS. All centrifugation steps were conducted at 400 ×g for 3 min at room temperature. The 50 µL washed avidin-agarose beads were added to each sample and incubated under continuous inverting (1 h, room temperature). Beads were washed three times with 1 mL 0.4% (w/v) SDS in PBS, two times with 6 M urea in ddH_2O and three times with 1 mL PBS. The beads were resuspended in 200 µL denaturation buffer (7 M urea, 2 M thiourea in 20 mM pH 7.5 HEPES buffer). For reduction, Tris(2-carboxyethyl)phosphine (TCEP, 500 mM, 2 µL, *Alfa Aesar, Haverhill, USA, Cat.# J60316*) was added, the tubes were mixed by vortexing shortly and incubated in a thermoshaker (600 rpm, 1 h, room temperature). Then 2-iodoacetamide (IAA, 500 mM, 4 µL, *Sigma-Aldrich, St. Louis, USA, Cat.# I6125*) was added for alkylation, the tubes were mixed by vortexing shortly and incubated in a thermoshaker (600 rpm, 30 min, room temperature, in the dark). Remaining IAA was quenched by the addition of dithiothreitol (DTT, 500 mM, 4 µL, *Sigma-Aldrich, St. Louis, USA, Cat.# 43819*). The tubes were shortly mixed by vortexing and incubated in a thermoshaker (600 rpm, 30 min, room temperature). LysC (0.5 µg/µL, *Fujifilm Wako Pure Chemicals, Minato, Japan, Cat.# 125-05061*) was thawed on ice and 1 µL was added to each microcentrifuge tube, the tubes were shortly mixed by vortexing and incubated in a thermoshaker (600 rpm, 2 h, room temperature, in the dark). Triethylammonium bicarbonate (TEAB) solution (600 µL, 50 mM in water) and then trypsin (1.5 µL, 0.5 µg/µL in 50 mM acetic acid, *Promega, Madison, USA, Cat.# VC551C*) were added to each tube with a short vortexing step after each addition. The microcentrifuge tubes were incubated in a thermoshaker (600 rpm, 16 h, 37 °C). The digest was stopped by adding 10 µL formic acid (FA) and vortexing followed by centrifugation (12,000 ×g, 3 min, room temperature). 50 mg *SepPak* C18 columns (*Waters, Milford, USA, Cat.# WAT054960*) were equilibrated by gravity flow two times with 1 mL acetonitrile and three times with 1 mL aqueous 0.1% trifluoroacetic acid (TFA) solution. Subsequently, the samples were loaded by gravity flow, washed three times with 1 mL aqueous 0.1% TFA solution and once with 0.5 mL aqueous 0.5% formic acid (FA) solution. Elution of peptides into new 2.0 mL Protein LoBind *Eppendorf* tubes was performed by two times addition of 250 µL elution buffer (80% acetonitrile, 0.5% FA) by gravity flow followed by 250 µL elution buffer by vacuum flow

until all liquid was eluted from the column. The eluates were lyophilized. Before MS measurement the samples were dissolved in 30 µL 1% FA by pipetting up and down, vortexing and sonication for 15 min (brief centrifugation after each step). *Millipore* centrifugal filter units (*Durapore PVDT 0.22 µm, Merck, Darmstadt, Germany, Cat.# UFC30GVNB*) were equilibrated with 300 µL 1% FA (13,000 g, 2 min, room temperature) and samples were filtered through the equilibrated filters (centrifugation: 12,000 ×g, 1 min, room temperature).

1.3.3 Thermal protein profiling (TPP)

The experiment was performed similar to TPP-TR experiments described by Franken et al. with minor modifications.[87] HEK293 cells were grown in 8 T175 flasks to approx. 80-90% confluency. Per replicate two T175 flask were treated with Ciprofloxacin (75 µM, 1 h, 37 °C) and two T175 flask with the same volume of 0.1 N HCl as vehicle control. Per condition two replicates were used, leading to a total of 8 T175 flasks. The cells were washed with PBS, detached with Accutase, the two flask per replicate condition combined and the cells pelletized (500 ×g, 3 min, r.t.). The medium was removed and each pellet (Cipro #1, Cipro #2, Ctrl. #1, Ctrl #2) washed twice with cold PBS. Each pellet was resuspended in 1.2 mL cold PBS supplemented with either 75 µM Ciprofloxacin or the same volume of 0.1 N HCl, depending on the sample. The cell suspension of each sample was distributed into 10 PCR tubes (100 µL per tube), resulting in 10 stripes á 4 tubes (2×2 conditions, 10 temperature points). The PCR tubes were subjected to the temperature gradient using a PCR cycler. Due to temperature gradient limitations, two separate programs had to be run to cover the desired temperature range (see **Table 5**). The PCR tubes were heat-treated according to the two programs for 3 min and directly snap frozen in liquid nitrogen. The samples were stored at −80 °C until further processing.

Table 5: PCR cycle program for heat-treatment of TPP samples.

Program 1 T = 43.5 °C Gradient = 13.5 °C	Position	1	5	8	11		
	Temp. [°C]	37.2	41.2	45.6	49.3		
Program 2 T = 60 °C Gradient = 17 °C	Position	1	3	5	7	9	12
	Temp. [°C]	52.6	54.5	57.8	60.9	64.1	67.5

The cells were thawed in a heating block set to 25 °C and directly snap-frozen again. This freeze-thaw cycle was repeated twice. 110 µL of the samples were transferred into ultracentrifugation tubes (*Beckman Coulter, Brea, USA*) and the original PCR tubes rinsed with 50 µL PBS and also transferred to the ultracentrifugation tubes. The samples were ultra-centrifuged (100,000 ×g, 20 min, 4 °C, *Beckman Coulter, Brea, USA*) and 100 µL of each supernatant transferred to low-bind Eppendorf tubes. Of the first two lowest concentrations additional 10 µL of supernatant were taken for protein quantification using *RotiQuant universal* bicinchoninic acid assay (BCA) assay (*Carl Roth, Karlsruhe, Germany, Cat.# 0120.*1) with BSA (*Sigma-Aldrich, St. Louis, USA, Cat.# P5619*) calibration curve according to manufacturer instructions. The average of the two temperature conditions was taken to adjust each sample accordingly to 60 µg total protein and precipitation was performed by addition of 4× excess of cold acetone and incubation at −20 °C overnight. The proteins were pelletized by centrifugation (21,000 ×g, 20 min, 4 °C) and washed once with 500 µL cold methanol (21,000 ×g, 20 min, 4 °C). The proteins were resuspended in 200 µL buffer X (7 M urea, 2 M thiourea in 20 mM HEPES pH 7.5) and 0.4 µL DTT (500 mM in H_2O) added and incubated for 45 min at room temperature in a thermoshaker (1000 rpm). Subsequently, alkylation was performed by addition of 2 µL iodoacetamide (IAA, 550 mM in 50 mM TEAB buffer) and the samples incubated at room temperature, 1000 rpm for 30 min. The alkylation was quenched by addition of 1.6 µL DTT (500 mM in H_2O) and incubation for 30 min at room temperature in a thermoshaker (1000 rpm). Proteins were pre-digested with 1 µL LysC (0.5 µg/µL, *Fujifilm Wako Pure Chemicals, Minato, Japan, Cat.# 125-05061*) for 2 h at room temperature (450 rpm). Subsequently, 600 µL of 50 mM TEAB buffer was added and 1.5 µL trypsin (0.5 µg/µL in 50 mM acetic acid, *Promega, Madison, USA, Cat.# VC551C*) added and incubated at 37 °C, 1000 rpm for 16 h. The digest was stopped by adding 8 µL formic acid (FA) and vortexing followed by centrifugation (12,000 ×g, 3 min, room temperature). 50 mg *SepPak* C18 columns (*Waters, Milford, USA, Cat.# WAT054960*) were equilibrated by gravity flow two times with 1 mL acetonitrile and three times with 1 mL aqueous 0.1% trifluoroacetic acid (TFA) solution. Subsequently, the samples were loaded by gravity flow, washed three times with 1 mL aqueous 0.1% TFA solution and once with 0.5 mL aqueous 0.5% formic acid (FA) solution. Elution of peptides into new 1.5 mL Protein LoBind *Eppendorf* tubes was performed by two times addition of 200 µL elution buffer (80% acetonitrile, 0.5% FA) by gravity flow followed by 200 µL elution buffer by vacuum flow until all liquid was eluted from the column. The eluates were concentrated to dryness in a SpeedVac (*Concentrator plus, Eppendorf, Hamburg, Germany*). The peptides were

reconstituted in 7.5 µL TMT labeling buffer (50 mM HEPES, 20% acetonitrile, pH 8.5) in a sonication bath (*VWR, Radnor, USA*) for 2× 5 min. After brief centrifugation, 5 µL of each aliquoted TMT10plex label (= 50 µg, *Thermo Fisher Scientific, Waltham, USA,* Cat.# *90110*) was added to the respective samples (labelling each temperature point with one individual TMT channel). And incubated for 1h at room temperature (400 rpm). The labeling reaction was quenched by addition of 1 µL hydroxylamine solution (5% (v/v) in H_2O) and 188.5 µL 0.1% (v/v) FA was added. 1 µL of each temperature point was combined and desalted *via* stage tipping to perform a test LC-MS/MS measurement to analyze TMT-labeling efficiency.

The rest of the samples were stored at − 80 °C until further processing. All 10 temperature-point samples of one replicate and compound-condition were pooled (resulting in 4 samples again: Cipro #1, Cipro #2, Ctrl. #1, Ctrl. #2) and concentrated to dryness in a SpeedVac (*Concentrator plus, Eppendorf, Hamburg, Germany*). After reconstitution in 500 µL 0.5% (v/v) FA, the samples were desalted using the 50 mg *SepPak* C18 columns (*Waters, Milford, USA, Cat.# WAT054960*) as described above. After concentration to dryness, the samples were reconstituted in 110 µL HILIC buffer A (95% (v/v) acetonitrile, 5% (v/v) H_2O, 0.1% (v/v) FA) and sonicated (10 s, 10% intensity, pulse 5) using a *Bandelin SONOPULS* equipped with *Bandelin UW2070* and *MS73* lance (*Bandelin electronic, Berlin Germany*). After centrifugation (21,000 ×g, 10 min, 4 °C) 105 µL were transferred into a HPLC vial and 100 µL of each of the 4 samples was separately offline-fractionated using a HILIC column (YMC-Pack PVA-Sil column, 5 µm, 150 x 2.1 mm, 120 Å, YMC Europe GmbH, Dinslaken, Germany) equipped to an *Ultimate 3000* HPLC system (*Dionex, Sunnyvale, USA*) using buffer A (95% MeCN, 5% H2O, 0.1% TFA) and buffer B (95% H2O, 5% MeCN, 0.1% TFA) in following gradient at a flow rate of 0.2 mL/min: 7.5 min 0% buffer B, 50 min to 30% buffer B, 3.5 min to 50% buffer B, 2.5 min to 100% buffer B, total gradient length 62.5 min. The fractions were pooled into 10 samples per replicate and condition (resulting in 4× 10 samples) and concentrated to dryness. After reconstitution in 30 µL 0.1% (v/v) FA, vortexing, sonication for 2× 5 min (brief centrifugation after each step) and filtering through *Millipore* centrifugal filter units (*Durapore PVDT 0.22 µm, Merck, Darmstadt, Germany, Cat.# UFC30GVNB*) equilibrated with 300 µL 1% FA (12,000 ×g, 2 min, room temperature), the samples were subjected to LC-MS/MS measurement.

1.3.4 LC-MS/MS measurement

Samples were measured either on a Orbitrap Q Exactive Plus (*Thermo Fisher Scientific, Waltham, USA*), LTQ Orbitrap Fusion (*Thermo Fisher Scientific, Waltham, USA*) or a Tims-TOF Pro (*Bruker, Billerica, USA*) instrument (see **Table 6**).

Table 6: LC-MS/MS instrument usage in proteomic experiments.

Experiment	Experiment type	Instrument
FQ Proteome Analysis in HEK293	Whole proteome analysis	Q Exactive Plus
FQ Proteome Analysis in PDL	Whole proteome analysis	TimsTOF Pro
FQ AfBPP in HEK293	Affinity-based protein profiling	Q Exactive Plus
FQ AfBPP in A549	Affinity-based protein profiling	Q Exactive Plus
FQ AfBPP in PDL	Affinity-based protein profiling	TimsTOF Pro
FQ TPP in HEK293	Thermal protein profiling	Orbitrap Fusion
Onc201 Proteome Analysis in HEK293	Whole proteome analysis	Orbitrap Fusion
FQ Proteome Analysis in ClpP KO HEK293	Whole proteome analysis	Orbitrap Fusion

LC-MS/MS method Q Exactive Plus

Samples were analyzed with an *UltiMate 3000 nano* HPLC system (*Dionex, Sunnyvale, USA*) using *Acclaim C18 PepMap100* 75µm ID x 2 cm trap and *Acclaim PepMap RSLC C18* (75 µm ID x 50 cm) separation columns (*Thermo Fisher Scientific, Waltham, USA*) in an EASY-spray setting coupled to a *Exactive Plus* (*Thermo Fisher Scientific, Waltham, USA*). Peptide samples were loaded on the trap column and washed with 0.1% TFA, then transferred to the separation column (buffer A: H2O with 0.1% FA, buffer B: MeCN with 0.1% FA, flow 0.3 µL/min, gradient: to 5% buffer B in 7 min, from 5% to 22% buffer B in 105 min, then to 32% buffer B in 10 min, to 90% buffer B in 10 min and hold at 90% buffer B for 10 min, then to 5% buffer B in 0.1min and hold 5% buffer B for 9.9 min) and ionized at spray voltage of 2.0 kV and a capillary temperature of 275°C. The *Q Exactive Plus* was operated in a TOP12 data dependent mode with full scan acquisition in the orbitrap at a resolution of R = 140,000 and an AGC target of $3e^6$ in a scan range of 300-1500 m/z with a maximum injection time of 80 ms. Monoisotopic precursor selection as well as dynamic exclusion (dynamic exclusion duration: 60 s) was enabled. Precursors with charge states >1 and intensities greater than $1e^4$ were selected for fragmentation. Isolation was performed in the quadrupole using a window of 1.6 m/z. Precursors were analyzed in a scan range of 200–2000 m/z to an AGC target of $1e^5$ and a maximum injection time of 100 ms. Peptide fragments were generated by higher-energy collisional dissociation (HCD) with a normalized collision energy of 27% and detected in the orbitrap.

LC-MS/MS method LTQ Orbitrap Fusion for whole proteome analysis

Samples were analyzed *via* HPLC-MS/MS using an *UltiMate 3000 nano* HPLC system (*Dionex, Sunnyvale, USA*) equipped with an *Acclaim* C18 PepMap100 75 µm ID x 2 cm trap and an *Acclaim* C18 PepMap RSLC, 75 µM ID x 15 cm separation columns (*Thermo Fisher Scientific, Waltham, USA*) coupled to a *LTQ Orbitrap Fusion* (*Thermo Fisher Scientific, Waltham, USA*). Samples were loaded on the trap and washed for 10 min with 0.1% FA (at 5 µL/min), then transferred to the separation column and separated using a, 112 min gradient from 4% to 35% MeCN followed by 4 min at 80% MeCN in 0.1% FA (at 200 nL/min flow rate). The *LTQ Orbitrap Fusion* was operated in a 3 second top speed data dependent mode. The full scan acquisition was performed in the orbitrap at a resolution of 120,000 and an ion target of $4e^5$ in a scan range of 300 –1700 m/z. The monoisotopic precursor selection as well as the dynamic exclusion for 60 sec were enabled. Precursors with charge states of 2–7 and intensities greater than $5e^3$ were selected for fragmentation. Isolation was performed in the quadrupole using a window of 1.6 m/z. Precursors were collected to a target of $1e^2$ for a maximum injection time of 250 ms with "inject ions for all available parallelizable time" enabled. Fragments were generated using higher-energy collisional dissociation (HCD) and detected in the ion trap at a rapid scan rate. Internal calibration was performed using the ion signal of fluoranthene cations (EASY-ETD/IC source).

LC-MS/MS method LTQ Orbitrap Fusion for thermal protein profiling (TPP)

TMT-labelled peptide of the TPP samples were analyzed on an *UltiMate 3000* nano HPLC system (*Dionex, Sunnyvale, USA*) equipped with an *Acclaim C18 PepMap100* (75 µm ID × 2 cm) trap column (*Thermo Fisher Scientific, Waltham, USA*) and an *Aurora* (25 cm × 75 µm ID, 1.6 µm FSC C18, *IonOpticks, Fitzroy, Australia*) separation column in a column oven (*Sonation, Biberach, Germany*) heated to 40 °C coupled to an *Orbitrap Fusion* (*Thermo Fisher Scientific, Waltham, USA*) in EASY-spray setting. Samples were loaded on the trap column and washed for 10 min with 0.1% (v/v) TFA in H_2O at a flow rate of 5 µL/min. Subsequently, peptides were transferred to the separation column and online separated using a 120 min gradient (Buffer A: H_2O + 0.1% (v/v) FA; Buffer B: Acetonitrile + 0.1% (v/v) FA) with a flow rate of 300 nL/min. The gradient was as follows: in 10 min to 5% buffer B, in 50 min from 5% to 22% buffer B and in 60 min from 22% to 35% buffer B. Subsequently, a column washing step using 90% buffer B for 10 min and column

re-equilibration with 5% buffer B for 5 min was performed. MS1 full scans were recorded at a resolution of 120.000 in the Orbitrap, parameters set as follows: Ion transfer tube temperature 275 °C, RF lens amplitude 60%, 375-1500 m/z scan range, automatic gain control (AGC) target of 4 x 10^5, 3 s cycle time and 50 ms maximal injection time. The monoisotopic precursor selection as well as the dynamic exclusion for 60 sec were enabled. Peptides with a higher intensity than 5.0 x 10^4 and charge states between 2 and 7 were selected for fragmentation in the higher-collisional induced dissociation (HCD) cell at 35% collision energy and analyzed in the Orbitrap, the isolation window was set to 1 m/z, the resolution to 60000 and an AGC target of 5 x 10^4 and a maximal injection time of 118 ms.

LC-MS/MS method TimsTOF Pro

Peptides were measured and online-separated using an *UltiMate 3000 nano* HPLC system (*Dionex, Sunnyvale, USA*) coupled to a *TimsTOF Pro* (*Bruker, Billerica, USA*) mass spectrometer *via* a *CaptiveSpray* nano-electrospray ion source (*Bruker, Billerica, USA*) and *Sonation* (*Biberach, Germany*) column oven. Peptides were first loaded on the trap column (*Acclaim PepMap 100 C18*, 75 µm ID x 2 cm, 3 µm particle size, *Thermo Fisher Scientific, Waltham, USA*), washed with 0.1% formic acid in water for 7 min at 5 µL/min and subsequently transferred to the separation column (*Aurora* C18 column, 25 cm × 75 µm, 1.7 µm, *IonOpticks, Fitzroy, Australia*) and separated over a 60 min gradient from 5% to 28% B, then to 40% B over 13 min, followed by 10 min at 95% before re-equilibration and at a flow rate of 400 nL/min. The mobile phases A and B were 0.1% (v/v) formic acid in water and 0.1% (v/v) formic acid in acetonitrile, respectively. The *timsTOF Pro* was operated in data-dependent PASEF mode with the dual TIMS analyzer operating at equal accumulation and ramp times of 100 ms each with a set 1/K0 ion mobility range from 0.85 to 1.40 V × s × cm-2. The capillary voltage of the *CaptiveSpray* source was set to 1500 V. 10 PASEF scans per topN acquisition cycle were performed, resulting in a total cycle time of 1.17 s. The mass range was set from 100 to 1700 m/z. Only precursors reaching an intensity threshold of 1750 arbitrary units were considered for fragmentation, precursors reaching a target intensity of 14500 arbitrary units were dynamically excluded for 0.4 min. The quadrupole isolation width was set to 2 m/z for $m/z < 700$ and to 3 m/z for $m/z > 800$. The collision energy was ramped linearly as a function of the mobility from 59 eV at 1/K0 = 1.6 V × s × cm-2 to 20 eV at 1/K0 = 0.6 V × s × cm-2. TIMS elution voltages were calibrated linearly to obtain the reduced ion mobility coefficients (1/K0) using three *Agilent*

(*Santa Clara, USA*) ESI-L Tuning Mix ions (m/z 622, 922 and 1,222) spiked on the *CaptiveSpray* source inlet filter.

1.3.5 Proteomics data analysis

Whole proteome analysis

Proteomic data analysis was performed similar as described before.[71] Peptide and protein identifications were performed using *MaxQuant* 1.6.17.0 software with *Andromeda* as search engine using following parameters: Cysteine carbamidomethylation was set as fixed modification and methionine oxidation and N-terminal acetylation as variable modifications, trypsin (without N-terminal cleavage to proline) as the proteolytic enzyme with max. of 2 missed cleavages. Label-free quantification (LFQ) mode was performed with a minimum ratio count of 2. Searches were performed with the Uniprot database for *H. sapiens* (reviewed, Uniprot entry UP000005640, organism ID 9606, downloaded 12.09.2021). The "match between runs" (0.7 min match and 20 min alignment time window) and second peptide identification options were activated. For *TimsTOF* data the TOF MS/MS match tolerance was set to 0.05 Da. All other parameters were used as pre-set in the software. Statistical analysis was performed with *Perseus* 1.6.14.0. LFQ intensities were log2(x) transformed. Putative contaminants, reverse peptides and peptides only identified by site were deleted. Valid values were filtered for at least 3 valid values in each group and a missing values imputation was performed over the total matrix (width 0.3, downshift 1.8). A two-sample student`s t-test with permutation-based FDR (0.05) and the significance thresholds were set at p-value = 0.05 (-log10(p-value) = 1.3) and an enrichment factor of 2 (log2(x) = 1) as indicated in the volcano plots.

Affinity-based protein profiling

MS raw files were processed with *MaxQuant* version 2.0.3.0 as described above. Statistical analysis was performed as described above using *Perseus* version 1.6.15.0, with the difference that filtering of valid values was performed with "three in at least one group". The significance thresholds after the t-test were set at p-value = 0.05 (-log10(p-value) = 1.3) and an enrichment factor of 4 (log2(x) = 2) as indicated in the volcano plots.

Thermal protein profiling (TPP)

MS raw data was analyzed using *MaxQuant* software (version 1.6.5.0) and peptides were searched against Uniprot database for Homo sapiens (taxon identifier: 9606, downloaded on 15.07.2019, canonical). Fractions were assigned for each experiment (10 fractions á 4 experiments). Group specific parameters were set to "Reporter ion MS2" with 10plex TMT isobaric labels for N-terminal and lysine modification selected. Carbamidomethylation of cysteines was set as fixed modification and oxidation of methionines and acetylation of N-termini were set as variable modifications. Trypsin was set as digestion enzyme, a maximum of 2 missed cleavages sites allowed. For main search, precursor mass tolerance was set to 4.5 ppm and fragment mass tolerance to 0.5 Da. The isotope correction factor was set for each TMT channel according to the data sheet of the TMT labels. The option "Second peptide identification" was enabled, and the false discovery rate (FDR) determination carried out by applying a decoy database and thresholds were set to 1% FDR at peptide-spectrum match and at protein levels. Furthermore, the "match between runs" (0.7 min match and 20 min alignment time windows) option was enabled. The remaining parameters were used as default settings. Calculated corrected reporter ion intensities were normalized to the channel corresponding to the lowest temperature and were used to determine the melting curves of the proteins and the resulting thermal shifts (T_m). These were calculated using R (version 4.1.1) and the TPP package (version 3.20.1) using the "analyzeTPPTR" function. Proteins that fulfilled all requirements were considered to have a significant thermal shift. For visualization of the TPP output files, the data was filtered as follows: $R2 > 0.8$ for all fitted curves, plateaus < 0.3 for HCl control curves, steepest slopes of melting curves < -0.06, difference in T_m between both HCl control replicates < 1.5 °C. The data was further visualized using *Perseus* version 1.6.13.0 and *GraphPad Prism 9.*

Pathway analysis

Pathway analysis of whole proteome analysis experiments was performed with the *ingenuity pathway analysis* tool (IPA, *Qiagen, Venlo, The Netherlands*) using the $\log_2$(fold-change) and –log(P-value) data of the proteins determined in *Perseus* as input.

1.4 Target validation experiments

1.4.1 ClpP target validation

hClpP expression and purification

Human ClpP was expressed and purified as described previously.[246] Briefly, an expression construct of human ClpP (Uniprot ID Q16740) covering residues 57-228[349] fused to a C-terminal Strep-II-tag in a pET301 plasmid was expressed in *E. coli* Rosetta 2 (DE3) cells at 25 °C for 20 h after induction with IPTG (500 µM). Following harvest and cell lysis by sonication in Strep binding/wash buffer (100 mM Tris HCl, 150 mM NaCl, 1 mM EDTA, pH 8.0), the protein was purified by affinity chromatography (*StrepTrap HP 5 mL, Cytiva, Marlborough, USA*; Step elution buffer: 100 mM Tris HCl, 150 mM NaCl, 1 mM EDTA; 2.5 mM desthiobiotin, pH 8.0) and subsequent size exclusion chromatography (*Superdex 200, Cytiva, Marlborough, USA*; Aloisius buffer: 20 mM HEPES, 100 mM NaCl, pH 7.0) using an *Äkta Purifier* FPLC system (*GE Healthcare, Chicago, USA*).

ClpP peptidase assay

The residual hClpP peptidase activity was measured upon treatment with compounds by monitoring the cleavage of the optimized fluorogenic substrate acetylalanylhomoarginyl-2-aminooctanoyl-7-amino-4-carbamoylmethylcoumarin (Ac-Ala-hArg-2-Aoc-ACC, custom-synthesis by *Bachem, Bubendorf, Switzerland*) as described previously.[246] In a black 96-well plate, 1 µL inhibitor or respective vehicle control (usually DMSO, except for oxociprofloxacin 0.1 N NaOH and ciprofloxacin 0.1 N HCl) was aliquoted in four replicates in three different concentrations (100 × stocks, final concentrations in assay: 1 µM, 10 µM, 100 µM). To exclude for vehicle effects, the respective other solvents were also added if necessary to achieve the same compositions in each condition. Subsequently, 98 µL enzyme buffer mix (final concentration of hClpP 0.4 µM in assay buffer 50 mM HEPES, 300 mM KCl, 1 mM DTT, 15% (v/v) glycerol, pH = 7.5) was added to the wells and incubated at 37 °C for 15 min. Kinetic measurement (1 min intervals) was started after adding 1 µL of peptide substrate Ac-Ala-hArg-2-Aoc-ACC (10 mM stock in DMSO, final concentration 100 µM). Fluorescence of the cleaved dye was detected for 120 min at 37 °C using an *Infinite M200 pro* (*Tecan, Männedorf, Switzerland,* excitation: 380 nm; emission: 430 nm, manual gain: 100) plate reader. The slope of the fluorescence over time signal was calculated *via* linear regression using *GraphPad Prism* (version 5.03), the first 5 min were usually disregarded to allow for thermal equilibration effects. The residual activity of inhibitor-treated protein was determined in comparison to vehicle-treated control samples which were

normalized to 100% activity. The experiments were repeated in at least $n = 2$ independent experiments.

ClpXP protease assay (GFPssrA-degradation assay)

For ClpXP protease activity assays human ClpP (expression & purification see above) and *E. coli* ClpX (kindly provided by *Thomas Gronauer*)[248] was used and the experiments conducted as described before with minor modifications.[246,248] As recombinant *H. sapiens* ClpX is instable and *E. coli* ClpX recognizes peptides C-terminally tagged with a short amino acid sequence and forms a functional complex with *H. sapiens* ClpP, it is suitable as a *H. Sapiens* ClpX substitute for *in vitro* protease activity assays.[248] Measurements were carried out in a total reaction volume of 60 µL in black, flat-bottom 96-well plates and the residual protease activity determined by monitoring the cleavage of ssrA-tagged GFP by the decrease of fluorescence signal. First, 0.6 µL inhibitor or respective vehicle control (usually DMSO, except for ciprofloxacin 0.1 N HCl) was aliquoted in four replicates in three different concentrations (100 × stocks, final concentrations in assay: 1 µM, 10 µM, 100 µM). To exclude for vehicle effects, the respective other solvents were also added to the master mix if necessary to achieve the same compositions in each condition. The master mixes were prepared with hClpP14 (0.1 µM), *E. coli* $ClpX_6$ (0.2 µM) in PZ buffer (25 mM HEPES, 200 mM KCl, 5 mM $MgCl_2$, 1 mM DTT, 10% (v/v) glycerol, pH 7.6) supplemented with 1 × ATP regeneration mix (10 × stock, 25 mM HEPES, 200 mM KCl, 5 mM $MgCl_2$, 1 mM DTT, 40 mM ATP, 160 mM creatine phosphate, 200 U/mL creatine kinase, 10% (v/v) glycerol, pH 7.6) and added to the wells. In the negative control no ClpP and ClpX was added to the master mix. After incubation at 37 °C for 15 min, the reactions were started by the addition of GFP-SsrA substrate to a final concentration of 0.6 µM and fluorescence was detected for 3 hours at 37 °C using an *Infinite M200 pro* (*Tecan, Männedorf, Switzerland,* excitation: 485 nm; emission: 535 nm, manual gain: 60) plate reader. The initial slopes of the fluorescence decays were calculated via linear regression using GraphPad Prism. The residual activity of compound-treated protein was determined in comparison to vehicle-treated control samples which were normalized to 100% activity. The experiments were repeated in at least $n = 2$ independent experiments.

ClpP wt vs ClpP KO full proteome Analysis

For whole proteome analysis HEK293T wild-type cells and HEK293T hClpP knockout cells (kindly provided by *Prof. Aleksandra Trifunovic, CECAD Cologne*)[223] were used and the experiment performed as described in the proteomics section.

1.4.2 IDH2 target validation

IDH2 activity assay

Recombinant human isocitrate dehydrogenase was purchased from *active motif* (*Carlsbad, USA, Cat.# 31615*). The literature known IDH2-inhibitor Enasidenib was purchased from *Cayman Chemical* (*Ann Arbor, USA, Cat.# 21277*). Activity assays were performed as previously described with minor modifications.[261] Briefly, the catalytic activity of converting isocitrate to 2-oxogluterate (α-ketoglutarate) converting the cofactor $NADP^+$ to NADPH was measured by a NADPH-coupled assay. The NADPH-dependent diaphorase (*Sigma-Aldrich, St. Louis, USA, Cat.# SLBT8928*) converted resazurin (*ACROS Organics, Thermo Fisher Scientific, Waltham, USA,* Cat.# 189900010) to fluorescent resorufin for activity read-out. To IDH2 (2 nM) in assay buffer (150 mM NaCl, 50 mM K_2HPO_4, 10 mM $MnCl_2$, 10% (v/v) glycerol, 0.03% (w/w) BSA, pH 7.0) was added $NADP^+$ cofactor (c_{end} = 44 µM) and β-mercaptoethanol (c_{end}= 2.5 mM) for a total reaction volume of 79 µL per well (black 96-well plate). Conditions lacking IDH2 were added as control. After addition of 1 µL of compound (100 × stock, final concentrations 500 µM, 100 µM, 10 µM and 1 µM) and/or the respective vehicle controls, the mixture was incubated at 25 °C for 1 h in the dark. Subsequently, the reaction was initiated by addition of 20 µL of substrate mix (0.2 mM isocitrate, 60 µg/mL diaphorase, 200 µM resazurin in assay buffer). Fluorescence was continuously measured using an *Infinite M200 pro* (*Tecan, Männedorf, Switzerland*, excitation: 544 nm, emission: 590 nm, manual gain: 80). The initial slopes of the fluorescence increases were calculated *via* linear regression using *GraphPad Prism* (version 9). The residual activity of compound-treated protein was determined in comparison to vehicle-treated control samples and IDH2-lacking control samples which were normalized to 100% and 0% activity, respectively. The experiments were repeated in at least n = 3 independent experiments.

Mitochondrial NADPH level determination

The isolation of mitochondria was performed as described in the "subcellular fractionation protocol" of *abcam* (*Cambridge, United Kingdom*) with minor modifications.[350] Briefly, PDL cells were seeded in 10 cm petri dishes at a density of 2.0 million cells/dish and grown overnight. On the next day, cells were stimulated for 6h with 7.5 µM Ciprofloxacin or 0.1 N HCl, respectively. Cells were scraped off with a rubber policeman in fractionation buffer, the cell suspension passed ten-times through a 27 G needle and the mitochondrial fraction obtained by differential centrifugation. In brief, the nuclear fraction was removed by centrifuging at 720 ×g for 5 min. The mitochondria containing supernatant was centrifuged at 10,000 ×g for 5 min to obtain the mitochondrial pellet. To increase the purity, the pellet was resuspended in fractionation buffer by passing it ten-times through a 25 G needle and re-centrifugation at 10,000 ×g for 10 min. The mitochondria fraction was resuspended in PBS, protein determination performed using Bradford assay, and all samples set to the same concentration with PBS. The *Promega* NADP/NADPH-Glo™ assay kit (*Promega, Walldorf, Germany, Cat.# G9081*) was used to measure NADPH levels individually according to the manufacture's instruction. NADP/NADPH-Glo™ detection reagent was added to the processed mitochondrial lysates and after 2 h incubation luminescence was recorded (*Orion II microplate luminometer, Titertek Berthold, Bad Wildbad, Germany*).

1.4.3 AIFM1 target validation

The expression and purification of recombinant AIFM1 and MIA40, as well as ultracentrifugation and analytical size-exclusion chromatography experiments were performed by *Alex Rothman* at the *University of Cologne*. As only preliminary results are discussed in this dissertation and experiments are ongoing, the final experimental procedures will be published in the journal publication of the project once optimized.

1.4.4 PTGR2 target validation

PTGR2 (*Antikoerper-online, Aachen, Germany, Cat.# ABIN1098255*) activity was measured as described before with minor modifications by *Wiebke Hutwelker* at the *BMWZ* of the *Leibniz University Hannover*.[351,352] Briefly, Ciprofloxacin 1 µL (1:50 stock in 0.1 N HCl) was added to 44 µL recombinant PTGR2 in buffer (200 nM, Tris Buffer, 1 mM EDTA,

50 mM TCEP, 300 µM NADPH) and incubated at 37 °C for 20 min. Subsequently, 5 µL of substrate solution (20 µM, 15-ketoprostaglandin, *Cayman Chemical, Ann Arbor, USA, Cat.# 14720*) was added and incubated for further 30 min at 37 °C. The reaction was terminated by addition of 800 µL EtOAc+0.5% AcOH, 300 µL H_2O and 100 µL internal standard (13,14-dihydro-15-ketoprostaglandin-d4, 300 pmol/sample, *Cayman Chemical, Ann Arbor, USA, Cat.# 10010606*). Of the organic phase 600 µL was transferred into a fresh Eppendorf tube and the solvent removed in a SpeedVac. The residue was dissolved in 100 µL acetonitrile/ H_2O (1:1) and measured with LC-MS/MS. Gradient: Solvent A = H_2O + 0.1% formic acid, solvent B = acetonitrile + 0.5% formic acid, flow rate = 0.4 mL/min, run length 6 min, gradient = 0 min 30% B, 1 min 30% B, 2 min 31.5% B, 2.1 min 95% B, 4 min 95% B, 4.1 min 30% B, 6 min 30% B. MS settings: Capillary = 3.0 kV, sampling cone = 20.0 kV, extraction cone 4.0 kV, source temperature = 100 °C, desolvation temperature = 350 °C, cone gas flow = 50.0 L/h, desolvation gas flow = 650.0 L/h, scan time = 0.250 s, inter-scan time = 0.020 s, mass range = 100-800 Da. Masses of 15-ketoprostaglandin (349.2 Da, collision energy = 21.0 eV), 13,14-dihydro-15-ketoprostaglandin (351.2 Da, collision energy = 18.0 eV) and 13,14-dihydro-15-ketoprostaglandin (355.2 Da, collision energy = 10.0 eV) were set for MRM. The areas under the curve (AUC) were used to quantify 15-keto-PGE2 and 13,14-dihydro-15-keto-PGE2 levels by determining peak areas in relation to internal standard PGE2-d4.

1.4.5 SCARB1 target validation

Microscale thermophoresis (MST) was performed as follows: Monolith His-Tag Labeling Kit RED-tris-NTA 2nd Generation (*NanoTemper Technologies, Munich, Germany, Cat.# MO-L018*) was used for K_D determination as recommended by the purchaser. Briefly, SCARB1 (*Hölzel Biotech, Cologne, Germany, Cat.# SC1-H82E5*) concentration (50 nM) was adjusted in assay buffer and labelled by the RED-tris-NTA dye (100 nM). This mixture was added to compound dilution series (c = 1 mM to 30 nM) and measured using *Monolith NT.115* (*NanoTemper Technologies, Munich, Germany*).

1.4.6 NUDT1 target validation

Recombinant NUDT1 expression & purification

Expression and purification of recombinant NUDT1 was done as in procedures described previously with minor modifications.[301,307] Full length NUDT1 gene synthesis (see insert sequence, not codon-optimized) and cloning into pET28a(+) using restriction sites NdeI and XhoI was ordered from *TWIST Bioscience* (*South San Francisco, USA*). Insert sequence:

GGCGCTAGCCGCTTGTATACGTTAGTGCTGGTTCTGCAGCCACAAAGAGTTTTG
CTTGGAATGAAAAAACGCGGATTTGGCGCAGGACGCTGGAATGGCTTCGGCGG
GAAAGTTCAGGAAGGTGAAACCATCGAAGATGGCGCGCGGCGTGAACTTCAG
GAAGAGTCTGGCTTGACGGTTGACGCGTTGCATAAAGTAGGTCAAATAGTTTT
TGAATTTGTGGGGGAGCCCGAACTGATGGATGTTCATGTGTTTTGTACTGACAG
TATACAAGGCACACCCGTGGAATCTGATGAAATGCGTCCGTGTTGGTTTCAGTT
GGACCAGATACCGTTCAAAGATATGTGGCCTGACGATAGCTACTGGTTTCCAC
TGTTACTGCAGAAAAAAAAGTTTCATGGTTACTTTAAATTTCAGGGCCAAGAT
ACCATTCTGGATTACACTTTACGTGAGGTGGACACCGTCTGA

The plasmid was transformed into chemically competent *E. coli* BL21 (DE3) and expression clones verified by sequencing. An overnight culture of the expression strain (LB + 1:1000 kanamycin) was grown and 1 L flasks (LB medium + 1:1000 kanamycin) were inoculated 1:100 and incubated at 37 °C, 200 rpm until OD_{600} = 0.5 – 0.6. The flasks were cooled on ice for 15 min, the overexpression induced by addition of IPTG (500 µM) and incubated at 20 °C, 200 rpm for 20 h. The bacteria were harvested, the pellet of 2 L culture combined, washed with cold PBS and stored at –80 °C. The pellet was resuspended in 30 mL Buffer A (10 mM Tris pH 7.4, 500 mM NaCl, 1 mM DTT, 10 mM imidazole) and lysis was performed by sonification (7 min 30% intensity, 3 min 70%, 7 min 30%, 3 min 70%, pulse 5, *Bandelin SONOPULS* equipped with *Bandelin UW2070* and *MS73* lance, *Bandelin electronic, Berlin Germany*). The lysate was cleared by centrifugation (40,000 ×g, 4 °C, 30 min) and filtered through a *Whatman* filter (0.45 µm PVDF w/GMF, *Cytiva, Marlborough, USA, Cat.# 6818-1304*). Nickel-affinity chromatography purification was performed with *Äkta Pure* system (*GE Healthcare, Chicago, USA*) using an in buffer A equilibrated HisTrap HP (5 mL, *Cytiva, Marlborough, USA, Cat.# 17-5248*) column. The filtered lysate was applied *via* the sample pump and subsequently the column was washed for 4.9 column volumes (CV) with buffer A, 6.9 CV with wash buffer 1 (10 mM Tris pH = 7.4, 1 M NaCl, 1 mM DTT, 10 mM imidazole) and 6.9 CV wash buffer 2 (10 mM Tris pH = 7.4, 500 mM NaCl, 1 mM DTT, 40 mM imidazole). Bound protein was eluted with elution buffer (10 mM Tris pH = 7.4, 500 mM NaCl, 1 mM DTT, 500 mM imidazole for 7 CV and NUDT1 containing fraction

identified *via* intact-protein MS (IPMS). The fractions were pooled and dialyzed in buffer (10 mM Tris pH = 7.4, 500 mM NaCl) with simultaneous thrombin cleavage by addition of 200 µL thrombin (200 U, 1 U/µL reconstituted in H_2O, *Sigma-Aldrich, St. Louis, USA, Cat.# T4648*) into the dialysis membrane (*Carl Roth, Karlsruhe, Germany, Cat.# E659.1*) overnight at 4 °C. Successful thrombin cleavage was verified by IPMS. Reverse nickel-affinity purification (same conditions as before), but this time collecting the non-bound flow-through, was performed to purify thrombin-cleaved protein. The fractions containing the cleaved protein were desalted on the *Äkta Pure* system (*HiTrap HP Desalting 5 mL, Cytiva, Marlborough, USA, Cat.# 17-1408*, elution with 1.5 CV buffer 1 = 20 mM Tris, pH 7.5, 1 mM DTT) and subjected to anion exchange chromatography (*Resource Q 1 mL, GE Healthcare, Chicago, USA, Cat.# 17-1177-01*) for further purification. The desalted sample was applied by sample pump, washed with buffer 1 for 5 CV and eluted with a linear gradient to 100% buffer 2 (20 mM Tris pH 7.5, 1 mM DTT, 1 M NaCl) over 20 CV. Fractions containing non-aggregated and active NUDT1 were concentrated using a 3 kDa MWCO Amicon (*Ultra-15, Merck Millipore, Darmstadt, Germany, Cat.# UFC9003*) to a concentration of 750 µM and snap-frozen in liquid nitrogen in aliquots to be stored at –80 °C. The identity of the recombinant protein was verified by IPMS (calc. 18,232.8 Da, found 18,232.5 Da) and SDS-PAGE (approx. 18 kDa).

NUDT1 Activity Assay

The activity assay was performed as described before with minor modifications.[306] Briefly, the conversion of dGTP (*New England Biolabs, Ipswich, USA, Cat.# N0442S*) to dGMP and inorganic pyrophosphatate (pp_i) by NUDT1 was monitored. The generation of pp_i was detected by conversion with inorganic pyrophosphatase (*E. coli, New England Biolabs, Ipswich, USA, Cat.#* M0361S) to inorganic phosphate (p_i) forming a green complex with malachite green and acidic ammonium molybdate. The known NUDT1 inhibitor (*S*)-crizotinib (*Sigma-Aldrich, St. Louis, USA, Cat.# PZ0240*) was used as positive control. The FQs Ciprofloxacin and Levofloxacin were tested in the concentrations 500 µM, 100 µM, 10 µM and 1 µM; (*S*)-crizotinib in 10 µM, 1 µM and 0.1 µM. In transparent 96-well plates 0.4 µL of compounds or respective vehicle controls (1:100 stocks, FQs in 0.1 N HCl, (*S*)-crizotinib in DMSO) were added in triplicates into the wells and 39 µL of enzyme master mix (50 nM NUDT1, 0.2 U/mL pyrophosphatase in assay buffer = 50 mM Tris pH 7.5, 100 mM NaCl, 10 mM $MgCl_2$ and 1 mM DTT) was added. Conditions with master mix

lacking NUDT1 were added as control. The plate was incubated for 30 min at r.t., and the enzymatic reaction was started by addition of 0.4 µL dGTP (10 mM in H_2O) to each well and the plate was further incubated for 30 min at room temperature. The malachite green reagent was obtained by mixing 1 volume of 4.2% (w/v) ammonium molybdate in 4 N HCl with 3 volumes of 0.045% (w/v) malachite green and addition of 0.01% (v/v) Tween20 (*Carl Roth, Karlsruhe, Germany, Cat.# 9005-64-5*) directly before use. The mixture was filtered through 0.2 µm PTFE syringe filters (25 mm, *fisherbrand, Thermo Fisher Scientific, Waltham, USA, Cat.# 15141499*) and 160 µL added to each well, after 5 min the absorbance at 630 nm was quantified using an *Infinite M200 Pro* (*Tecan, Männedorf, Switzerland*) plate reader. The residual activity of compound-treated protein was determined using *GraphPad Prism* (version 9) in comparison to vehicle-treated control and NUDT1-lacking control samples which were normalized to 100% and 0% activity, respectively. The experiments were repeated in at least $n = 3$ independent experiments.

Recombinant NUDT1 labelling

For gel-based fluorescence labelling of recombinant NUDT1, 1 µM recombinant protein was spiked-in to PBS or PBS-diluted HeLa cell lysate (20 µg per reaction sample). The total reaction volume per condition was 20 µL using PCR tubes. For NUDT1 heat-control samples, the protein was denatured at 95 °C for 10 min prior to addition of the photo-crosslinker probes. After addition of the respective probes (5 µM) the samples were incubated at room temperature for 30 min. For competition conditions samples were incubated with the parent compound (Ciprofloxacin or Levofloxacin) for 30 min at room temperature prior to probe addition. Subsequently, the samples were irradiated on ice for 5 min with UV light (365 nm for **P1** probes, *TL-D BLB 18 W, Philips, Amsterdam, The Netherlands*, 300 nm for **P2** probes, *LZC-UVB 8 W, Luzchem, Ottawa, Canada*). Click Master-mix (1 µL, 100 µM TAMRA-azide, *Baseclick, Neuried, Germany, Cat.# BCFA-008-10*, 500 µM BTTAA ligand, *Jena Bioscience, Jena, Germany, CLK-067*, 1 mM $CuSO_4$) was added and the CuAAC reaction started by addition of 920 nL of aq. sodium ascorbate ($c_{end} = 2$ mM). The reaction was incubated in the dark at room temperature for 1 h and subsequently, 2× SDS loading buffer (23 µL) was added, the samples denatured at 95 °C for 10 min and subjected to SDS-PAGE. Fluorescence scanning was performed using by a *Las-3000* fluorescence darkbox (*Fujifilm, Minato, Japan*) with a *Fujinon* VRF 43LMD Lens, 605DF40 filter and 520 nm EPI excitation wavelength and loading controls were developed with Coomassie stain afterwards.

1.4.7 ADAL1 target validation

Recombinant ADAL1 expression & purification was performed similar to published procedures with minor modifications.[298] Full length ADAL1 gene synthesis (see insert sequence, not codon-optimized) and cloning into pET28a(+) using restriction sites NdeI and XhoI was ordered from *TWIST Bioscience* (*South San Francisco, USA*). Insert sequence:

ATGATAGAGGCAGAAGAGCAACAGCCTTGCAAGACAGACTTCTATTCTGAATT
GCCAAAAGTGGAACTTCATGCCCACTTGAATGGATCCATTAGTTCTCATACCAT
GAAGAAATTAATAGCCCAGAAGCCAGATCTTAAAATCCACGATCAGATGACTG
TGATTGACAAGGGAAAGAAAAGAACTTTGGAAGAATGTTTCCAGATGTTTCAA
ACTATTCATCAGCTTACTAGTAGCCCTGAAGATATTCTAATGGTCACAAAAGAT
GTCATAAAAGAATTTGCAGATGACGGCGTCAAGTACCTGGAACTAAGGAGCAC
ACCCAGAAGAGAAAATGCTACTGGAATGACTAAAAAGACTTATGTGGAATCTA
TACTTGAAGGTATAAAACAGTCCAAACAAGAAAACTTGGACATTGATGTTAGG
TATTTGATAGCAGTTGACAGAAGAGGTGGCCCTTTAGTAGCCAAGGAGACTGT
AAAACTTGCCGAGGAGTTCTTCCTTTCTACTGAGGGTACAGTTCTTGGCCTTGA
CCTCAGTGGAGACCCTACTGTAGGACAAGCAAAAGACTTCTTGGAACCTCTTT
TAGAAGCTAAGAAAGCAGGTCTGAAGTTAGCATTGCATCTTTCAGAGATTCCA
AACCAAAAAAAAGAAACACAAATACTCCTGGATCTGCTTCCTGACAGAATCGG
GCATGGAACATTTCTCAACTCCGGTGAGGGAGGATCCCTGGATCTGGTGGACT
TTGTGAGGCAACATCGGATACCACTGGAACTCTGTTTGACCTCAAACGTCAAA
AGTCAGACAGTTCCATCTTATGACCAGCACCATTTCGGATTCTGGTACAGCATT
GCCCATCCTTCTGTGATCTGTACTGATGATAAGGGTGTTTTTGCAACACACCTT
TCTCAAGAGTACCAGCTGGCAGCTGAAACATTTAATTTGACCCAGTCTCAGGT
GTGGGATCTGTCTTATGAATCCATCAACTACATCTTTGCTTCTGACAGCACCAG
ATCTGAACTGAGGAAGAAATGGAATCACCTGAAGCCCAGAGTGTTACATATTT
AA

The plasmid was transformed into chemically competent *E. coli* BL21 (DE3) and expression clones verified by sequencing. An overnight culture of the expression strain (LB + 1:1000 kanamycin) was grown and 1 L flasks (LB medium + 1:1000 kanamycin) were inoculated 1:100 and incubated at 37 °C, 200 rpm until OD_{600} = 0.5 – 0.6. The flasks were cooled on ice for 15 min, the overexpression induced by addition of IPTG (500 µM) and incubated at 20 °C, 200 rpm for 20 h. The bacteria were harvested, the pellet of 2 L culture combined, washed with cold PBS and stored at –80 °C. The pellet was resuspended in 30 mL Buffer A (50 mM Tris pH 8.0, 300 mM NaCl, 5 mM β-mercaptoethanol, 0.1% (v/v) NP40, 10% (v/v) glycerol and 20 mM imidazole) and lysis was performed by sonification (7 min 30% intensity, 3 min 70%, 7 min 30%, 3 min 70%, pulse 5, *Bandelin SONOPULS* equipped with *Bandelin UW2070* and *MS73* lance, *Bandelin electronic, Berlin Germany*). The lysate was cleared by centrifugation (40,000 ×g, 4 °C, 30 min) and filtered through a *Whatman* filter (0.45 µm PVDF w/GMF, *Cytiva, Marlborough, USA, Cat.# 6818-1304*). Nickel-affinity

chromatography purification was performed with *Äkta Pure* system (*GE Healthcare, Chicago, USA*) using an HisTrap HP (5 mL, *Cytiva, Marlborough, USA, Cat.# 17-5248*) column equilibrated in buffer A. The filtered lysate was applied *via* the sample pump and subsequently the column was washed for 15 column volumes (CV) with buffer A, before gradient elution with buffer B (50 mM Tris pH 8.0, 300 mM NaCl, 5 mM β-mercaptoethanol, 0.1% (v/v) NP40, 10% (v/v) glycerol and 400 mM imidazole) from 0% to 100% buffer B over for 25 CV. ADAL1 containing fractions were identified *via* SDS-PAGE, pooled and dialyzed in buffer 1 (20 mM Tris pH 8.0, 1 mM DTT, 10% (v/v) glycerol) in a dialysis membrane (*Carl Roth, Karlsruhe, Germany, Cat.# E659.1*) overnight at 4 °C. Anion exchange chromatography (*Resource Q 1 mL*, *GE Healthcare*, *Chicago*, *USA*, *Cat.# 17-1177-01*) was performed for further purification. The dialyzed sample was applied by sample pump, washed with buffer 1 for 5 CV and eluted with a linear gradient to 100% buffer 2 (20 mM Tris pH 8.0, 1 mM DTT, 10% (v/v) glycerol, 1 M NaCl) over 20 CV. Fractions containing non-aggregated and active ADAL1 were concentrated using a 10 kDa MWCO *Amicon* (*Ultra-15, Merck Millipore, Darmstadt, Germany, Cat.# UFC901024*) to a concentration of 42 µM and snap-frozen in liquid nitrogen in aliquots to be stored at –80 °C. The identity of the recombinant protein was verified by SDS-PAGE (approx. 42 kDa) and *in vitro* activity assays.

ADAL1 activity assay

The ADAL1 *in vitro* activity assay was performed as previously reported.[298] Briefly, the conversion of N^6-methyl-AMP (*Cayman Chemical, Ann Arbor, USA*, Cat.# 23382) to inosine by ADAL1 was monitored by the shift of the absorbance maxima of educt (265 nm) and product (250 nm). The FQs Ciprofloxacin and Levofloxacin were tested in the concentrations 500 µM, 300 µM, 200 µM and 100 µM. In a *UVStar* (*Greiner, Kremsmünster, Austria, Cat.# 655801*) 96-well plate 1 µL of compounds or vehicle controls (1:100 stocks, FQs in 0.1 N HCl) were added in triplicates into the wells and 98 µL of enzyme master mix (100 nM ADAL1 in 50 mM potassium phosphate buffer pH 6.7, 2 mM DTT and 100 µg/mL BSA) was added. Conditions with master mix lacking NUDT1 were added as control. The plate was incubated for 30 min at 37 °C and subsequently the enzyme reaction started by addition of the substrate N^6-methyl-AMP (1 µL of 20 mM stock in PBS). The absorbance at 265 nm was continuously measured using a *Infinite M200 Pro (Tecan, Männedorf, Switzerland)* plate reader. The initial slopes of the absorbance readings were

calculated *via* linear regression using *GraphPad Prism* (version 9). The residual activity of compound-treated protein was determined in comparison to vehicle-treated control samples and ADAL1-lacking control samples which were normalized to 100% and 0% activity, respectively. The experiments were repeated in at least $n = 2$ independent experiments.

1.4.8 Lysosomal cell imaging

HeLa cells were seeded in *ibiTreat* 8-well µ-slides (*ibidi, Munich, Germany*) at a density of 0.03 million cells per well and grown overnight. Next day, cells were labelled with 20 µM Cipro P2 probe or DMSO for 1 h. Then cells wells were washed with PBS + Ca^{2+}/Mg^{2+} for 10 min before fixing the cells with 4% PFA in PBS for 15 min at room temperature. Afterwards wells were washed with PBS for 5 min and permeabilized with 0.1% Triton X-100 in PBS for 10 min at room temperature. After another 5 min washing step cells were blocked with 5% BSA in PBS for 1 h at room temperature and then again washed for 5 min. A fresh click chemistry mix was prepared consisting of the following components: 1 mM $CuSO_4$, 1 mM TCEP, 100 µM TBTA and 10 µM Alexa Fluor™ azide (*Thermo Fisher Scientific, Waltham, USA, Cat # A10277*) in PBS. 200 µL click mix were added per well and slide was incubated for 2 h in the dark at room temperature while vigorously shaking. Then cells were washed thrice with PBS and incubated with a primary anti-LAMP1 antibody (*Developmental Studies Hybridomy Bank, Iowa City, USA, ID H4A3*) overnight at 4 °C while gently shaking. On the next day wells were washed thrice with PBS for 5 min in the dark and subsequently incubated with an Alexa Fluor™ 488 labeled anti-mouse secondary antibody (*Thermo Fisher Scientific, Waltham, USA, Cat.# A-11001*) and counter-stained with *Hoechst 33342* (*Sigma Aldrich, St. Louis, USA*) for 1 h at room temperature in the dark while gently shaking. After another 3 x 5 min washing steps with PBS, wells were mounted (*FluorSave™, Merck Millipore, Darmstadt, Germany*), covered with a glass slip, and imaged with a *Leica TCS SP8* confocal microscope (*Leica Microsystems, Wetzlar, Germany*). 50 cells per repetition were analyzed and co-localization of the green and red channel was quantified with the help of the *Coloc2 ImageJ* plugin and delineated as mean Pearson's r value.

1.5 Chemical synthesis

1.5.1 General working methods

All air or water sensitive reactions were carried out under inert-gas atmosphere (Argon) in oven-dried glassware with anhydrous solvents utilizing standard Schlenk-techniques unless notes otherwise. Reagents and solvents were purchased from *Sigma-Aldrich*, *Alfa Aesar*, *Acros Organics*, *TCI Europe* or *Merck* and were of reagent grade or better and used without further purification. All reactions were magnetically stirred and temperatures measured externally. Yields refer to isolated homogeneous and spectroscopically pure materials. Sensitive samples were stored in a freezer (–20 °C). Solvents were removed *in vacuo* at 42 °C. Reactions and fractions of flash column chromatography were monitored by qualitative thin layer chromatography /TLC) on aluminum-baked TLC silica gel plates (TLC Silica gel 60 F_{254}, *Merck KGaA*). In order to visualize the substances on the plates UV light (λ_{max} = 254 nm) and staining solutions, such as $KMnO_4$, CAM and *p*-anisaldehyde, were used. Flash column chromatography (FCC) was performed with slurry packed silica gel (40-63 μm) from *VWR* and elution solvents distilled prior to use. NMR spectra were recorded using an internal deuterium lock at ambient probe temperature on a Bruker instruments (300 MHz, 400 MHz or 500 MHz). The ^{1}H NMR chemical shifts are reported in ppm related to the chemical shift of TMS and calibrated to the residual protic solvent peaks of $CDCl_3$ (7.26 ppm) and DMSO-d_6 (2.50 ppm). ^{13}C NMR shifts were calibrated to the center of the multiplet signal of the residual solvent peak ($CDCl_3$ = 77.16 ppm, DMSO-d_6 = 39.52 ppm) and quoted to the nearest 0.1 ppm. ^{1}H NMR spectroscopic data are reported as follows: Chemical shift to the nearest 0.01 ppm (multipilicity, coupling constants *J*, integration intensity). For the multiplicities the abbreviations s (singlet), br s (broad singlet), d (doublet), t (triplet), q (quartet) and m (multiplet) have been used. High-resolution mass spectrometry (HRMS) measurements were recorded with a *Thermo Scientific* LTQ FT Ultra or LTQ Orbitrap instrument with ESI ionization.

1.5.2 Synthetic procedures

3-(but-3-yn-1-yl)-3-(2-iodoethyl)-3*H*-diazirine (MPC-I)

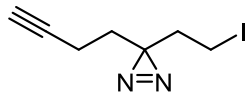

$C_8H_9IN_2$
M = 248.07 g/mol
MCP-I

The iodo-derivative of the minimalist photo-crosslinker **MPC-I** was synthesized according to literature procedures by *Li et al.* starting from the commercially available alcohol derivative. Analytical data were in accordance with the literature values.[75]

^{1}H-NMR (500 MHz, $CDCl_3$): δ[ppm] = 2.89 (t, *J* = 7.6 Hz, 2H), 2.12 (t, *J* = 7.6 Hz, 2H), 2.00-2.05 (m, 3H), 1.69 (t, *J* = 7.2 Hz, 2H).

(*S*)-3-amino-2-(((benzyloxy)carbonyl)amino)propanoic acid (3)

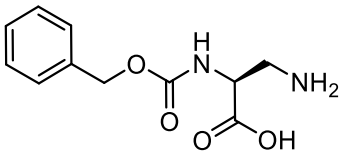

$C_{11}H_{14}N_2O_4$
M = 238.24 g/mol
3

To *N*-benzyloxycarbonyl-*L*-asparagine **2** (2.00 g, 7.51 mmol, 1.0 eq.) in EtOAc (18 mL), MeCN (19 mL) and H_2O (10 mL) PIDA (2.90 g, 9.01 mmol, 1.2 eq.) was added at 0 °C. After stirring for 30 min at 0 °C the reaction mixture was stirred overnight at room temperature. The resulting dispersion was cooled to 0 °C and the solid precipitate was filtered. After washing with EtOAc and drying *in vacuo* **5** (1.67 g, 7.01 mmol, 93%) was isolated as a colorless solid. The spectroscopic data are in accordance with the literature.[353]

^{1}H-NMR (500 MHz, DMSO-d_6): δ[ppm] = 7.88 (br s, 2H), 7.65 (d, *J* = 8.7 Hz, 1H), 7.35-7.25 (m, 5H), 5.05 (s, 2H), 4.31 (dq, *J* = 9.0, 4.6 Hz, 1H), 3.20-3.28 (m, 1H), 3.07-2.99 (m, 1H).

(*S*)-3-[(*tert*-butyloxycarbonyl)-amino]-2-[(benzyloxycarbonyl)-amino]-propanoic acid (4)

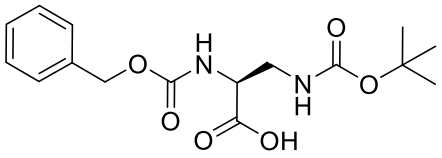

$C_{16}H_{22}N_2O_6$
M = 338.36 g/mol
4

To **3** (1.00 g, 4.20 mmol, 1.0 eq.) in H_2O/dioxane (25 mL/25mL) sodium carbonate (1.33 g, 12.6 mmol, 3.0 eq.) was added and the mixture was cooled to 0 °C. Di-*tert*-butyl dicarbonate (1.10 g, 5.04 mmol, 1.2 eq.) was added at 0 °C. After stirring for 5 min at 0 °C the reaction mixture was stirred overnight at room temperature. The resulting reaction mixture was freeze-dried. The solid precipitate was dissolved in H_2O (15 mL) and 2 M HCl was added dropwise until pH 2 was reached. The mixture was extracted with EtOAc (3 × 50 mL). The combined organic layers were washed with brine (100 mL), dried over Na_2SO_4, filtered and concentrated to obtain **4** (1.30 g, 3.84 mmol, 91%) as a colorless solid. The spectroscopic data are in accordance with the literature.[354]

^{1}H-NMR (400 MHz, $CDCl_3$): δ[ppm] = 7.35 (s, 5H), 5.13 (s, 2H), 4.37 (br s, 1H), 3.50-3.65 (m, 2H), 1.43 (s, 9H).

(*S*)-2-amino-3-((*tert*-butoxycarbonyl)amino)propanoic acid (5)

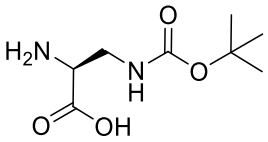

$C_8H_{16}N_2O_4$
M = 204.23 g/mol
5

Di-protected amino acid **4** (1.20 g, 3.55 mmol, 1.0 eq.) was dissolved in methanol (30 mL) and degassed under argon atmosphere. Pd/C (38.3 mg, 360 µmol, 0.1 eq., 10% w/w) was carefully added. The atmosphere was evacuated and then replaced with H_2. After 3.5 h stirring at r.t. the reaction mixture was checked *via* TLC, filtered over celite and the filtrate was concentrated to give the product **5** (710 mg, 3.47 mmol, 98%) as a colorless solid. The spectroscopic data are in accordance with the literature.[355]

^{1}H-NMR (500 MHz, D_2O): δ[ppm] = 3.80-3.82 (m, 1H), 3.64 (dd, *J* = 15.1, 3.4 Hz, 1H), 3.47 (dd, *J* = 15.1, 7.1 Hz, 1H), 1.44 (s, 9H).

tert-butyl ((3*H*-diazirin-3-yl)methyl)carbamate (6)

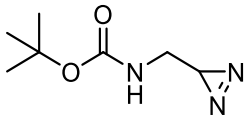

$C_7H_{13}N_3O_2$
M = 171.20 g/mol
6

To **5** (240 mg, 1.18 mmol, 1.0 eq.) in a methanolic solution of ammonia (3 mL, 21.1 mmol, 7 N) was added PIDA (1.14 g, 3.53 mmol, 3.0 eq.) at 0 °C under argon atmosphere. After stirring for 30 min at 0 °C the reaction mixture was stirred for 1 h at room temperature. Methanol was evaporated under reduced pressure and the crude product was purified by flash column chromatography (0-20% EtOAc in hexane) to provide compound **6** (150 mg, 876 µmol, 74%) as a colorless solid. The spectroscopic data are in accordance with literature.[74]

^{1}H-NMR (500 MHz, $CDCl_3$): δ[ppm] = 4.52 (s, 1H), 3.05 (s, 2H), 1.45 (s, 9H), 1.08 (t, *J* = 4.0 Hz, 1H).

tert-butyl ((3*H*-diazirin-3-yl)methyl)(prop-2-yn-1-yl)carbamate (7)

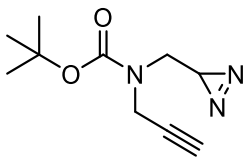

$C_{10}H_{15}N_3O_2$
M = 209.25 g/mol
7

To a stirred solution of sodium hydride (39.6 mg, 990 µmol, 1.13 eq., 60% (w/w)) in dry THF (3 mL) at 0 °C under argon atmosphere was dropwise added a solution of **6** (150 mg, 867 µmol, 1.0 eq.) in dry THF (3 mL) over 10 min. The resulting mixture was stirred for

20 min at 0 °C. After the dropwise addition of propargyl bromide (147 mg, 990 µmol, 1.13 eq., 80% (w/w)) at 0 °C the mixture was stirred for 5 min at 0 °C and then at room temperature for an additional 2 h. THF was removed under reduced pressure and the crude mixture was redissolved in water (6 mL) and extracted with diethyl ether (3 × 30 mL). The combined organic layers were washed with saturated aqueous $NaHCO_3$ solution (10 mL), dried over Na_2SO_4 and filtered. The crude was concentrated and purified by column chromatography using a Hex/EtOAc gradient (95:5→9:1→8:1) to obtain the product **7** as a yellow oil (47.9 mg, 229 µmol, 26%). As 69.7 mg of the reactant **6** could be reisolated, overall, it resulted in a yield of 49% of the product **7**. The spectroscopic data are in accordance with literature.[74]

^{1}H-NMR (400 MHz, $CDCl_3$): δ[ppm] = 4.10 (s, 2H), 3.23 (d, *J* = 4.0 Hz, 2H), 2.23 (t, *J* = 2.5 Hz, 1H), 1.47 (s, 9H), 1.09 (t, *J* = 3.8 Hz, 1H).

***N*-((3*H*-diazirin-3-yl)methyl)prop-2-yn-1-amine TFA salt (BPC)**

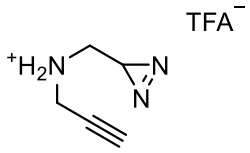

$C_5H_7N_3$ • TFA
M = 223.15 g/mol
BPC

Carbamate **7** (180 mg, 860 µmol, 1.0 eq.) was dissolved in DCM (3 mL) and 50% TFA in DCM (3 mL) was added at 0 °C. After stirring for 2 h at room temperature the reaction mixture was evaporated under reduced pressure to give the TFA salt of **BCP** (259 mg, 1.16 mmol, quant.) as a brown oil. The analytical data were in accordance with the literature values.[74]

^{1}H-NMR (400 MHz, $CDCl_3$): δ[ppm] = 4.06 (d, *J* = 2.6 Hz, 2H), 3.11 (d, *J* = 5.2 Hz, 2H), 2.60 (t, *J* = 2.6 Hz, 1H), 1.37 (t, *J* = 5.2 Hz, 1H).

7-(4-(2-(3-(but-3-yn-1-yl)-3*H*-diazirin-3-yl)ethyl)piperazin-1-yl)-1-cyclopropyl-6-fluoro-4-oxo-1,4-dihydroquinoline-3-carboxylic acid (Cipro P1)

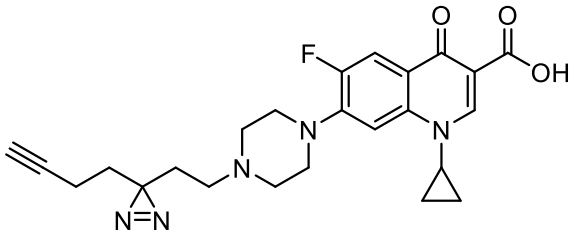

$C_{24}H_{26}FN_5O_3$
M = 451.50 g/mol
Cipro P1

To a suspension of ciprofloxacin (54 mg, 0.165 mmol, 1.0 eq.) and Cs_2CO_3 (194 mg, 0.594 mmol, 3.0 eq.) in H_2O (1.5 mL) was added a solution of **MPC-I** (49 mg, 0.198 mmol, 1.2 eq.) in MeCN (1.5 mL). The reaction was heated to 70 °C in a sealed vial and stirred overnight. The mixture was concentrated in vacuo and the residue dissolved in H_2O and EtOAc. After extraction with EtOAC (3 × 10 mL) and drying of the pooled organic phases over $MgSO_4$, the solvent was removed in vacuo and the crude product purified by reverse phase preparative HPLC (Gradient 2% to 70% MeCN in H_2O) to afford the title compound as white solid (25 mg, 0.055 mmol, 33%) after lyophilization.

^{1}H-NMR (500 MHz, DMSO-d_6): δ[ppm] = 15.11 (br s, 1H), 8.69 (s, 1H), 7.97 (d, *J* = 13.0 Hz, 1H), 7.60 (d, *J* = 7.4 Hz, 1H), 3.84 (td, *J* = 7.2, 3.7 Hz, 1H), 3.40 – 3.14 (br m, 10H), 2.89 (t, *J* = 2.7 Hz, 1H), 2.05 (td, *J* = 7.3, 2.7 Hz, 2H), 1.83 (br s, 2H), 1.66 (t, *J* = 7.4 Hz, 2H), 1.32 (q, *J* = 7.1, 6.3 Hz, 2H), 1.22 – 1.15 (m, 2H). – **^{13}C-NMR** (125 MHz, DMSO-d_6): δ[ppm] = 176.5, 176.4, 165.9, 153.9, 151.9, 148.3, 143.7, 139.1, 119.5, 119.4, 111.4, 111.2, 107.1, 106.9, 83.0, 72.2, 50.7, 50.3, 46.6, 36.0, 30.9, 27.3, 26.7, 12.7, 7.7. – **HR-MS** (ESI) *m/z* for $C_{24}H_{27}FN_5O_3^+$ [$(M+H)^+$]: calcd. 452.2092, found 452.2093.

In the 1H NMR the broad multiplet signal 3.40 – 3.14 (br m, 10H) is due to the aliphatic positions of and next to the piperazine, the signals partially overlay with residual water in DMSO-d6. Complexity arises from coupling with fluorine. Additional signals due to presence of TFA after the reparative HPLC purification are detected in the ^{1}H NMR (δ = 10.05 (br s)) and the ^{13}C NMR (δ[ppm] = 158.5, 158.3, 158.0, 157.8, 118.4, 116.0).

(*S*)-9-fluoro-3,7-dihydro-3-methyl-7-oxo-10-(piperazin-1-yl)-2*H*-[1,4]oxazino[2,3,4-*ij*]quinoline-6-carboxylic acid (1)

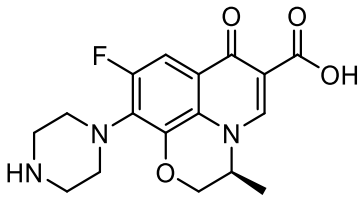

$C_{17}H_{18}FN_3O_4$
M = 347.35 g/mol
1

To a solution of levofloxacin Q-acid (400 mg, 1.42 mmol, 1.0 eq.) in MeCN (15 mL) piperazine (167 µL, 2.13 mmol, 1.5 eq.) was added and the mixture was stirred for 30 min at room temperature. After addition of triethylamine (591 µL, 4.27 mmol, 3.0 eq.) the resulting reaction mixture was heated to reflux for 12 h. The reaction was cooled to room temperature and the precipitate was isolated by filtration, washed with MeCN, refluxed in EtOH and cooled to room temperature overnight. The precipitate was removed by filtration and the supernatant concentrated *in vacuo* to obtain the title compound (245 mg, 705 µmol, 50%) as a green-white solid. The spectroscopic data are in accordance with the literature.[356]

^{1}H-NMR (300 MHz, DMSO-d_6): δ[ppm] = 8.95 (s, 1H), 7.57 (d, *J* = 12.5 Hz, 1H), 4.91 (d, *J* = 6.6 Hz, 1H), 4.57 (d, *J* = 11.3 Hz, 1H), 4.36 (d, *J* = 11.3 Hz, 1H), 3.22 (d, *J* = 6.1 Hz, 4H), 2.81 (t, *J* = 5.0 Hz, 4H), 1.44 (d, *J* = 6.8 Hz, 3H).

(*S*)-10-(4-(2-(3-(but-3-yn-1-yl)-3*H*-diazirin-3-yl)ethyl)piperazin-1-yl)-9-fluoro-3-methyl-7-oxo-2,3-dihydro-7*H*-[1,4]oxazino[2,3,4-*ij*]quinoline-6-carboxylic acid (Levo P1)

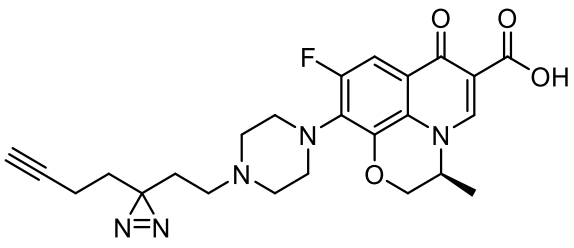

$C_{24}H_{26}FN_5O_4$
M = 467.50 g/mol
Levo P1

To a solution of **1** (50 mg, 0.14 mmol, 1.0 eq.) in H_2O (3 mL) $CsCO_3$ (140 mg, 0.43 mmol, 3.0 eq.) was added. Then minimal **MPC-I** (43 mg, 0.17 mmol, 1.2 eq.) in MeCN (3 mL) was added and the mixture was stirred overnight at 70 °C under argon atmosphere. The reaction mixture was concentrated *in vacuo* to remove MeCN and further lyophilized to remove the water. The crude product was purified by flash column chromatography (5% to 10% MeOH in dichloromethane) and additional preparative HPLC to afford the title compound (47 mg, 0.10 mmol, 70%) as white solid after lyophilization**.**

^{1}H-NMR (400 MHz, $CDCl_3$): δ[ppm] = 15.10 (s, 1H), 9.00 (s, 1H), 7.62 (d, *J* = 12.0 Hz, 1H), 4.99 – 4.90 (m, 1H), 4.59 (dd, *J* = 11.5, 1.8 Hz, 1H), 4.40 (dd, *J* = 11.5, 2.5 Hz, 1H), 3.62 – 3.45 (m, 6H), 3.23 – 3.07 (m, 4H), 2.89 (t, *J* = 2.7 Hz, 1H), 2.06 (td, *J* = 7.4, 2.7 Hz, 2H), 1.93 – 1.80 (m, 2H), 1.65 (t, *J* = 7.4 Hz, 2H), 1.45 (d, *J* = 6.7 Hz, 3H). – **^{13}C-NMR** (125 MHz, DMSO-d_6): δ[ppm] = 176.4, 176.4, 165.9, 156.6, 154.1, 146.4, 140.7, 140.7, 130.3, 130.2, 124.7, 120.7, 120.6, 106.9, 103.4, 103.1, 82.9, 72.0, 68.3, 54.8, 51.7, 50.3, 47.1, 30.9, 27.1, 26.5, 17.9, 12.7. – **HR-MS** (ESI) *m/z* for $C_{24}H_{27}FN_5O_4^+$ [$(M+H)^+$]: calcd. 468.2042, found 468.2036.

Complexity arises from coupling with fluorine. Additional signals due to presence of TFA after the reparative HPLC purification are detected in the ^{1}H NMR (δ = 10.05 (br s)) and the ^{13}C NMR.

7-[4-*tert*-butoxycarbonyl-piperazin-1-yl]-1-cyclopropyl-6-fluoro-1,4-dihydro-4-oxo-quinoline-3-carboxylic acid (8)

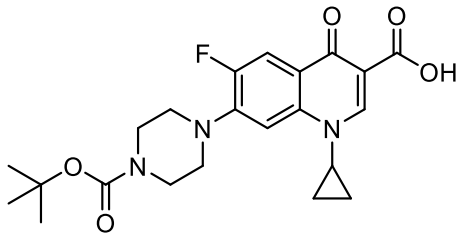

$C_{22}H_{26}FN_3O_5$
M = 431.46 g/mol
8

To a solution of ciprofloxacin (500 mg, 1.51 mmol, 1.0 eq.) in H_2O (4 mL) and dioxane (4 mL) NaOH (90.5 mg, 2.26 mmol, 1.5 eq.) was added. The mixture was cooled to 0 °C and di-*tert*-butyl dicarbonate (494 mg, 2.26 mmol, 1.5 eq.) was added. After stirring for

5 min at 0 °C the reaction mixture was stirred for 3 h at room temperature. The solvent was removed *in vacuo*, acetone (30 mL) was added, and the formed precipitate was filtered off. The filtrate was extracted with DCM (3 × 30 mL), the pooled organic phases washed with brine (50 mL), dried over $MgSO_4$, and concentrated. The residue was combined with the precipitate, providing compound **8** (587 mg, 1.36 mmol, 90%). The spectroscopic data are in accordance with literature values.[357]

^{1}H-NMR (500 MHz, $CDCl_3$): δ[ppm] = 8.79 (s, 1H), 8.06 (d, J = 12.8 Hz, 1H), 7.41 (d, J = 6.9 Hz, 1H), 3.68 (t, J = 5.0 Hz, 4H), 3.54 (s, 1H), 3.30 (t, J = 5.0 Hz, 4H), 1.50 (s, 9H), 1.40 (d, J = 5.6 Hz, 2H), 1.21 (s, 2H).

_N_-((3_H_-diazirin-3-yl)methyl)-1-cyclopropyl-6-fluoro-4-oxo-7-(piperazin-1-yl)-_N_-(prop-2-yn-1-yl)-1,4-dihydroquinoline-3-carboxamide (Cipro P2)

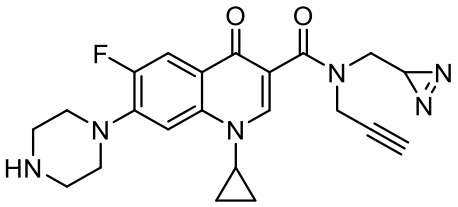

$C_{22}H_{23}FN_6O_2$
M = 422.46 g/mol
Cipro P2

To a solution of **8** (100 mg, 0.23 mmol, 1.0 eq.) in DCM (20 mL) HBTU (220 mg, 0.58 mmol, 2.5 eq.) and DMAP (cat.) were added. After stirring for 10 min at room temperature, DIPEA (202 µL, 1.16 mmol, 5.0 eq.) and **BPC** (32.9 mg, 0.30 mmol, 1.3 eq.) were added. The reaction mixture was heated to reflux for 3 h. The reaction was concentrated *in vacuo* and purified by column chromatography (MeOH:DCM = 2:98 to 4:96) to afford the amine coupling product as a light-yellow solid that was directly subjected to Boc-deprotection conditions. The solid was dissolved in CH_2Cl_2 (3 mL) and 2 mL TFA (50% (v/v) in CH_2Cl_2) was added dropwise at 0 °C. After stirring for 2 h at room temperature, the solvent was removed *in vacuo* and the crude product was purified by preparative HPLC (2-70% MeCN in H_2O over 26 min), affording compound **Cipro P2** (45.4 mg, 0.11 mmol, 46% over 2 steps) as a colorless solid.

^{1}H-NMR (500 MHz, $CDCl_3$): δ[ppm] = 9.96 (s, 2H), 8.08 (s, 1H), 7.95 (d, *J* = 12.7 Hz, 1H), 7.36 (d, *J* = 6.9 Hz, 1H), 4.34 (d, *J* = 153.2 Hz, 2H), 3.56 – 3.44 (m, 8H), 3.32 (s, 1H), 2.56 – 2.15 (m, 3H), 1.33 (d, *J* = 6.9 Hz, 3H), 1.18 – 1.11 (m, 2H). – **^{13}C-NMR** (125 MHz, $CDCl_3$): δ[ppm] = 172.4, 172.2, 167.5, 154.3, 152.3, 144.9, 143.6, 143.5, 138.5, 122.6, 122.6, 113.1, 113.0, 105.8, 78.5, 72.7, 47.0, 43.6, 34.7, 19.9, 8.3, 1.1. – **HR-MS** (ESI) *m/z* for $C_{22}H_{24}FN_6O_2^+$ [$(M+H)^+$]: calcd. 423.1939, found 423.1939.

Complexity arises from coupling with fluorine. Additional signals due to presence of TFA after the reparative HPLC purification are detected in the ^{1}H NMR and the ^{13}C NMR.

(*S*)-*N*-((3*H*-diazirin-3-yl)methyl)-9-fluoro-3-methyl-10-(4-methylpiperazin-1-yl)-7-oxo-*N*-(prop-2-yn-1-yl)-2,3-dihydro-7*H*-[1,4]oxazino[2,3,4-*ij*]quinoline-6-carboxamide (Levo P2)

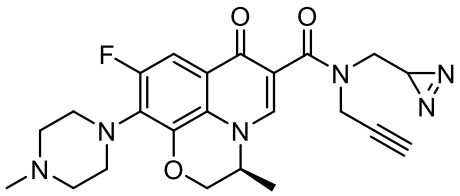

$C_{23}H_{25}FN_6O_3$
M = 452.49 g/mol
Levo P2

To a solution of levofloxacin (100 mg, 0.28 mmol, 1.0 eq.) in DCM (24 mL) HBTU (262 mg, 0.69 mmol, 2.5 eq.) and DMAP (cat.) were added. After stirring for 10 min at room temperature, DIPEA (242 µL, 1.38 mmol, 5.0 eq.) and **BCP** (39.3 mg, 0.36 mmol, 1.3 eq.) were added. The reaction mixture was heated to reflux for 3 h. Subsequently, the mixture was concentrated *in vacuo* and purified by preparative HPLC (2-70% MeCN in H_2O over 26 min) to obtain the product **Levo P2** (43.2 mg, 0.96 mmol, 35%) as a brown oil.

^{1}H-NMR (400 MHz, $CDCl_3$): δ[ppm] = 7.85 (s, 1H), 7.38 (t, *J* = 10.5 Hz, 1H), 4.46 (s, 1H), 4.40 – 4.31 (m, 3H), 4.22 – 4.01 (m, 1H), 3.54 (s, 4H), 3.40 (t, *J* = 19.5 Hz, 1H), 3.15 (s, 4H), 2.76 (s, 3H), 2.27 (t, *J* = 2.5 Hz, 1H), 1.98 (s, 2H), 1.49 (s, 3H), 1.32 – 1.21 (m, 1H). – **^{13}C-NMR** (125 MHz, $CDCl_3$): δ[ppm] = 171.6, 167.4, 167.2, 156.3, 154.3, 142.7, 142.3, 140.2, 140.2, 129.7, 129.6, 124.4, 122.9, 116.6, 116.3, 104.6, 104.4, 104.3, 78.7, 78.4, 73.4, 72.6, 68.3, 54.6, 54.3, 48.9, 48.3, 45.7, 44.3, 39.6, 35.3, 20.0, 19.8, 18.4, 2.0. – **HR-MS** (ESI) *m/z* for $C_{23}H_{26}FN_6O_3^+$ [$(M+H)^+$]: calcd. 453.2045, found 453.2040.

Complexity arises from coupling with fluorine. Additional signals due to presence of TFA after the reparative HPLC purification are detected in the ^{1}H NMR and the ^{13}C NMR.

1-cyclopropyl-6-fluoro-4-oxo-7-(4-sulfopiperazin-1-yl)-1,4-dihydroquinoline-3-carboxylic acid (Sulfo-Cipro)

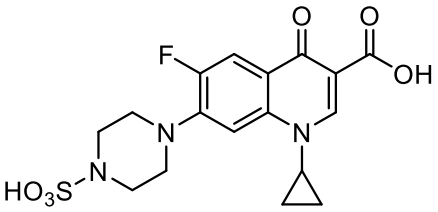

$C_{17}H_{18}FN_3O_6S$
M = 411.40 g/mol
Sulfo-Cipro

Ciprofloxacin (99.4 mg, 0.3 mmol, 1 eq.) and triethylamine (84 µL, 0.6 mmol, 2 eq.) were dissolved in DCM (3 mL) and cooled to 0 °C. Chlorosulfonic acid (20 µL, 0.3 mmol, 1 eq.) was added dropwise and the mixture was stirred at room temperature overnight. More chlorosulfonic acid (20 µL, 0.3 mmol, 1 eq.) was added dropwise and the mixture was stirred for another 2 h. The solvent was removed *in vacuo*, the residue was suspended in water and filtered off. Purification with prep-HPLC and subsequent removal of the aqueous solvent mixture by lyophilization gave **Sulfo-Cipro** as a pale-yellow powder (9 mg, 0.02 mmol, 7%).

^{1}H-NMR (400 MHz, DMSO-d_6): δ[ppm] = 15.15 (s, 1H), 8.87 (s, 1H), 8.68 (d, J = 13.4 Hz, 1H), 7.95 (dd, J = 21.9, 13.2 Hz, 1H), 7.60 (dd, J = 11.6, 7.4 Hz, 1H), 3.90 – 3.80 (m, 1H), 3.57 – 3.48 (m, 4H), 3.42 (t, J = 5.0 Hz, 2H), 3.17 (t, J = 4.9 Hz, 2H), 1.37 – 1.28 (m, 2H), 1.22 – 1.14 (m, 2H). – **^{13}C NMR** (126 MHz, DMSO-d_6) δ[ppm] = 176.8, 176.8, 166.3, 154.3, 152.3, 148.7, 144.5, 144.5, 139.5, 119.9, 119.8, 111.8, 111.6, 107.4, 107.3, 46.9, 46.9, 43.1, 40.4, 40.2, 40.1, 39.9, 39.7, 39.6, 39.4, 36.4, 8.1. – **LR-MS** (ESI) *m/z* for $C_{17}H_{17}FN_3O_6S^-$ [$(M-H)^-$]: 410.08; found: 410.27.

Complexity in the spectroscopic signals arises from coupling with fluorine.

1-cyclopropyl-6-fluoro-7-(4-formylpiperazin-1-yl)-4-oxo-1,4-dihydroquinoline-3-carboxylic acid (Formyl-Cipro)

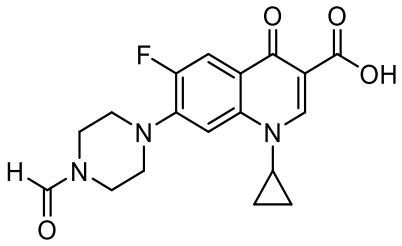

$C_{18}H_{18}FN_3O_4$
M = 359.36 g/mol
Formyl-Cipro

Ciprofloxacin (66.3 mg, 0.2 mmol, 1 eq.) was dispersed in DMF (1.0 mL). The reaction mixture was stirred at 120 °C for 48 h under argon atmosphere. The solvent was removed *in vacuo*, and the crude product was recrystallized from methanol, yielding **Formyl-Cipro** (34.4 mg, 0.10 mmol, 50%) as an off-white solid.

^{1}H NMR (400 MHz, DMSO-d_6) δ[ppm] = 15.07 (s, 1H), 8.67 (s, 1H), 8.13 (s, 1H), 7.92 (d, J = 13.1 Hz, 1H), 7.60 (d, J = 7.4 Hz, 1H), 3.87 – 3.77 (m, 1H), 3.62 (q, J = 5.4 Hz, 4H), 3.36 (t, J = 5.1 Hz, 2H), 3.30 (t, J = 5.2 Hz, 2H), 1.38 – 1.29 (m, 2H), 1.23 – 1.16 (m, 2H). – **^{13}C NMR** (126 MHz, DMSO-d_6) δ[ppm] = 176.8, 176.8, 166.3, 161.5, 154.4, 152.5, 148.6, 145.4, 145.3, 139.5, 119.5, 119.4, 111.5, 111.4, 107.5, 107.5, 107.2, 50.6, 50.6, 49.5, 49.5, 44.9, 40.4, 40.2, 40.1, 39.9, 39.7, 39.6, 39.4, 39.4, 36.3, 8.0. – **LR-MS** (ESI-Quadrupole): m/z: $[M+H]^+$ calcd. for $C_{18}H_{19}FN_3O_4^+$: 360.14; found: 360.34. – **HR-MS** (ESI) *m/z* for $C_{18}H_{19}FN_3O_4^+$ $[(M+H)^+]$: calcd. 360.1354, found 360.1355.

Complexity in the spectroscopic signals arises from coupling with fluorine.

***tert*-butyl (2-aminoethyl)carbamate (12)**

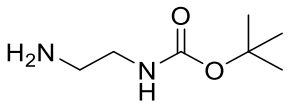

$C_7H_{16}N_2O_2$
M = 160.21 g/mol
12

1,2-Diaminoethane (180 mg, 3.0 mmol, 1 eq.) was dissolved in THF (3 mL). Di-*tert*-butyldicarbonat (196 mg, 0.9 mmol, 0.33 eq.) in THF (1.5 mL) was added dropwise to the

first solution at 0 °C. The mixture was stirred for 30 min, before it was warmed to RT and stirred overnight. The solvent was removed, the residue was taken up in EtOAc, washed with brine and dried, providing **12** (103 mg, 0.64 mmol, 71%) as a pale yellow, highly viscous oil. The crude product was directly used in the next step without further purification.

LR-MS (ESI-Quadrupole): *m/z* $[M+H]^+$ calcd. for $C_7H_{17}N_2O_2^+$: 161.13; found: 161.20.

7-((2-aminoethyl)amino)-1-cyclopropyl-6-fluoro-4-oxo-1,4-dihydroquinoline-3-carboxylic acid (Desethylen-Cipro)

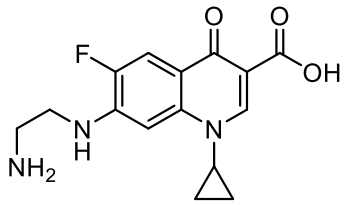

$C_{15}H_{16}FN_3O_3$
M = 305.31 g/mol
Desethylen-Cipro

1-cyclopropyl-6,7-difluoro-1,4-dihydro-4-oxoquinoline-3-carboxylic acid (**10**, 94 mg, 0.35 mmol, 1 eq.) was dissolved in DMSO (0.7 mL). DABCO (79 mg, 0.71 mmol, 2 eq.) and *tert*-butyl-(2-aminoethyl)carbamate (**12**, 68 mg, 0.42 mmol, 1.2 eq.) were added. The mixture was heated to 130 °C for 1 h, then cooled to room temperature and adjusted to pH 5 with 1 M HCl (aq.). After water (0.7 mL) was added, the precipitate was filtered off and washed with water and methanol. The resulting powder was dried before it was dissolved in 1 mL of a 1:3 mixture of TFA and DCM. The mixture was stirred at room temperature for 24 h. The solvents were removed *in vacuo* and the crude product was recrystallized from methanol to afford **Desethylen-Cipro** (69 mg, 0.23 mmol, 65%) as a white solid.

^{1}H NMR (400 MHz, DMSO-d_6) δ[ppm] = 15.54 (s, 1H), 8.59 (s, 1H), 8.01 (s, 3H), 7.82 (d, J = 11.8 Hz, 1H), 7.17 (d, J = 7.3 Hz, 1H), 7.13 (td, J = 5.7, 2.4 Hz, 1H), 3.86 – 3.70 (m, 1H), 3.59 (q, J = 6.1 Hz, 2H), 3.14 (t, J = 6.2 Hz, 2H), 1.41 – 1.27 (m, 2H), 1.19 – 1.11 (m, 2H). – **^{13}C NMR** (101 MHz, DMSO-d_6) δ[ppm] = 176.5, 176.4, 166.6, 158.9, 158.6, 151.7, 149.2, 147.6, 142.6, 142.5, 140.8, 114.8, 114.8, 109.5, 109.3, 106.8, 97.2, 97.2, 40.6, 40.4, 40.2, 39.9, 39.7, 39.5, 39.3, 37.6, 36.3, 8.0. – **LR-MS** (ESI-Quadrupole): m/z: $[M+H]^+$ calcd.

for $C_{15}H_{17}FN_3O_3^+$: 306.12; found: 306.33. – **HR-MS** (ESI) *m/z* for $C_{15}H_{17}FN_3O_3^+$ [$(M+H)^+$]: calcd. 306.1248, found 306.1248.

Complexity in the spectroscopic signals arises from coupling with fluorine.

1-cyclopropyl-6-fluoro-4-oxo-7-(3-oxopiperazin-1-yl)-1,4-dihydroquinoline-3-carboxylic acid (Oxo-Cipro)

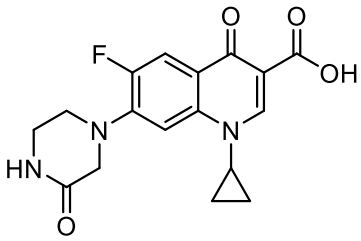

$C_{17}H_{16}FN_3O_4$
M = 345.33 g/mol
Oxo-Cipro

1-cyclopropyl-6,7-difluoro-1,4-dihydro-4-oxoquinoline-3-carboxylic acid (**10**, 53 mg, 0.2 mmol, 1 eq.) was dissolved in DMSO (0.5 mL). DABCO (45 mg, 0.4 mmol, 2 eq.) and piperazin-2-one (**13**, 24 mg, 0.24 mmol, 1.2 eq.) were added. The mixture was heated to 130 °C for 1 h, then cooled to room temperature and adjusted to pH 5 with 1 M HCl (aq.). After water (0.5 mL) was added, the precipitate was filtered off and washed with water and methanol to give **Oxo-Cipro** (14 mg, 0.04 mmol, 20%) as a white powder.

^{1}H NMR (500 MHz, DMSO-d_6) δ[ppm] = 8.68 (s, 1H), 8.21 (s, 1H), 7.95 (d, *J* = 13.4 Hz, 1H), 7.55 (d, *J* = 7.5 Hz, 1H), 3.97 (s, 2H), 3.88 – 3.81 (m, 1H), 3.62 (dd, *J* = 6.4, 4.3 Hz, 2H), 3.41 – 3.38 (m, 2H), 1.35 – 1.29 (m, 2H), 1.22 – 1.17 (m, 2H). – **^{13}C NMR** (126 MHz, DMSO-d_6) δ[ppm] = 176.4, 166.3, 166.0, 148.1, 139.2, 129.7, 106.7, 52.3, 46.5, 36.0, 35.1, 31.3, 29.1, 28.7, 22.1, 14.0, 7.6. – **LR-MS** (ESI-Quadrupole): m/z: $[M+H]^+$ calcd. for $C_{17}H_{17}FN_3O_4^+$: 346.12; found: 346.31. – **HR-MS** (ESI) *m/z* for $C_{17}H_{17}FN_3O_4^+$ [$(M+H)^+$]: calcd. 346.1198, found 346.1200.

Complexity in the spectroscopic signals arises from coupling with fluorine.

2. Materials and methods of the nitroimidazole project

The experimental procedures for this project have been published with the publication and is additionally provided in this dissertation.[71]

2.1 Biochemistry and proteomics experiments

2.1.1 Minimal inhibitory concentrations (MIC) assay

MIC were determined with the broth dilution method. The overnight culture was diluted 1:10,000 in fresh medium and 99 µL aliquots were added to 96-well plates containing various concentrations of compounds (1 µL in DMSO) and DMSO (1 µL) as a negative control in triplicates. After 20 h incubation at 200 rpm at 37 °C, the turbidity of the wells was analysed.

2.1.2 MIC shift assay

The MIC shift assay was performed similarly as described before.[358] Briefly, salmon sperm DNA (low molecular weight, *Sigma Aldrich*) was dissolved in TE buffer (10 mM Tris, pH 8.0, 0.1 mM ethylenediaminetetraacetic acid, EDTA). Serial dilutions of the compounds (1 µL, 1:100 stock) in triplicates with or without DNA (0, 500, 50, 5 µg/mL) were prepared in 96-well plates with a total volume of 50 µL and preincubated at 37 °C for 30 min. Subsequently, a bacterial overnight culture was diluted 1:5000 in B medium and 50 µL each added to the wells. The MICs were determined as described in 2.3 after 20 h incubation at 200 rpm at 37°C.

2.1.3 Nitroreductase absorbance assay

Recombinant *E. coli* nitroreductase NfsB was a gift from Dr. Stephan Hacker. In a 96-well plate, 100 µM nitroimidazole indolin-2-one hybrid **1** was incubated in the presence of 1 mM NADH with or without recombinant NfsB (15 µM) in phosphate buffer (50 mM, pH 7.0). The total reaction volume was 100 µL. Each condition was measured in quadruplicates. The conversion of nitroimidazole indolin-2-one hybrid **1** was observed by the decrease of absorbance at 355 nm (λ_{max} of **1**) using a *Tecan Infinite M200Pro* measuring with 1 min intervals at 25 °C. The data was plotted using *GraphPad Prism* 5.03.

2.1.4 Topoisomerase IV Decatenation Assay

S. aureus topoisomerase IV decatenation assay kit was purchased from *Inspiralis* and conducted according to manufacturer conditions. Briefly, 1 U *S. aureus* topoisomerase IV was used to decatenate 200 ng kDNA by incubating in presence of controls or compound in provided assay buffer (10 mM Tris pH 7.5, 1 mM $MgCl_2$, 1 mM DTT, 0.3 mM ATP, 70 mM potassium glutamate, 0.01 mg/mL albumin) in 30 µL total volume for 30 min at 37 °C. The reactions were stopped by addition of 2.25 µL EDTA (250 mM) and mixed with appropriate amounts of agarose loading buffer. 10 µL aliquots were separated on a 0.8% agarose gel at 80 V for 1 h. Since an intercalator (Gel-Red, *Biotium*) was present for visualisation, decatenated products resolved in open circular and relaxed forms. Bands were quantified using *ImageJ* (version 1.53a) and the data was plotted using *GraphPad Prism* 5.03. The data represent results from 3 independent experiments performed with triplicates for each condition.

2.1.5 MTT Assay

Cell viability assays were performed in HeLa cells cultured in DMEM medium (*Sigma Aldrich*) supplemented with 10% FCS (*Sigma Aldrich*) and 2 mM glutamine (*Sigma Aldrich*) in 5% CO_2 atmosphere at 37 °C. During standard cell passaging Accutase® (*Sigma Aldrich*) was used for cell detachment. HeLa cells (4,000 per well) were seeded into a 96-well plate and grown for 24 h. Subsequently, the medium was carefully removed by suction and 100 µL FCS-free medium with either DMSO (1% (v/v)) or a concentration range of compound 1 (1% final DMSO concentration) was added. The cells were grown in presence of the compound and controls for 24 h and 20 µL thiazolyl blue tetrazolium bromide (MTT, 5 mg/mL in PBS, *Sigma Aldrich*) were added and incubated for 2 h at 37 °C, 5% CO_2 to allow the MTT reagent to be metabolized. The medium was removed by suction and the formed formazan crystals dissolved in 200 µL DMSO. The read-out was performed with a *Tecan* Infinite M200 microplate reader at 570 nm and background was subtracted at 630 nm. The absorbance values were normalized to DMSO controls and the apparent IC_{50} value calculated in *GraphPad Prism* (Version 5.03) by regression. The experiment was performed with triplicates per condition in four independent experiments.

2.1.6 Frequency of resistance assay

Aliquots of 100 µL of an overnight culture of *S. aureus* NCTC8325 were plated with sterile glass beads in triplicates on selective B agar plates (**1** or Ciprofloxacin, *Sigma Aldrich*, 4x MIC or 6x MIC; MIC (Ciprofloxacin) = 310 nM, determined *via* MIC broth dilution assay). The total number of viable cells was determined simultaneously by plating appropriate dilutions on non-selective B agar plates (colony forming unit (CFU) assay). Colonies were counted after 24 h incubation at 37 °C. The frequency of resistance was calculated by dividing the mean number of resistant colonies by the total number of viable cells in the 100 µL aliquots.

2.1.7 Analytical gel-based ABPP

Bacterial strains were cultivated under defined growth conditions to stationary phase. Cultures were collected in a 50 mL falcon tube, pelletized (6,000 g, 10 min, 4 °C) and washed with PBS (pH = 7.4). The pellet was then resuspended in PBS to a final OD600 = 40. To 200 µL aliquots of the adjusted bacterial suspension, 2 µL of the respective activity-based probe (1:100) or DMSO as a control were added, the suspension mixed and incubated for 2 h at 200 rpm at 37 °C. The bacterial suspension was centrifuged (6,000 g, 10 min, 4 °C), the supernatant was removed and the pellets were stored at –80 °C. Pellets were resuspended in 200 µL PBS (4 °C) and the suspension was lysed by sonication (five times, 20 sec pulses, 80% intensity) on ice. The suspension was incubated two times for 0.5 h at 200 rpm at 37 °C after addition of 4 µL of lysostaphin (2 mg/mL, *Sigma Aldrich*) and then 6 µL of 10% (w/v) SDS in PBS solution in that order. Subsequently, click chemistry was carried out with 20 µL Click reagent mix (4 µL RhN3(5 mM rhodamine-azide in DMSO), 4 µL TCEP (50 mM tris(2-carboxyethyl)phosphine in ddH_2O), 12 µL TBTA ligand (1.667 mM Tris(benzyltriazolylmethyl)amine in 80% tBuOH and 20% DMSO). After shortly vortexing the samples, the Click reaction was initiated by adding 4 µL of $CuSO_4$ solution (50 mM in ddH2O). The mixture was incubated for 1 h at room temperature and the reaction stopped by addition of 200 µL 2x SDS-gel loading buffer. After the samples were heated up to 95 °C for 10 min at 600 rpm, they were shortly centrifuged. 40 µL of each sample was applied on the analytical SDS-PAGE gel, which was developed for 3 h under 150 V under constant cooling. Fluorescent bands were visualized by a *Fujifilm* Las-3000 Fluorescence Darkbox with a *Fujinon* VRF 43LMD Lens, 605DF40 filter and 520 nm EPI excitation wavelength. Subsequently, total protein bands were visualized by Coomassie staining as loading controls.

2.1.8 Gel-free quantitative ABPP

An overnight culture of the bacteria was grown. After 1:100 dilution of the culture with fresh medium, the cultures were grown until stationary phase. Cultures were collected in a 50 mL falcon tube and centrifuged (6,000 g, 10 min, 4 °C). The supernatant was disposed and the pellet was resuspended in PBS to reach OD_{600} = 40. 500 µL of this suspension and 5 µL of the respective activity-based probe (1:100 in DMSO) or DMSO as a control were mixed and incubated for 2 h at 200 rpm at 37 °C. The bacterial suspension was centrifuged (6,000 g, 10 min, 4 °C), the supernatant was removed and the pellets were stored at –80 °C. Pellets were resuspended in 500 µL PBS (4 °C) and the suspension was lysed by sonication with 5 x 20 sec pulsed at 80% max. power on ice. The suspension was incubated two times for 0.5 h at 200 rpm at 37 °C after each addition of first 10 µL of lysostaphin (2 mg/mL, *Sigma Aldrich*) and then 25 µL of 10% (w/v) SDS in PBS solution. Protein concentration was determined using a bicinchoninic acid (BCA, *Roth*) assay and the concentration was adjusted to 1 mg/mL with PBS. In a 15 mL falcon tube, 500 µL of the adjusted solution were treated with 43 µL Click reagent mix (3 µL Biotin-PEG3-N3 (*Jena Bioscience*, CLK-AZ104P4-100, 10 mM in DMSO), 10 µL TCEP (50 mM in ddH_2O), 30 µL TBTA ligand (*abcr*, 1.667 mM in 80% tBuOH and 20% DMSO)). Resulting in final concentrations of: 233 µM Biotin-PEG3-N3, 581 µM TCEP and 58.2 µM TBTA Ligand. The lysates were mixed by vortexing and 10 µL $CuSO_4$ solution (50 mM in ddH_2O) were added to start the click reaction. The lysates were mixed by vortexing and incubated for 1 h at room temperature in the dark. Subsequently, 4 mL of cold acetone (–80 °C, MS grade) were added and proteins were precipitated overnight at –80 °C. The precipitated proteins were pelletized (10,000 g, 15 min, 4 °C) and the supernatant was disposed. Proteins were washed two times with 1 mL cold methanol (–80 °C, MS grade). Resuspension was achieved by sonication (10 s, 10% intensity) and proteins were pelletized *via* centrifugation (10,000 g, 10 min, 4 °C). After the washing steps the supernatant was disposed and the pellet resuspended in 500 µL 0.4% SDS in PBS at room temperature by sonication (10 s, 10% intensity). 50 µL avidin-agarose beads (*Sigma Aldrich*) were prepared by washing three times with 1 mL 0.4% SDS in PBS. All centrifugation steps were conducted at 400 g for 3 min at room temperature. 500 µL protein solution was added to the washed avidin-agarose beads and incubated under continuous inverting (1 h, room temperature). Beads were washed three times with 1 mL 0.4% SDS in PBS, two times with 6 M urea in ddH_2O and three times with 1 mL PBS. The beads were resuspended in 200 µL denaturation buffer (7 M urea, 2 M thiourea in 20 mM pH 7.5 HEPES buffer). For reduction, Dithiothreitol (DTT, *Sigma Aldrich*, 500 mM, 0.4 µL) was added, the

tubes were mixed by vortexing shortly and incubated in a thermoshaker (600 rpm, 60 min, room temperature). Then 2-iodoacetamide (IAA, *Sigma Aldrich*, 500 mM, 4 µL) was added for alkylation, the tubes were mixed by vortexing shortly and incubated in a thermoshaker (600 rpm, 30 min, room temperature, in the dark). Remaining IAA was quenched by the addition of dithiothreitol (DTT, 500 mM, 4 µL). The tubes were shortly mixed by vortexing and incubated in a thermoshaker (600 rpm, 30 min, room temperature). LysC (*Fujifilm*, 0.5 µg/µL) was thawed on ice and 1 µL was added to each microcentrifuge tube, the tubes were shortly mixed by vortexing and incubated in a thermoshaker (600 rpm, 2 h, room temperature, in the dark). Triethylammonium bicarbonate (TEAB) solution (600 µL, 50 mM in water) and then trypsin (*Promega*, 1.5 µL, 0.5 µg/µL in 50 mM acetic acid) were added to each tube with a short vortexing step after each addition. The microcentrifuge tubes were incubated in a thermoshaker (600 rpm, 15 h, 37 °C). The digest was stopped by adding 10 µL formic acid (FA) and vortexing followed by centrifugation (13,000 g, 3 min, room temperature). 50 mg SepPak C18 columns (*Waters*) were equilibrated by gravity flow two times with 1 mL acetonitrile and three times with 1 mL aqueous 0.1% trifluoroacetic acid (TFA) solution. Subsequently, the samples were loaded by gravity flow, washed three times with 1 mL aqueous 0.1% TFA solution and once with 0.5 mL aqueous 0.5% formic acid (FA) solution. Elution of peptides into new 2.0 mL Protein LoBind *Eppendorf* tubes was performed by two times addition of 250 µL elution buffer (80% acetonitrile, 0.5% FA) by gravity flow followed by 250 µL elution buffer by vacuum flow until all liquid was eluted from the column. The eluates were lyophilized. Before MS measurement the samples were dissolved in 30 µL 1% FA by pipetting up and down, vortexing and sonication for 15 min (brief centrifugation after each step). 0.22 µm centrifugal filter units (*VWR*) were equilibrated with 300 µL 1% FA (13,000 g, 2 min, room temperature) and samples were filtered through the equilibrated filters (centrifugation: 13,000 g, 1 min, room temperature). Samples were analyzed with an UltiMate 3000 nano HPLC system (*Dionex*) using Acclaim C18 PepMap100 75µm ID x 2 cm trap and Acclaim PepMap RSLC C18 (75 µm ID x 50 cm) separation columns in an EASY-spray setting coupled to a Qexactive Plus (*Thermo Fisher*). 5 µL peptide samples were loaded on the trap column and washed with 0.1% TFA, then transferred to the separation column (buffer A: H2O with 0.1% FA, buffer B: MeCN with 0.1% FA, flow 0.3 µL/min, gradient: to 5% buffer B in 7 min, from 5% to 22% buffer B in 105 min, then to 32% buffer B in 10 min, to 90% buffer B in 10 min and hold at 90% buffer B for 10 min, then to 5% buffer B in 0.1min and hold 5% buffer B for 9.9 min) and ionized at spray voltage of 2.0 kV and a capillary temperature of 275°C. The Q Exactive

Plus was operated in a TOP12 data dependent mode with full scan acquisition in the orbitrap at a resolution of R = 140,000 and an AGC target of $3e^6$ in a scan range of 300-1500 m/z with a maximum injection time of 80 ms. Monoisotopic precursor selection as well as dynamic exclusion (dynamic exclusion duration: 60 s) was enabled. Precursors with charge states >1 and intensities greater than $1e^4$ were selected for fragmentation. Isolation was performed in the quadrupole using a window of 1.6 m/z. Precursors were analyzed in a scan range of 200–2000 m/z to an AGC target of $1e^5$ and a maximum injection time of 100 ms. Peptide fragments were generated by higher-energy collisional dissociation (HCD) with a normalized collision energy of 27% and detected in the orbitrap.

2.1.9 Proteomic data processing and statistical analysis

Peptide and protein identifications were performed using *MaxQuant* 1.6.17.0 software with *Andromeda* as search engine using following parameters: Cysteine carbamidomethylation was set as fixed modification and methionine oxidation and N-terminal acetylation as variable modifications, trypsin (without N-terminal cleavage to proline) as the proteolytic enzyme with max. of 2 missed cleavages. Label-free quantification (LFQ) mode was performed with a minimum ratio count of 2. Searches were performed with the Uniprot database for *S. aureus* NCTC8325 (taxon identifier: 93061, downloaded on 13.05.2021). The “match between runs” (0.7 min match and 20 min alignment time window) and second peptide identification options were activated. All other parameters were used as pre-set in the software.

Statistical analysis was performed with Perseus 1.6.2.2. LFQ intensities were log2(x) transformed. Putative contaminants, reverse peptides and peptides only identified by site were deleted. Valid values were filtered for three in at least one group and a missing values imputation was performed over the total matrix (width 0.3, downshift 1.8). A two-sample student`s t-test with permutation-based FDR (0.05) and the significance cut-off was set at p-value = 0.05 (-log10(p-value) = 1.3) and an enrichment factor of 2 (log2(x) = 1) or 4 (log2(x) = 2) as indicated in the plots.

2.1.10 Competition ABPP experiment

The procedure was followed as described in gel-free ABPP in chapter 3.1.2, but for competition, the bacteria suspension was pretreated with the parent compound in DMSO (or

just DMSO as a control) for 45 min at 200 rpm at 37 °C, and then treated with the alkyne probe in DMSO for 45 min at 200 rpm at 37 °C.

2.1.11 Full proteome analysis

An overnight culture of *S. aureus* was grown in 5 mL B medium in a plastic culture tube. After 1:100 dilution of the culture with fresh B medium, the cultures were grown for 2 h until the OD_{600} value was between 0.4 and 0.6. The cultures were diluted into B medium to give a final OD_{600} of 0.3 and then 12 mL diluted cultures were incubated with the 0.5x MIC concentration (60 nM) of compound **1** in DMSO or DMSO as control, in triplicates respectively, for 2 h at room temperature. The bacteria suspension was centrifuged at 6,000 g for 10 min at 4 °C and the supernatant was disposed. The pellet was washed with PBS and again centrifuged at 6,000 g for 10 min at 4 °C. The supernatant was removed and the pellets were stored at –80 °C. Pellets were resuspended in 200 µL 100 mM Tris pH 7.4 and lysed by sonication with 5 x 20 s pulses at 80% intensity on ice. 75 µL solution of 10% (w/v) SDS and 1.25% (w/v) sodium deoxycholate in lysis buffer was added and samples heated for 10 min at 90 °C. Lysates were sonicated for 10 s at 10% intensity to shear nucleic acids and centrifuged at 10,000 g for 15 min at 4 °C to pellet debris. The protein concentration was determined using a bicinchoninic acid (BCA) assay and the concentration was adjusted to 1 mg/mL with PBS, and the samples were adjusted to equal protein amounts (0.5 mg/mL). Subsequently, proteins were precipitated with 4 mL of cold acetone (–80 °C, MS grade) overnight at –80 °C. The precipitated proteins were thawed on ice, pelletized (12,000 g, 20 min, 4 °C) and the supernatant was disposed. The proteins were washed three times with 1 mL cold methanol (–80 °C, MS grade). Resuspension was achieved by sonication (10 sec at 10% intensity) and the proteins were pelletized *via* centrifugation (12,000 g, 20 min, 4 °C). The following steps from digestion to filtering, were performed as described in gel-free ABPP in chapter 3.1.2 (without the enrichment step). Samples were analyzed *via* HPLC-MS/MS using an UltiMate 3000 nano HPLC system (*Dionex*, Sunnyvale, California, USA) equipped with an *Acclaim* C18 PepMap100 75 µm ID x 2 cm trap and an *Acclaim* C18 PepMap RSLC, 75 µM ID x 15 cm separation columns coupled to Thermo Fischer Orbitrap Fusion (*ThermoFisher* Scientific Inc., Waltham, Massachusetts, USA). Samples were loaded on the trap and washed for 10 min with 0.1% FA (at 5 µL/min), then transferred to the separation column and separated using a, 112 min gradient from 4% to 35% MeCN followed by 4 min at 80% MeCN in 0.1% FA (at 200 nL/min flow rate). The LTQ Orbitrap Fusion

was operated in a 3 second top speed data dependent mode. The full scan acquisition was performed in the orbitrap at a resolution of 120,000 and an ion target of $4e^5$ in a scan range of 300 –1700 m/z. The monoisotopic precursor selection as well as the dynamic exclusion for 60 sec were enabled. Precursors with charge states of 2 –7 and intensities greater than $5e^3$ were selected for fragmentation. Isolation was performed in the quadrupole using a window of 1.6 m/z. Precursors were collected to a target of $1e^2$ for a maximum injection time of 250 ms with "inject ions for all available parallelizable time" enabled. Fragments were generated using higher-energy collisional dissociation (HCD) and detected in the ion trap at a rapid scan rate. Internal calibration was performed using the ion signal of fluoranthene cations (EASY-ETD/IC source). MS raw files were processed with MaxQuant version 1.6.17.0 as described above. Statistical analysis was performed as described above using Perseus version 1.6.2.2, with the difference that filtering of valid values was performed with "at least 3 valid values in each group".

2.1.12 Redoxpotential Measurements

Cyclic voltammetry measurements were carried out with a BioLogic SP200 potentiostat with the EC-Lab software. Glassy carbon disk electrodes (3 mm diameter, PalmSens, Houten, Netherlands) were used as working and counter electrodes. Ag/AgCl (1 M KCl) was used as a reference electrode separated via a Vycor 3535 frit (Advanced Glass & Ceramics, Holden, MA). Measurements were performed in a five-neck glass cell under argon atmosphere, on samples (c = 1 mM) in deoxygenated 6:4 DMF:citrate buffer (15 mM, pH 9.0, 300 mM KCl, 100 mM tetra-*n*-butylammonium iodide, TBAI), with a scan rate of 100 mV/s, unless noted otherwise. Redox potentials are reported with reference to the normal hydrogen electrode ($E(Ag/AgCl;1\ M\ KCl) = 236\ mV_{NHE}$; V_{NHE} = potential vs. normal hydrogen electrode (NHE)).

2.2 Chemical synthesis

Synthetic procedures of the probe syntheses by Kyu M. Lee are given in the publication and the supporting information of the publication. Additionally synthesized derivatives are additionally described here in the dissertation. NMR spectra of all final probes and derivatives needed for the *E*-configuration determination are given in the appendix.

2.1 General working methods

All air or water sensitive reactions were carried out under inert-gas atmosphere (Argon) in oven-dried glassware with anhydrous solvents utilising standard Schlenk-techniques unless notes otherwise. Reagents and solvents were purchased from *Sigma-Aldrich*, *Alfa Aesar*, *Acros Organics*, *TCI Europe* or *Merck* and were of reagent grade or better and used without further purification. All reactions were magnetically stirred and temperatures measured externally. Yields refer to isolated homogeneous and spectroscopically pure materials. Sensitive samples were stored in a freezer (–20 °C). Solvents were removed *in vacuo* at 42 °C. Reactions and fractions of flash column chromatography were monitored by qualitative thin layer chromatography /TLC) on aluminium-baked TLC silica gel plates (TLC Silica gel 60 F_{254}, *Merck KGaA*). In order to visualize the substances on the plates UV light (λ_{max} = 254 nm) and staining solutions, such as $KMnO_4$, CAM and *p*-anisaldehyde, were used. Flash column chromatography (FCC) was performed with slurry packed silica gel (40-63 μm) from VWR and elution solvents distilled prior to use. NMR spectra were recorded using an internal deuterium lock at ambient probe temperature on a Bruker instruments (300 MHz, 400 MHz or 500 MHz). The ^{1}H NMR chemical shifts are reported in ppm related to the chemical shift of TMS and calibrated to the residual protic solvent peaks of $CDCl_3$ (7.26 ppm) and DMSO-d_6 (2.50 ppm). ^{13}C NMR shifts were calibrated to the centre of the multiplet signal of the residual solvent peak ($CDCl_3$ = 77.16 ppm, DMSO-d_6 = 39.52 ppm) and quoted to the nearest 0.1 ppm. ^{1}H NMR spectroscopic data are reported as follows: Chemical shift to the nearest 0.01 ppm (multipilicity, coupling constants *J*, integration intensity). For the multiplicities the abbreviations s (singlet), br s (broad singlet), d (doublet), t (triplet), q (quartet) and m (multiplet) have been used. High-resolution mass spectrometry (HRMS) measurements were recorded with a *Thermo Scientific* LTQ FT Ultra or LTQ Orbitrap instrument with ESI ionization.

2.2 Synthetic procedures

3-((1-methyl-5-nitro-1*H*-imidazol-2-yl)methyl)-5-nitroindolin-2-one (Hybrid 2)

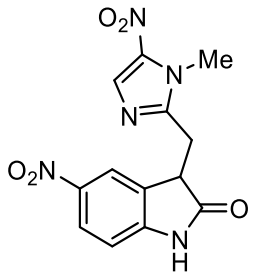

Hybrid 2
$C_{13}H_{11}N_5O_5$
M = 317.26 g/mol

To a solution of nitroindolidone **Hybrid 1** (50.0 mg, 0.158 mmol, 1.00 eq.) in DMF (10 mL) was added sodium borohydride (7.18 mg, 0.190 mmol, 1.20 eq.) at 0 °C. The reaction was stirred at 0 °C for 15 – 30 min and subsequently sat. aq. NH_4Cl was added. The mixture was extracted with EtOAc, the organic phases were combined and dried over $MgSO_4$ and the solvent removed *in vacuo*. The crude product was purified by FCC (2% MeOH in DCM) to afford the title compound (26.0 mg, 0.082 mmol, 52%) as pale yellow solid. – ^{1}H NMR (400 MHz, DMSO-d_6): δ (ppm) = 11.17 (s, 1H), 8.14 (dd, J = 8.5 Hz, 1.7 Hz, 2H), 7.94 (s, 1H), 7.02 – 6.99 (m, 1H), 4.17 – 4.13 (m, 1H), 3.85 (s, 3H), 3.66 (dd, J = 17.3 Hz, 4.6 Hz, 1H), 3.39 – 3.34 (m, 1H). – ^{13}C NMR (100 MHz, DMSO-d_6): δ (ppm) = 178.3, 150.5, 149.7, 141.6, 139.1, 131.8, 130.3, 125.2, 119.6, 109.1, 42.3, 33.0, 26.0. – HRMS (ESI+) calcd. for $C_{13}H_{12}N_5O_5$ $[M+H]^+$ 318.0832, found 318.0826.

(*E*)-3-((1-methyl-5-nitro-1H-imidazol-2-yl)methylene)indolin-2-one (Hybrid 3)

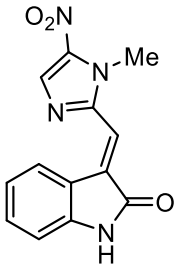

Hybrid 3
$C_{13}H_{10}N_4O_3$
M = 270.25 g/mol

General procedure for the condensation of imidazole and indolin-2-one fragments:

To a solution of indolin-2-one compound (1.00 eq.) in EtOH (0.3 M), piperidine or TMP (1.50 eq.) and the imidazole derivative (1.05 eq.) were added. The reaction was refluxed for 4 h, then cooled to room temperature and the formed precipitation filtered. The filter cake was washed with EtOH three times, collected and dried *in vacuo* to afford the title compounds.

The title compound was prepared according to the general procedure using 6-iodoindolin-2-one (100 mg, 0.752 mmol), piperidin (0.111 mL, 96.2 mg, 1.13 mmol) and 1-methyl-5-nitro-1*H*-imidazole-2-carbaldehyd **4** (122 mg, 0.786 mmol) to afford 110 mg (0.407 mmol, 54%) as red solid. – ^{1}H NMR (400 MHz, DMSO-d_6): δ (ppm) = 10.74 (s, 1H), 9.02 (dd, J = 8.1 Hz, 1.2 Hz, 1H), 8.43 (s, 1H), 7.35 – 7.30 (m, 2H), 7.01 (td, J = 7.6 Hz, 1.1 Hz, 1H), 6.88 (d, J = 7.7 Hz, 1H), 4.09 (s, 3H). – ^{13}C NMR (100 MHz, DMSO-d_6): δ (ppm) = 168.5, 146.4, 144.0, 139.6, 133.5, 132.2, 131.9, 127.9, 121.4, 120.5, 116.2, 109.9, 33.5. – HRMS (ESI+) calcd. for $C_{13}H_{11}N_4O_3$ $[M+H]^+$ 271.0825, found 271.0825.

The *E*-configuration was confirmed by ROESY 2D-NMR (NMR Spectra Appendix).

V – References

1. Gil, J. Antimicrobial use in livestock farming. *Nat. Food* **4**, 138–138 (2023).

2. Piscioneri, F. Role of Antibiotics in Surgery. in *Emergency Surgery for Low Resource Regions* 3–5 (Springer, Cham, 2021). doi:10.1007/978-3-030-68099-2_1.

3. Hutchings, M., Truman, A. & Wilkinson, B. Antibiotics: past, present and future. *Curr. Opin. Microbiol.* **51**, 72–80 (2019).

4. Ehrlich, P. Address in pathology, on chemiotherapy. *Br. Med. J.* **2**, 353–359 (1913).

5. Gelpi, A., Gilbertson, A. & Tucker, J. D. Magic bullet: Paul Ehrlich, Salvarsan and the birth of venereology. *Sex. Transm. Infect.* **91**, 68–69 (2015).

6. Otten, H. Domagk and the development of the sulphonamides. *J. Antimicrob. Chemother.* **17**, 689–690 (1986).

7. Fleming, A. On the antibacterial action of cultures of a penicillium, with special reference to their use in the isolation of B. influenzae. 1929. *Bull. World Health Organ.* **79**, 780–790 (2001).

8. Waksman, S. A., Schatz, A. & Reynolds, D. M. Production of antibiotic substances by actinomycetes. *Ann. N. Y. Acad. Sci.* **1213**, 112–124 (2010).

9. Wasan, H., Singh, D., Reeta, K. H. & Gupta, Y. K. Landscape of Push Funding in Antibiotic Research: Current Status and Way Forward. *Biology (Basel).* **12**, (2023).

10. Lakemeyer, M., Zhao, W., Mandl, F. A., Hammann, P. & Sieber, S. A. Thinking Outside the Box-Novel Antibacterials To Tackle the Resistance Crisis. *Angew. Chemie Int. Ed.* **57**, 14440–14475 (2018).

11. Beckh, W. & Kulchar, G. V. Treatment-resistant syphilis: An evaluation of the causative factors in eighteen cases. *Arch. Derm. Syphilol.* **40**, 1–12 (1939).

12. Stekel, D. First report of antimicrobial resistance pre-dates penicillin. *Nature* **562**, 192 (2018).

13. Murray, C. J. *et al.* Global burden of bacterial antimicrobial resistance in 2019: a systematic analysis. *Lancet* **399**, 629–655 (2022).

14. Tacconelli, E. *et al.* Discovery, research, and development of new antibiotics: the WHO priority list of antibiotic-resistant bacteria and tuberculosis. *Lancet Infect. Dis.* **18**, 318–327 (2018).

15. Rice, L. B. Federal Funding for the Study of Antimicrobial Resistance in Nosocomial Pathogens: No ESKAPE. *J. Infect. Dis.* **197**, 1079–1081 (2008).

16. Peterson, E. & Kaur, P. Antibiotic resistance mechanisms in bacteria: Relationships between resistance determinants of antibiotic producers, environmental bacteria, and clinical pathogens. *Front. Microbiol.* **9**, 426686 (2018).

17. Darby, E. M. *et al.* Molecular mechanisms of antibiotic resistance revisited. *Nat. Rev. Microbiol.* **21**, 280–295 (2023).

18. Wang, Q., Wei, S., Silva, A. F. & Madsen, J. S. Cooperative antibiotic resistance facilitates horizontal gene transfer. *ISME J.* **17**, 846–854 (2023).

19. Lerminiaux, N. A. & Cameron, A. D. S. Horizontal transfer of antibiotic resistance genes in clinical environments. *Can. J. Microbiol.* **65**, 34–44 (2019).

20. De Oliveira, D. M. P. *et al.* Antimicrobial resistance in ESKAPE pathogens. *Clin. Microbiol. Rev.* **33**, (2020).

21. Balaban, N. Q. *et al.* Definitions and guidelines for research on antibiotic persistence. *Nat. Rev. Microbiol.* **17**, 441–448 (2019).

22. Yan, J. & Bassler, B. L. Surviving as a Community: Antibiotic Tolerance and Persistence in Bacterial Biofilms. *Cell Host Microbe* **26**, 15–21 (2019).

23. Lehar, S. M. *et al.* Novel antibody-antibiotic conjugate eliminates intracellular S. aureus. *Nature* **527**, 323–328 (2015).

24. O`Neill, J. *Tackling Drug-Resistance Infections Globally: Final Report and Recommendations. The review on Antimicrobial Resistance Chaired by Jim O`Neill*. https://amr-review.org/sites/default/files/160518_Final paper_with cover.pdf (2016).

25. de Kraker, M. E. A., Stewardson, A. J. & Harbarth, S. Will 10 Million People Die a Year due to Antimicrobial Resistance by 2050? *PLOS Med.* **13**, e1002184 (2016).

26. NOAH responds to the O'Neill review. *Vet. Rec.* **179**, 132–132 (2016).

27. 2019 Antibiotic Resistance Threats Report | CDC. https://www.cdc.gov/drugresistance/biggest-threats.html.

28. WHO. Antimicrobial resistance: global report on surveillance. https://www.who.int/publications/i/item/9789241564748.

29. Miethke, M. *et al.* Towards the sustainable discovery and development of new antibiotics. *Nat. Rev. Chem. 2021 510* **5**, 726–749 (2021).

30. Prescott, J. F. The resistance tsunami, antimicrobial stewardship, and the golden age of microbiology. *Vet. Microbiol.* **171**, 273–278 (2014).

31. Singh, S. B., Young, K. & Miesel, L. Screening strategies for discovery of antibacterial natural products. *Expert Rev. Anti. Infect. Ther.* **9**, 589–613 (2011).

32. Newman, D. J. & Cragg, G. M. Natural Products as Sources of New Drugs from 1981 to 2014. *J. Nat. Prod.* **79**, 629–661 (2016).

33. Rodrigues, T., Reker, D., Schneider, P. & Schneider, G. Counting on natural products for drug design. *Nat. Chem.* **8**, 531–541 (2016).

34. Galloway, W. R. J. D., Bender, A., Welch, M. & Spring, D. R. The discovery of antibacterial agents using diversity-oriented synthesis. *Chem. Commun.* 2446 (2009) doi:10.1039/b816852k.

35. Isidro-Llobet, A. *et al.* Diversity-oriented synthesis of macrocyclic peptidomimetics. *Proc. Natl. Acad. Sci. U. S. A.* **108**, 6793–6798 (2011).

36. Hwang, H. J. *et al.* Diversity-oriented routes to thiopeptide antibiotics: total synthesis and biological evaluation of micrococcin P2. *Org. Biomol. Chem.* **20**, 1893–1899 (2022).

37. Hughes, J. P., Rees, S. S., Kalindjian, S. B. & Philpott, K. L. Principles of early drug discovery. *Br. J. Pharmacol.* **162**, 1239–1249 (2011).

38. Davis, R. L. Mechanism of Action and Target Identification: A Matter of Timing in Drug Discovery. *iScience* **23**, 101487 (2020).

39. Farha, M. A. & Brown, E. D. Drug repurposing for antimicrobial discovery. *Nat. Microbiol. 2019 44* **4**, 565–577 (2019).

40. Boyd, N. K., Teng, C. & Frei, C. R. Brief Overview of Approaches and Challenges in New Antibiotic Development: A Focus On Drug Repurposing. *Front. Cell. Infect. Microbiol.* **11**, 684515 (2021).

41. Alm, R. A. & Lahiri, S. D. Narrow-Spectrum Antibacterial Agents—Benefits and Challenges. *Antibiotics* **9**, 418 (2020).

42. Melander, R. J., Zurawski, D. V. & Melander, C. Narrow-spectrum antibacterial agents. *Medchemcomm* **9**, 12–21 (2018).

43. Ii, J. K. M. *et al.* A Dual-Mechanism Antibiotic Kills Gram-Negative Bacteria and Avoids Drug Resistance In Brief A Dual-Mechanism Antibiotic Kills Gram-Negative Bacteria and Avoids Drug Resistance. *Cell* **181**, 1518-1532.e14 (2020).

44. Pokrovskaya, V. & Baasov, T. Dual-acting hybrid antibiotics: A promising strategy to combat bacterial resistance. *Expert Opin. Drug Discov.* **5**, 883–902 (2010).

45. Theuretzbacher, U. Dual-mechanism antibiotics. *Nat. Microbiol.* **5**, 984–985 (2020).

46. Rasko, D. A. & Sperandio, V. Anti-virulence strategies to combat bacteria-mediated disease. *Nat. Rev. Drug Discov.* **9**, 117–128 (2010).

47. Mühlen, S. & Dersch, P. Anti-virulence strategies to target bacterial infections. *Curr. Top. Microbiol. Immunol.* **398**, 147–183 (2016).

48. Rezzoagli, C., Archetti, M., Mignot, I., Baumgartner, M. & Kümmerli, R. Combining antibiotics with antivirulence compounds can have synergistic effects and reverse selection for antibiotic resistance in Pseudomonas aeruginosa. *PLOS Biol.* **18**, e3000805 (2020).

49. Bragg, R., van der Westhuizen, W., Lee, J. Y., Coetsee, E. & Boucher, C. Bacteriophages as potential treatment option for antibiotic resistant bacteria. *Adv. Exp. Med. Biol.* **807**, 97–110 (2014).

50. Yosef, I., Kiro, R., Molshanski-Mor, S., Edgar, R. & Qimron, U. Different approaches for using bacteriophages against antibiotic-resistant bacteria. *Bacteriophage* **4**, e28491 (2014).

51. Romero-Calle, D., Benevides, R. G., Góes-Neto, A. & Billington, C. Bacteriophages as alternatives to antibiotics in clinical care. *Antibiotics* **8**, 138 (2019).

52. Balasegaram, M. & Piddock, L. J. V. The Global Antibiotic Research and Development Partnership (GARDP) Not-for-Profit Model of Antibiotic Development. *ACS Infect. Dis.* **6**, 1295–1298 (2020).

53. Alm, R. A. & Gallant, K. Innovation in Antimicrobial Resistance: The CARB-X Perspective. *ACS Infect. Dis.* **6**, 1317–1322 (2020).

54. Rex, J. H. & Outterson, K. Antibiotic reimbursement in a model delinked from sales: A benchmark-based worldwide approach. *Lancet Infect. Dis.* **16**, 500–505 (2016).

55. Mahase, E. UK launches subscription style model for antibiotics to encourage new development. *BMJ* **369**, m2468 (2020).

56. Uchil, R. R., Kohli, G. S., Katekhaye, V. M. & Swami, O. C. Strategies to combat

antimicrobial resistance. *J. Clin. Diagn. Res.* **8**, ME01-4 (2014).

57. Wetmore, K. M. *et al.* Rapid quantification of mutant fitness in diverse bacteria by sequencing randomly bar-coded transposons. *MBio* **6**, 1–15 (2015).

58. Santiago, M. *et al.* A new platform for ultra-high density Staphylococcus aureus transposon libraries. *BMC Genomics* **16**, 252 (2015).

59. Klobucar, K. & Brown, E. D. Use of genetic and chemical synthetic lethality as probes of complexity in bacterial cell systems. *FEMS Microbiol. Rev.* **42**, 81–99 (2018).

60. Majumder, A., Biswal, M. R. & Prakash, M. K. One Drug Multiple Targets: An Approach to Predict Drug Efficacies on Bacterial Strains Differing in Membrane Composition. *ACS Omega* **4**, 4977–4983 (2019).

61. Talevi, A. Multi-target pharmacology: possibilities and limitations of the "skeleton key approach" from a medicinal chemist perspective. *Front. Pharmacol.* **6**, 156790 (2015).

62. Rossi, M. *et al.* Sustainable Drug Discovery of Multi-Target-Directed Ligands for Alzheimer's Disease. *J. Med. Chem.* **64**, 4972–4990 (2021).

63. Hoffman, P. S. Antibacterial discovery: 21st century challenges. *Antibiotics* **9**, (2020).

64. Fonović, M. & Bogyo, M. Activity-based probes as a tool for functional proteomic analysis of proteases. *Expert Rev. Proteomics* **5**, 721–730 (2008).

65. Evans, M. J. & Cravatt, B. F. Mechanism-based profiling of enzyme families. *Chem. Rev.* **106**, 3279–3301 (2006).

66. Cravatt, B. F., Wright, A. T. & Kozarich, J. W. Activity-Based Protein Profiling: From Enzyme Chemistry to Proteomic Chemistry. *Annu. Rev. Biochem.* **77**, 383–414 (2008).

67. Wright, M. H. & Sieber, S. A. Chemical proteomics approaches for identifying the cellular targets of natural products. *Nat. Prod. Rep.* **33**, 681–708 (2016).

68. Niphakis, M. J. & Cravatt, B. F. Enzyme inhibitor discovery by activity-based protein profiling. *Annu. Rev. Biochem.* **83**, 341–377 (2014).

69. Li, G. *et al.* Currently Available Strategies for Target Identification of Bioactive Natural Products. *Front. Chem.* **9**, 761609 (2021).

70. Fang, H. *et al.* Recent advances in activity-based probes (ABPs) and affinity-based probes (AfBPs) for profiling of enzymes. *Chem. Sci.* **12**, 8288–8310 (2021).

71. Reinhardt, T., Lee, K. M., Niederegger, L., Hess, C. R. & Sieber, S. A. Indolin-2-one Nitroimidazole Antibiotics Exhibit an Unexpected Dual Mode of Action. *ACS Chem. Biol.* **17**, 3077–3085 (2022).

72. Kolb, H. C., Finn, M. G. & Sharpless, K. B. Click Chemistry: Diverse Chemical Function from a Few Good Reactions. *Angew. Chemie Int. Ed.* **40**, 2004–2021 (2001).

73. Fang, H. *et al.* Recent advances in activity-based probes (ABPs) and affinity-based probes (AfBPs) for profiling of enzymes. *Chem. Sci.* **12**, 8288–8310 (2021).

74. Conway, L. P. *et al.* Evaluation of fully-functionalized diazirine tags for chemical proteomic applications. *Chem. Sci.* **12**, 7839–7847 (2021).

75. Li, Z. *et al.* Design and synthesis of minimalist terminal alkyne-containing diazirine photo-crosslinkers and their incorporation into kinase inhibitors for cell- and tissue-based proteome profiling. *Angew. Chemie - Int. Ed.* **52**, 8551–8556 (2013).

76. West, A. V. *et al.* Labeling Preferences of Diazirines with Protein Biomolecules. *J. Am. Chem. Soc.* **143**, 6691–6700 (2021).

77. Mateus, A., Määttä, T. A. & Savitski, M. M. Thermal proteome profiling: Unbiased assessment of protein state through heat-induced stability changes. *Proteome Sci.* **15**, 13 (2017).

78. Lo, M.-C. *et al.* Evaluation of fluorescence-based thermal shift assays for hit identification in drug discovery. *Anal. Biochem.* **332**, 153–159 (2004).

79. Molina, D. M. *et al.* Monitoring drug target engagement in cells and tissues using the cellular thermal shift assay. *Science* **341**, 84–87 (2013).

80. Martinez Molina, D. & Nordlund, P. The Cellular Thermal Shift Assay: A Novel Biophysical Assay for In Situ Drug Target Engagement and Mechanistic Biomarker Studies. *Annu. Rev. Pharmacol. Toxicol.* **56**, 141–161 (2016).

81. Savitski, M. M. *et al.* Tracking cancer drugs in living cells by thermal profiling of the proteome. *Science* **346**, (2014).

82. Mateus, A. *et al.* Thermal proteome profiling in bacteria: probing protein state in vivo. *Mol. Syst. Biol.* **14**, e8242 (2018).

83. Mateus, A. *et al.* Thermal proteome profiling for interrogating protein interactions. *Mol. Syst. Biol.* **16**, e9232 (2020).

84. Jarzab, A. *et al.* Meltome atlas—thermal proteome stability across the tree of life. *Nat. Methods* **17**, 495–503 (2020).

85. Ting, L., Rad, R., Gygi, S. P. & Haas, W. MS3 eliminates ratio distortion in isobaric multiplexed quantitative proteomics. *Nat. Methods* **8**, 937–940 (2011).

86. Weiner, S. *et al.* Optimized sample preparation and data analysis for TMT proteomic analysis of cerebrospinal fluid applied to the identification of Alzheimer's disease biomarkers. *Clin. Proteomics* **19**, 13 (2022).

87. Franken, H. *et al.* Thermal proteome profiling for unbiased identification of direct and indirect drug targets using multiplexed quantitative mass spectrometry. *Nat. Protoc.* **10**, 1567–1593 (2015).

88. Boersema, P. J., Mohammed, S. & Heck, A. J. R. Hydrophilic interaction liquid chromatography (HILIC) in proteomics. *Anal. Bioanal. Chem.* **391**, 151–159 (2008).

89. Cox, J. *et al.* Accurate proteome-wide label-free quantification by delayed normalization and maximal peptide ratio extraction, termed MaxLFQ. *Mol. Cell. Proteomics* **13**, 2513–2526 (2014).

90. Cox, J. & Mann, M. MaxQuant enables high peptide identification rates, individualized p.p.b.-range mass accuracies and proteome-wide protein quantification. *Nat. Biotechnol.* **26**, 1367–1372 (2008).

91. Becher, I. *et al.* Thermal profiling reveals phenylalanine hydroxylase as an off-target of panobinostat. *Nat. Chem. Biol.* **12**, 908–910 (2016).

92. Kleiner, P., Heydenreuter, W., Stahl, M., Korotkov, V. S. & Sieber, S. A. A Whole Proteome Inventory of Background Photocrosslinker Binding. *Angew. Chemie - Int. Ed.* **56**, 1396–1401 (2017).

93. Zanon, P. R. A., Lewald, L. & Hacker, S. M. Isotopically Labeled Desthiobiotin Azide (isoDTB) Tags Enable Global Profiling of the Bacterial Cysteinome. *Angew. Chemie Int. Ed.* **59**, 2829–2836 (2020).

94. Bach, K., Beerkens, B. L. H., Zanon, P. R. A. & Hacker, S. M. Light-Activatable, 2,5-Disubstituted Tetrazoles for the Proteome-wide Profiling of Aspartates and Glutamates in Living Bacteria. *ACS Cent. Sci.* **6**, 546–554 (2020).

95. Zanon, P. R. A. *et al.* Profiling the proteome-wide selectivity of diverse electrophiles. (2021) doi:10.26434/CHEMRXIV-2021-W7RSS-V2.

96. Reinhard, F. B. M. *et al.* Thermal proteome profiling monitors ligand interactions with cellular membrane proteins. *Nat. Methods* **12**, 1129–1131 (2015).

97. Gaetani, M. *et al.* Proteome Integral Solubility Alteration: A High-Throughput Proteomics Assay for Target Deconvolution. *J. Proteome Res.* **18**, 4027–4037 (2019).

98. Mitscher, L. A. Bacterial topoisomerase inhibitors: Quinolone and pyridone antibacterial agents. *Chem. Rev.* **105**, 559–592 (2005).

99. Idowu, T. & Schweizer, F. Ubiquitous Nature of Fluoroquinolones: The Oscillation between Antibacterial and Anticancer Activities. *Antibiotics* **6**, 26 (2017).

100. Lesher, G. Y., Froelich, E. J., Gruett, M. D., Bailey, J. H. & Brundage, R. P. 1,8-Naphthyridine Derivatives. A New Class of Chemotherapeutic Agents. *J. Med. Pharm. Chem.* **5**, 1063–1065 (1962).

101. Rohlfing, S. R., Gerster, J. F. & Kvam, D. C. Bioevaluation of the antibacterial flumequine for urinary tract use. *Antimicrob. Agents Chemother.* **10**, 20–24 (1976).

102. Domagala, J. M. Structure-activity and structure-side-effect relationships for the quinolone antibacterials. *J. Antimicrob. Chemother.* **33**, 685–706 (1994).

103. McKeage, K. Finafloxacin: First global approval. *Drugs* **75**, 687–693 (2015).

104. Markham, A. Delafloxacin: First Global Approval. *Drugs* **77**, 1481–1486 (2017).

105. Hoshino, K. *et al.* Comparison of inhibition of Escherichia coli topoisomerase IV by quinolones with DNA gyrase inhibition. *Antimicrob. Agents Chemother.* **38**, 2623–2627 (1994).

106. Pommier, Y., Leo, E., Zhang, H. & Marchand, C. DNA topoisomerases and their poisoning by anticancer and antibacterial drugs. *Chem. Biol.* **17**, 421–433 (2010).

107. Aldred, K. J., McPherson, S. A., Turnbough, C. L., Kerns, R. J. & Osheroff, N. Topoisomerase IV-quinolone interactions are mediated through a water-metal ion bridge: mechanistic basis of quinolone resistance. *Nucleic Acids Res.* **41**, 4628–4639 (2013).

108. Strahilevitz, J. & Hooper, D. C. Dual targeting of topoisomerase IV and gyrase to reduce mutant selection: Direct testing of the paradigm by using WCK-1734, a new fluoroquinolone, and ciprofloxacin. *Antimicrob. Agents Chemother.* **49**, 1949–1956 (2005).

109. Skepper, C. K. *et al.* Topoisomerase Inhibitors Addressing Fluoroquinolone Resistance in Gram-Negative Bacteria. *J. Med. Chem.* **63**, 7773–7816 (2020).

110. Peterson, L. R. Quinolone Molecular Structure-Activity Relationships: What We Have Learned about Improving Antimicrobial Activity. *Clin. Infect. Dis.* **33**, S180–S186 (2001).

111. Ellsworth, E. L. *et al.* 3-Aminoquinazolinediones as a new class of antibacterial agents demonstrating excellent antibacterial activity against wild-type and multidrug resistant organisms. *J. Med. Chem.* **49**, 6435–6438 (2006).

112. Huband, M. D. *et al.* In vitro and in vivo activities of PD 0305970 and PD 0326448, new bacterial gyrase/topoisomerase inhibitors with potent antibacterial activities versus multidrug-resistant gram-positive and fastidious organism groups. *Antimicrob. Agents Chemother.* **51**, 1191–1201 (2007).

113. Hutchings, K. M. *et al.* Synthesis and antibacterial activity of the C-7 side chain of 3-aminoquinazolinediones. *Bioorganic Med. Chem. Lett.* **18**, 5087–5090 (2008).

114. Linder, J. A., Huang, E. S., Steinman, M. A., Gonzales, R. & Stafford, R. S. Fluoroquinolone prescribing in the United States: 1995 to 2002. *Am. J. Med.* **118**, 259–268 (2005).

115. Outpatient Antibiotic Prescriptions — United States, 2011 | Antibiotic Use | CDC. https://www.cdc.gov/antibiotic-use/data/report-2011.html.

116. Outpatient Antibiotic Prescriptions — United States, 2012 | Antibiotic Use | CDC. https://www.cdc.gov/antibiotic-use/data/report-2012.html.

117. Outpatient Antibiotic Prescriptions — United States, 2013 | Antibiotic Use | CDC. https://www.cdc.gov/antibiotic-use/data/report-2013.html.

118. Outpatient Antibiotic Prescriptions — United States, 2014 | Antibiotic Use | CDC. https://www.cdc.gov/antibiotic-use/data/report-2014.html.

119. Outpatient Antibiotic Prescriptions — United States, 2015 | Antibiotic Use | CDC. https://www.cdc.gov/antibiotic-use/data/report-2015.html.

120. Outpatient Antibiotic Prescriptions — United States, 2016 | Antibiotic Use | CDC. https://www.cdc.gov/antibiotic-use/data/report-2016.html.

121. Outpatient Antibiotic Prescriptions — United States, 2017 | Antibiotic Use | CDC. https://www.cdc.gov/antibiotic-use/data/report-2017.html.

122. Outpatient Antibiotic Prescriptions — United States, 2018 | Antibiotic Use | CDC. https://www.cdc.gov/antibiotic-use/data/report-2018.html.

123. Outpatient Antibiotic Prescriptions — United States, 2019 |Antibiotic Use | CDC. https://www.cdc.gov/antibiotic-use/data/report-2019.html.

124. Outpatient Antibiotic Prescriptions — United States, 2020 | Antibiotic Use | CDC. https://www.cdc.gov/antibiotic-use/data/report-2020.html.

125. Ross, R. K., Kinlaw, A. C., Herzog, M. M., Funk, M. J. & Gerber, J. S. Fluoroquinolone antibiotics and tendon injury in adolescents. *Pediatrics* **147**, (2021).

126. Blum, M. D., Graham, D. J. & Mc Closkey, C. A. Temafloxacin Syndrome: Review of 95 Cases. *Clin. Infect. Dis.* **18**, 946–950 (1994).

127. Mandell, L. & Tillotson, G. Safety of Fluoroquinolones: An Update. *Can. J. Infect. Dis. Med. Microbiol.* **13**, 54–61 (2002).

128. Kalghatgi, S. *et al.* Bactericidal antibiotics induce mitochondrial dysfunction and oxidative damage in mammalian cells. *Sci. Transl. Med.* **5**, 192ra85 (2013).

129. Jiang, T. *et al.* Mitochondrial dysfunction is underlying fluoroquinolone toxicity: an integrated mitochondrial toxicity assessment. *Mol. Cell. Toxicol.* **19**, 333–342 (2023).

130. Marchant, J. When antibiotics turn toxic. *Nature* **555**, 431–433 (2018).

131. Tennyson, L. E. & Averch, T. D. An Update on Fluoroquinolones: The Emergence of a Multisystem Toxicity Syndrome. *Urol. Pract.* **4**, 383–387 (2017).

132. Huruba, M. *et al.* A VigiBase descriptive study of fluoroquinolone induced disabling and potentially permanent musculoskeletal and connective tissue disorders. *Sci. Rep.* **11**, 1–11 (2021).

133. Ellis, D. E. *et al.* Comparative neurological safety of fluoroquinolones versus therapeutic alternatives. *Pharmacoepidemiol. Drug Saf.* **30**, 797–805 (2021).

134. Freeman, M. Z., Cannizzaro, D. N., Naughton, L. F. & Bove, C. Fluoroquinolones-Associated Disability: It Is Not All in Your Head. *NeuroSci* **2**, 235–253 (2021).

135. Baggio, D. & R Ananda-Rajah, M. Fluoroquinolone antibiotics and adverse events. *Aust. Prescr.* **44**, 161–164 (2021).

136. Bennett, A. C., Bennett, C. L., Witherspoon, B. J. & Knopf, K. B. An evaluation of reports of ciprofloxacin, levofloxacin, and moxifloxacin-association neuropsychiatric toxicities, long-term disability, and aortic aneurysms/dissections disseminated by the Food and Drug Administration and the European Medicines Agency. *Expert Opin. Drug Saf.* **18**, 1055–1063 (2019).

137. Guzzardi, D. G. *et al.* Induction of human aortic myofibroblast-mediated extracellular matrix dysregulation: A potential mechanism of fluoroquinolone-associated aortopathy. *J. Thorac. Cardiovasc. Surg.* **157**, 109-119.e2 (2019).

138. Wee, I. *et al.* The association between fluoroquinolones and aortic dissection and aortic aneurysms: a systematic review and meta-analysis. *Sci. Rep.* **11**, 11073 (2021).

139. Jun, C. & Fang, B. Current progress of fluoroquinolones-increased risk of aortic aneurysm and dissection. *BMC Cardiovasc. Disord.* **21**, 470 (2021).

140. Nyyssönen, T., Lantto, I., Lüthje, P., Selander, T. & Kröger, H. Drug treatments associated with Achilles tendon rupture. A case-control study involving 1118 Achilles tendon ruptures. *Scand. J. Med. Sci. Sport.* **28**, 2625–2629 (2018).

141. Stephenson, A. L., Wu, W., Cortes, D. & Rochon, P. A. Tendon injury and fluoroquinolone use: A systematic review. *Drug Saf.* **36**, 709–721 (2013).

142. Godoy-Santos, A. L. *et al.* Fluoroquinolones and the Risk of Achilles Tendon Disorders: Update on a Neglected Complication. *Urology* **113**, 20–25 (2018).

143. Bisaccia, D. R., Aicale, R., Tarantino, D., Peretti, G. M. & Maffulli, N. Biological and chemical changes in fluoroquinolone-associated tendinopathies: a systematic review. *Br. Med. Bull.* **130**, 39–49 (2019).

144. Marchant, J. When antibiotics turn toxic. *Nature* **555**, 431–433 (2018).

145. FDA reinforces safety information about serious low blood sugar levels and mental health side effects with fluoroquinolone antibiotics; requires label changes | FDA. https://www.fda.gov/drugs/drug-safety-and-availability/fda-reinforces-safety-information-about-serious-low-blood-sugar-levels-and-mental-health-side.

146. Prac. Quinolones and fluoroquinolones Art. 31 PhV - Assessment Report for publication. (2018).

147. Khaliq, Y. & Zhanel, G. G. Fluoroquinolone-Associated Tendinopathy: A Critical Review of the Literature. *Clin. Infect. Dis.* **36**, 1404–1410 (2003).

148. Hazell, L. & Shakir, S. A. W. Under-reporting of adverse drug reactions: A systematic review. *Drug Saf.* **29**, 385–396 (2006).

149. Alves, C., Mendes, D. & Marques, F. B. Fluoroquinolones and the risk of tendon injury: a systematic review and meta-analysis. *Eur. J. Clin. Pharmacol.* **75**, 1431–1443 (2019).

150. Daneman, N., Lu, H. & Redelmeier, D. A. Fluoroquinolones and collagen associated severe adverse events: a longitudinal cohort study. *BMJ Open* **5**, e010077 (2015).

151. Yasui, Y. *et al.* The Risk of Achilles Tendon Rupture in the Patients with Achilles Tendinopathy: Healthcare Database Analysis in the United States. *Biomed Res. Int.* **2017**, 1–4 (2017).

152. Dai, X. C. *et al.* Relationship between fluoroquinolones and the risk of aortic diseases: A meta-analysis of observational studies. *BMC Cardiovasc. Disord.* **20**, 49 (2020).

153. Gopalakrishnan, C. *et al.* Association of Fluoroquinolones with the Risk of Aortic Aneurysm or Aortic Dissection. *JAMA Intern. Med.* **180**, 1596–1605 (2020).

154. Dong, Y. H. *et al.* Association of Infections and Use of Fluoroquinolones with the Risk of Aortic Aneurysm or Aortic Dissection. *JAMA Intern. Med.* **180**, 1787–1795 (2020).

155. Etminan, M., Brophy, J. M. & Samii, A. Oral fluoroquinolone use and risk of peripheral neuropathy: A pharmacoepidemiologic study. *Neurology* **83**, 1261–1263 (2014).

156. Morales, D. *et al.* Association between Peripheral Neuropathy and Exposure to Oral Fluoroquinolone or Amoxicillin-Clavulanate Therapy. *JAMA Neurol.* **76**, 827–833 (2019).

157. Bennett, A., Qureshi, Z. & Bennett, C. A Novel Genetic Marker Has Been Identified in patients With Fluoroquinolone-Associated Neuropsychiatric Toxicity: Preliminarys Findings. in *Federal Practitioner* 30 (2017).

158. Pham, L., Christensen, J. M. & Rodriguez-Proteau, R. Pharmacokinetic Prediction of Levofloxacin Accumulation in Tissue and Its Association to Tendinopathy. *Pharmacol. Pharm.* **04**, 121–131 (2013).

159. Vance-Bryan, K., Guay, D. R. P. & Rotschafer, J. C. Clinical Pharmacokinetics of Ciprofloxacin. *Clin. Pharmacokinet.* **19**, 434–461 (1990).

160. Bertino, J. & Fish, D. The safety profile of the fluoroquinolones. *Clin. Ther.* **22**, 798–817 (2000).

161. Wise, B. L., Peloquin, C., Choi, H., Lane, N. E. & Zhang, Y. Impact of age, sex,

obesity, and steroid use on quinolone-associated tendon disorders. *Am. J. Med.* **125**, 1228.e23-1228.e28 (2012).

162. Kempka, G., Ahr, H. J., Rüther, W. & Schlüter, G. Effects of fluoroquinolones and glucocorticoids on cultivated tendon cells in vitro. *Toxicol. Vitr.* **10**, 743–754 (1996).

163. Ma, H. H. M., Chiu, F. C. K. & Li, R. C. Mechanistic investigation of the reduction in antimicrobial activity of ciprofloxacin by metal cations. *Pharm. Res.* **14**, 366–370 (1997).

164. Seedher, N. & Agarwal, P. Effect of metal ions on some pharmacologically relevant interactions involving fluoroquinolone antibiotics. *Drug Metabol. Drug Interact.* **25**, 17–24 (2010).

165. Badal, S., Her, Y. F. & James Maher, L. Nonantibiotic effects of fluoroquinolones in mammalian cells. *J. Biol. Chem.* **290**, 22287–22297 (2015).

166. Sendzik, J., Shakibaei, M., Schäfer-Korting, M. & Stahlmann, R. Fluoroquinolones cause changes in extracellular matrix, signalling proteins, metalloproteinases and caspase-3 in cultured human tendon cells. *Toxicology* **212**, 24–36 (2005).

167. Tsai, W.-C. *et al.* Ciprofloxacin up-regulates tendon cells to express matrix metalloproteinase-2 with degradation of type I collagen. *J. Orthop. Res.* **29**, 67–73 (2011).

168. Corps, A. N. *et al.* Ciprofloxacin enhances the stimulation of matrix metalloproteinase 3 expression by interleukin-1β in human tendon-derived cells: A potential mechanism of fluoroquinolone-induced tendinopathy. *Arthritis Rheum.* **46**, 3034–3040 (2002).

169. Cannizzaro, D. N. *et al.* A New Criterion for Fluoroquinolone-Associated Disability Diagnosis: Functional Gastrointestinal Disorders. *Med.* **57**, 1371 (2021).

170. Sanders, V. R., Sweeney, A., Topf, M. & Millar, N. S. Stoichiometry-Selective Antagonism of α4β2 Nicotinic Acetylcholine Receptors by Fluoroquinolone Antibiotics. *ACS Chem. Neurosci.* **13**, 1805–1817 (2022).

171. Sarro, A. & Sarro, G. Adverse Reactions to Fluoroquinolones. An Overview on Mechanistic Aspects. *Curr. Med. Chem.* **8**, 371–384 (2001).

172. Arensman, K. *et al.* Fluoroquinolone versus Beta-Lactam Oral Step-Down Therapy for Uncomplicated Streptococcal Bloodstream Infections. *Antimicrob. Agents Chemother.* **64**, (2020).

173. Wise, R. & Honeybourne, D. Pharmacokinetics and pharmacodynamics of fluoroquinolones in the respiratory tract. *Eur. Respir. J.* **14**, 221–229 (1999).

174. Wagenlehner, F. M. E., Kinzig-Schippers, M., Sörgel, F., Weidner, W. & Naber, K. G. Concentrations in plasma, urinary excretion and bactericidal activity of levofloxacin (500 mg) versus ciprofloxacin (500 mg) in healthy volunteers receiving a single oral dose. *Int. J. Antimicrob. Agents* **28**, 551–559 (2006).

175. Bergan, T., Dalhoff, A. & Rohwedder, R. Pharmacokinetics of ciprofloxacin. *Infection* **16**, S3–S13 (1988).

176. Dan, M., Verbin, N., Gorea, A., Nagar, H. & Berger, S. A. Concentrations of ciprofloxacin in human liver, gallbladder, and bile after oral administration. *Eur. J. Clin. Pharmacol.* **32**, 217–218 (1987).

177. Ahmad, J. & Rafat, D. HbA1c and iron deficiency: A review. *Diabetes Metab. Syndr. Clin. Res. Rev.* **7**, 118–122 (2013).

178. Smith, A., Rish, K. R., Lovelace, R., Hackney, J. F. & Helston, R. M. Role for copper in the cellular and regulatory effects of heme-hemopexin. *BioMetals* **22**, 421–437 (2009).

179. Kruzel, M. L., Zimecki, M. & Actor, J. K. Lactoferrin in a context of inflammation-induced pathology. *Front. Immunol.* **8**, 256587 (2017).

180. Yachie, A. Heme Oxygenase-1 Deficiency and Oxidative Stress: A Review of 9 Independent Human Cases and Animal Models. *Int. J. Mol. Sci.* **22**, 1514 (2021).

181. Srinivas, A. N. *et al.* Emerging roles of AATF: Checkpoint signaling and beyond. *J. Cell. Physiol.* **236**, 3383–3395 (2021).

182. Nirgude, S. & Choudhary, B. Insights into the role of GPX3, a highly efficient plasma antioxidant, in cancer. *Biochem. Pharmacol.* **184**, 114365 (2021).

183. Wang, Y. *et al.* Mst1 promotes mitochondrial dysfunction and apoptosis in oxidative stress-induced rheumatoid arthritis synoviocytes. *Aging (Albany. NY).* **12**, 1–13 (2020).

184. He, A., Dean, J. M. & Lodhi, I. J. Peroxisomes as cellular adaptors to metabolic and environmental stress. *Trends Cell Biol.* **31**, 656–670 (2021).

185. Dammanahalli, K. J., Stevens, S. & Terkeltaub, R. Vanin-1 Pantetheinase Drives Smooth Muscle Cell Activation in Post-Arterial Injury Neointimal Hyperplasia. *PLoS One* **7**, e39106 (2012).

186. Zheng, Z., Granado, H. S. & Li, C. Fibromodulin, a Multifunctional Matricellular Modulator. *J. Dent. Res.* **102**, 125–134 (2023).

187. Zhang, H. *et al.* FN1 promotes chondrocyte differentiation and collagen production via TGF-β/PI3K/Akt pathway in mice with femoral fracture. *Gene* **769**, (2021).

188. Tan, X. *et al.* Transcriptional control of a collagen deposition and adhesion process that promotes lung adenocarcinoma growth and metastasis. *JCI Insight* **7**, (2022).

189. Bielajew, B. J., Hu, J. C. & Athanasiou, K. A. Collagen: quantification, biomechanics and role of minor subtypes in cartilage. *Nat. Rev. Mater.* **5**, 730–747 (2020).

190. Uivarosi, V. Metal Complexes of Quinolone Antibiotics and Their Applications: An Update. *Molecules* **18**, 11153–11197 (2013).

191. Ferreira, J. C. B. Mitochondrial Dysfunction in Degenerative Diseases. *Cells* **11**, (2022).

192. Liu, Y. *et al.* Mitochondrial Dysfunction and Therapeutic Perspectives in Cardiovascular Diseases. *Int. J. Mol. Sci.* **23**, 16053 (2022).

193. Papayannopoulos, V. Neutrophil extracellular traps in immunity and disease. *Nat. Rev. Immunol.* **18**, 134–147 (2018).

194. Hazeldine, J. *et al.* Impaired neutrophil extracellular trap formation: a novel defect in the innate immune system of aged individuals. *Aging Cell* **13**, 690–698 (2014).

195. van Daalen, K. R., Reijneveld, J. F. & Bovenschen, N. Modulation of Inflammation

by Extracellular Granzyme A. *Front. Immunol.* **11**, 532952 (2020).

196. Martinvalet, D., Dykxhoorn, D. M., Ferrini, R. & Lieberman, J. Granzyme A Cleaves a Mitochondrial Complex I Protein to Initiate Caspase-Independent Cell Death. *Cell* **133**, 681–692 (2008).

197. Singh, C. K. *et al.* The Role of Sirtuins in Antioxidant and Redox Signaling. *Antioxidants Redox Signal.* **28**, 643–661 (2018).

198. Lee, I. H. Mechanisms and disease implications of sirtuin-mediated autophagic regulation. *Exp. Mol. Med.* **51**, 1–11 (2019).

199. Wu, Q. J. *et al.* The sirtuin family in health and disease. *Signal Transduct. Target. Ther.* **7**, 1–74 (2022).

200. Adikwu, E. & Brambaifa, N. Ciprofloxacin induced chondrotoxicity and tendinopathy. *Am. J. Pharmacol. Toxicol.* **7**, 94–100 (2012).

201. Casparian, J. M., Luchi, M., Moffat, R. E. & Hinthorn, D. Quinolones and tendon ruptures. *South. Med. J.* **93**, 488–491 (2000).

202. Farndale, R. W. Collagen-induced platelet activation. *Blood Cells, Mol. Dis.* **36**, 162–165 (2006).

203. Semeniak, D., Faber, K., Öftering, P., Manukjan, G. & Schulze, H. Impact of Itga2-Gp6-double collagen receptor deficient mice for bone marrow megakaryocytes and platelets. *PLoS One* **14**, e0216839 (2019).

204. Pouzaud, F. *et al.* In Vitro Discrimination of Fluoroquinolones Toxicity on Tendon Cells: Involvement of Oxidative Stress. *J. Pharmacol. Exp. Ther.* **308**, 394–402 (2004).

205. Lowes, D. A., Wallace, C., Murphy, M. P., Webster, N. R. & Galley, H. F. The mitochondria targeted antioxidant MitoQ protects against fluoroquinolone-induced oxidative stress and mitochondrial membrane damage in human Achilles tendon cells. *Free Radic. Res.* **43**, 323–328 (2009).

206. Stockert, J. C., Horobin, R. W., Colombo, L. L. & Blázquez-Castro, A. Tetrazolium salts and formazan products in Cell Biology: Viability assessment, fluorescence imaging, and labeling perspectives. *Acta Histochem.* **120**, 159–167 (2018).

207. Boya, P. *et al.* Lysosomal membrane permeabilization induces cell death in a mitochondrion-dependent fashion. *J. Exp. Med.* **197**, 1323–1334 (2003).

208. Conway, L. P. *et al.* Evaluation of fully-functionalized diazirine tags for chemical proteomic applications. *Chem. Sci.* **12**, 7839–7847 (2021).

209. Tillotson, G. S. Quinolones: Structure-activity relationships and future predictions. *J. Med. Microbiol.* **44**, 320–324 (1996).

210. Zhang, L. H., Kauffman, G. S., Pesti, J. A. & Yin, J. Rearrangement of Nα-Protected L-Asparagines with Iodosobenzene Diacetate. A Practical Route to β-Amino-L-alanine Derivatives. *J. Org. Chem.* **62**, 6918–6920 (1997).

211. Glachet, T. *et al.* Iodonitrene in Action: Direct Transformation of Amino Acids into Terminal Diazirines and 15N2-Diazirines and Their Application as Hyperpolarized Markers. *J. Am. Chem. Soc.* **141**, 13689–13696 (2019).

212. Alt, S., Mitchenall, L. A., Maxwell, A. & Heide, L. Inhibition of DNA gyrase and DNA topoisomerase IV of Staphylococcus aureus and Escherichia coli by aminocoumarin antibiotics. *J. Antimicrob. Chemother.* **66**, 2061–2069 (2011).

213. Takei, M., Fukuda, H., Kishii, R. & Hosaka, M. Target preference of 15 quinolones against Staphylococcus aureus, based on antibacterial activities and target inhibition. *Antimicrob. Agents Chemother.* **45**, 3544–3547 (2001).

214. Tanaka, M., Onodera, Y., Uchida, Y., Sato, K. & Hayakawa, I. Inhibitory activities of quinolones against DNA gyrase and topoisomerase IV purified from Staphylococcus aureus. *Antimicrob. Agents Chemother.* **41**, 2362–2366 (1997).

215. Rostovtsev, V. V, Green, L. G., Fokin, V. V & Sharpless, K. B. A Stepwise Huisgen Cycloaddition Process: Copper(I)-Catalyzed Regioselective "Ligation" of Azides and Terminal Alkynes. *Angew. Chemie Int. Ed.* **41**, 2596–2599 (2002).

216. Chang, E. Y.-C. *et al.* Inhibition of Prostaglandin Reductase 2, a Putative Oncogene Overexpressed in Human Pancreatic Adenocarcinoma, Induces Oxidative Stress-Mediated Cell Death Involving xCT and CTH Gene Expressions through 15-Keto-PGE2. *PLoS One* **11**, e0147390–e0147390 (2016).

217. Wu, Y. H. *et al.* Structural Basis for Catalytic and Inhibitory Mechanisms of Human Prostaglandin Reductase PTGR2. *Structure* **16**, 1714–1723 (2008).

218. Chou, W. L. *et al.* Identification of a novel prostaglandin reductase reveals the involvement of prostaglandin E2 catabolism in regulation of peroxisome proliferator-activated receptor γ activation. *J. Biol. Chem.* **282**, 18162–18172 (2007).

219. Acton, S. *et al.* Identification of scavenger receptor SR-BI as a high density lipoprotein receptor. *Science* **271**, 518–520 (1996).

220. Shen, W.-J., Azhar, S. & Kraemer, F. B. SR-B1: A Unique Multifunctional Receptor for Cholesterol Influx and Efflux. *Annu. Rev. Physiol.* **80**, 95–116 (2018).

221. Ishizawa, J. *et al.* Mitochondrial ClpP-Mediated Proteolysis Induces Selective Cancer Cell Lethality. *Cancer Cell* **35**, 721-737.e9 (2019).

222. Cole, A. *et al.* Inhibition of the Mitochondrial Protease ClpP as a Therapeutic Strategy for Human Acute Myeloid Leukemia. *Cancer Cell* **27**, 864–876 (2015).

223. Szczepanowska, K. *et al.* A salvage pathway maintains highly functional respiratory complex I. *Nat. Commun.* **11**, 1–18 (2020).

224. Wu, D. Isocitrate dehydrogenase 2 inhibits gastric cancer cell invasion via matrix metalloproteinase 7. *Tumor Biol.* **37**, 5225–5230 (2016).

225. Yi, W. R., Li, Z. H., Qi, B. W., Hu, X. & Yu, A. X. Downregulation of IDH2 exacerbates the malignant progression of osteosarcoma cells via increased NF-KB and MMP-9 activation. *Oncol. Rep.* **35**, 2277–2285 (2016).

226. Salscheider, S. L. *et al.* AIFM1 is a component of the mitochondrial disulfide relay that drives complex I assembly through efficient import of NDUFS5. *EMBO J.* **41**, e110784 (2022).

227. Reinhardt, C. *et al.* AIF meets the CHCHD4/Mia40-dependent mitochondrial import pathway. *Biochim. Biophys. Acta - Mol. Basis Dis.* **1866**, 165746 (2020).

228. Wischhof, L., Scifo, E., Ehninger, D. & Bano, D. AIFM1 beyond cell death: An

overview of this OXPHOS-inducing factor in mitochondrial diseases. *eBioMedicine* **83**, 104231 (2022).

229. Gagestein, B. *et al.* Chemical Proteomics Reveals Off-Targets of the Anandamide Reuptake Inhibitor WOBE437. *ACS Chem. Biol.* **2022**, 1174–1183 (2022).

230. Zheng, B. *et al.* Cell- and Tissue-Based Proteome Profiling and Bioimaging with Probes Derived from a Potent AXL Kinase Inhibitor. *Chem. - An Asian J.* **13**, 2601–2605 (2018).

231. Tang, G. *et al.* Orthogonal Strategies for Profiling Potential Cellular Targets of Anandamide and Cannabidiol. *Chem. – A Eur. J.* **29**, e202300682 (2023).

232. Parker, C. G. *et al.* Chemical Proteomics Identifies SLC25A20 as a Functional Target of the Ingenol Class of Actinic Keratosis Drugs. *ACS Cent. Sci.* **3**, 1276–1285 (2017).

233. Tonazzi, A., Giangregorio, N., Console, L., Palmieri, F. & Indiveri, C. The mitochondrial carnitine acyl-carnitine carrier (Slc25a20): Molecular mechanisms of transport, role in redox sensing and interaction with drugs. *Biomolecules* **11**, 521 (2021).

234. Chantemargue, B. *et al.* Structural patterns of the human ABCC4/MRP4 exporter in lipid bilayers rationalize clinically observed polymorphisms. *Pharmacol. Res.* **133**, 318–327 (2018).

235. Bebes, A. *et al.* The expressions of ABCC4 and ABCG2 xenobiotic transporters in human keratinocytes are proliferation-related. *Arch. Dermatol. Res.* **304**, 57–63 (2012).

236. Dang, Y. *et al.* Molecular mechanism of substrate recognition by folate transporter SLC19A1. *Cell Discov. 2022 81* **8**, 1–11 (2022).

237. Wright, N. J. *et al.* Methotrexate recognition by the human reduced folate carrier SLC19A1. *Nature* **609**, 1056–1062 (2022).

238. Ohta, H., Kimura, I., Konishi, M. & Itoh, N. Neudesin as a unique secreted protein with multi-functional roles in neural functions, energy metabolism, and tumorigenesis. *Front. Mol. Biosci.* **2**, 24 (2015).

239. Camodeca, C. *et al.* Discovery of a new selective inhibitor of A Disintegrin and Metalloprotease 10 (ADAM-10) able to reduce the shedding of NKG2D ligands in Hodgkin's lymphoma cell models. *Eur. J. Med. Chem.* **111**, 193–201 (2016).

240. Nguyen, S. T. *et al.* Preparation and antibacterial evaluation of decarboxylated fluoroquinolones. *Bioorganic Med. Chem. Lett.* **21**, 5961–5963 (2011).

241. Petersen, U., Grohe, K., Zeiler, H.-J. & Metzger, K. G. 1-cyclopropyl-6-fluoro-1,4-dihydro-4-oxo-7-(3-oxo-1-piperazinyl)-3-quinolinecarboxylic acid antibacterial agents. (1986).

242. Douat-Casassus, C. *et al.* Synthetic anticancer vaccine candidates: Rational design of antigenic peptide mimetics that activate tumor-specific T-cells. *J. Med. Chem.* **50**, 1598–1609 (2007).

243. Ishizawa, J. *et al.* Mitochondrial ClpP-Mediated Proteolysis Induces Selective Cancer Cell Lethality. *Cancer Cell* **35**, 721-737.e9 (2019).

244. Szczepanowska, K. *et al.* A salvage pathway maintains highly functional respiratory

complex I. *Nat. Commun.* **11**, 1–18 (2020).

245. Graves, P. R. *et al.* Mitochondrial Protease ClpP is a Target for the Anticancer Compounds ONC201 and Related Analogues. *ACS Chem. Biol.* **14**, 1020–1029 (2019).

246. Gersch, M. *et al.* Barrel-shaped ClpP Proteases Display Attenuated Cleavage Specificities. *ACS Chem. Biol.* **11**, 389–399 (2016).

247. Gronauer, T. F. *et al.* Design and synthesis of tailored human caseinolytic protease P inhibitors. *Chem. Commun.* **54**, 9833–9836 (2018).

248. Nguyen, T., Gronauer, T. F., Nast-Kolb, T., Sieber, S. A. & Lang, K. Substrate Profiling of Mitochondrial Caseinolytic Protease P via a Site-Specific Photocrosslinking Approach. *Angew. Chemie Int. Ed.* **61**, e202111085 (2022).

249. Fu, Y. *et al.* Mutations in isocitrate dehydrogenase 2 accelerate glioma cell migration via matrix metalloproteinase-2 and 9. *Biotechnol. Lett.* **34**, 441–446 (2012).

250. Smolková, K. *et al.* SIRT3 and GCN5L regulation of NADP+- and NADPH-driven reactions of mitochondrial isocitrate dehydrogenase IDH2. *Sci. Rep.* **10**, 1–12 (2020).

251. Zou, X. *et al.* SIRT3-mediated dimerization of IDH2 directs cancer cell metabolism and tumor growth. *Cancer Res.* **77**, 3990–3999 (2017).

252. Yoo, H., Antoniewicz, M. R., Stephanopoulos, G. & Kelleher, J. K. Quantifying reductive carboxylation flux of glutamine to lipid in a brown adipocyte cell line. *J. Biol. Chem.* **283**, 20621–20627 (2008).

253. Leonardi, R., Subramanian, C., Jackowski, S. & Rock, C. O. Cancer-associated isocitrate dehydrogenase mutations inactivate NADPH-dependent reductive carboxylation. *J. Biol. Chem.* **287**, 14615–14620 (2012).

254. Wise, D. R. *et al.* Hypoxia promotes isocitrate dehydrogenasedependent carboxylation of α-ketoglutarate to citrate to support cell growth and viability. *Proc. Natl. Acad. Sci. U. S. A.* **108**, 19611–19616 (2011).

255. Metallo, C. M. *et al.* Reductive glutamine metabolism by IDH1 mediates lipogenesis under hypoxia. *Nature* **481**, 380–384 (2012).

256. Mullen, A. R. *et al.* Reductive carboxylation supports growth in tumour cells with defective mitochondria. *Nature* **481**, 385–388 (2012).

257. Cambronne, X. A. *et al.* Biosensor reveals multiple sources for mitochondrial NAD+. *Science* **352**, 1474–1477 (2016).

258. Lian, C. G. *et al.* Loss of 5-hydroxymethylcytosine is an epigenetic hallmark of Melanoma. *Cell* **150**, 1135–1146 (2012).

259. Comprehensive, Integrative Genomic Analysis of Diffuse Lower-Grade Gliomas. *N. Engl. J. Med.* **372**, 2481–2498 (2015).

260. Memon, A. A., Chang, J. W., Oh, B. R. & Yoo, Y. J. Identification of differentially expressed proteins during human urinary bladder cancer progression. *Cancer Detect. Prev.* **29**, 249–255 (2005).

261. Yen, K. *et al.* AG-221, a First-in-Class Therapy Targeting Acute Myeloid Leukemia Harboring Oncogenic IDH2 Mutations. *Cancer Discov.* **7**, 478–493 (2017).

262. Du, X. & Hu, H. The Roles of 2-Hydroxyglutarate. *Front. Cell Dev. Biol.* **9**, 651317 (2021).

263. Berillis, P. The Role of Collagen in the Aorta's Structure. *Open Circ. Vasc. J.* **6**, 1–8 (2013).

264. Corps, A. N., Harrall, R. L., Curry, V. A., Hazleman, B. L. & Riley, G. P. Contrasting effects of fluoroquinolone antibiotics on the expression of the collagenases, matrix metalloproteinases (MMP)-1 and -13, in human tendon-derived cells. *Rheumatology* **44**, 1514–1517 (2005).

265. Sharma, C. *et al.* Effect of fluoroquinolones on the expression of matrix metalloproteinase in debrided cornea of rats. *Toxicol. Mech. Methods* **21**, 6–12 (2011).

266. Zhao, S. *et al.* Glioma-derived mutations in IDH1 dominantly inhibit IDH1 catalytic activity and induce HIF-1α. *Science* **324**, 261–265 (2009).

267. Liu, T., Zhang, L., Joo, D. & Sun, S. C. NF-κB signaling in inflammation. *Signal Transduct. Target. Ther. 2017 21* **2**, 1–9 (2017).

268. Liu, S., Yang, J. & Wu, Z. The regulatory role of a-ketoglutarate metabolism in macrophages. *Mediators Inflamm.* **2021**, (2021).

269. Li, Z. Z., Gopala, L., Tangadanchu, V. K. R., Gao, W. W. & Zhou, C. H. Discovery of novel nitroimidazole enols as Pseudomonas aeruginosa DNA cleavage agents. *Bioorganic Med. Chem.* **25**, 6511–6522 (2017).

270. Wang, X. *et al.* α-Ketoglutarate-Activated NF-κB Signaling Promotes Compensatory Glucose Uptake and Brain Tumor Development. *Mol. Cell* **76**, 148-162.e7 (2019).

271. Chen, J. Y. *et al.* The oncometabolite R-2-hydroxyglutarate activates NF-κB-dependent tumor-promoting stromal niche for acute myeloid leukemia cells. *Sci. Rep.* **6**, 1–12 (2016).

272. Davis, M. I., Shen, M., Simeonov, A. & Hall, M. D. Diaphorase Coupling Protocols for Red-Shifting Dehydrogenase Assays. *Assay Drug Dev. Technol.* **14**, 207–212 (2016).

273. Slemc, L. & Kunej, T. Transcription factor HIF1A: downstream targets, associated pathways, polymorphic hypoxia response element (HRE) sites, and initiative for standardization of reporting in scientific literature. *Tumor Biol.* **37**, 14851–14861 (2016).

274. NF-kB Transcription Factors | Boston University. https://www.bu.edu/nf-kb/.

275. Ma, R. & Yun, C. H. Crystal structures of pan-IDH inhibitor AG-881 in complex with mutant human IDH1 and IDH2. *Biochem. Biophys. Res. Commun.* **503**, 2912–2917 (2018).

276. Panavas, T., Sanders, C. & Butt, T. R. SUMO fusion technology for enhanced protein production in prokaryotic and eukaryotic expression systems. *Methods Mol. Biol.* **497**, 303–317 (2009).

277. Kim, S. *et al.* Suppression of tumorigenesis in mitochondrial NADP+-dependent isocitrate dehydrogenase knock-out mice. *Biochim. Biophys. Acta - Mol. Basis Dis.* **1842**, 135–143 (2014).

278. Tan, L. & Shi, Y. G. Tet family proteins and 5-hydroxymethylcytosine in development and disease. *Development* **139**, 1895–1902 (2012).

279. Allis, C. D. & Jenuwein, T. The molecular hallmarks of epigenetic control. *Nat. Rev. Genet.* **17**, 487–500 (2016).

280. Goll, M. G. & Bestor, T. H. Eukaryotic cytosine methyltransferases. *Annu. Rev. Biochem.* **74**, 481–514 (2005).

281. Globisch, D. *et al.* Tissue Distribution of 5-Hydroxymethylcytosine and Search for Active Demethylation Intermediates. *PLoS One* **5**, e15367 (2010).

282. Hahn, M. A., Li, A. X., Wu, X. & Pfeifer, G. P. Single base resolution analysis of 5-methylcytosine and 5-hydroxymethylcytosine by RRBS and TAB-RRBS. in *Cancer Epigenetics: Risk Assessment, Diagnosis, Treatment, and Prognosis* 273–287 (Springer New York, 2014). doi:10.1007/978-1-4939-1804-1_14.

283. Herrmann, J. M. & Riemer, J. Apoptosis inducing factor and mitochondrial NADH dehydrogenases: Redox-controlled gear boxes to switch between mitochondrial biogenesis and cell death. *Biol. Chem.* **402**, 289–297 (2021).

284. Hangen, E. *et al.* Interaction between AIF and CHCHD4 Regulates Respiratory Chain Biogenesis. *Mol. Cell* **58**, 1001–1014 (2015).

285. Klein, J. A. *et al.* The harlequin mouse mutation downregulates apoptosis-inducing factor. *Nature* **419**, 367–374 (2002).

286. Chang, E. Y.-C. *et al.* Inhibition of Prostaglandin Reductase 2, a Putative Oncogene Overexpressed in Human Pancreatic Adenocarcinoma, Induces Oxidative Stress-Mediated Cell Death Involving xCT and CTH Gene Expressions through 15-Keto-PGE2. *PLoS One* **11**, e0147390 (2016).

287. Shen, W.-J., Azhar, S. & Kraemer, F. B. SR-B1: A Unique Multifunctional Receptor for Cholesterol Influx and Efflux. *Annu. Rev. Physiol.* **80**, 95–116 (2018).

288. Olayinka, E. T., Ore, A. & Ola, O. S. Influence of Different Doses of Levofloxacin on Antioxidant Defense Systems and Markers of Renal and Hepatic Dysfunctions in Rats. *Adv. Toxicol.* **2015**, 385023 (2015).

289. Tilley, B. J., Cook, J. L., Docking, S. I. & Gaida, J. E. Is higher serum cholesterol associated with altered tendon structure or tendon pain? A systematic review. *Br. J. Sports Med.* **49**, 1504–1509 (2015).

290. Huang, L. & Zhang, C. Microscale Thermophoresis (MST) to Detect the Interaction Between Purified Protein and Small Molecule. *Methods Mol. Biol.* **2213**, 187–193 (2021).

291. Bialkowski, K. & Szpila, A. Specific 8-oxo-dGTPase activity of MTH1 (NUDT1) protein as a quantitative marker and prognostic factor in human colorectal cancer. *Free Radic. Biol. Med.* **176**, 257–264 (2021).

292. Satou, K., Kawai, K., Kasai, H., Harashima, H. & Kamiya, H. Mutagenic effects of 8-hydroxy-dGTP in live mammalian cells. *Free Radic. Biol. Med.* **42**, 1552–1560 (2007).

293. Satou, K., Harashima, H. & Kamiya, H. Mutagenic effects of 2-hydroxy-dATP on replication in a HeLa extract: induction of substitution and deletion mutations.

Nucleic Acids Res. **31**, 2570–2575 (2003).

294. Cheng, K. C., Cahill, D. S., Kasai, H., Nishimura, S. & Loeb, L. A. 8-Hydroxyguanine, an abundant form of oxidative DNA damage, causes G → T and A → C substitutions. *J. Biol. Chem.* **267**, 166–172 (1992).

295. Fujikawa, K., Kamiya, H., Yakushiji, H., Nakabeppu, Y. & Kasai, H. Human MTH1 protein hydrolyzes the oxidized ribonucleotide, 2-hydroxy-ATP. *Nucleic Acids Res.* **29**, 449–454 (2001).

296. Ishibashi, T. *et al.* Mammalian enzymes for preventing transcriptional errors caused by oxidative damage. *Nucleic Acids Res.* **33**, 3779–3784 (2005).

297. Scaletti, E. R. *et al.* MutT homologue 1 (MTH1) removes N6-methyl-dATP from the dNTP pool. *J. Biol. Chem.* **295**, 4761–4772 (2020).

298. Murakami, E. *et al.* Adenosine Deaminase-like Protein 1 (ADAL1): Characterization and Substrate Specificity in the Hydrolysis of N 6 - or O 6 -Substituted Purine or 2-Aminopurine Nucleoside Monophosphates. *J. Med. Chem.* **54**, 5902–5914 (2011).

299. Schinkmanová, M., Votruba, I. & Holý, A. N6-Methyl-AMP aminohydrolase activates N6-substituted purine acyclic nucleoside phosphonates. *Biochem. Pharmacol.* **71**, 1370–1376 (2006).

300. Carter, M. *et al.* Crystal structure, biochemical and cellular activities demonstrate separate functions of MTH1 and MTH2. *Nat. Commun.* **6**, 1–10 (2015).

301. Gad, H. *et al.* MTH1 inhibition eradicates cancer by preventing sanitation of the dNTP pool. *Nature* **508**, 215–221 (2014).

302. Nakabeppu, Y., Ohta, E. & Abolhassani, N. MTH1 as a nucleotide pool sanitizing enzyme: Friend or foe? *Free Radic. Biol. Med.* **107**, 151–158 (2017).

303. Farand, J. *et al.* Discovery of Potent and Selective MTH1 Inhibitors for Oncology: Enabling Rapid Target (In)Validation. *ACS Med. Chem. Lett.* **11**, 358–364 (2020).

304. Huber, K. V. M. *et al.* Stereospecific targeting of MTH1 by (S)-crizotinib as an anticancer strategy. *Nature* **508**, 222–227 (2014).

305. Peng, C. *et al.* Inhibitor development of MTH1 via high-throughput screening with fragment based library and MTH1 substrate binding cavity. *Bioorg. Chem.* **110**, 104813 (2021).

306. Yokoyama, T., Kitakami, R. & Mizuguchi, M. Discovery of a new class of MTH1 inhibitor by X-ray crystallographic screening. *Eur. J. Med. Chem.* **167**, 153–160 (2019).

307. Zhou, W. *et al.* Potent and specific MTH1 inhibitors targeting gastric cancer. *Cell Death Dis.* **10**, 1–19 (2019).

308. Maier, S. A., Galellis, J. R. & McDermid, H. E. Phylogenetic analysis reveals a novel protein family closely related to adenosine deaminase. *J. Mol. Evol.* **61**, 776–794 (2005).

309. Schinkmanová, M. *et al.* Human N6-methyl-AMP/dAMP aminohydrolase (abacavir 5-monophosphate deaminase) is capable of metabolizing N6-substituted purine acyclic nucleoside phosphonates. *Collect. Czechoslov. Chem. Commun.* **73**, 275–291 (2008).

310. Chen, M. *et al.* m 6 A RNA Degradation Products Are Catabolized by an Evolutionarily Conserved N 6 -Methyl-AMP Deaminase in Plant and Mammalian Cells. *Plant Cell* **30**, 1511–1522 (2018).

311. Wang, F., Gómez-Sintes, R. & Boya, P. Lysosomal membrane permeabilization and cell death. *Traffic* **19**, 918–931 (2018).

312. Maeda, K., Osato, T. & Umezawa, H. A new antibiotic, azomycin. *J. Antibiot. (Tokyo).* **6**, 182 (1953).

313. Ang, C. W., Jarrad, A. M., Cooper, M. A. & Blaskovich, M. A. T. Nitroimidazoles: Molecular Fireworks That Combat a Broad Spectrum of Infectious Diseases. *J. Med. Chem.* **60**, 7636–7657 (2017).

314. O'Brien, R. W. & Morris, J. G. The Ferredoxin-dependent reduction of chloramphenicol by clostridium acetobutylicum. *J. Gen. Microbiol.* **67**, 265–271 (1971).

315. Ehlhardt, W. J., Beaulieu, B. B. & Goldman, P. Formation of an amino reduction product of metronidazole in bacterial cultures: Lack of bactericidal activity. *Biochem. Pharmacol.* **36**, 259–264 (1987).

316. Mukherjee, T. & Boshoff, H. Nitroimidazoles for the treatment of TB: Past, present and future. *Future Med. Chem.* **3**, 1427–1454 (2011).

317. Lancini, G. C. & Lazzari, E. The synthesis of azomycin (2-Nitroimidazole). *Experientia* **21**, 83 (1965).

318. Sharma, R. Nitroimidazole Radiopharmaceuticals in Hypoxia: Part II Cytotoxicity and Radiosensitization Applications. *Curr. Radiopharm.* **4**, 379–393 (2011).

319. Kizaka-Kondoh, S. & Konse-Nagasawa, H. Significance of nitroimidazole compounds and hypoxia-inducible factor-1 for imaging tumor hypoxia. *Cancer Sci.* **100**, 1366–1373 (2009).

320. Stover, C. K. *et al.* A small-molecule nitroimidazopyran drug candidate for the treatment of tuberculosis. *Nature* **405**, 962–966 (2000).

321. Matsumoto, M. *et al.* OPC-67683, a Nitro-Dihydro-Imidazooxazole Derivative with Promising Action against Tuberculosis In Vitro and In Mice. *PLoS Med.* **3**, e466 (2006).

322. Dingsdag, S. A. & Hunter, N. Metronidazole: an update on metabolism, structure–cytotoxicity and resistance mechanisms. *J. Antimicrob. Chemother.* **73**, 265–279 (2017).

323. Wayne, L. G. & Sramek, H. A. Metronidazole is bactericidal to dormant cells of Mycobacterium tuberculosis. *Antimicrob. Agents Chemother.* **38**, 2054–2058 (1994).

324. Church, D. L. & Laishley, E. J. Reduction of metronidazole by hydrogenase from clostridia. *Anaerobe* **1**, 81–92 (1995).

325. Dingsdag, S. A. & Hunter, N. Metronidazole: An update on metabolism, structure-cytotoxicity and resistance mechanisms. *J. Antimicrob. Chemother.* **73**, 265–279 (2018).

326. Moore, R. A., Beckthold, B. & Bryan, L. E. Metronidazole uptarke in helicobacter pylori. *Can. J. Microbiol.* **41**, 746–749 (1995).

327. Jackson, D., Salem, A. & Coombs, G. H. The *in-vitro* activity of metronidazole against strains of *Escherichia coli* with impaired DNA repair systems. *J. Antimicrob. Chemother.* **13**, 227–236 (1984).

328. Yeung, T. C., Beaulieu, B. B., McLafferty, M. A. & Goldman, P. Interaction of metronidazole with DNA repair mutants of Escherichia coli. *Antimicrob. Agents Chemother.* **25**, 65–70 (1984).

329. Kaster, A. K., Moll, J., Parey, K. & Thauer, R. K. Coupling of ferredoxin and heterodisulfide reduction via electron bifurcation in hydrogenotrophic methanogenic archaea. *Proc. Natl. Acad. Sci. U. S. A.* **108**, 2981–2986 (2011).

330. Roldán, M. D., Pérez-Reinado, E., Castillo, F. & Moreno-Vivián, C. Reduction of polynitroaromatic compounds: The bacterial nitroreductases. *FEMS Microbiol. Rev.* **32**, 474–500 (2008).

331. Etxeberria, A., Lonneville, S., Rutgers, M. P. & Gille, M. Metronidazole-cerebellopathy associated with peripheral neuropathy, downbeat nystagmus, and bilateral ocular abduction deficit. *Rev. Neurol. (Paris).* **168**, 193–195 (2012).

332. Hobbs, K., Stern-Nezer, S., Buckwalter, M. S., Fischbein, N. & Finley Caulfield, A. Metronidazole-Induced Encephalopathy: Not Always a Reversible Situation. *Neurocrit. Care* **22**, 429–436 (2015).

333. Ingham, H. R., Eaton, S., Venables, C. W. & Adams, P. C. Bacteroides Fragilis resistant to metronidazole after long-termin therapy. *Lancet* **311**, 214 (1978).

334. Edwards, D. I. Nitroimidazole drugs - action and resistance mechanisms II. Mechanisms of resistance. *J. Antimicrob. Chemother.* **31**, 201–210 (1993).

335. Čerkasovová, A., Čerkasov, J. & Kulda, J. Metabolic differences between metronidazole resistant and susceptible strains of Tritrichomonas foetus. *Mol. Biochem. Parasitol.* **11**, 105–118 (1984).

336. Sindar, P., Britz, M. L. & Wilkinson, R. G. Isolation and properties of metronidazole-resistant mutants of Clostridium perfringens. *J. Med. Microbiol.* **15**, 503–509 (1982).

337. Ansell, B. R. E. *et al.* Transcriptomics indicates active and passive metronidazole resistance mechanisms in three seminal Giardia lines. *Front. Microbiol.* **8**, 398 (2017).

338. Zhou, Y. *et al.* Discovery of hybrids of indolin-2-one and nitroimidazole as potent inhibitors against drug-resistant bacteria. *J. Antibiot. (Tokyo).* **71**, 887–897 (2018).

339. Howard-Varona, C., Hargreaves, K. R., Abedon, S. T. & Sullivan, M. B. Lysogeny in nature: mechanisms, impact and ecology of temperate phages. *ISME J. 2017 117* **11**, 1511–1520 (2017).

340. Xia, G. & Wolz, C. Phages of Staphylococcus aureus and their impact on host evolution. *Infect. Genet. Evol.* **21**, 593–601 (2014).

341. Wagner, P. L. & Waldor, M. K. Bacteriophage control of bacterial virulence. *Infect. Immun.* **70**, 3985–3993 (2002).

342. Jancheva, M. & Böttcher, T. A Metabolite of Pseudomonas Triggers Prophage-Selective Lysogenic to Lytic Conversion in Staphylococcus aureus. *J. Am. Chem. Soc.* **143**, 8344–8351 (2021).

343. Fey, P. D. *et al.* A Genetic Resource for Rapid and Comprehensive Phenotype

Screening of Nonessential Staphylococcus aureus Genes. *MBio* **4**, (2013).

344. Elgrishi, N. *et al.* A Practical Beginner's Guide to Cyclic Voltammetry. *J. Chem. Educ.* **95**, 197–206 (2018).

345. Nepali, K., Lee, H. Y. & Liou, J. P. Nitro-Group-Containing Drugs. *J. Med. Chem.* **62**, 2851–2893 (2019).

346. Adams, G. E. *et al.* Nitroheterocyclic compounds as radiation sensitizers and bioreductive drugs. *Radiother. Oncol.* **20**, 85–91 (1991).

347. Ma, Z. *et al.* Design, Synthesis, and Characterization of TNP-2198, a Dual-Targeted Rifamycin-Nitroimidazole Conjugate with Potent Activity against Microaerophilic and Anaerobic Bacterial Pathogens. *J. Med. Chem.* **65**, 4481–4495 (2022).

348. Wiśniewski, J. R., Zougman, A., Nagaraj, N. & Mann, M. Universal sample preparation method for proteome analysis. *Nat. Methods* **6**, 359–362 (2009).

349. Corydon, T. J. *et al.* A human homologue of Escherichia coli CIpP caseinolytic protease: Recombinant expression, intracellular processing and subcellular localization. *Biochem. J.* **331**, 309–316 (1998).

350. Subcellular fractionation protocol | Abcam. https://www.abcam.com/protocols/subcellular-fractionation-protocol.

351. Parker, C. G. *et al.* Ligand and Target Discovery by Fragment-Based Screening in Human Cells. *Cell* **168**, 527-541.e29 (2017).

352. Lum, K. M. *et al.* Mapping Protein Targets of Bioactive Small Molecules Using Lipid-Based Chemical Proteomics. *ACS Chem. Biol.* **12**, 2671–2681 (2017).

353. Vallet, C. *et al.* Functional Disruption of the Cancer-Relevant Interaction between Survivin and Histone H3 with a Guanidiniocarbonyl Pyrrole Ligand. *Angew. Chemie Int. Ed.* **59**, 5567–5571 (2020).

354. Zhang, Z. *et al.* Synthesis of alanine and proline amino acids with amino or guanidinium substitution on the side chain. *Tetrahedron* **56**, 2513–2522 (2000).

355. Rosowsky, A. *et al.* Methotrexate Analogues. 26. Inhibition of Dihydrofolate Reductase and Folylpolyglutamate Synthetase Activity and in Vitro Tumor Cell Growth by Methotrexate and Aminopterin Analogues Containing a Basic Amino Acid Side Chain. *J. Med. Chem.* **29**, 655–660 (1986).

356. Nakhaei, A., Ramezani, S., Shams-Najafi, S. J. & Farsinejad, S. Nano-Fe3O4@ZrO2-SO3H as Highly Efficient Recyclable Catalyst for the Green Synthesis of Fluoroquinolones. *Lett. Org. Chem.* **15**, 739–746 (2018).

357. Alsayed, S. S. R., Lun, S., Payne, A., Bishai, W. R. & Gunosewoyo, H. Facile synthesis and antimycobacterial activity of isoniazid, pyrazinamide and ciprofloxacin derivatives. *Chem. Biol. Drug Des.* **97**, 1137–1150 (2021).

358. Paudel, A., Panthee, S., Hamamoto, H. & Sekimizu, K. GPI0363 inhibits the interaction of RNA polymerase with DNA in: Staphylococcus aureus. *RSC Adv.* **9**, 37889–37894 (2019).

359. Perez-Riverol, Y. *et al.* The PRIDE database resources in 2022: A hub for mass spectrometry-based proteomics evidences. *Nucleic Acids Res.* **50**, D543–D552 (2022).

VI – Appendix

1. List of figures

2. List of schemes

3. List of tables

4. List of abbreviations

For gene and protein names consult the respective tables given in the figures.

5cadC	5-carboxyldeoxycytidine
5fdC	5-formyldeoxycytidine
5hmdC	5-hydroxymethyldeoxycytidine
5mdC	5-methyldeoxycytidine
A549	Adenocarcinomic human alveolar basal epithelial cells
ABC-MP	Abacavir monophosphate
ABP	Activity-based probe
ABPP	Activity-based protein profiling
AfBPP	Affinity-based protein profiling
AMP	Adenosine monophosphate
AMR	Antimicrobial resistance
ATP	Adenosine triphosphate
AUC	Area under the curve
BGCs	Biosynthetic gene clusters
Boc	*tert*-Butyloxycarbonyl (protecting group)
CARB-X	Combating Antibiotic-Resistant Bacteria Biopharmaceutical Accelerator
Cbz	Benzyloxycarbonyl (protecting group)
CDC	Unites States Centers for Disease Control and Prevention
CECAD	Cluster of Excellence Cellular Stress Responses in Aging-Associated Diseases
CETSA	Cellular thermal shift assay
Cipro	Ciprofloxacin
CNS	Central nervous system
CuAAC	Copper(I)-catalyzed azide-alkyne cycloaddition
CV	Cyclic voltammetry
DABCO	1,4-diazabicyclo[2.2.2]octane
DIPEA	*N*,*N*-diisopropylethylamine (non-nucleophilic base)
DMAP	*N*,*N*-dimethylaminopyridin
DMF	Dimethylformamide
DMSO	Dimethyl sulfoxide

DNA	Deoxynucleic acid
dNTP	Deoxynucleoside triphosphate
DOS	Diversity-oriented synthesis
EC_{50}	Half maximal effective concentration
ECM	Extracellular matrix
EMA	European Medicines Agency
$E_{p,c}$	Cathodic peak potential
EPS	Extracellular polymeric structures
ETC	Electron transport chain
ETD	Electron transfer dissociation
FACS	Fluorescence-activated cell sorting
FCS	Fetal calf serum
FDA	U.S. Food and Drug Administration
FQ	Fluoroquinolone
FQAD	Fluroquinolone-associated disability
GABA	Gamma-aminobutyric acid (neurotransmitter)
GARDP	Global Antibiotic Research and Development Partnership
GDH1	Glutamate dehydrogenase 1
GTP	Guanosine triphosphate
HBTU	Hexafluorophosphate Benzotriazole Tetramethyl Uronium
HCD	Higher-energy collisional dissociation
HDL	High density lipoprotein
HEK-293	Human embryonic kidney 293 cells
HIF1	Hypoxia-inducible factor 1
HIF1	hypoxia-inducible factor 1
HILIC	Hydrophilic interaction liquid chromatography
HIPS	Helmholtz-Institut für Pharmazeutische Forschung Saarland
HPLC	High-performance liquid chromatography
IC	Isocitric acid, isocitrate
IC_{50}	Half maximal inhibitory concentration
IκB	Inhibitor of NF-κB
IMS	Intramembrane space
ITPG	Isopropyl β-D-1-thiogalactopyranoside
kDNA	Kinetoplast (circular) DNA (deoxyribonucleic acid)
KO	Genetic knock-out
LC-MS/MS	Liquid chromatography coupled mass spectrometry
LDL	Low density lipoprotein

Levo	Levofloxacin
LFQ	Label-free quantification
LMP	Lysosomal membrane permeabilization
LPS	Lipopolysaccharides
MeCN	Acetonitrile
me-PMEDAP	Methylated prodrug of 9-(2-phosphonylmethoxyethyl)-2,6-diaminopurine
MIC	Minimal inhibitory concentration
MMP	Matrix metalloprotease
MMP	Mitochondrial membrane permeabilization
MoA	Mode of action
mRNA	Messenger ribonucleic acid
MS	Mass spectrometry
MST	Microscale thermophoresis
mtDNA	Mitochondrial DNA
MTS	Mitochondrial targeting sequence
MTT	3-(4,5-dimethylthiazol-2-yl)-2,5-diphenyltetrazolium bromide
NAD^+/NADH	Nicotinamide adenine dinucleotide (oxidized and reduced form)
$NADP^+$/NADPH	Nicotinamide adenine dinucleotide phosphate (oxidized and reduced form)
NET	Neutrophil extracellular trap
NF-κB	Nuclear factor 'kappa-light-chain-enhancer' of activated B-cells
NHE	Normal hydrogen electrode
NHS-ester	*N*-hydroxysuccinimide ester
NP	Natural product
NTR	Nitroreductase
PAL	Photo-affinity labeling
PDL	Periodontal ligament
PFOR	Pyruvate:ferredoxin oxidoreductase
PHD	Prolylhydroxylases
PIDA	Phenylidodine(III) acetate / (Diacetoxyiodo)benzene
PISA	Proteome integral solubility alteration
PTM	Posttranslational modification
qPCR	Quantitative polymerase chain reaction
QRDR	Quinolone resistance-determining region
R&D	Research & development
r.t.	Room temperature
REPAIR	Replenishing and Enabling the Pipeline for Anti-Infective Resistance
RNA	Ribonucleic acid

ROESY	Rotating frame Overhauser Enhancement Spectroscopy
ROS	Reactive-oxygen species
R-script	Script of R programming language
SAR	Structure-activity relationship
SD	Standard deviation
SDS-PAGE	Sodium dodecyl sulfate polyacrylamide gel electrophoresis
S_NAr	Nucleophilic aromatic substitution
SPR	Surface-plasmon resonance
TAMRA	5-Carboxytetramethylrhodamin (fluorophore)
TCA cycle	Tricarboxylic acid cycle (citric acid cycle)
TET enzymes	Human ten-eleven translocation enzymes
TFA	Trifluoroacetic acid
T_m	Melting point temperature
TMT	Tandem mass tag
TPP	Thermal proteome profiling
TPP-CCR	Concentration-range thermal proteome profiling
TPP-TR	Temperature-range thermal proteome profiling
TRIC	Temperature related intensity change
TSA	Thermal shift assay
TUM	Technical University of Munich
U.S.	United States (of America)
UV	Ultra-violet (light)
WHO	World Health Organization
αKG	alpha-ketoglutarate

5. NMR spectra of the fluoroquinolone project

^{1}H NMR **Cipro P1** (500 MHz, DMSO-d6):

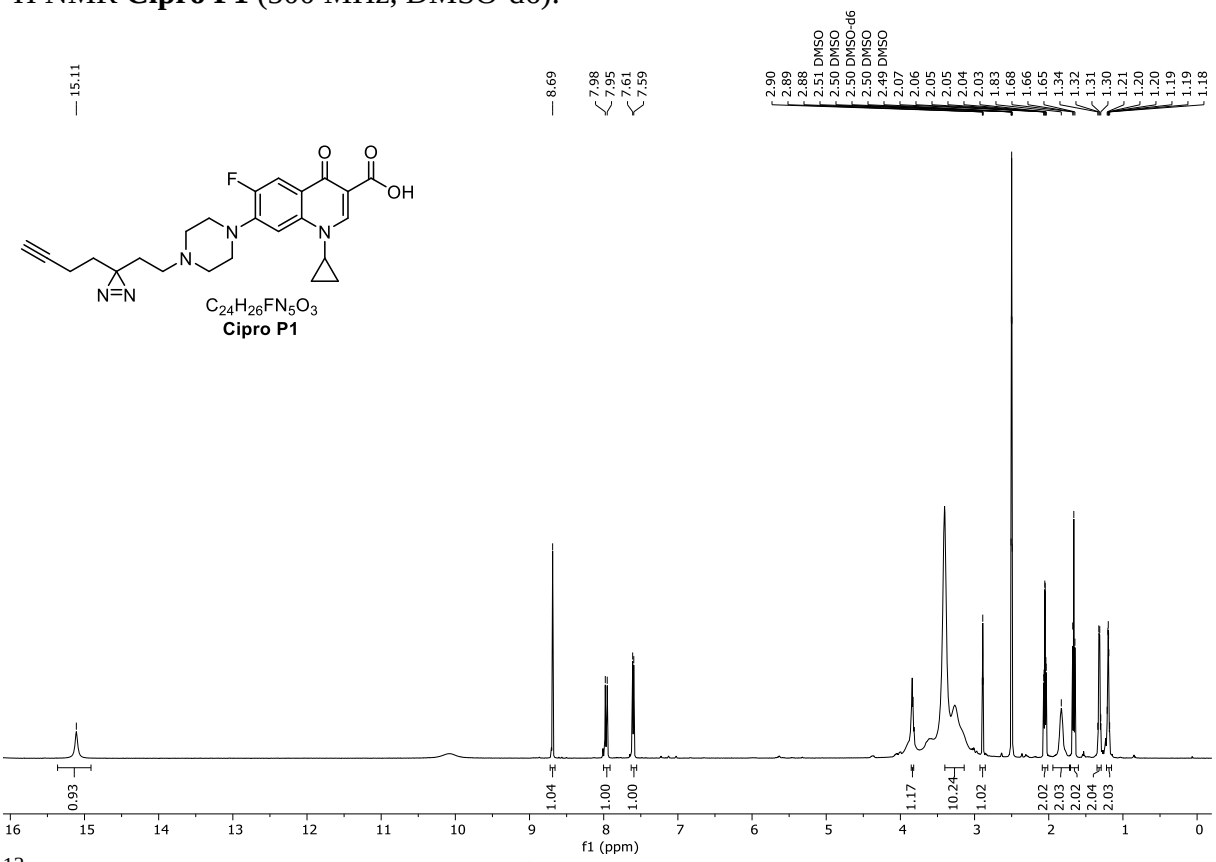

^{13}C NMR **Cipro P1** (125 MHz, DMSO-d6):

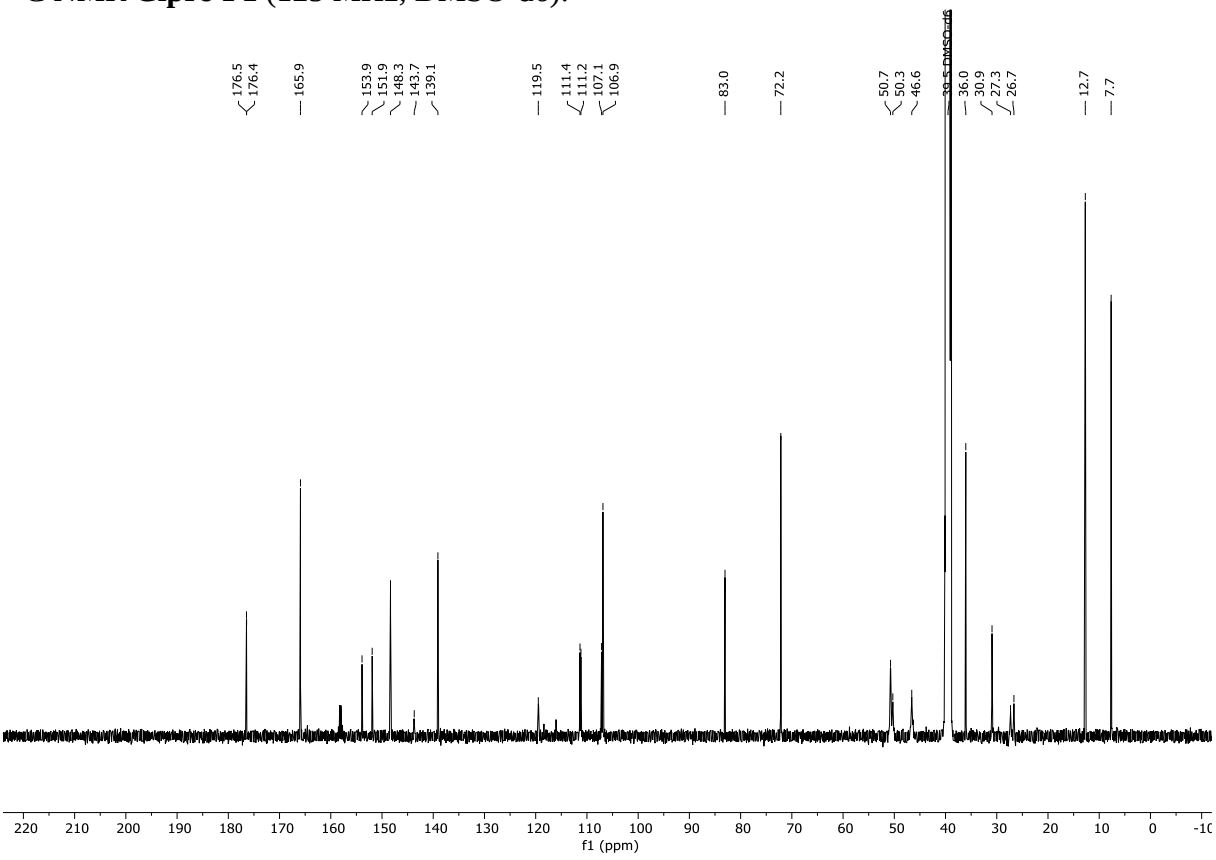

^{1}H NMR **Levo P1** (400 MHz, DMSO-d6):

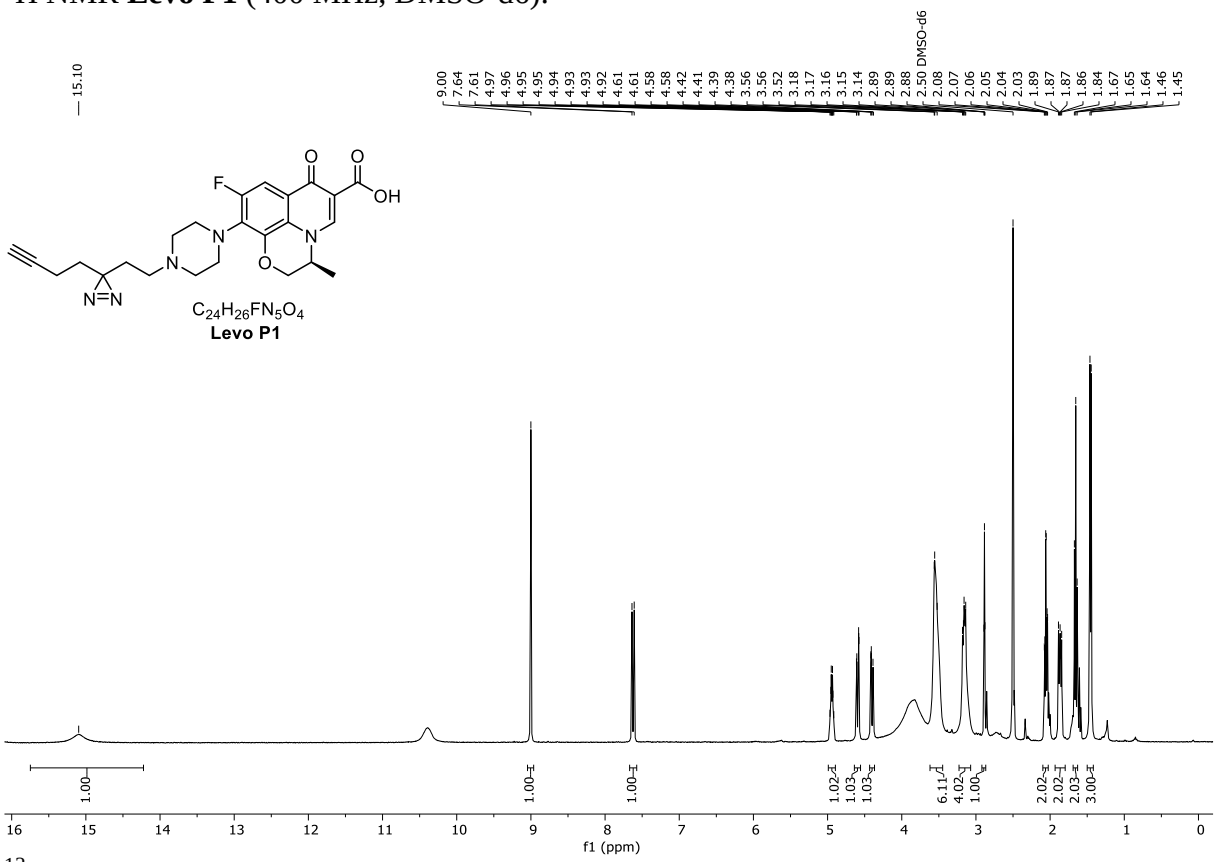

^{13}C NMR **Levo P1** (125 MHz, DMSO-d6):

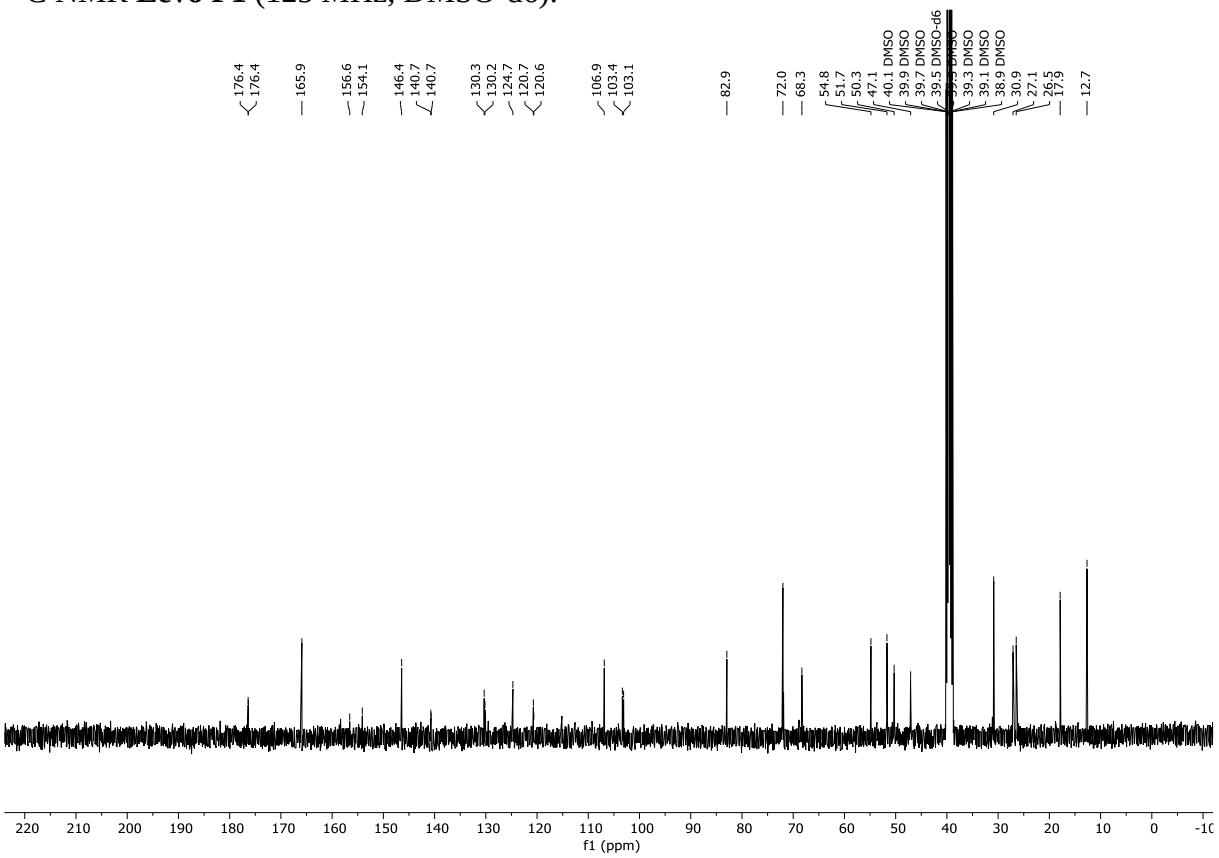

^{1}H NMR **Cipro P2** (500 MHz, $CDCl_3$):

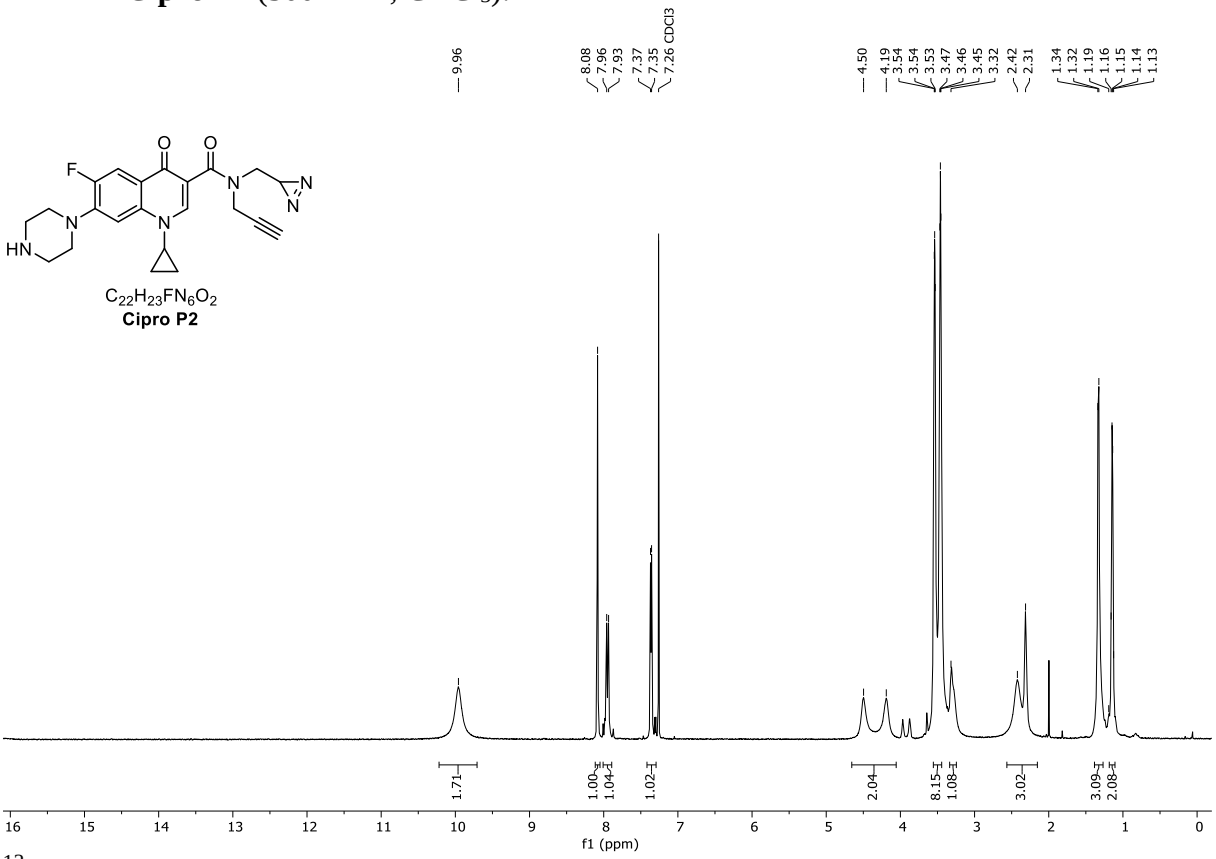

^{13}C NMR **Cipro P2** (125 MHz, $CDCl_3$):

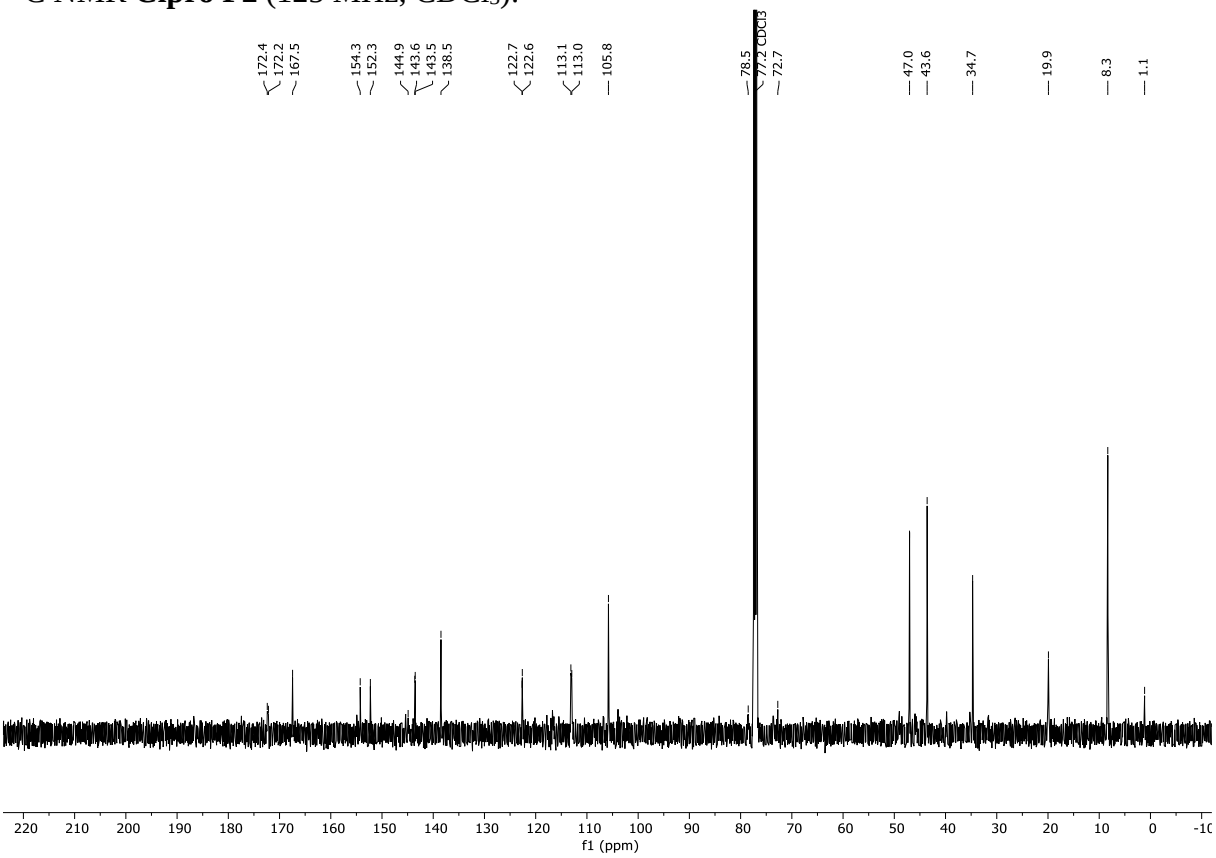

^{1}H NMR **Levo P2** (400 MHz, $CDCl_3$):

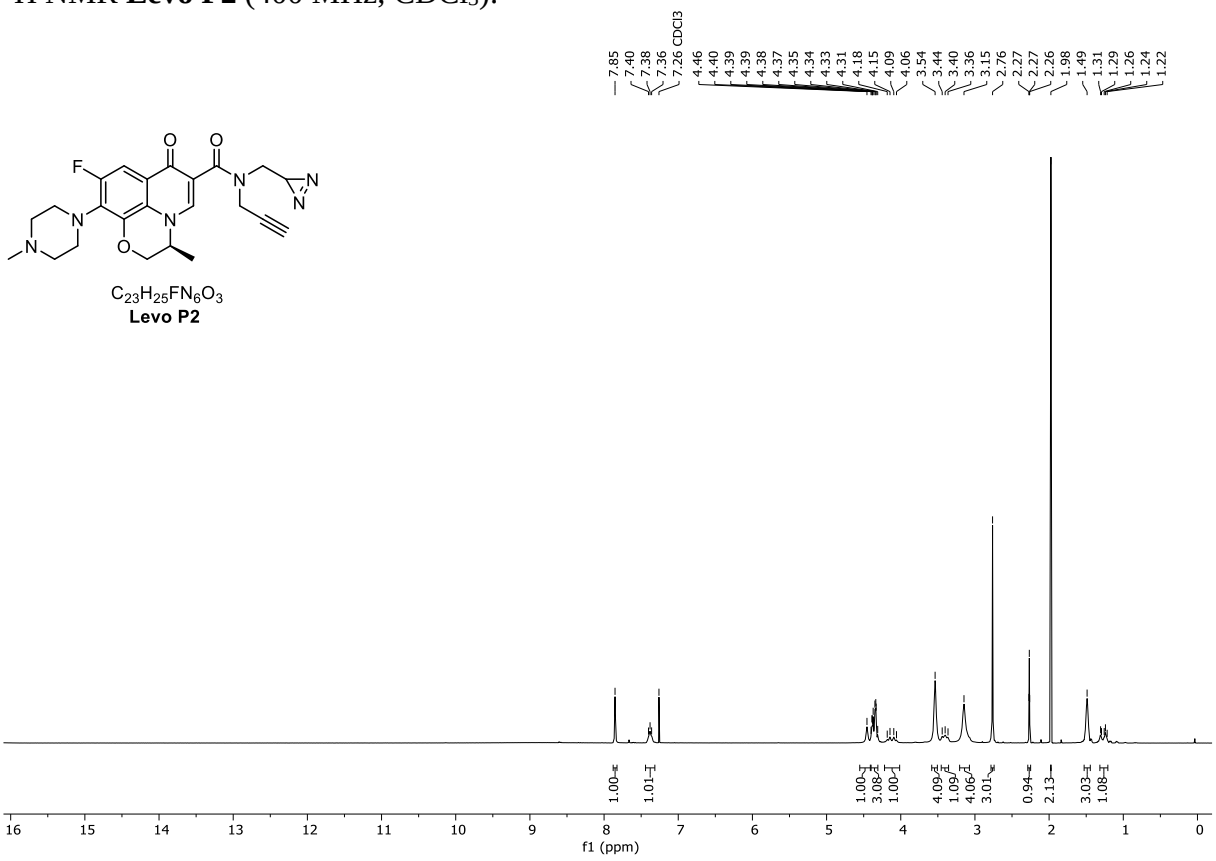

^{13}C NMR **Levo P2** (125 MHz, $CDCl_3$):

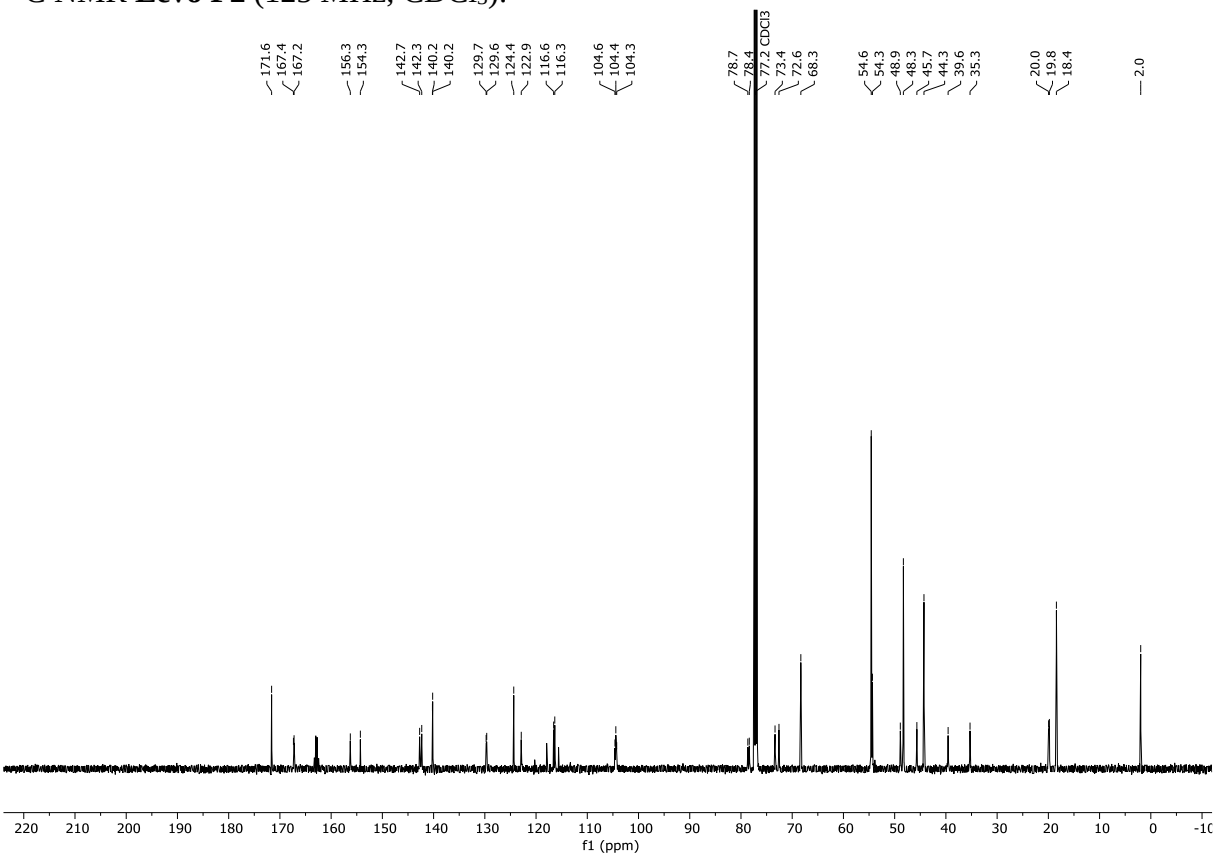

^{1}H NMR **Sulfo-Cipro** (400 MHz, DMSO-d6):

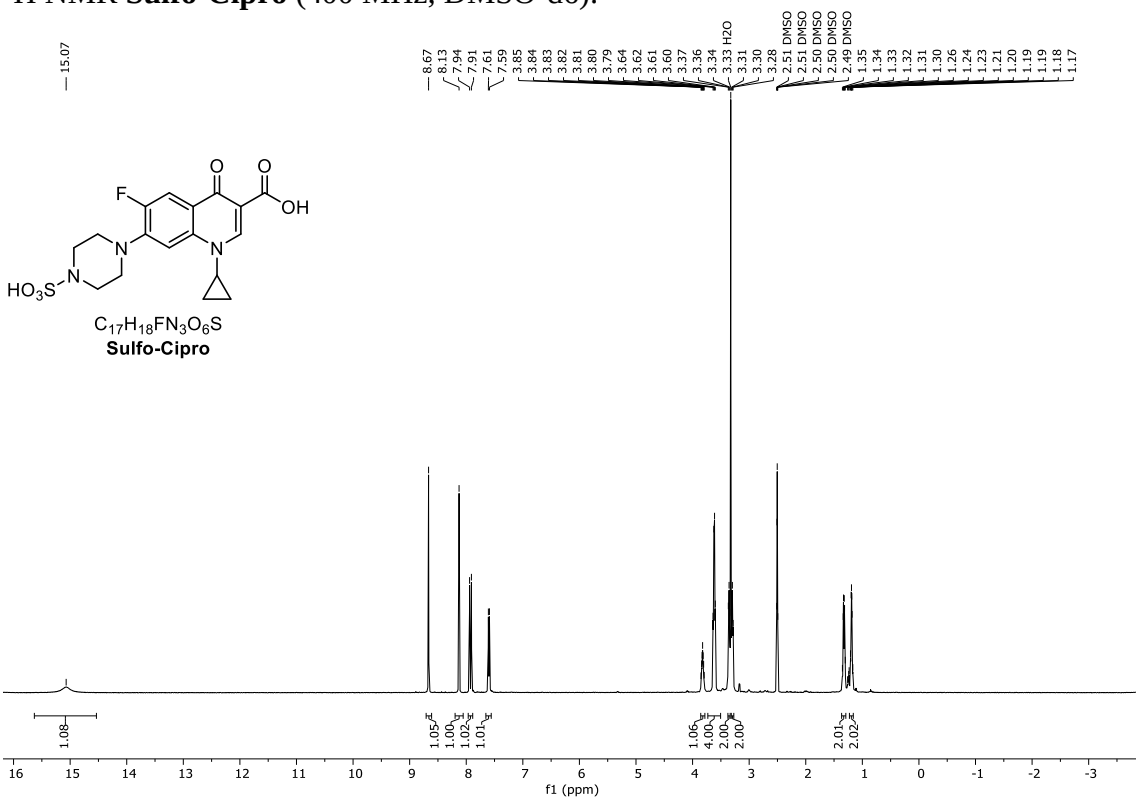

^{13}C NMR **Sulfo-Cipro** (125 MHz, DMSO-d6):

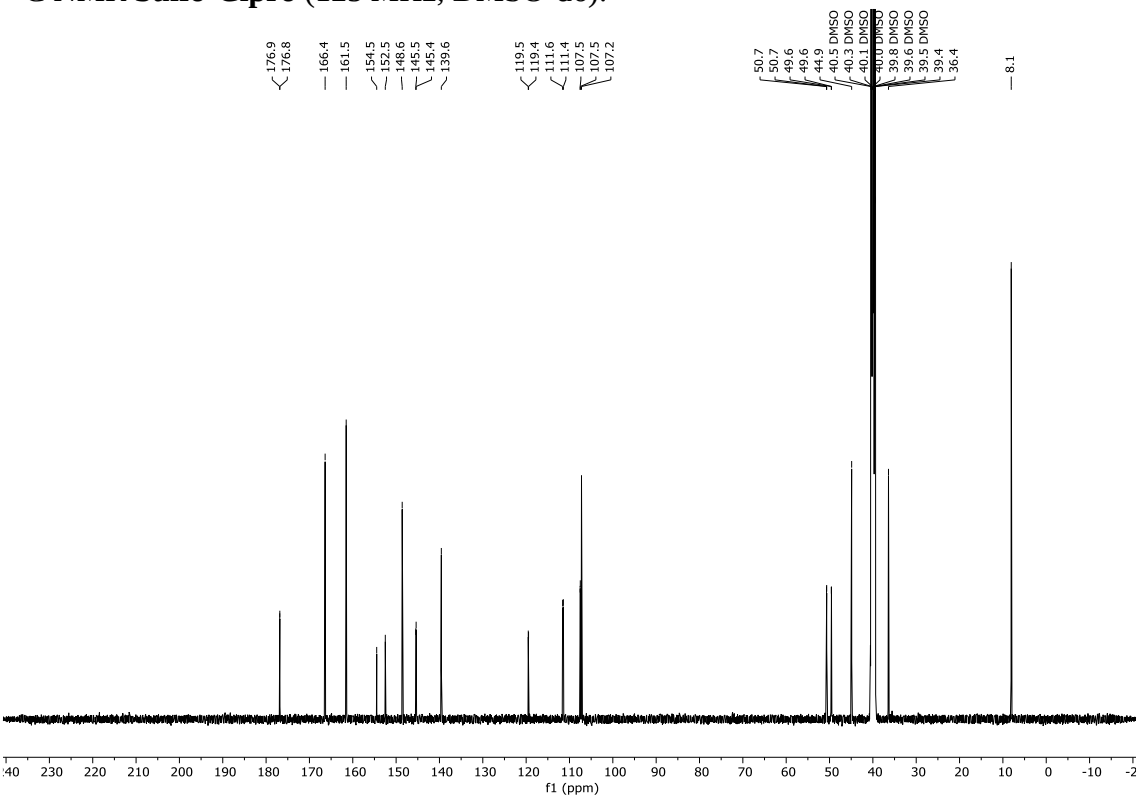

^{1}H NMR **Formyl-Cipro** (400 MHz, DMSO-d6):

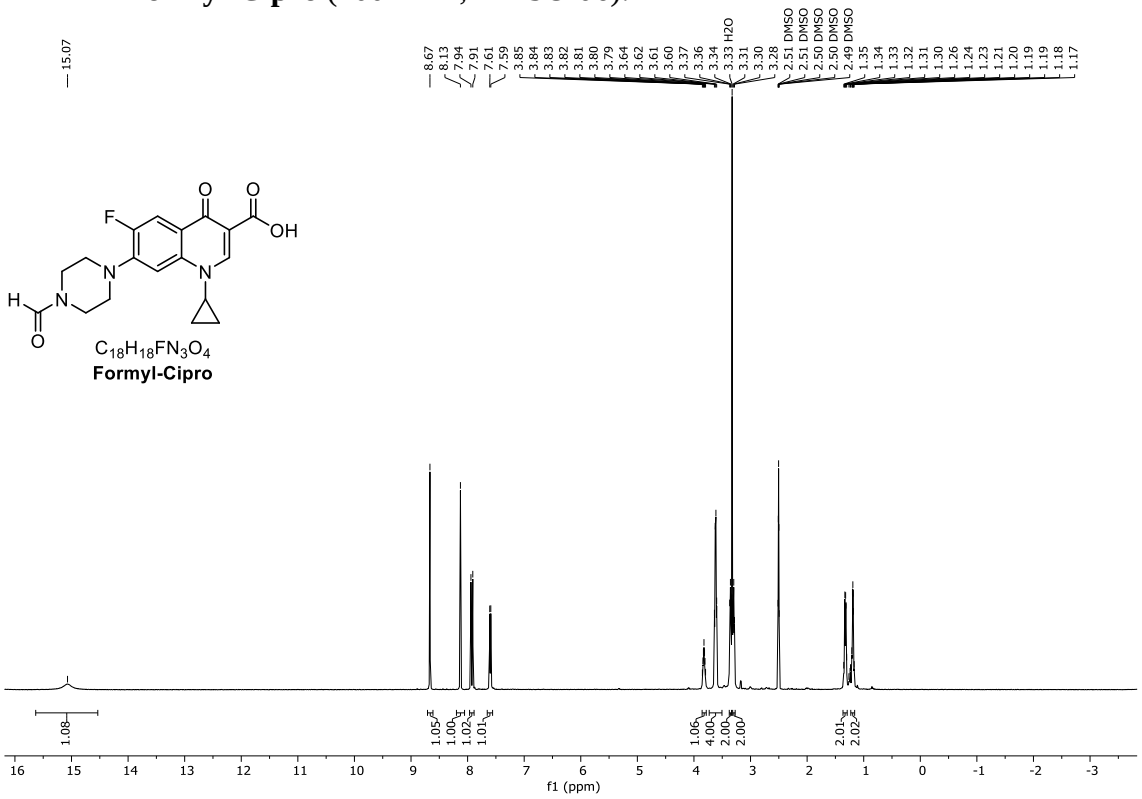

^{13}C NMR **Formyl-Cipro** (125 MHz, DMSO-d6):

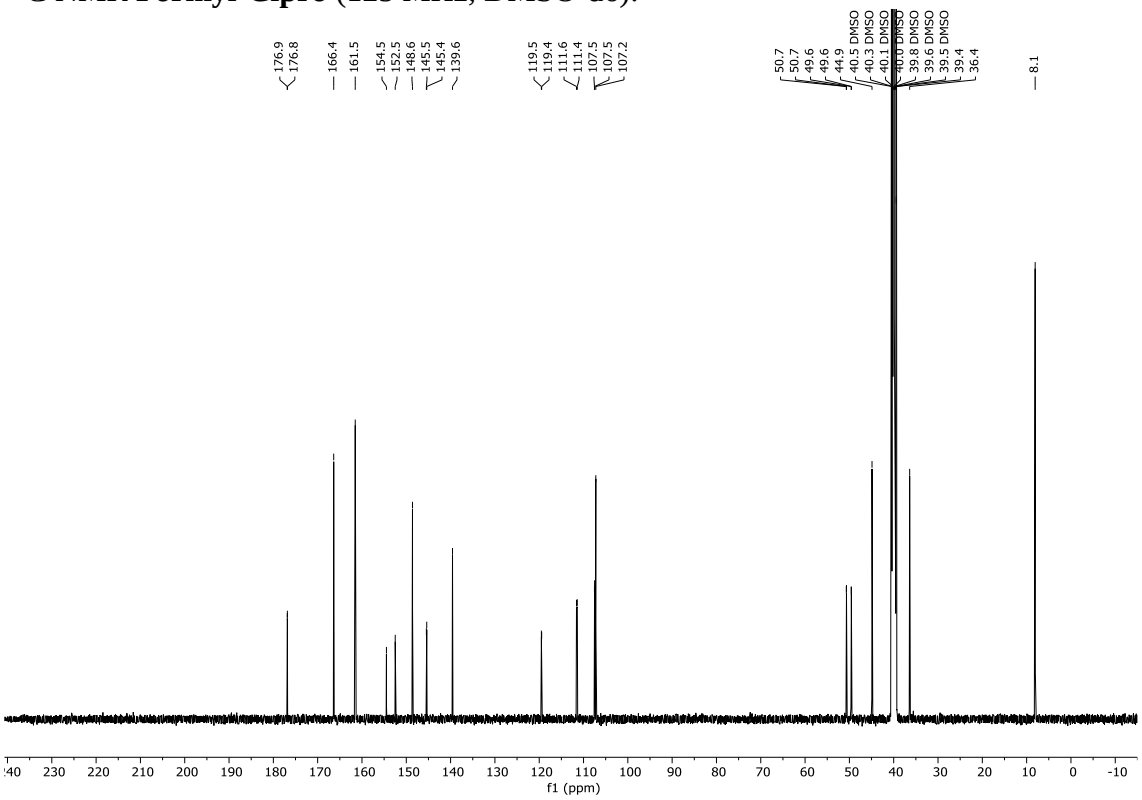

^{1}H NMR **Desethylen-Cipro** (400 MHz, DMSO-d6):

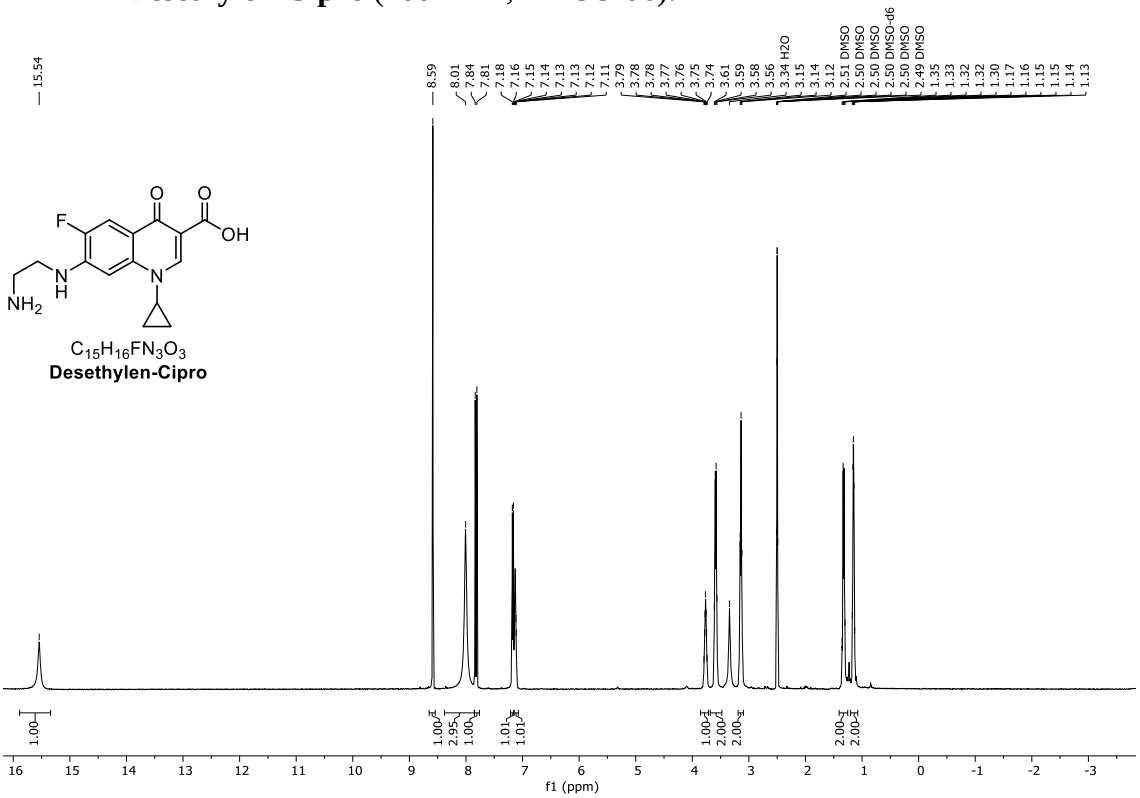

^{13}C NMR **Desethylen-Cipro** (125 MHz, DMSO-d6):

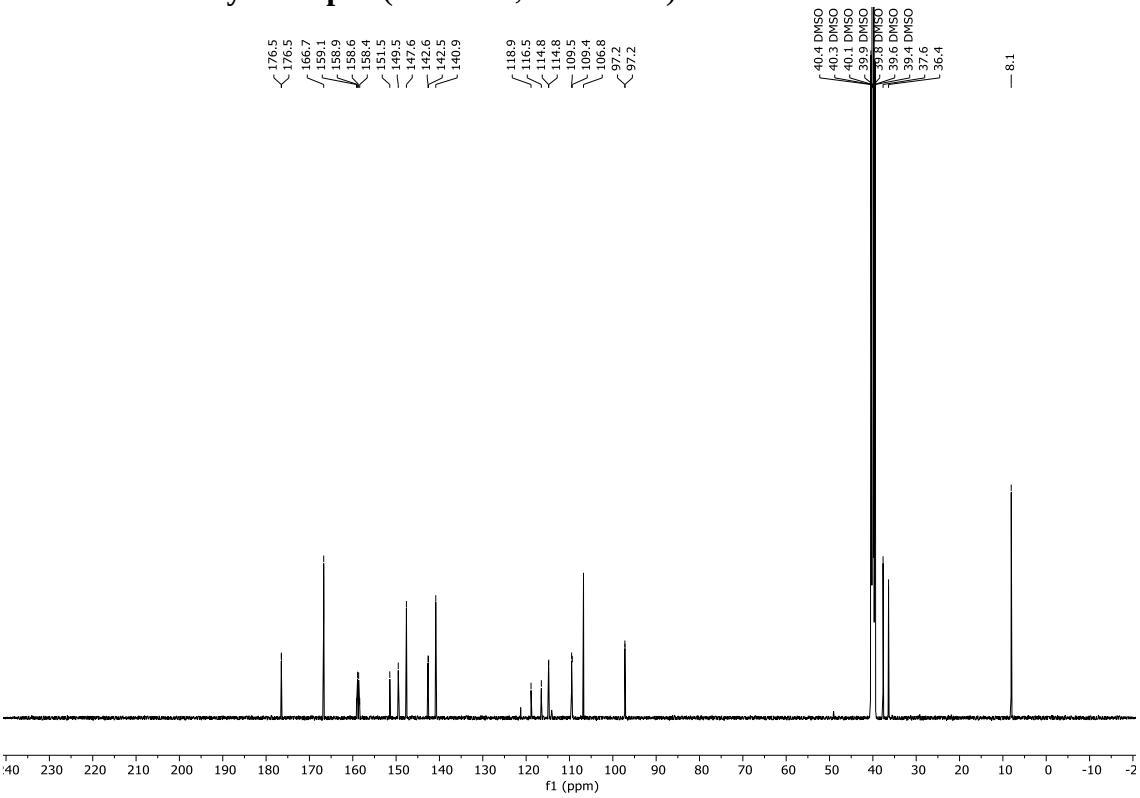

^{1}H NMR **Oxo-Cipro** (400 MHz, DMSO-d6):

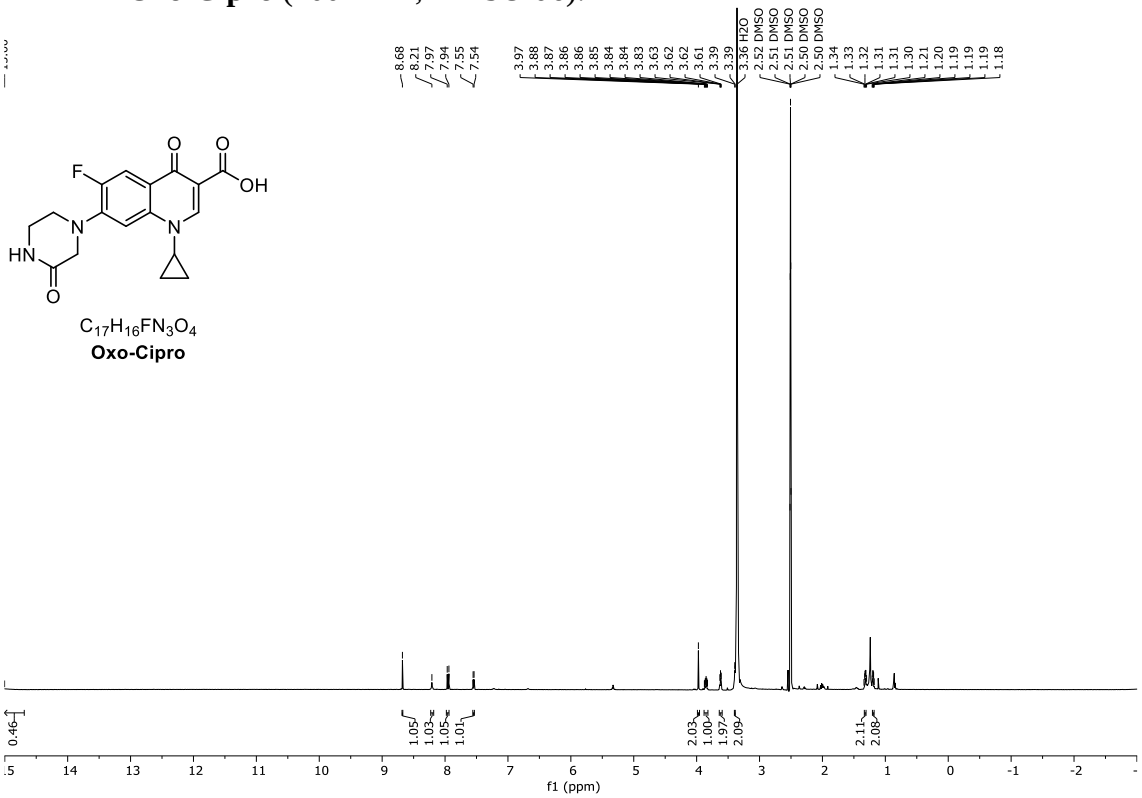

^{13}C NMR **Oxo-Cipro** (125 MHz, DMSO-d6):

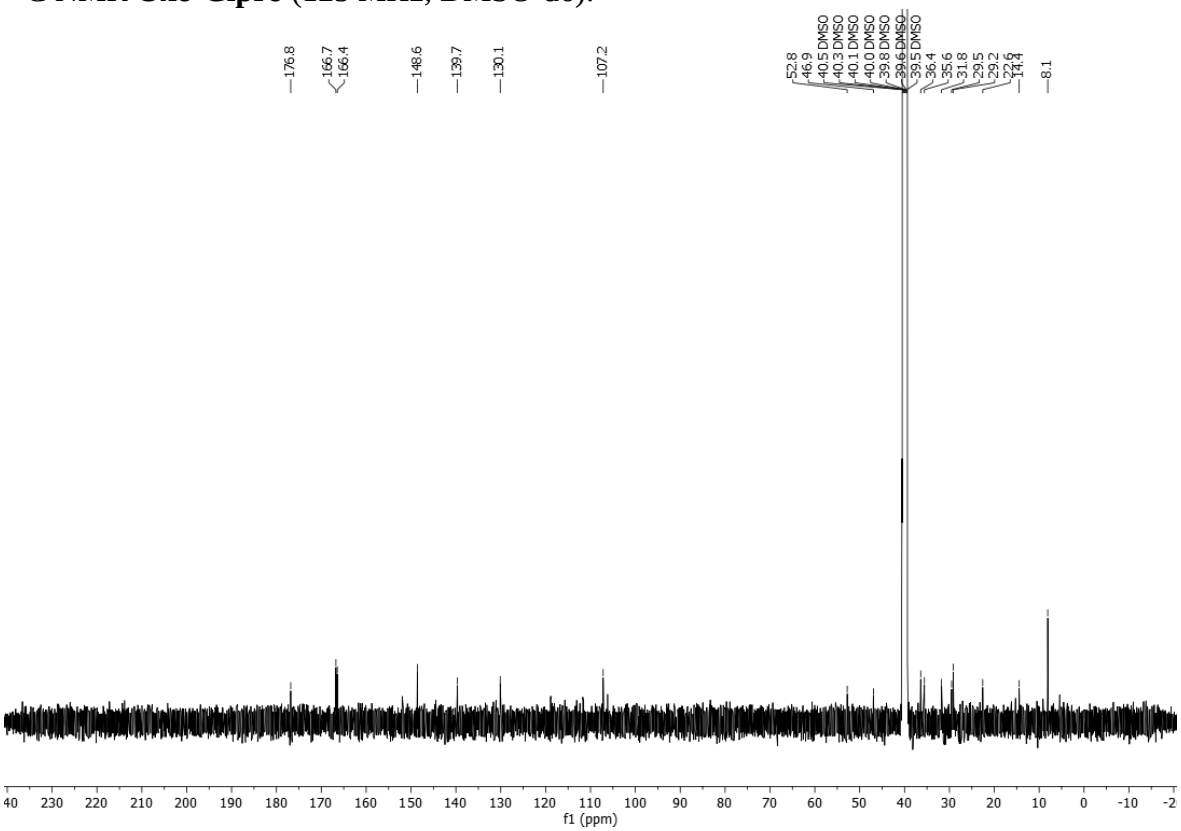

6. NMR spectra of the nitroimidazole project

Compound **Hybrid 1** - ^{1}H NMR (500 MHz, DMSO-d_6):

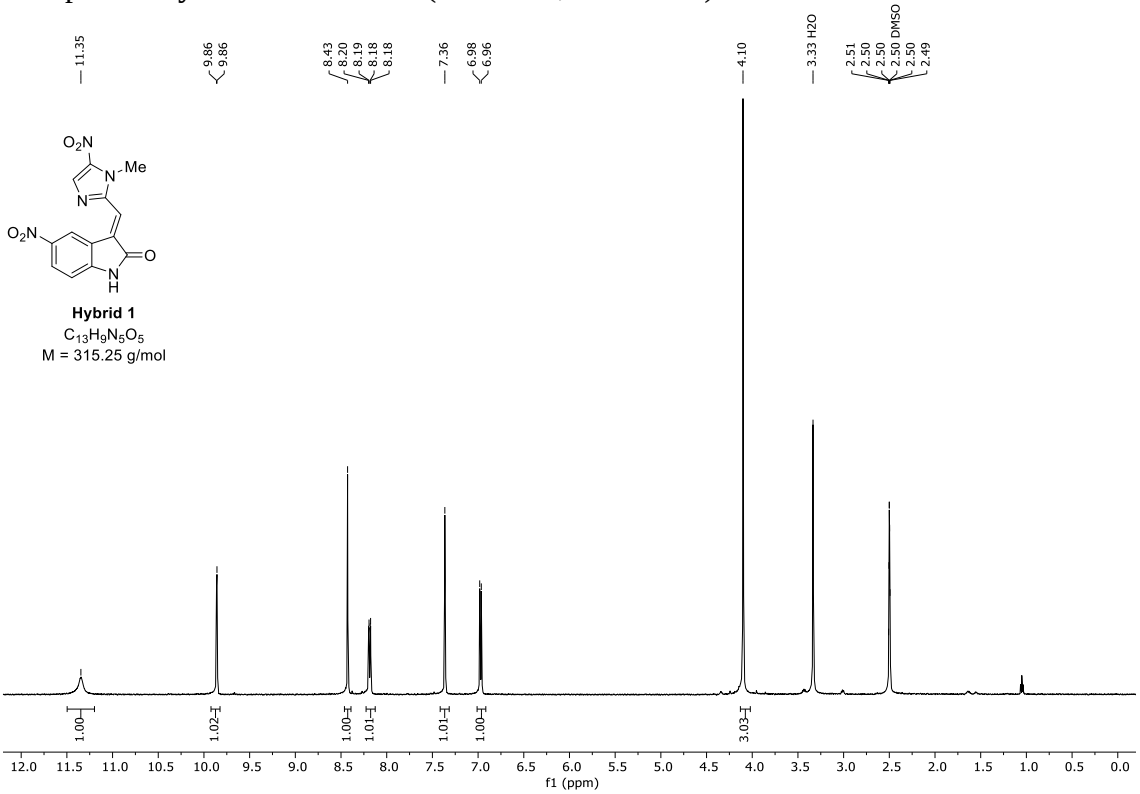

Compound **Hybrid 1** – ^{13}C NMR (100 MHz, DMSO-d_6):

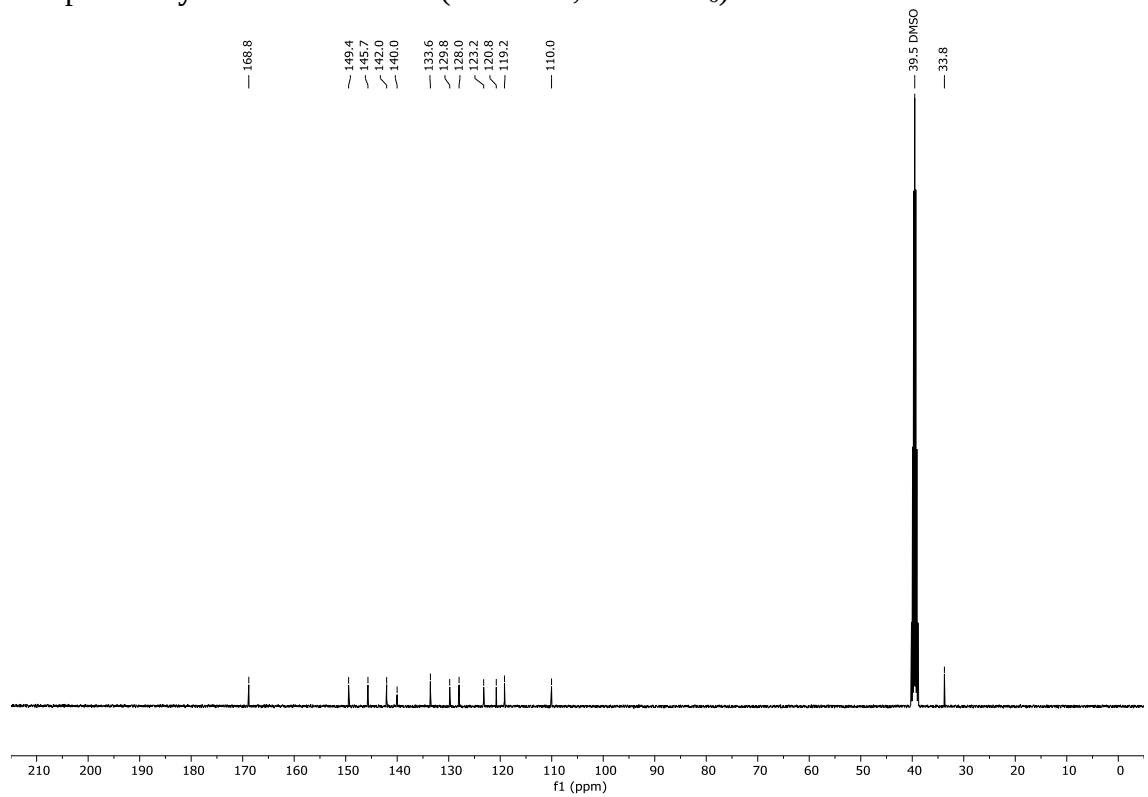

Compound **Hybrid 1** – ROESY 2D-NMR for determination of (*E*)-configuration:

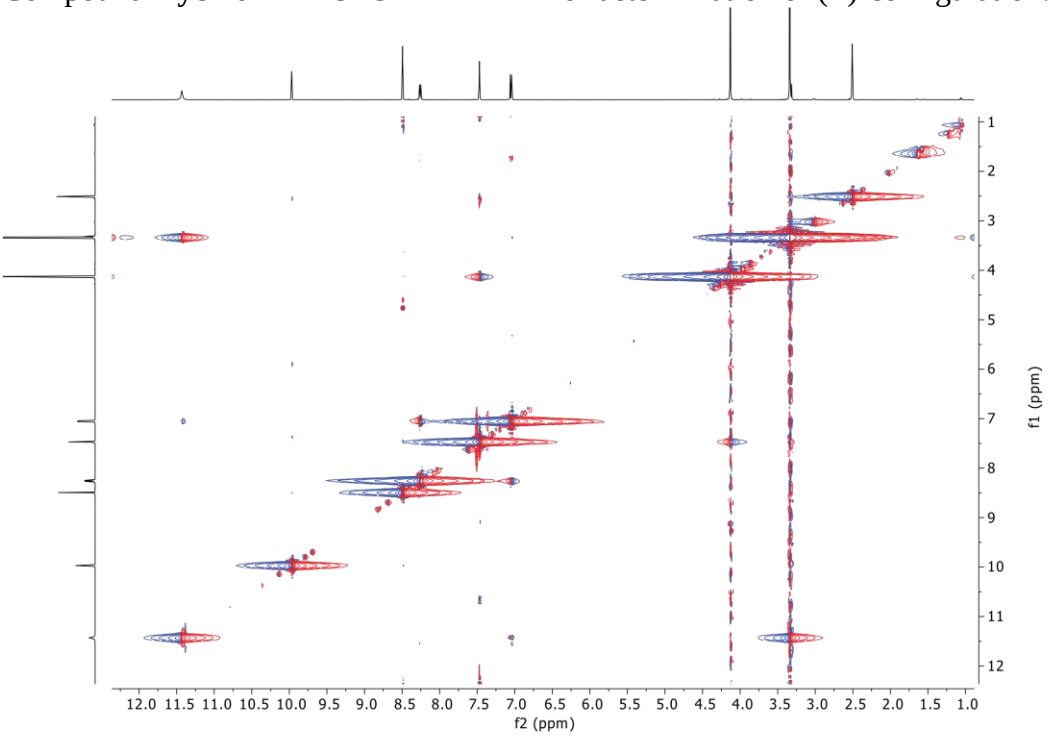

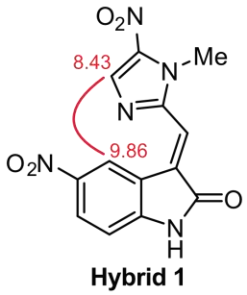

Hybrid 1

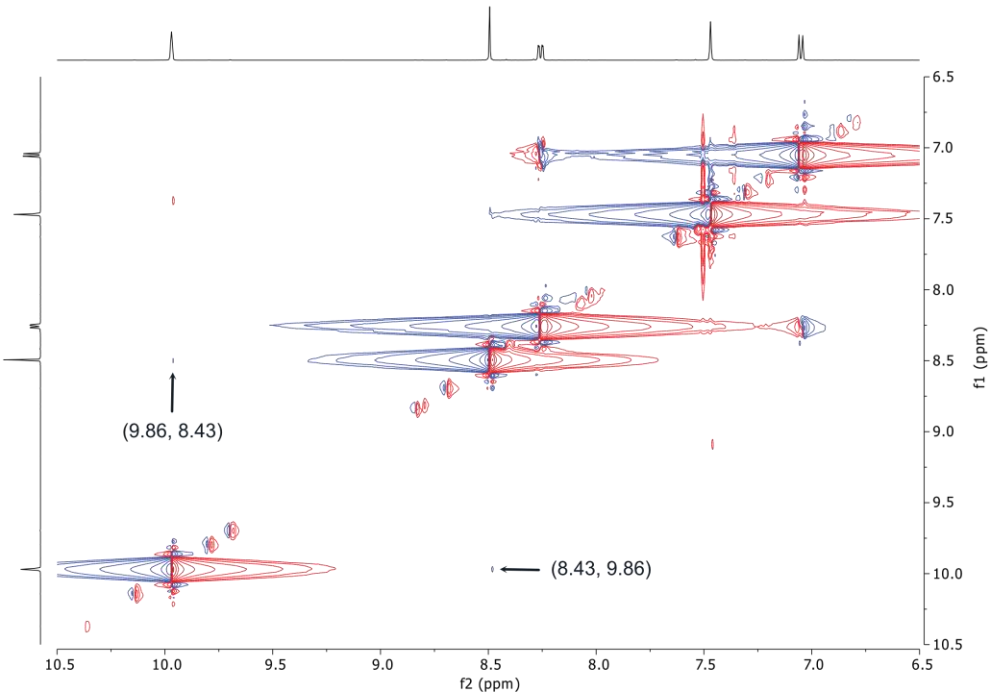

Compound **ABP1** - ^{1}H NMR (400 MHz, DMSO-d_6):

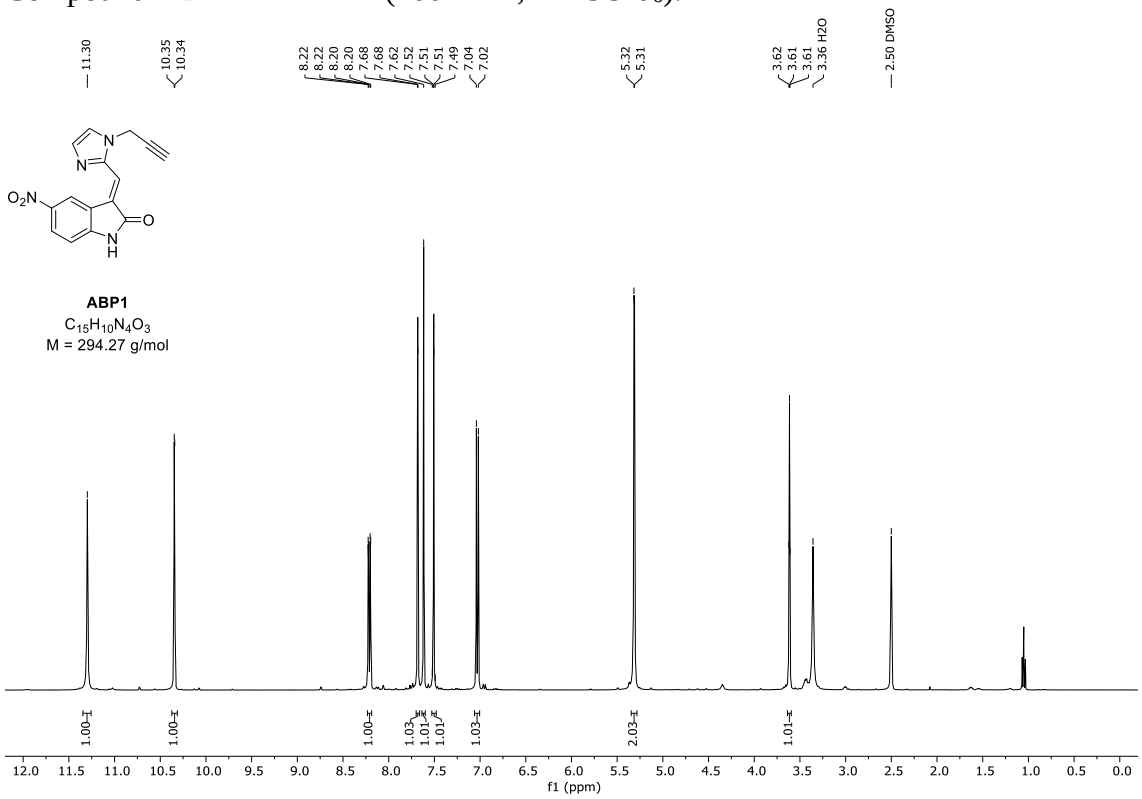

Compound **ABP1** – ^{13}C NMR (100 MHz, DMSO-d_6):

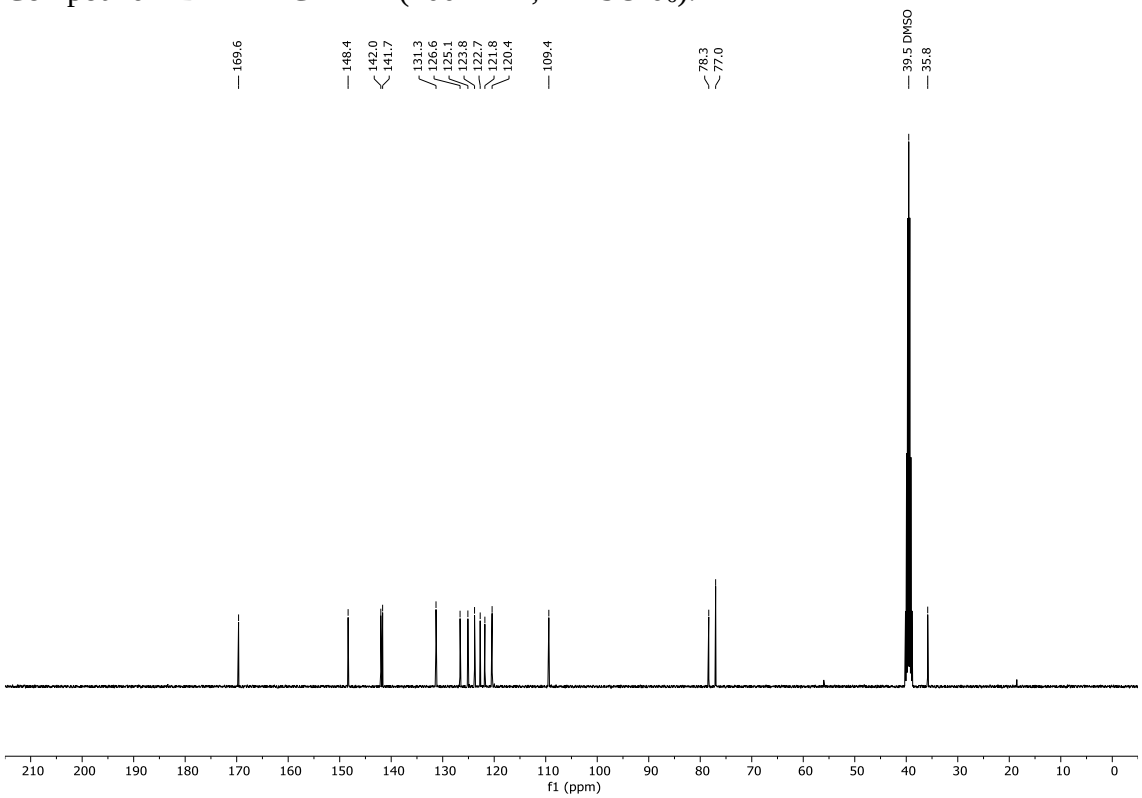

Compound **ABP1** – ROESY 2D-NMR for determination of (*E*)-configuration:

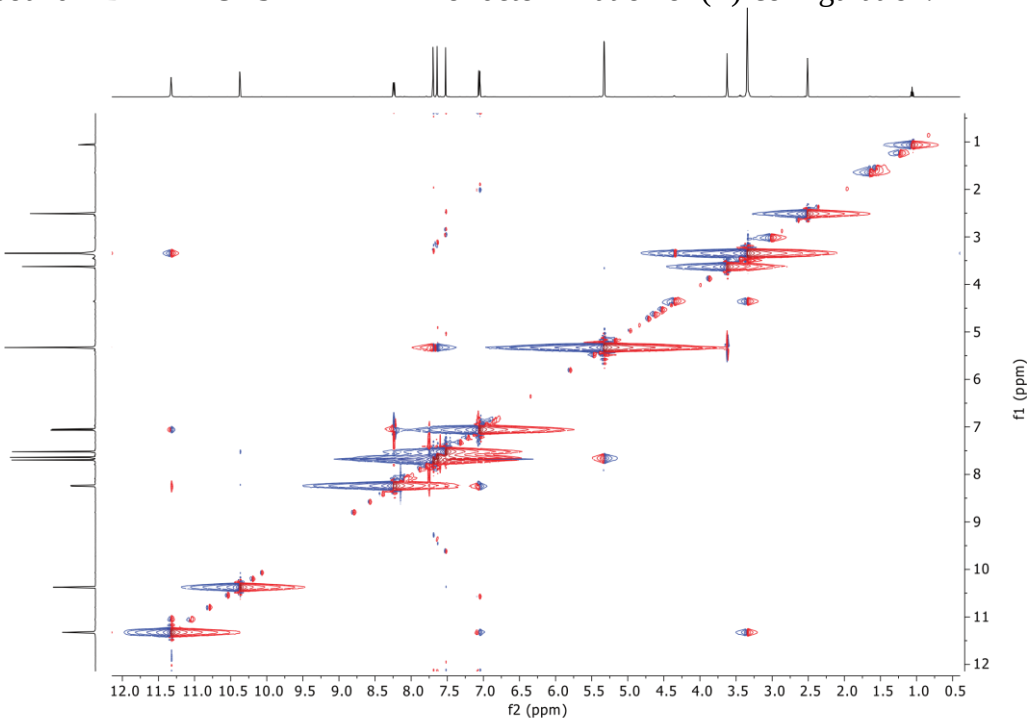

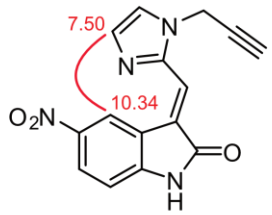

ABP 1

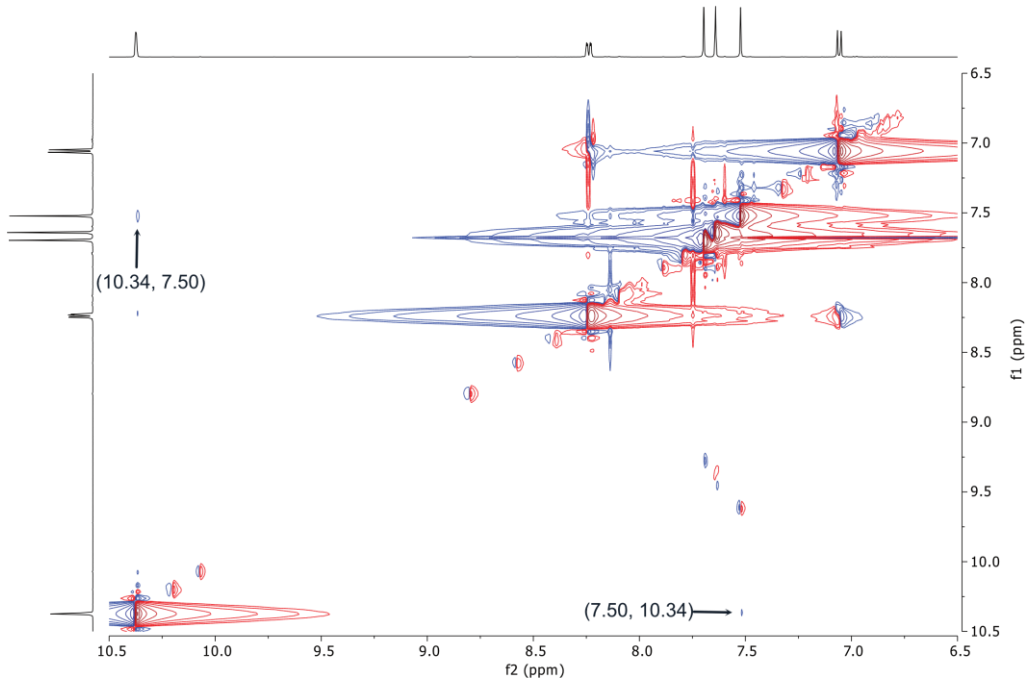

Compound **ABP2** - ^{1}H NMR (400 MHz, DMSO-d_6):

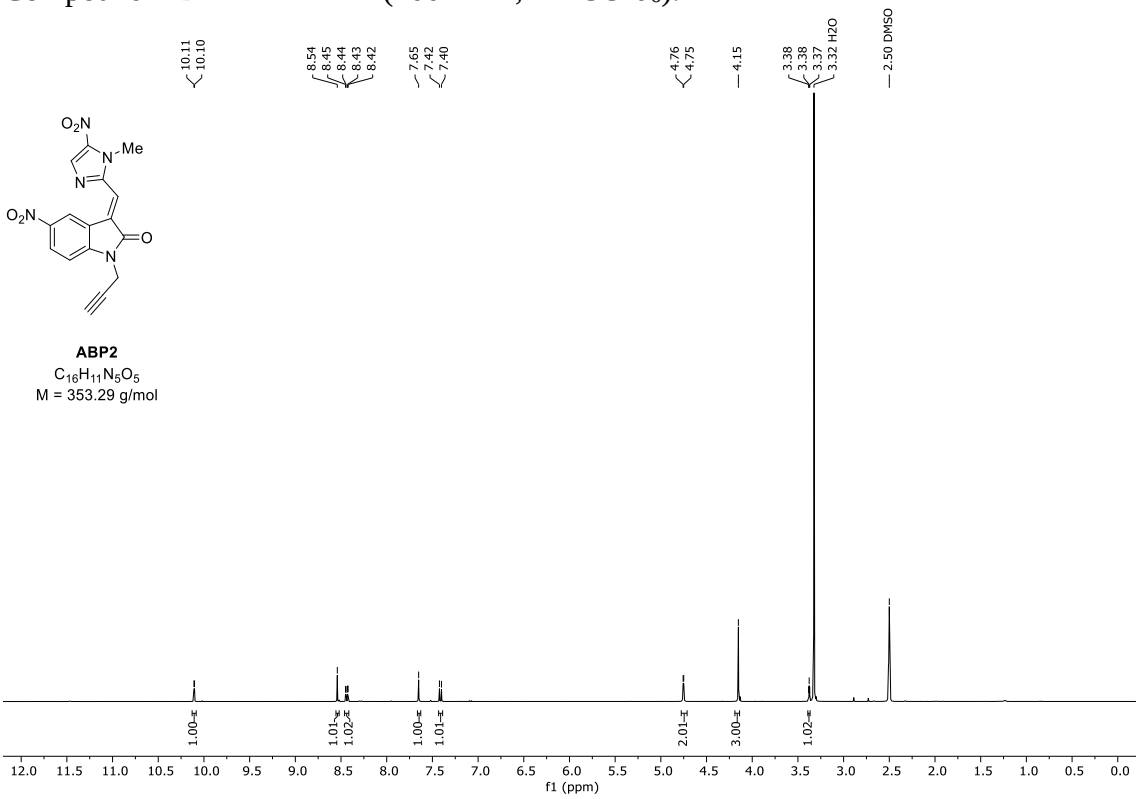

Compound **ABP2** – ^{13}C NMR (100 MHz, DMSO-d_6):

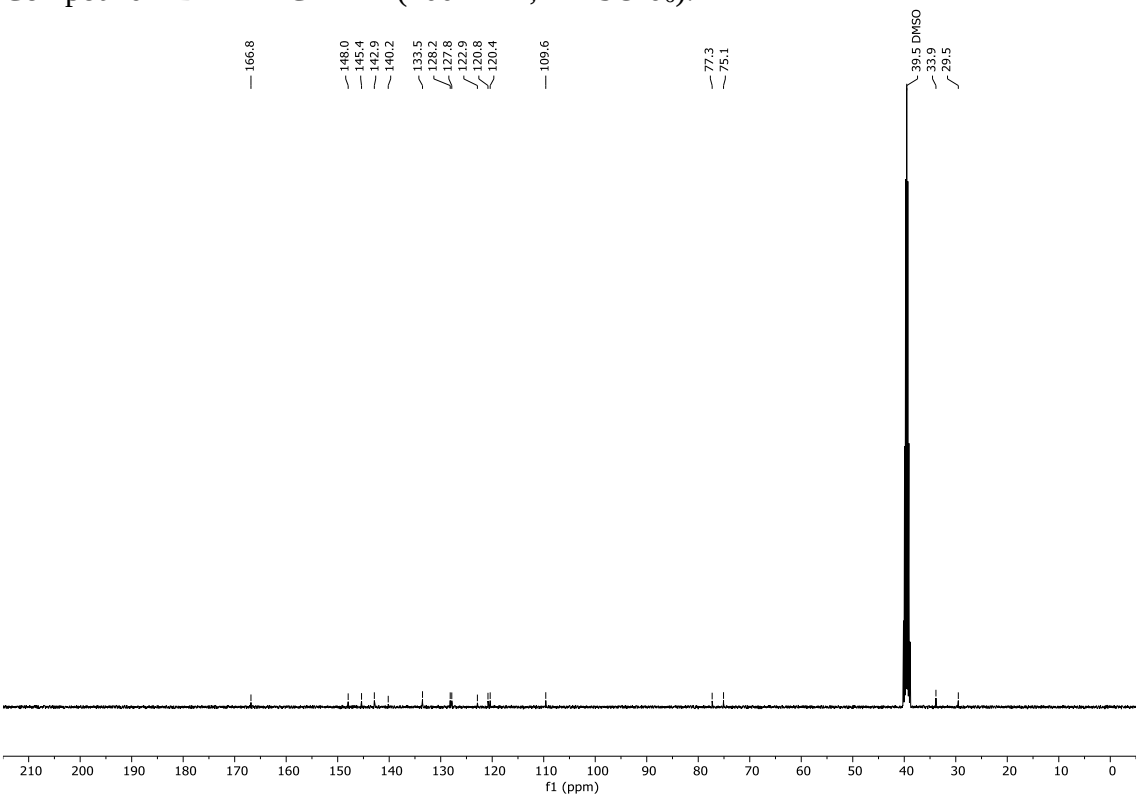

Compound **ABP3** - ^{1}H NMR (300 MHz, DMSO-d_6):

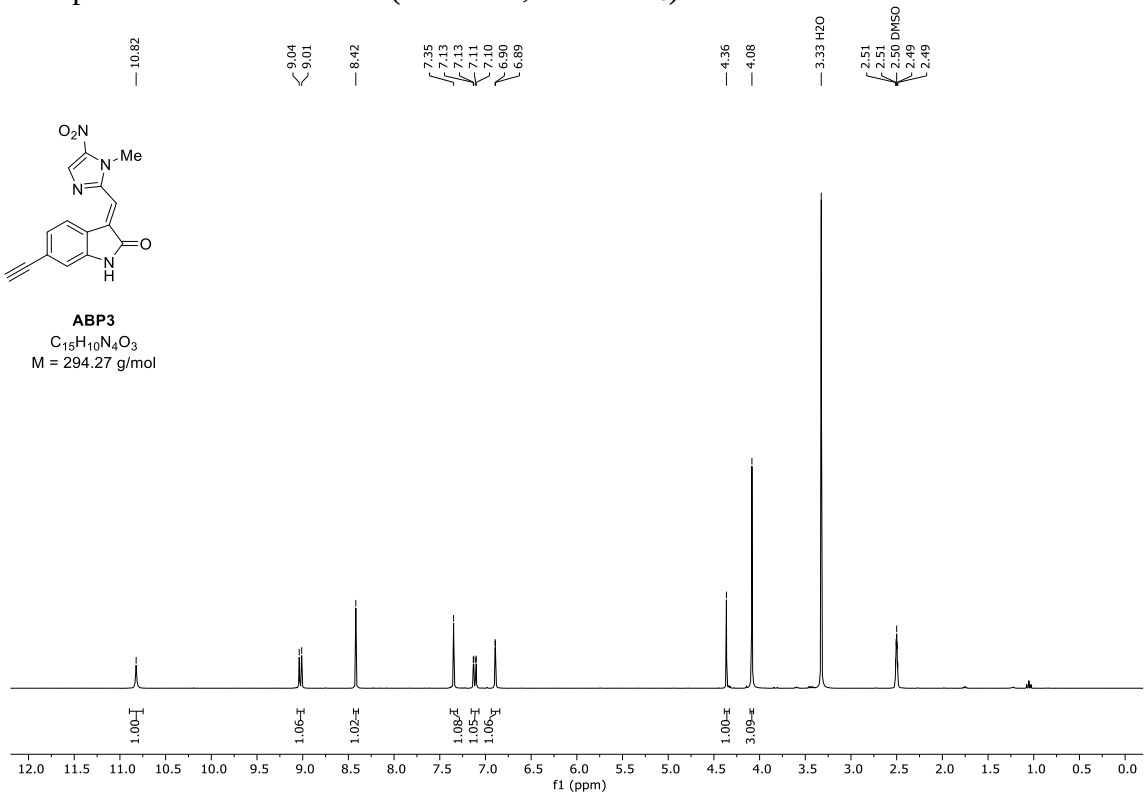

Compound **ABP3** – ^{13}C NMR (75 MHz, DMSO-d_6):

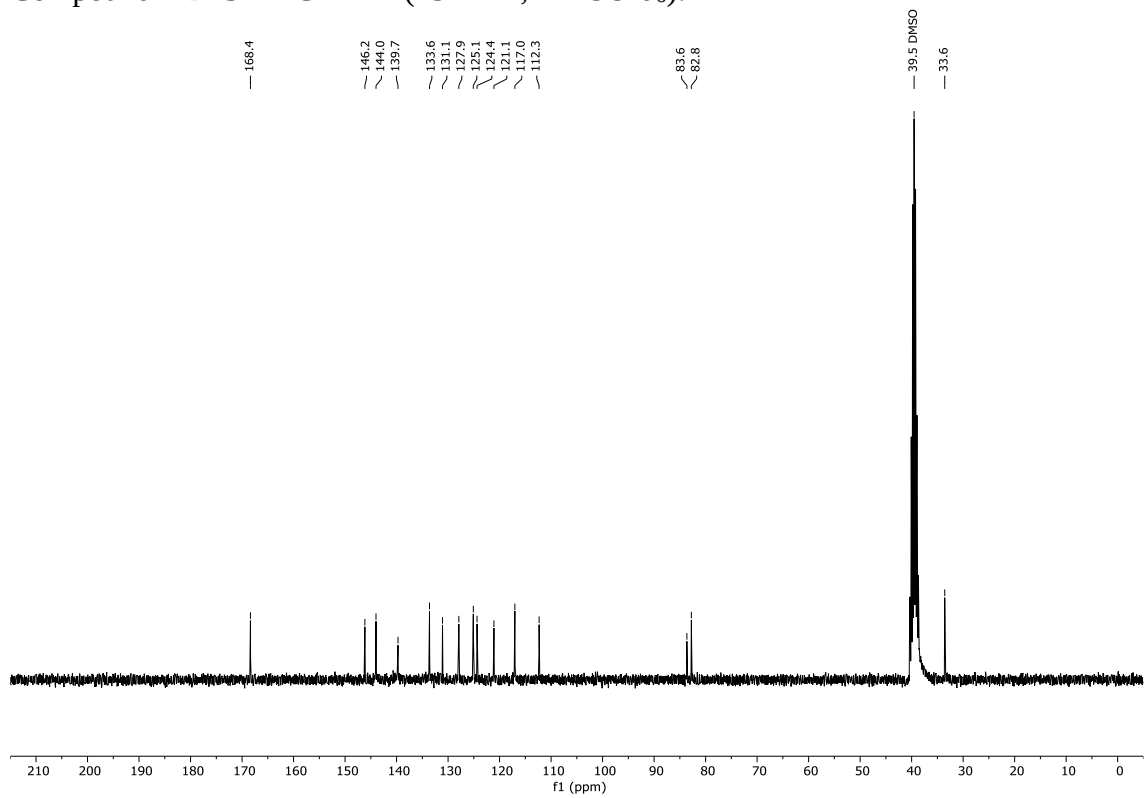

ABP3 precursor – ROESY 2-D NMR for determination of (*E*)-configuration:

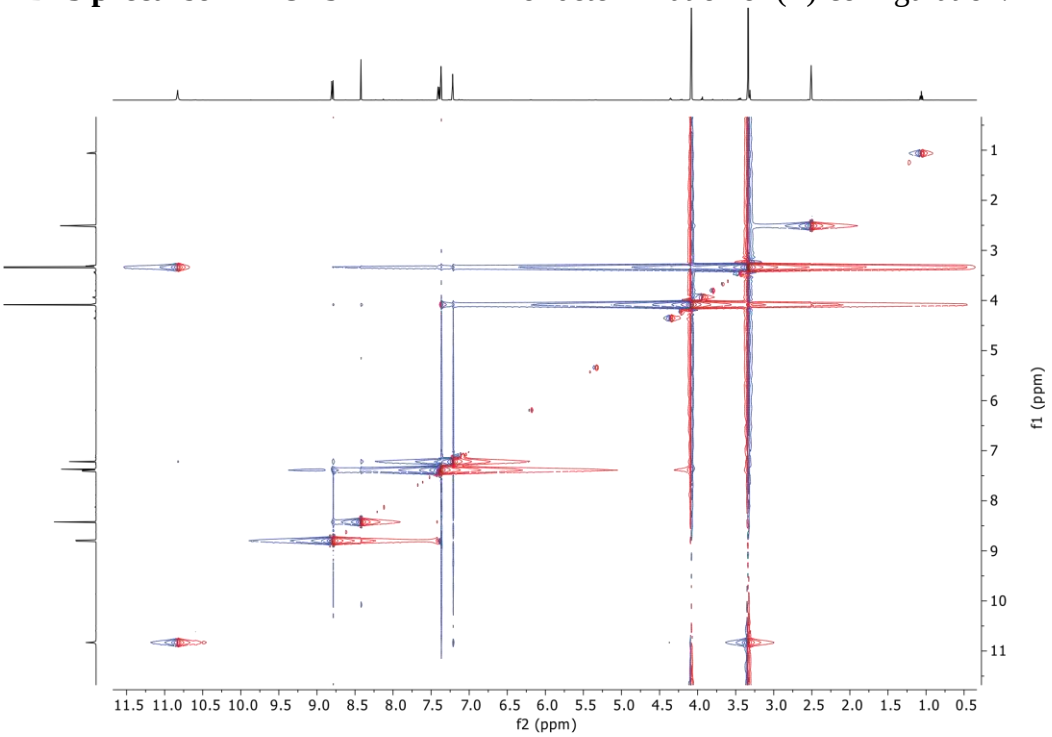

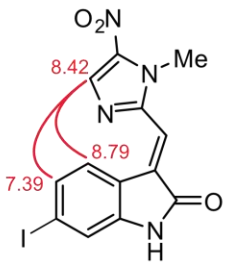

ABP3 precursor

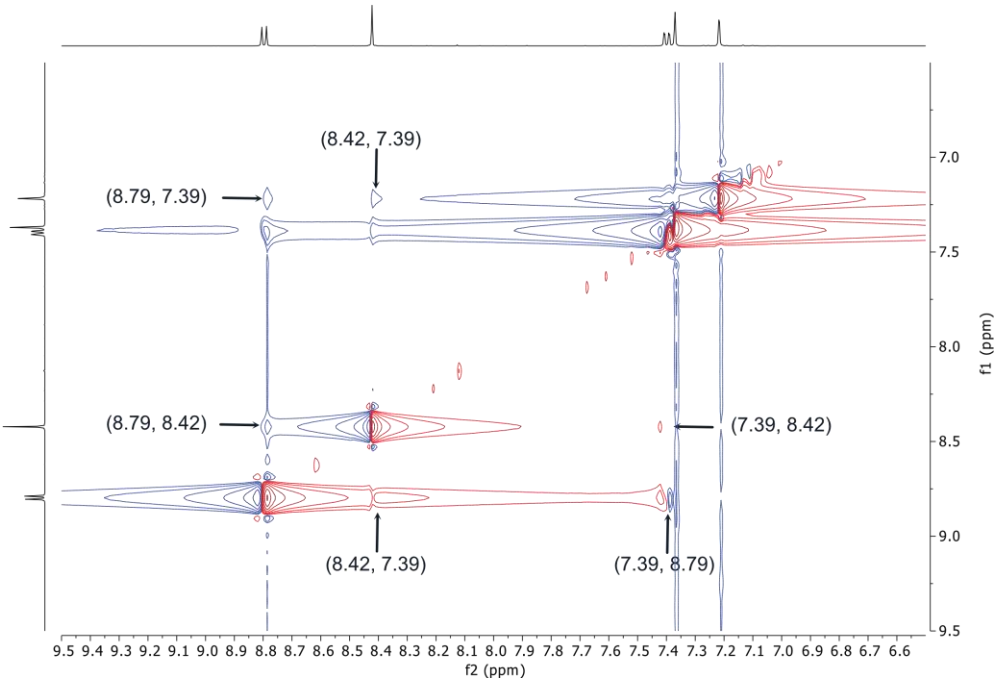

Compound **ABP4** - ^{1}H NMR (400 MHz, DMSO-d_6):

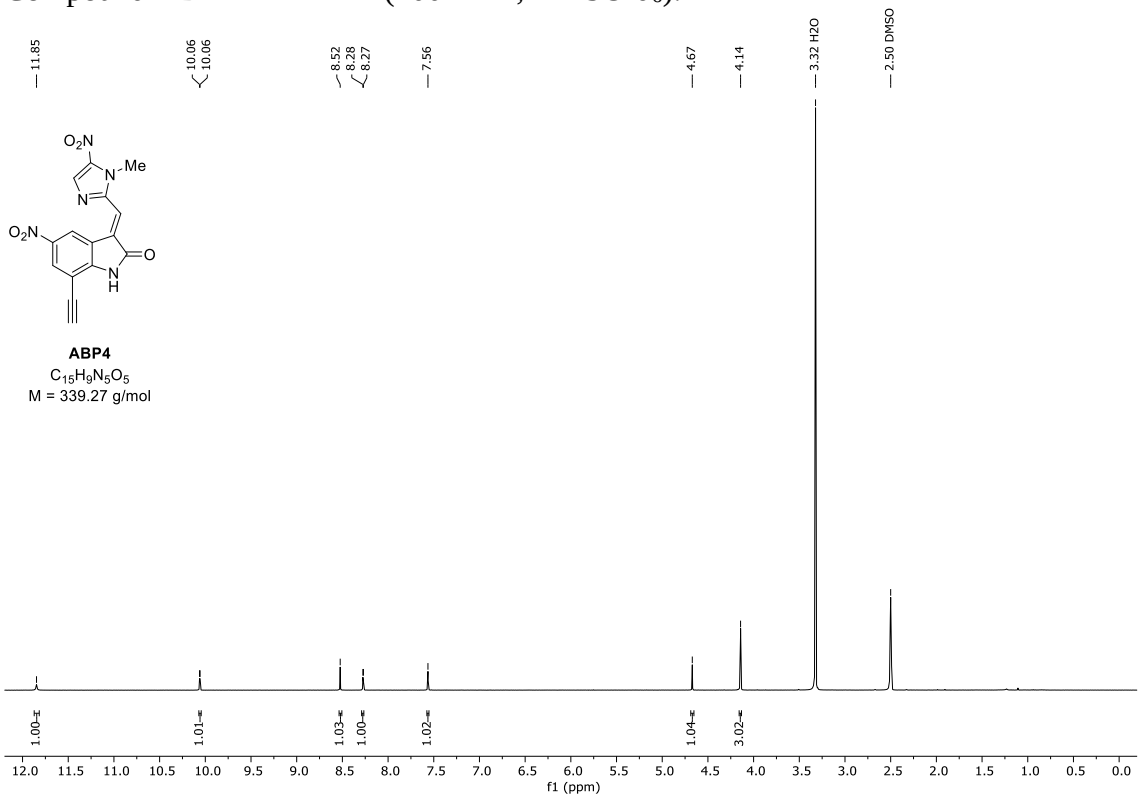

Compound **ABP4** – ^{13}C NMR (75 MHz, DMSO-d_6):

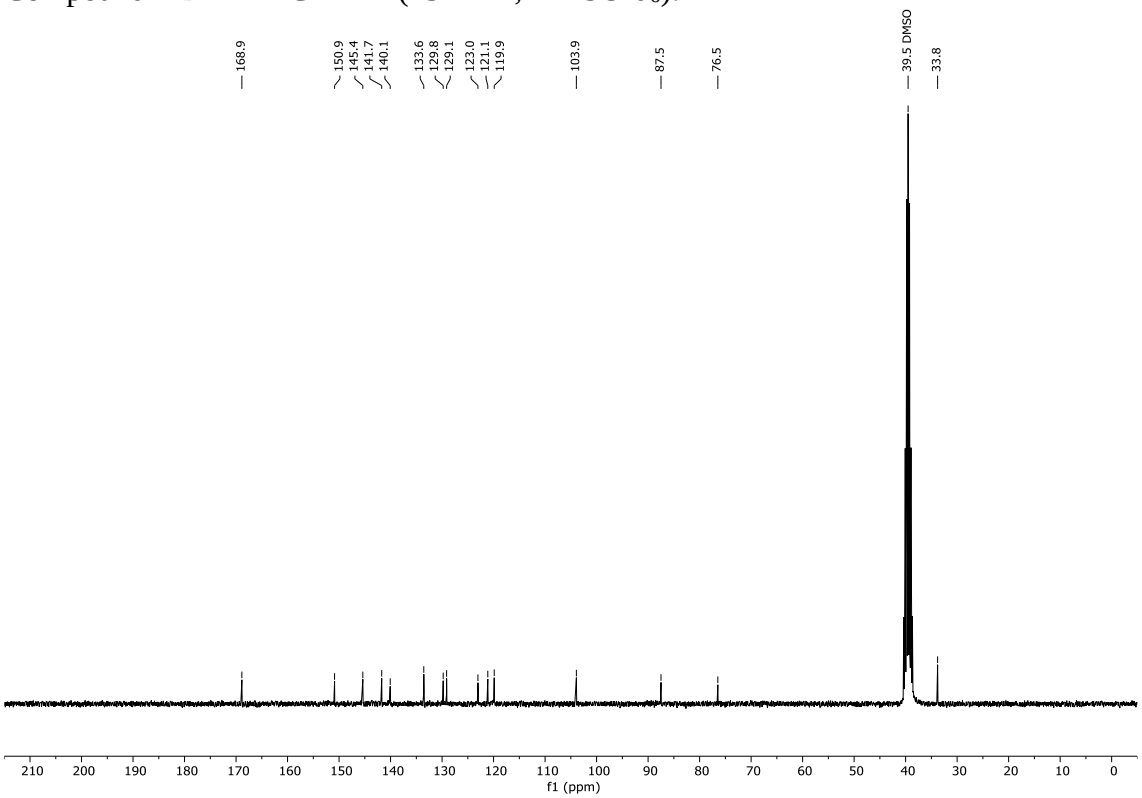

Compound **Hybrid 2** - ^{1}H NMR (400 MHz, DMSO-d$_6$):

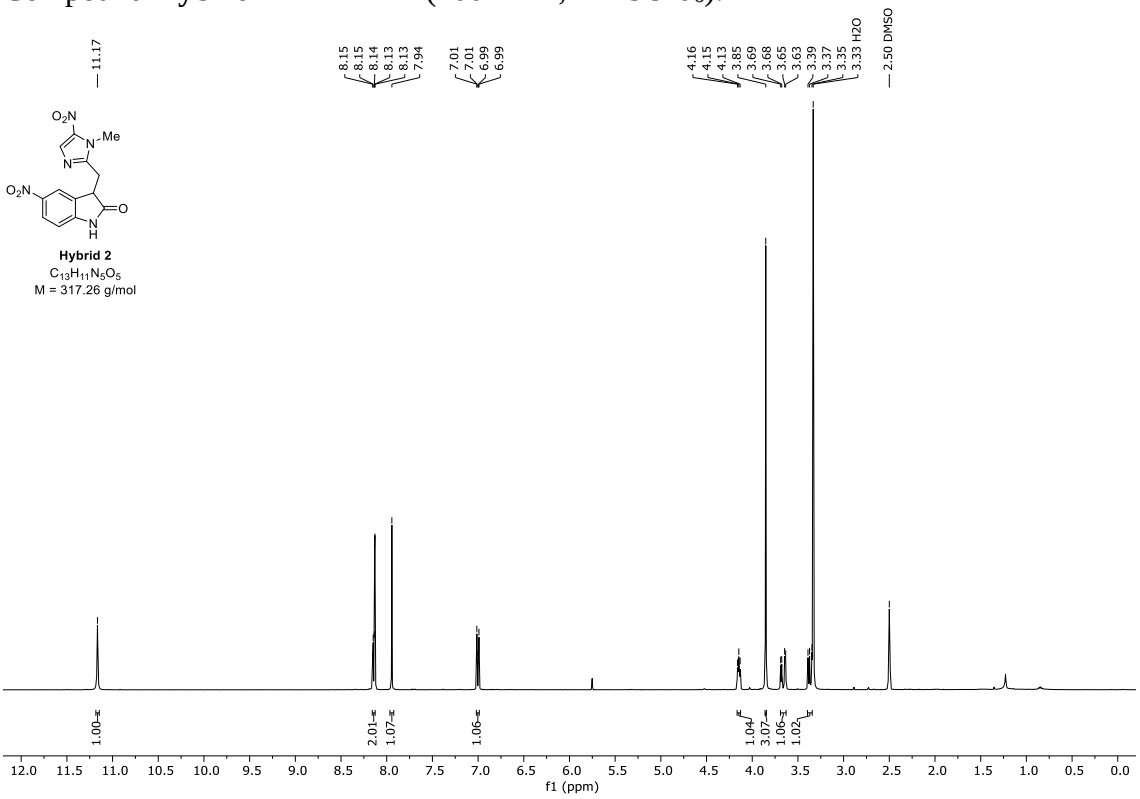

Compound **Hybrid 2** – ^{13}C NMR (100 MHz, DMSO-d$_6$):

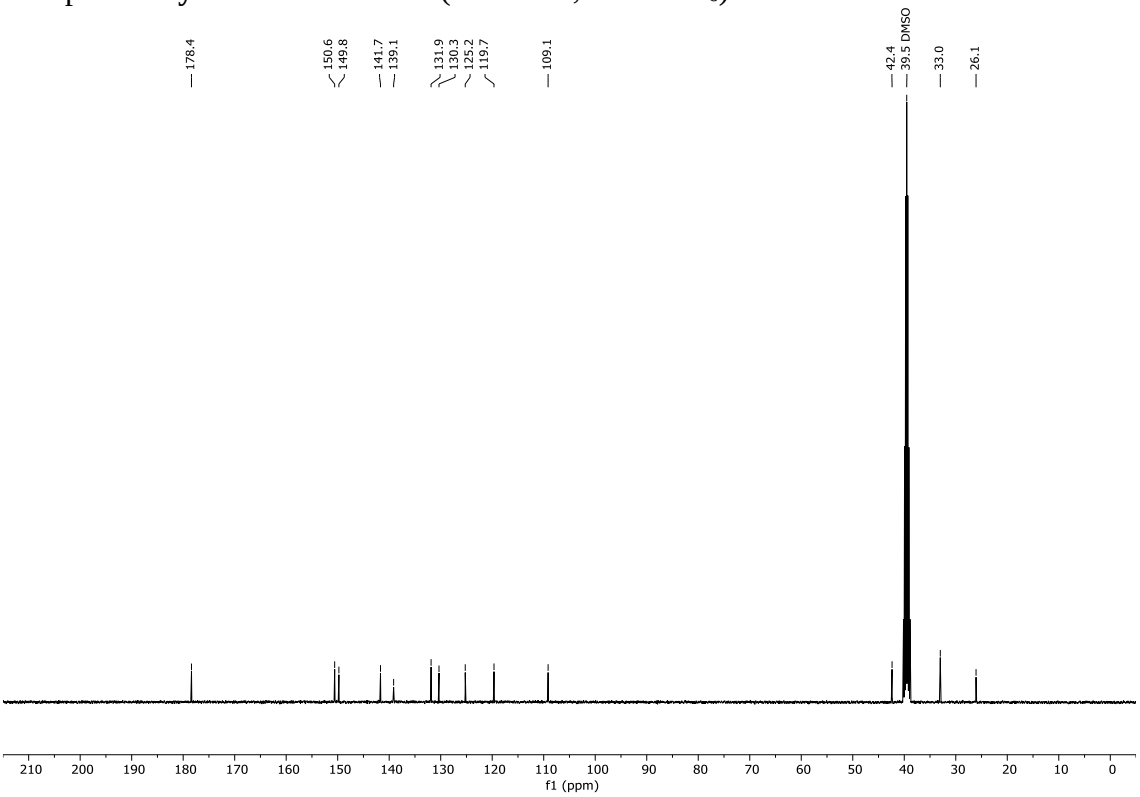

Compound **Hybrid 3** - ^{1}H NMR (400 MHz, DMSO-d_6):

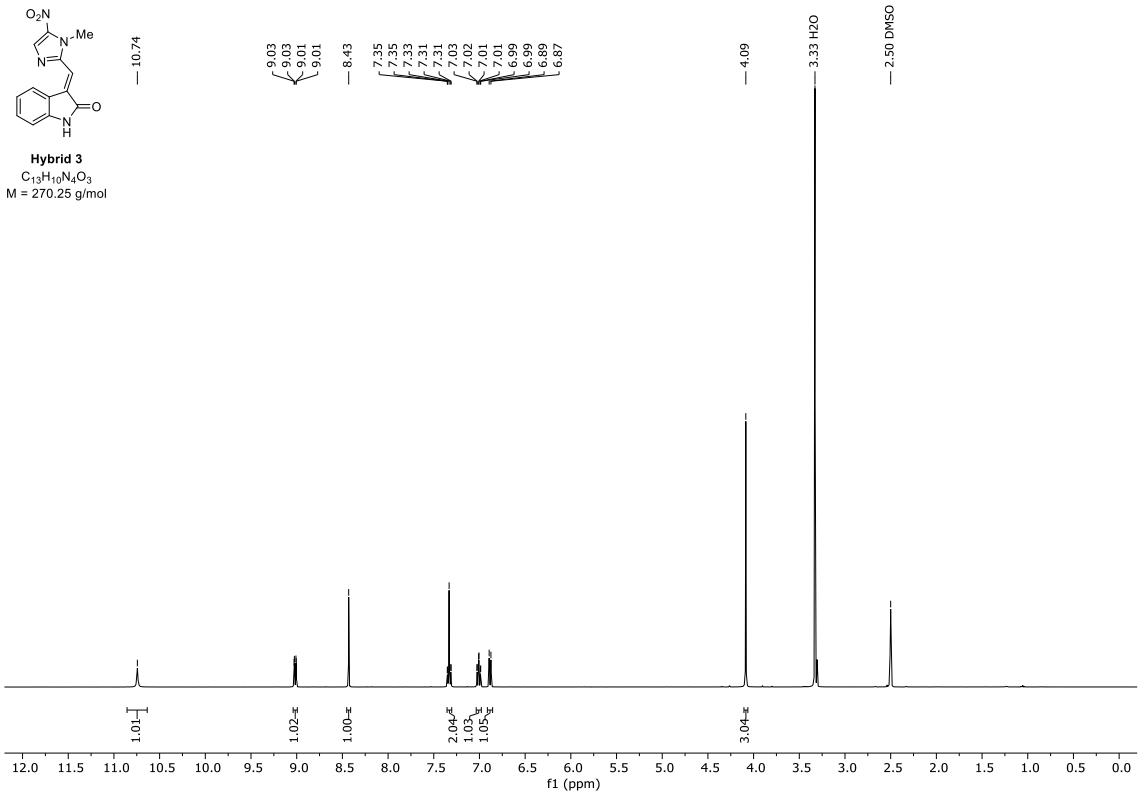

Compound **Hybrid 3** – ^{13}C NMR (100 MHz, DMSO-d_6):

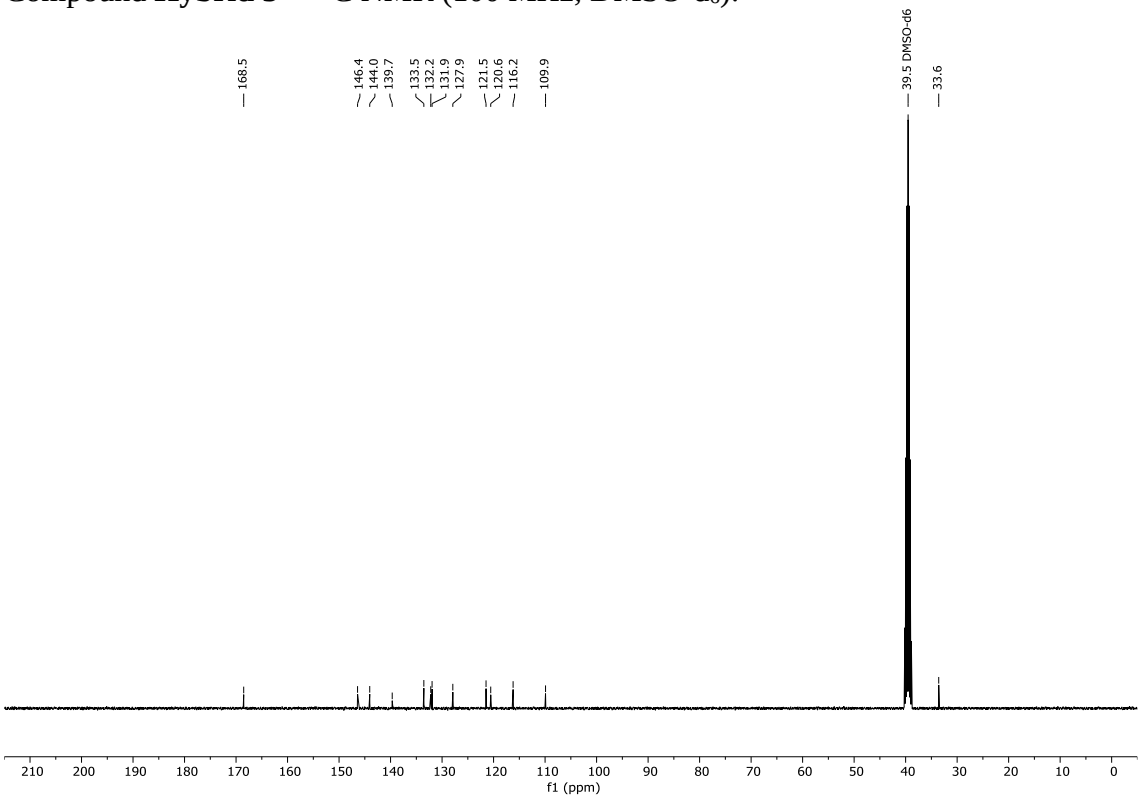

Compound **Hybrid 3** – ROESY 2D-NMR for determination of (*E*)-configuration:

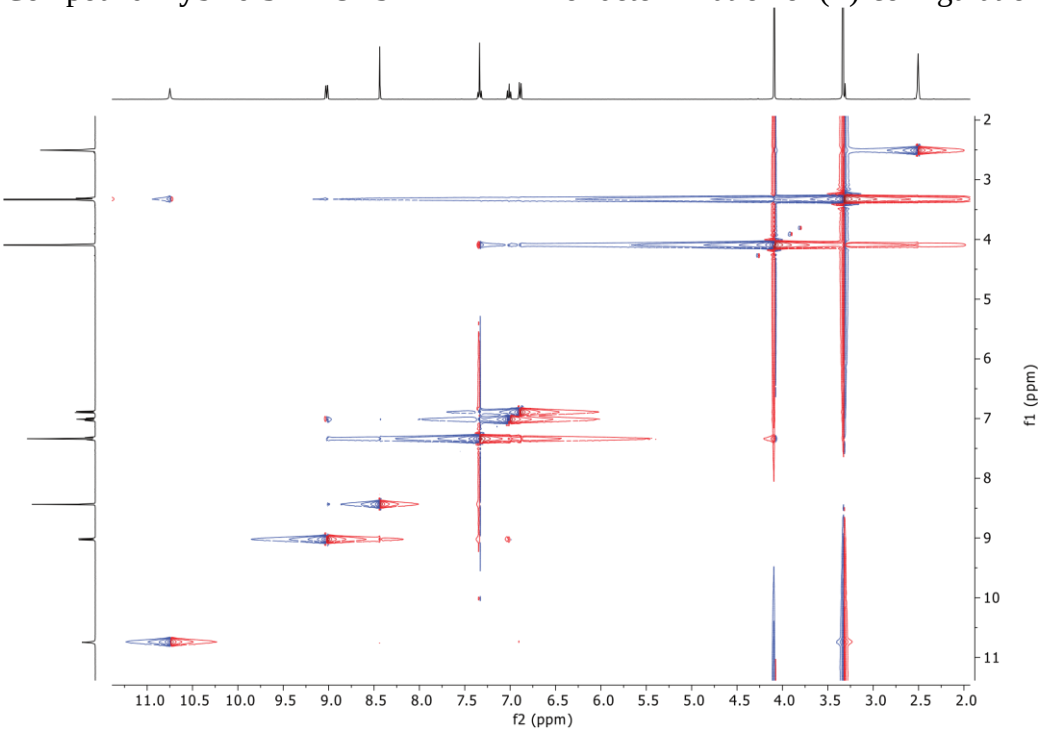

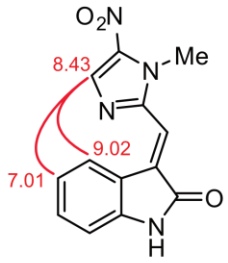

Hybrid 3

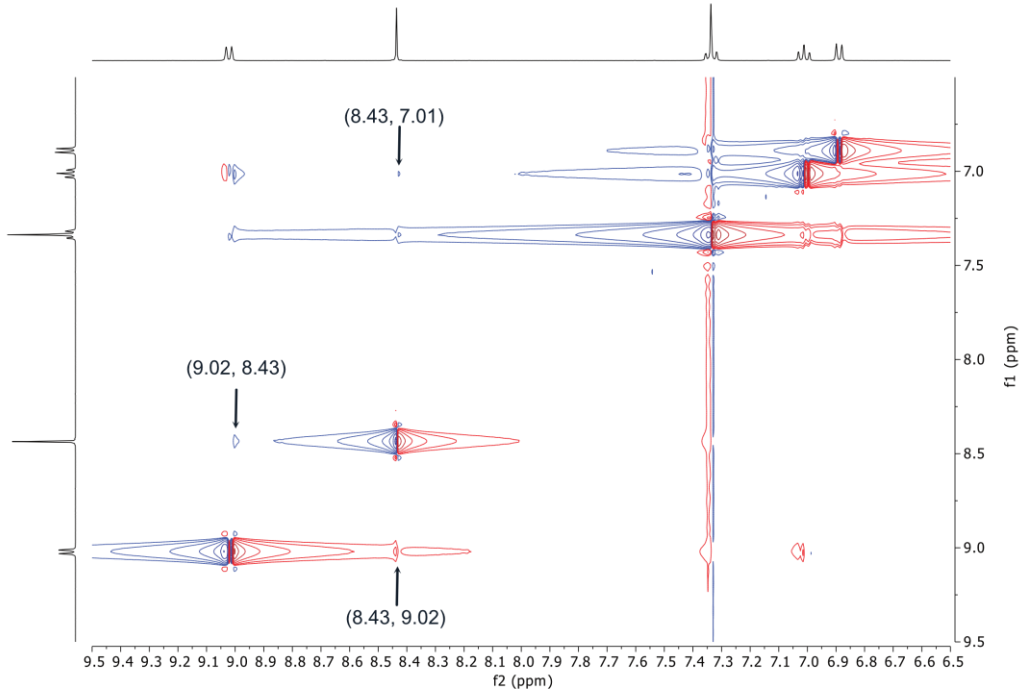

7. Licenses

Journal publications:

Various figures in this dissertation were adapted from the following publication:

T. Reinhardt*, K. M. Lee*, L. Niederegger, C. R. Hess, S. A. Sieber, Indolin-2-one Nitroimidazole Antibiotics Exhibit an Unexpected Dual Mode of Action. *ACS Chem. Biol.* **17**, 3077–3085 (2022).

* Authors contributed equally

The article was published in open-access with a Creative Commons CC-BY-NC-ND license in ACS Chemical Biology. Rights and permissions are with the authors (including myself, Till Reinhardt).

Biorender:

Various figures were created with BioRender.com.

MS Data:

The mass spectrometry proteomics data of the fluoroquinolone off-target discovery project will be deposited to the ProteomeXchange Consortium *via* the PRIDE partner repository in due course, upon submission and publication of the publication that is currently in preparation.[359]

The mass spectrometry proteomics data of the indolin-2-one nitroimidazole project have been deposited to the ProteomeXchange Consortium *via* the PRIDE partner repository with the data set identifier PXD033128.[359]